Investigation of Rain Attenuation Effect on 5G Millimeter Wave Short-Range Fixed Links

OTHMAN ZAHID

Investigation of Rain Attenuation Effect on 5G Millimeter Wave Short-Range Fixed Links

Othman Zahid

A Thesis presented for the degree of
Doctor of Philosophy

The Centre for Communication Systems
Department of Engineering
University of Durham
England

Submitted in August 2023

Dedication

To my parents, my sisters, my brother, my wife, and to my friend Jose and his family.

Abstract

The evolution of wireless communication has been driven by the limitations of spectrum availability below 6 GHz. As a solution, Fifth Generation (5G) networks have embraced Millimeter Wave (mmWave) frequency bands to meet the demand for higher data throughput across diverse applications. Implementing mmWave frequencies for short-range fixed links, specifically in 5G Fixed Wireless Access (FWA), holds the potential for better user experiences through high data rates, low latency, and cost-effective deployment.

However, the promising potential of mmWave frequencies is accompanied by a significant challenge – rain attenuation. Rain-induced signal degradation poses a substantial threat to signal quality in mmWave short-range fixed links. In response, this thesis undertakes an extensive measurement campaign utilizing experimental fixed link setups operating at distinct frequencies: 25.84 GHz, 77.54 GHz, and 77.125 GHz. These setups span two short-range fixed links, measuring 36 m and 200 m. Augmented by a sophisticated weather station, which facilitates a comprehensive assessment of rain-induced attenuation and scattering effects. The incorporation of various weather parameters, such as rain intensity, drop size distribution, temperature, and refractive index, enhances the accuracy of attenuation measurement and prediction models.

The thesis delves into the investigation of the obtained measurement results, meticulously analyzing rain attenuation across the two short-range links and mmWave frequencies. Key parameters influencing attenuation behaviour, including drop diameter, velocity, and antenna wetness, are examined. A pivotal contribution of this research is the establishment of correlations between measured radio links and weather data. This correlation enhances ITU-R guidelines and guides optimization for FWA 5G networks, particularly impactful in weather-variable regions.

Declaration

The work in this thesis is based on research conducted at Durham University's Centre for Communications Systems, Department of Engineering, and under the funding of Wave-ComBE project partners. No part of this thesis has been submitted elsewhere for any other degree or qualification to this or any other university or institute of learning and it is all my own work unless referenced to the contrary in the text.

Statement of Copyright

Acknowledgements

I would like to thank Professor Sana Salous for the opportunity to work on this interesting research topic, as well as for her supervision and guidance for my PhD.

I would like to acknowledge the support of the WaveComBE project, under Horizon 2020 research and innovation program with grant agreement No. 766231.

Special thanks to the electronics workshop technicians for setting up the weather station and fixed links as well for their support and hardware maintenance during my research project.

I express my sincere gratitude to Dr.-Ing. Jose F. Monserrat for the support and guidance during my career as an Engineer, and during my PhD.

Finally, I want to express my gratitude to my family for their encouragement and support throughout the years.

Contents

List of Figures

List of Tables

Acronyms

3G Third Generation.

4G Fourth Generation.

5G Fifth Generation.

ADSL Asymmetric Digital Subscriber Line.

AnR Antenna Array.

AP Access Point.

AR Augmented Reality.

BRE Bistatic Radar Equation.

BS Bistatic Scattering.

BSCS Bistatic Scattering Cross Section.

BSRE Bistatic Scattering Radar Equation.

CCDFs Complementary Cumulative Distribution Functions.

CMLs Commercial Microwave Links.

CW Continuous Wave.

dB Decibels.

DBSG-3 Data Base Study Group 3.

DDFS Direct Digital Frequency Synthesiser.

DNs Distribution Networks.

DSD Drop Size Distribution.

DSL Digital Subscriber Line.

EMS Electromagnetic Interference.

FDTD Finite-Difference Time-Domain.

FFT Fast Fourier Transform.

FMCW Frequency Modulated Continuous Wave.

FTTX Fiber-To-The-X.

FWA Fixed Wireless Access.

GCD Greatest Common Divisor.

GUI Graphical User Interface.

IOT Internet Of Things.

IP Internet Protocol.

ITU-R International Telecommunication Union Radiocommunication Sector.

LO Local Oscillator.

LoS Line of Sight.

mDN mmWave distribution network.

MIMO Multiple-Input Multiple-Output.

mmWave Millimeter Wave.

NLoS Non-Line-of- Sight.

NTP Network Time Protocol.

OLN Orange Labs Network.

OTT Over-the-Top.

PCB Printed Circuit Board.

PLL Phase Locked Loop.

PoP Point of Presence.

PTP Point To Point.

QoS Quality of Service.

RF Radio Frequency.

RMS Root Mean Square.

RMSE Root Mean Square Error.

RR Rain Rate.

RSS Root-Sum-of-Squares.

SAR Statistical Attenuation Ratio.

SMA SubMiniature version A.

SNR Signal-to-Noise Ratio.

VAR Virtual Augmented Reality.

WAE Wet Antenna Effect.

WMO World Meteorological Organisation.

Chapter 1

Introduction

1.1 Motivation and Objectives

Due to the limited spectrum below 6 GHz for current wireless systems, mmWave frequencies now support Fifth Generation (5G). This enables a broad range of services and applications needing ample bandwidth for high customer data throughput. Fixed link systems are among the networks and applications that operate in the higher frequency bands [4]. Leveraging mmWave for these links enhances internet quality of service, ensuring a smoother customer experience with high data rates, low latency, cost-effectiveness, and improved performance [1]. Such links provide a variety of deployment scenarios, that require optic fibre cables, including broadband household access WiFi Access Point (AP), small cell backhaul, and streaming media exchange. On the other hand, rain attenuation becomes the primary fading process at higher frequency bands above 10 GHz. In this context, mmWave is notably more affected by rainfall attenuation than multipath, a characteristic seen at lower frequencies [5; 6]. Furthermore, rain attenuation not only decreases received power but also introduces time oscillations in received power. Fixed link systems employing the mmWave frequency band and analogue beam-forming will necessitate a precise evaluation of system performance to guarantee that practical performance in the field fulfils the requirements.

Given that short-distance fixed links operating at mmWave frequencies experience significant attenuation due to precipitation, we need to develop a technique to estimate and

measure the annual percentage of time that these links might experience service interruptions caused by precipitation-induced attenuation. This is critical for designing and optimizing mmWave networks at a low cost. Furthermore, accurately modelling the impact of rain attenuation across different link distances necessitates extensive measurement data, especially for short links under 300 meters, which are potential options for 5G mmWave Fixed Wireless Access (FWA) applications. It's important to highlight that weather datasets significantly impact both measured and predicted attenuation. The variability of these datasets across locations makes it impractical to rely on universal weather data for attenuation prediction.

As a necessary consequence, this thesis focuses on investigating the impact of rain attenuation on mmWave short-range fixed links for 5G FWA applications. Additionally, it analyses the scattering effect induced by raindrops. The study employs a long-term measurement campaign, utilizing two experimental fixed link setups on the building's roof. These setups simulate point-to-point over-the-air transmission. The system is operating at 25.84 GHz and 77.54 GHz over 36 m direct and side links and 77.125 GHz over 200 m point-to-point links. The research work study is accompanied by a high-capability weather station, which provides a variety of precipitation datasets for attenuation prediction, modelling, accuracy, and reliability of the study. The weather data includes rain intensity, raindrop size distribution, temperature, the refractive index of water, and rainfall velocity.

To attain the main goal, it was required to form and meet targeted objectives, which included:

- Deploy measurement systems on the building's roof to simulate short-range fixed links (36 m and 200 m links) that operate on Continuous Wave (CW) at 25.84 GHz and 77.54 GHz with dual polarization. The PWS100 weather sensor was used to collect weather data.
- Carry out long-term measurement campaigns for both radio data for loss measurement and weather data for prediction and modelling statistics.
- Measure rain attenuation from the received signal.

- For results evaluation, the measurement results are matched against the prediction models.

- Gain insights into signal behaviour during various rainfall events by incorporating additional parameters that influence overall attenuation. These parameters include drop diameter, velocity, and other relevant factors, particularly for the 36 m and 200-point-to-point links. Additionally, the study will explore the impact of the wet antenna on signal performance.

- Validate measurement results against models while evaluating and investigating the suitability of prediction models for short-range links. This evaluation aims to improve rain attenuation predictions beyond conventional approaches, enabling telecommunications providers to deliver higher-quality service at a reduced cost during rainy events. By refining prediction models, telecoms providers can optimize their network planning, resource allocation, and operational efficiency. For instance, a more accurate understanding of rain attenuation allows providers to implement adaptive modulation and coding schemes, minimizing service disruptions and ensuring consistent performance during adverse weather conditions. Moreover, advancements in prediction accuracy can lead to the design of more robust and cost-effective infrastructure. For instance, the ability to precisely predict rain attenuation levels enables providers to optimize the deployment of costly signal amplification and compensation mechanisms, ensuring they are selectively utilized when necessary. This strategic approach not only enhances service quality but also contributes to cost reduction by avoiding unnecessary investments.

  The study will be based on datasets from Northeast England and it is aligned with International Telecommunication Union Radiocommunication Sector (ITU-R) recommendations. Furthermore, the analyses aim to ensure the reliability and universality of the proposed improvements in rain attenuation predictions for short-range links.

- Compute the bistatic scattering parameters utilizing a realistic side link and weather data to study the interference due to raindrops scattering.

- Evaluate ITU-R distance factor for short-range rain attenuation measurement and input for optimization engineers by establishing a realistic correlation between radio links data for Fixed Wireless Access (FWA) 5G applications and weather precipitation data. This research aims to enhance the accuracy and effectiveness of ITU-R guidelines and optimization strategies by incorporating relevant insights from the combination of these datasets. The ultimate goal is to improve the performance and reliability of FWA 5G networks, particularly in areas prone to varying weather conditions.

1.2 Thesis Contribution

This research work has received support from the WaveComBE project, which is part of the Horizon 2020 Marie Curie program. The thesis makes a significant contribution to the current literature in the following ways:

- This research work meticulously explores rain attenuation measurements within mmWave frequency bands, with a specific focus on short-distance fixed links. This departure from the prevalent emphasis on long-distance fixed links exceeding 1 km addresses a critical gap in the existing literature. Short links hold significance as they are integral components of various communication systems, particularly in urban environments with high population density, where compact network infrastructures are essential.

  To ensure the utmost precision and reliability of the study, a diverse set of realistic radio and weather data was collected. This was achieved through the implementation of a sophisticated mmWave channel sounder setup and a state-of-the-art weather station. The comprehensive approach of the project involves analyzing rain attenuation from various perspectives. Beyond just examining rainfall intensity, the study has been expanded to assess the influence of Drop Size Distribution (DSD), drop diameter, velocity, number of dominating drops, and antenna wetness effect.

  Understanding the intricacies of rain attenuation in short-distance fixed links is crucial for optimizing the performance of mmWave communication systems. These

systems, which are becoming increasingly prevalent, especially in 5G networks, heavily rely on short-distance links for high-speed and low-latency connectivity. Therefore, the research not only contributes to the scientific understanding of rain attenuation but also directly addresses the practical challenges faced by modern communication networks.

- In order to address the lack of readily accessible one-minute rain rate data for specific locations, this study has introduced one-minute and 0.01% precipitation data from locations with comparable weather conditions. This approach ensures that relevant information is available even when direct one-minute rain rate data is unavailable for a particular location.

- The evaluation of rain attenuation prediction models heavily relies on the path reduction factor's significance. In this research endeavour, we make a substantial academic contribution by investigating the appropriateness of the currently recommended actual distance factor, as proposed by ITU-R, for short-range links. It is worth noting that the existing factor is predominantly derived from long-range datasets, raising pertinent concerns about its suitability for shorter distances. Long-range datasets typically encapsulate scenarios where signals travel extended distances, encountering diverse atmospheric conditions. While this information is invaluable for understanding rain attenuation at substantial distances, its applicability to short-range links is questionable. Short-distance fixed links, common in urban and densely populated areas, exhibit unique characteristics and face distinct challenges that long-range datasets may not fully capture.

  The critical concern arises from the fact that relying on long-range datasets for short-range predictions can lead to inaccuracies and suboptimal performance in mmWave communication systems. Short links are subject to different environmental conditions, terrain characteristics, and signal propagation dynamics compared to their long-range counterparts. Therefore, the need to specifically tailor rain attenuation predictions for short-distance links becomes imperative to ensure the reliability and effectiveness of mmWave communication systems in diverse scenarios.

  By conducting a meticulous and thorough study using measurement data, we demon-

strate the inadequacy of the prescribed distance factor restriction of 2.5 put forth by ITU-R SG3. This scholarly investigation sheds light on the limitations of the current approach and highlights the need for a more precise consideration of distance factors for short-range links.

- The findings of this study hold valuable implications for the assessment of transmission system design in point-to-point links below 300 m. These results are particularly relevant for evaluating FWA and mmWave distribution network (mDN) in rainy weather conditions. The significance lies in the scarcity of measurements dedicated to studying the characteristics of wireless fixed transmission links under such weather conditions. Therefore, this research offers a crucial contribution by presenting a near-perfect scenario for FWA and mDN networks, enabling a more informed and effective design approach for short-range transmission systems in adverse weather conditions.

- In this study, a meticulous analysis approach was adopted to quantify the scattering characteristics of raindrops. To investigate interference-induced scattering caused by rainfall, a real side link was utilized, specifically focusing on Non-Line-of- Sight (NLoS) components. Additionally, meteorological data and the well-established Mie methodology were incorporated to identify and assess the scattering phenomena involved. By employing this comprehensive methodology, the research aims to gain valuable insights into the scattering caused by raindrops, providing a deeper understanding of the interference effects in practical scenarios.

The long-term measurement data, consisting of disdrometer-meteorological records spanning three years and collected from the PWS100, has now become available. The data were submitted to the ITU-R Data Base Study Group 3 (DBSG-3). The results of the present study, based on the data, were submitted for review during the June 2021 ITU-R Study Group 3 meeting. The study's outcomes were instrumental in effecting a significant change in the ITU-R P.530-18 guidelines. Specifically, the restriction on the distance value, set at 2.5, was approved for deletion in the new version of ITU-R P.530-18. This proposal emerged following thorough discussions surrounding the original empirical derivation of the distance factor value restriction. Recognizing the study's substantial in-

fluence, it is crucial to emphasize the need for ongoing efforts to maintain the relevance of ITU-R guidelines. The availability of robust data, as demonstrated in this study, positions it as a valuable asset for continuous updates. To mitigate potential stagnation, establishing a systematic approach for regular reviews and revisions is recommended. This proactive strategy ensures that the guidelines remain adaptive to the evolving telecommunications landscape. Moreover, fostering collaborative initiatives among researchers, industry experts, and regulatory bodies will strengthen the iterative process, enhancing the guidelines' responsiveness to emerging technologies. The study's emphasis on data quality serves as a catalyst for reinforcing the guidelines' effectiveness, positioning them as a dynamic and influential resource within the telecommunications community.

1.3 Organisation of the Thesis

This thesis is structured as follows:

The **second chapter** of this thesis offers a comprehensive overview of fixed link systems and their use cases in 5G applications, with a particular focus on adopting mmWave frequency bands. Within this chapter, a detailed description of the mechanisms that influence precipitation's impact on mmWave propagation is presented. This knowledge proves crucial for accurate link budget calculations, particularly in the context of FWA short-distance networks.

In the **third chapter**, the fixed link experimental setup employed for rain attenuation measurement is comprehensively described. The chapter offers a detailed overview of the rooftop point-to-point transmission system, covering its various components, including the 36 m direct link, side link, and 200 m link. Additionally, a dedicated weather station was installed to collect precise precipitation data, crucial for attenuation prediction and modelling in the experimental setup. Furthermore, the chapter describes the data collection methodology adopted for both weather and radio data. The procedures used for acquiring and recording the essential information are thoroughly outlined, ensuring a meticulous and systematic approach to data gathering. By presenting this comprehensive account of the experimental setup, data collection, and measurement procedures, the third

chapter lays the groundwork for sound and reliable rain attenuation measurement in the context of fixed link systems. The integration of the rooftop point-to-point transmission system, coupled with accurate weather data, contributes to the robustness of the study's results and enhances our understanding of rain-induced attenuation in practical scenarios.

The **fourth chapter** presents long-term weather data statistics and rain attenuation predictions for the specified frequency bands. This analysis provides insights into weather patterns throughout the measurement period and helps assess the impact of rainfall on transmission performance.

In the **fifth chapter** we present the measurement results obtained from the 36m direct and side fixed links. The chapter offers a detailed analysis and thorough evaluation of the received signals, allowing for the derivation and comprehensive examination of the measured attenuation. Various characteristics of attenuation are explored and discussed in depth. Moreover, the chapter delves into the scattering measurement conducted via the side link, providing valuable insights and observations related to this aspect of the study. Through meticulous investigation and interpretation of the measurement data, this chapter contributes essential findings to the overall research, enhancing our understanding of rain attenuation and scattering effects in the context of fixed links for further advancement in the field.

In **Chapter six**, we present the measurement results obtained from the 200 m link utilizing Filtronic transceivers. The chapter provides an investigation of the measurement data, enabling a deeper understanding of the link's performance in terms of attenuation and its sensitivity to different environmental factors. By presenting and analyzing these results, the research advances our knowledge of the behaviour of point-to-point transmission systems over a 200 m link. These findings contribute valuable insights to the broader field of telecommunications, enhancing our ability to optimize and design reliable communication networks in rain-prone environments.

In **chapter seven**, conclusions have been drawn, and proposals for future research work are provided.

1.4 Contributions & Publications

Contribution to the ITU-R SG3:

- Fixed Link Long-term Measurements. ITU-R WP3M Contribution 218, United Kingdom of Great Britain and Northern Ireland.
- Submission of Rain Statistics for DBSG-3. ITU-R WP3M Contribution 224. United Kingdom of Great Britain and Northern Ireland.

The following papers have been published in conferences, accepted for publication in journals, and to be submitted:

- **O. Zahid**, J. Huang and S. Salous, "Long Term Rain Attenuation Measurements at Millimeter Wave Bands for Direct and Side Short-Range Fixed Links," 2020 XXXIIIrd General Assembly and Scientific Symposium of the International Union of Radio Science, 2020, pp. 1-4, doi: 10.23919/URSIGASS49373.2020.9232024.
- J. Huang, **O. Zahid** and S. Salous, "Clutter Loss Measurements and Modelling at 25.84 GHz Band," 2020 XXXIIIrd General Assembly and Scientific Symposium of the International Union of Radio Science, 2020, pp. 1-4, doi: 10.23919/URSIGASS49373.2020.9232316.
- **O. Zahid** and S. Salous "Long Term Rain Attenuation Measurement for short-range mmWave Fixed Link using DSD and ITU-R Prediction Models. Radio Science, April 2022, 57(4), https://doi.org/10.1029/2021rs007307.

Presentations were given and deliverables:

- **O.Zahid**, J. Huang, and S.Salous "Long Term Rain Attenuation Measurements for Millimeter Wave Short-range Fixed Links," in Festival of Radio Science URSI, 16 Dec 2019 in Manchester University, UK.
- **Othman Zahid** and Sana Salous "Two Years Rainfall Statistics for 5G mmWaves Rain Attenuation Prediction in Durham, England" AGU Fall meeting, New Orleans 2021.

- **Othman Zahid** and Sana Salous ”Precipitation effects and potential interference between mmW radio links”, WaveComBE project deliverable number 2.3, July 2021.

Chapter 2

Millimeter Wave Fade Mechanism Due to Precipitation

Millimeter Wave technology has the capability to attain significantly broader bandwidths, facilitating high-speed data transmission and accurate detection for point-to-point links within the framework of FWA. Investigating and analyzing the efficiency loss experienced by fixed wireless networks during precipitation events yields comprehensive characteristics for loss estimation, link performance evaluation, and optimal link design and deployment. This chapter provides an in-depth exploration of the fixed link concept for 5G applications employing mmWave frequency bands. Additionally, it delves into the fade mechanism of mmWave communication resulting from precipitation attenuation and scattering, shedding light on the challenges and considerations in deploying mmWave technology for FWA.

2.1 Basics of Fixed Wireless Access

The traditional telecommunications network relies extensively on copper cables for connectivity, taking advantage of copper's durability and resistance to environmental variables [7]. While fibre optic connections provide more bandwidth, copper's well-established infrastructure covers bandwidth requirements for voice and basic data services [8]. Copper's historical use in effectively transmitting signals over great distances, combined with its low cost, makes it an ideal candidate for last-mile connectivity to the central office

[9]. However, copper cables are prone to electromagnetic interference, which degrades internet connection quality [8]. However, larger organizations with higher traffic volumes have the option to be linked through fibre optics or point-to-point microwave links. This network of interconnected links is commonly referred to as the local access network. Fixed wireless links have been in existence for several years. Thanks to advancements in technology, especially hardware innovations in radio communication, there has been a successful utilization of increasingly higher frequency bands. FWA networks, essentially, represent yet another means of connecting client buildings to the existing network. As cellular communication, data transmission, and digital streaming technologies converge, the demand for flexible broadband communications directly to small businesses and homes is rapidly increasing.

Upgrading current networks to support broadband capabilities through fibre optics can be a resource-intensive process in terms of both costs and time. In such cases, adopting fixed link systems as a delivery mechanism offers various advantages. Fixed wireless networks are considered a much less costly alternative to wired networks, eliminating the need to lay pipes or deploy wires, thus significantly reducing implementation time scales. Currently, appropriate technologies in a proven condition exist to satisfy these service needs. A considerable number of businesses already provide solutions that provide end-user connectivity at rates ranging from 2 to 8 Mbits per second. However, the potential increasing demand for data transfer, high throughput, and the quickly emerging of industry 4.0 technologies such Internet Of Things (IOT) applications introduce a non-satisfaction in terms of data throughput. As a necessary consequence, higher frequency bands (mmWaves) are being promoted to be used for fixed link systems, particularly short-range point-to-point links such as building-to-building or lamppost-to-lamppost transmission. FWA is a system that uses wireless technology rather than fixed wires to deliver high data throughput access to households. According to recent figures, Verizon's fixed wireless customers spend an average of 300GB of data per month, while T-Mobile's FWA subscribers use approximately 450 GB of data per month [10]. Forecasts suggest that FWA connections will increase significantly, with an estimated 165 million homes and businesses linked by 2027, up from 70 million in 2021 [11]. According to Ericsson's research, over 80% of mobile service providers provide FWA packages [12]. However, previous wireless

mobile communication networks such as the Third Generation (3G) and the Fourth Generation (4G) were utilized to provide fixed internet access, but they could not provide high download data speed or low latency levels that could match fibre broadband connection. 5G FWA might solve these issues by employing 5G network technologies such as array antennas, beam-forming, and a high-frequency mmWave spectrum to give services comparable to those provided by a fibre broadband network [13].

In early 2018, some vendors launched 5G user trials in many locations around the world utilizing mmWave frequencies to deliver FWA pre-commercial service in various cities and residential areas throughout Western Europe, China, and the United States. Orange Group in France has initiated the global 5G testing and trials program in Europe. Orange has conducted Europe's first 5G FWA field testing in Orange Labs Network (OLN), using 26 GHz radio stations. Such type of short-range fixed link offers great performance and capacity with minimal latency, in addition to providing an alternate solution to Asymmetric Digital Subscriber Line (ADSL) broadband, WIFI, and Wi-Max and targeting more new business. Furthermore, one of the primary functions of 5G FWA is to supply customers with quality broadband internet, Over-the-Top (OTT) video or TV channels, and telephone/wireless services. Such a system intends to use Augmented Reality (AR) and Virtual Augmented Reality (VAR) technologies, which will allow for the real-time integration of digital content with the live stream or the user's environment. Users' awareness and demand for services that employ AR and VAR technology is growing, as is the number of devices that use this technology. As a result, operators must alter their networks to enable such applications, and 5G FWA is a promising option. Thanks to 5G technology and the IEEE 802.11ay standardization, many scenarios use cases can be implemented using mmWave frequency bands within licensed mmWave spectrum. As an alternate approach, 802.11ay proposes the conception of the mmWave distribution network (mDN), which gets to run on the unlicensed 60 GHz spectrum. Because of the lower cost of network equipment and higher speeds compared to Fiber-To-The-X (FTTX) networks, FWA has subsequently drawn a lot of interest from service providers. The mDN employs a multi-hop multi-point mesh network architecture with a high density of allocation nodes Distribution Networks (DNs) and client nodes. Although under situations, i.e., scenarios or conditions in which devices within the mmWave distribution networks operate. These

situations may involve factors such as environmental conditions, interference, or obstacles that can impact the operation of the network. For example, mmWave signals often require a clear LoS for optimal performance. Devices in the mmWave distribution networks operate in an outside environment with Line of Sight (LoS) channels as shown in Figure. 2.1. The distance between the paired DNs is usually less than 300 meters for each hop. The downlink viable data transmission requirement per DN is greater than 4 Gbps, while the latency need is less than 15 ms. When addressing possible mDN problems such

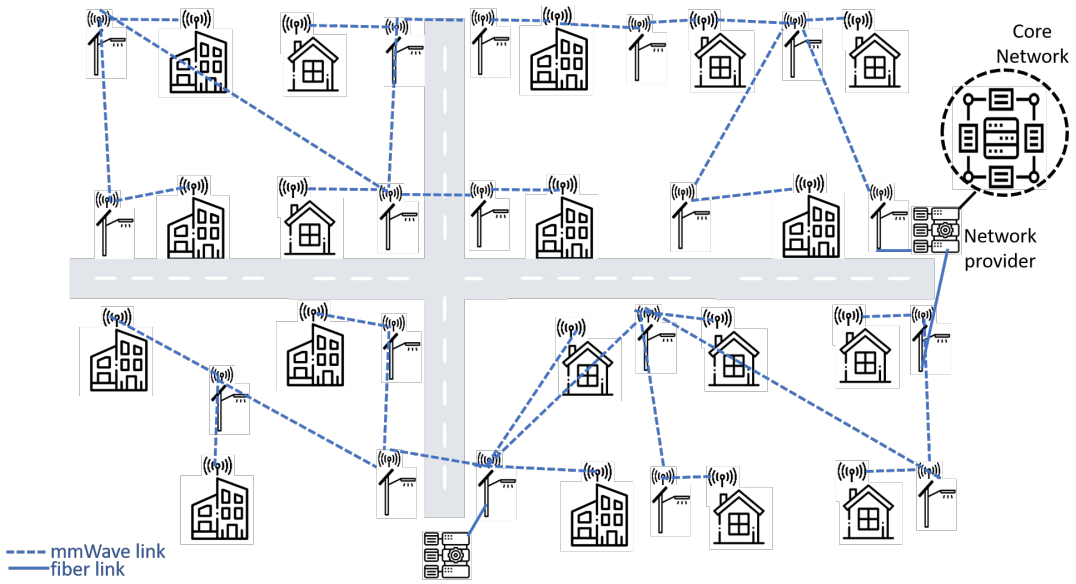

Figure 2.1: Air interface design for 5G FWA and mmWave distribution network (conception copied from the research work that has been performed in [1]

as interference and beam tracking, LoS link among DNs is essential. The DNs in the mDN may be placed on a variety of surfaces, including rooftops, house sidewalls, and public street lampposts. The mDN is linked to the provider network through an optical fibre link at a Point of Presence (PoP). The distance between DNs can be up to 1000 m for roofs and 300 m for street lampposts, respectively, whereas the distance between a DN and CN can be up to 100 m [1; 14; 15]. Besides the features of efficient deployment, fewer physical boundaries, and high throughput provided, FWA applications use narrow beams due to higher frequency bands implemented, which critically limits the number of users. High-gain antennas have often been used in fixed links. Although, since it is widely recognized, Multiple-Input Multiple-Output (MIMO) communication lines may yield a significant boost in system efficiency. However, works like in [16] showed that

using antenna arrays may significantly improve a system's user capacity, allowing several users to access the same narrowband spectrum at the same time. The antenna beamwidth and directivity are major design parameters for such purposes. These must be properly tuned to avoid overall system loss due to unintended mismatch. The majority of Line of Sight (LoS) links are built for LoS communications in outdoor environments where devices are subjected to weather and environmental conditions that might degrade Quality of Service (QoS).

2.2 Millimeter Waves for FWA

The utilization of mmWave in the frequency range of 30 to 300 GHz offers several advantages, making it an attractive choice. This frequency range provides a substantial amount of raw bandwidth, enabling data rate transmission with throughputs of many gigabits per second (Gbps) [4; 17]. Millimeter waves have proven successful in long-range wireless communication systems, specifically in Point To Point (PTP) setups [18; 19]. They have also demonstrated effectiveness in certain short-range links [20–23]. The mmWave spectrum's broad bandwidth, operational at frequencies up to 3 GHz, offers a cost-effective solution compared to cable, Digital Subscriber Line (DSL), and fiber across diverse applications. This enables the acquisition of essential bandwidth to support emerging 5G applications for households in both metropolitan and rural areas. Despite certain challenges and criticisms regarding the propagation qualities of mmWave spectrum, Fixed Wireless Access (FWA) stands out as a high-performer in this domain, providing significant contributions to fast data throughput, compact antenna sizes, and RF circuits. Addressing the transmission characteristics of mmWave signals can be complex due to their relatively high path loss compared to lower frequency systems, along with additional losses caused by precipitation. However, the short wavelength of mmWave frequencies allows for solving this issue by incorporating a large number of antennas into a confined space, facilitating adaptive alignment of transmission and receiving beams through array technologies.

Precipitation, on the other hand, can lead to a substantial reduction in the received Signal-to-Noise Ratio (SNR), requiring extra precautions. As mmWave fixed link transceiver

units are often located outdoors, such as on street lamps or building rooftops, raindrops and snow can result in intolerable outage probability unless the link budget is effectively maintained on a regular basis. This challenge is particularly daunting for mmWave fixed links, where attenuation can cause significant SNR loss, sometimes by several decibels (dB).

2.3 Fade Mechanism & Link budget

To establish a Line-of-Sight (LoS) fixed link using mmWave between the Radio Frequency (RF) transmitter and receiver, a comprehensive analysis of the propagated power is essential to ensure optimal bandwidth efficiency for the specific propagation channel. Generally, mmWave systems face challenges in terms of their sensitivity to the propagation environment, with precipitation attenuation being a significant limiting factor for mmWave fixed links. The received power for a particular link can be described in equation 2.3.1:

$$P_{RX} = P_{TX} + G_{TX} + G_{RX} - P_L - A_{TM} - L_{OT} \tag{2.3.1}$$

where $P_{TX}(\text{ dB})$ and $P_{RX}(\text{ dB})$ are transmit and receive signal power, G_{TX} (dBi) and G_{RX} (dBi) are transmitter and receiver antenna gain, $P_L(\text{ dB})$ is the propagation path loss (2), $A_{TM}(\text{ dB})$ is the atmospheric loss (5), and $L_{OT}(\text{ dB})$ refers to losses from other factors such as cables, system stability, connectors, and RF/antennas mismatch.

2.3.1 Atmospheric Effect on mmWave FWA

This absorption attenuation occurs when the electromagnetic radiation's oscillating electric and magnetic fields contact with polar molecules like water vapour and oxygen, causing them to oscillate and rotate. These induced molecular oscillations and rotations remove energy from the advancing electromagnetic wave by converting it to kinetic energy, which results in wave energy absorption. Higher frequencies see higher attenuation as

induced molecular oscillations become more efficient at releasing energy. As a result, electromagnetic propagation in the atmosphere is subject to an inherent attenuation process caused by absorption by polar atmospheric gases that exist regardless of weather conditions. This attenuation is unavoidable since these molecules constitute a fundamental aspect of the atmosphere. A simplified approach for atmospheric attenuation A_{TM} can be expressed in equation 2.3.2:

$$A_{TM} = A_{RR} + A_{VP} + A_{DA} + A_{OT} \tag{2.3.2}$$

where A_{RR} attenuation due to rain, A_{VP} water vapour attenuation. A_{DA} represents dry air attenuation and A_{OT} represents additional factors that include various minor contributions, such as aerosol attenuation, cloud attenuation, or other atmospheric phenomena that impact the transmission of electromagnetic waves.

2.3.1.1 Gaseous Attenuation

Atmospheric gaseous absorption causes attenuation of electromagnetic signals propagating through the atmosphere. This absorption attenuation is affected by the temperature, pressure, and humidity or water vapor density of the air. Higher temperatures, pressures, and water vapor content will increase gaseous absorption losses. The absorption is caused by molecules in the air interacting with the electromagnetic waves. Oxygen and water vapor are two key absorbers. Oxygen molecules absorb electromagnetic radiation through magnetic dipole rotational transitions and molecular vibrational transitions. Water vapor absorbs radiation through electric dipole rotational transitions [24; 25].

As electromagnetic waves propagate through the atmosphere, their oscillating electric and magnetic fields stimulate these molecular rotations and vibrations. The energy absorbed by the molecules from the electromagnetic fields leads to the heating of the air. In effect, the propagating radio signal loses energy to stimulate the molecular motions, attenuating the radio wave through the conversion of its energy into heating the atmosphere. The amount of absorption, and resulting attenuation, depends on the concentration of oxygen and water vapor molecules which can interact with the radiation. Higher

humidity means more water vapor molecules able to absorb energy. Higher temperatures and pressures mean faster molecular motions and more molecular interactions with the electromagnetic fields per unit volume. This increases the absorption attenuation under those conditions [26]. In general, atmospheric gaseous absorption by oxygen and water vapor leads to the conversion of electromagnetic signal energy into heating of the air. This causes an inherent attenuation of radio signals passing through the atmosphere, even in clear conditions.

Recommendation ITU-R P.676-10 proposed a method for determining atmospheric gaseous attenuation properly. The specific attenuation (dB/km) by atmospheric gases as γ_g is the combination of specific attenuation of dry air γ_d(dB/km) and specific attenuation of water vapour γ_w dB/km, where the oxygen attenuation usually remains constant, with just minor variations. As altitude increases, pressure drops and each of these absorption lines becomes apparent, i.e., the absorption lines refer to spikes in attenuation at frequencies where atmospheric gases like water vapor resonate and absorb energy. For water vapour attenuation, the water vapour molecule contains a persistent electric dipole, which creates a resonance that causes attenuation. Because attenuation relies on water vapour density, the fluctuation of attenuation due to water vapour is significantly larger than that of oxygen. This is often stronger during the summer months and in hot, humid circumstances such as those seen in tropical places; but, for any location, the greatest attenuation owing to water vapour occurs during the season with the most rainfall [27]. The specific gaseous attenuation (dB/km) is given by equation 2.3.3:

$$\gamma = \gamma_d + \gamma_w = 0.1820 f N''(f) \tag{2.3.3}$$

where $N''(f)$ given by equation 2.3.4 is the imaginary part of the frequency-dependent complex refractivity:

$$N''(f) = \sum_i S_i F_i + N''_D(f) \tag{2.3.4}$$

S_i is the strength of the i-th line, F_i is the line shape factor and the sum extends over all the lines expressed in ITU-R P.676-10.

2.3.1.2 Scintillation Enhancement

Scintillation can be defined by rapid fluctuations in the amplitude and phase of a radio signal sent over a turbulent atmosphere. It is induced by small-scale variations in the refractive index of the air along its propagation route. These index inhomogeneities are caused by changes in meteorological variables including temperature, pressure, and humidity. Numerous investigations have shown that higher temperature and humidity cause more turbulence and scintillation [28]. The stochastic fluctuations in the refractive index cause dispersion effects, which modify the phase and amplitude of the signal. To effectively model tropospheric scintillation, detailed measurements of temperature, pressure, humidity, and turbulence throughout the propagation path are required. However, complete measurements of these climatic parameters are frequently insufficient. This has forced the construction of semi-empirical scintillation models using more constrained data [29]. To further improve scintillation prediction capabilities, more targeted field investigations are needed to better characterise the links between fine-scale weather variability and propagation effects across climate areas. These increased propagation data sets can help refine physics-based scintillation models.

2.3.1.3 Cloud Attenuation

Clouds consist of dispersed water droplets that form in supersaturated air. The attenuation of clouds is influenced by the quantity of liquid water present and the cloud type. Precise calculation of cloud attenuation relies on accurately assessing the density of water vapour within the cloud. As frequency increases, cloud attenuation becomes a more significant concern, particularly for higher frequency bands, as cloud particles are orders of magnitude smaller than raindrops. Rec. ITU-R P.840-4 provides guidelines for modelling and quantifying cloud attenuation, and it can be expressed in equation 2.3.5:

$$\gamma_c = K_l M \quad (\text{ dB/km}) \tag{2.3.5}$$

where:

γ_c : specific attenuation (dB/km) within the cloud,

K_l : specific attenuation coefficient $\left((\text{dB/km})/\left(\text{g/m}^3\right)\right)$ and

M : liquid water density in the cloud or fog $\left(\mathrm{g/m^3}\right)$.

2.3.1.4 Rain and Snow Attenuation

Rain is a meteorological phenomenon in which droplets of liquid water descend towards the Earth's surface and can be classified as convective or stratiform. Convective rain tends to be more intense and slightly longer-lasting than stratiform rain, which occurs when excess moisture is driven over sloping topography [30; 31]. To gain a proper understanding of how signals attenuate along mmWave fixed links when they encounter precipitation, one must first grasp the concept of precipitation. Precipitation in Earth's atmosphere takes various forms, including liquid rain, clouds, snow grains, snowflakes, graupel, sleet, hail, and drizzle, among others. Rain, being the most common form of precipitation, occurs worldwide, but its spatial variation, nature, and causes vary depending on the location.

2.3.2 Velocity

Raindrop and rainfall velocity are key parameters in estimating rain attenuation within the DSD prediction model. Works in [32; 33] result in the terminal velocity equation 4.3.10:

$$v(D) = 9.65 - 10.3\exp(-0.6D) \tag{2.3.6}$$

where $v(D)$ is the raindrop velocity of drop diameter D in $\mathrm{ms^{-1}}$.

2.3.3 Refractive Index of Water

In physics, the index of refraction is the ratio of the speed of light in space to the speed of light in a material. A material's index of refraction may be calculated using the formula (n = λ_0/λ_n), where λ_0 is the wavelength of light in the vacuum and λ_n is the wavelength in the material. Water's dielectric characteristics are often represented at mmWave frequencies by the complex refractive index [34]. It is given by equation 2.3.7:

$$N = n' + in'' \tag{2.3.7}$$

The imaginary element of N is associated with wave attenuation, whereas the real part is linked to phase difference or wave velocity.

2.3.4 Rain Attenuation

Prior studies, including [35], have highlighted the significant impact of rain attenuation on mmWave systems, underscoring its potential to limit system reliability, and making it a crucial consideration for fixed links. Raindrops smaller than a wavelength absorb energy from the transmitted wave, resulting in a heating response that diminishes the wave's energy. This constitutes a major source of rain attenuation, the severity of which depends on the frequency. On the other hand, raindrops larger than a wavelength scatter the incident mmWave propagation, leading to a reduction in signal amplitude at the receiving point. The extent of scattering is influenced by the distribution, direction, and intensity of the raindrops. Additionally, raindrops depolarize the incident wave polarization, mainly through scattering.

As a response to these challenges, various analytical and empirical studies ([36–48]) have been conducted to estimate the effect of rain attenuation on terrestrial channels. Evaluating the interplay between signal degradation and rainfall is essential for achieving efficient long-range terrestrial links or terrestrial-to-satellite links. However, few studies have specifically focused on the effect of rain attenuation over mmWave FWA links.

2.3.5 Specific Rain Attenuation

The specific attenuation γ_R given by equation 2.3.8 defines the attenuation of a radio wave per unit distance given in dB/km. ITU-R P.838-3 provides a power law relationship between the Rain Rate (RR) in mm/h and the frequency and polarization dependent coefficients k and α given in ITU-R P.838-3.

$$\gamma_R = k.(RR)^{\alpha} \tag{2.3.8}$$

2.3.6 Short Range Links

As previously mentioned, the loss characteristics of FWA communication systems operating at mmWave frequencies are significantly affected by rain attenuation. To design an economical system at these frequencies, understanding the occurrence of rain attenuation at the system's location is crucial. Developing a methodology to predict the number of minutes per year that a radio link will experience service outages due to excessive rain attenuation is essential for a given link range. The term "range" refers to the distance between two antennas in a wireless network that can communicate with each other. However, the range encompasses more than just the distance between the transmitter and receiver; factors like obstructions, topography, radio physics, antenna design, and noise levels all play a role in determining the effective range of the link. When implementing fixed links systems using mmWave frequency bands, several considerations, such as data rate, noise level, free space loss, diffraction, multipath effects, and wavelength, should be taken into account for range selection.

To model the rain attenuation effect across various link lengths, significant propagation measurements are required, particularly for short-range fixed link rain attenuation synthesis, as short links below 300 m are considered a promising solution for 5G mmWave FWA applications. Existing research in the literature that focuses on short-range rain attenuation is diverse but limited in terms of available radio measurement data, weather data, or measuring techniques. Most studies assess measurement accuracy using prediction models such as ITU-R, and they often only consider rain intensity. However, for these types of links, the analysis should extend to factors that directly impact the mmWave signal, such as raindrop diameter, velocity, number of drops, or Drop Size Distribution (DSD).

2.3.7 Rain Rate

The DSD models and drop shape models can be utilized to predict attenuation, but obtaining the necessary input data presents challenges. Disdrometers capable of measuring the DSD are still uncommon and not routinely available to many system designers. Likewise, instrumentation to accurately characterize individual drop shapes in situ remains costly and scarce. Consequently, despite the availability of DSD and drop-shape models, their

application for attenuation prediction is practically limited by the lack of extensive measurements of these properties in operational propagation links. Rain rate is also typically related to attenuation since it is a quantity that is widely recognized and its statistics are well understood and can be applied to utilize simplified models given the case that the DSD data is not available. Rain rate, often known as rain intensity, is measured in millimetres per hour (mm/h). It should be emphasised that the prerequisite of one-minute rain rate data for estimating rain attenuation is a significant challenge because it is not always easily available for every location. The 0.01% exceeded rainfall rate, denoted $R_{0.01}\%$, represents the rainfall rate exceeded for only 0.01% of an average year. The 0.01% threshold corresponds to periods of very heavy rainfall that occur quite rarely but can profoundly impact system performance. Designing the radio link budget and fade mitigation strategies to handle the attenuation and impairment effects during such infrequent but intense rain events helps ensure reliable availability and connectivity for the desired 99.99% of the time statistically. The ITU Rain Model utilizes $R_{0.01}\%$, in conjunction with other factors like frequency, polarization, path length, and drop size distribution, to predict rain attenuation on links. So while extreme rainfall may be rare, accounting for the 0.01% exceeded rainfall rate is essential for robust radio system engineering and deployment [49]. Specifying and designing for the appropriate $R_{0.01}\%$ value for the geographic climate ensures the requisite availability for the radio network.

These rainfall intensities vary greatly depending on location. $R_{0.01}\%$ can be approximately in the range of 20-39 mm/h in temperate zones, but just a few mm/h in drier locations where rainfall is rare. In tropical areas during rainy seasons, the $R_{0.01}$ might be as high as 50-120 mm/h. Typically, telecommunication designers will build a PTP fixed link to have 99.99% availability in an ordinary year and fail when rain rates exceed $R_{0.01}\%$.

The rain rate is classified into five types as given in [50]:

- Light rainfall ($R \leq 1$ mm/h)
- Moderate (1 mm/h $< R \leq 4$ mm/h)
- Heavy (4 mm/h $< R \leq 16$ mm/h)
- Very heavy (16 mm/h $< R \leq 50$ mm/h)

- Torrential rainfall (R $>$ 50 mm/h)

2.3.8 Rain Drop Shape

The model proposed by Beard and Chuang in [51] has been employed to study raindrop shapes influenced by vertical electric fields and drop charges. This model takes into account parameters such as surface energy, pressure gradient, and dynamic pressure. According to this numerical model described in [51], the shape of the raindrop is determined by its size. Small droplets are considered spherical, while significantly larger drops exhibit an oval shape with a flattened base. The raindrops have axial symmetry about their vertical axis but lack any planes of symmetry orthogonal to this axis. For the current research, only raindrops with a high degree of axial symmetry will be considered, and highly asymmetric particles will not be included.

While using spherical scatterers is a strategy that simplifies computations using Mie theory, it is important to review the significant body of earlier research that uses non-spherical drop forms. Pivotal early reviews have been authored by Oguchi in 1981 and 1983 [52; 53]. Oguchi's research highlights that raindrops exhibit a variety of non-spherical shapes, including oblate and prolate spheroids as well as irregular forms. These shapes introduce complexity into the scattering process, as reviewed comprehensively in seminal papers in 1981 and 1983. Compared to spherical drops, non-spherical raindrops alter the polarization, phase, and amplitude of scattered waves. This work showed how factors like drop oscillation modes, internal resonances, and bulk scattering properties depend on shape. His work underscores the need to accurately characterize raindrop shapes and account for oblateness to match measurements and model phenomena like differential attenuation. Building on early spherical approximations, Oguchi contributed to the understanding of how non-spherical raindrop shapes influence radar rainfall estimation, remote sensing, and other applications.

The work by Ekelund in [54] investigates how raindrop shapes beyond idealized spheres affect the scattering of microwave radiation. Through numerical simulations using the discrete dipole approximation, they analyzed the single-scattering properties of oblate and prolate spheroidal raindrops across a range of sizes and frequencies up to 35 GHz.

Their results reveal distinct shape-dependent scattering patterns, with non-spherical drops exhibiting variations in radar reflectivity, polarization signatures, and frequency response compared to equivalent-volume spheres. These differences become more pronounced for larger aspect ratio deviations from spherical and at higher frequencies relevant for remote sensing. The authors highlight the need to accurately represent oblate and prolate geometries to improve rainfall estimation by weather radars and interpretation of microwave satellite observations. By elucidating the scattering properties of realistically shaped raindrops, Ekelund et al.'s work contributes to enhanced precipitation retrieval and sheds light on the significant role of raindrop shapes in governing microwave interactions. Their open-source scattering database provides a valuable resource to advance modelling capabilities.

Beyond these insightful reviews, significant research efforts have concentrated on developing computational methods tailored to non-spherical particle scattering. Among the prominent methods are T-matrix theory [55] and the discrete dipole approximation [56]. T-matrix theory, as formulated by Mishchenko et al. (1996), offers an exact solution to Maxwell's equations for scattering by non-spherical particles. This method utilizes vector spherical wave functions to handle diverse particle shapes, including spheroids, cylinders, and Chebyshev particles. On the other hand, the discrete dipole approximation, introduced by Draine and Flatau (1994), represents scattering particles as an array of discrete dipoles. By interacting these dipoles with the incident field, it efficiently models scattering by particles with arbitrary geometries. Both methods have demonstrated success in addressing a myriad of non-spherical scattering phenomena. This synthesis not only highlights the valuable contributions of Ekelund et al. but also underscores the evolution of computational methodologies in tackling the challenges posed by non-spherical particle scattering.

In their investigation into raindrop shapes, Beard and Chuang conducted a study, where they quantified the scattering properties of raindrops modeled as oblate and prolate spheroids within a range of equivolume sphere diameters from 1-6 mm [57]. Their research aimed at understanding crucial scattering parameters like the back-scattering cross-section and the asymmetry parameter. Subsequently, the research work in [58] utilized the T-matrix theory to analyze the scattering properties of raindrops with air bubbles and drop oscilla-

tions, revealing distinct scattering behavior compared to equivalent-volume spheres.

In summary, the exploration of raindrop shapes and their scattering properties spans a rich array of research endeavours, with seminal contributions. Research by Oguchi (1981, 1983) highlights the impact of non-spherical raindrop shapes on scattering, emphasizing variations in polarization and amplitude. Ekelund et al. (2020) focus on microwave scattering, revealing distinct patterns for oblate and prolate spheroids compared to spheres. Beard and Chuang (1987) quantitatively assess scattering properties for non-spherical raindrops, while Thurai et al. (2007) explore complex shapes using T-matrix theory. Recent studies by Yee et al. (2013) and Kahnert and Rother (2011) employ numerical methods to investigate resonance phenomena and optical scattering, respectively, advancing our understanding of precipitation processes and remote sensing capabilities.

2.4 Bistatic Scattering Effect

Scattering refers to the diversion of electromagnetic radiation away from the straight-line propagation path, arising from interactions with particles or irregularities in the transmission medium. In the context of radio wave propagation through rain, a distinction can be made between forward scattering in the direction of the main propagation link versus off-axis bistatic or diffuse scattering. Forward scattering results in a redirected signal that still arrives at the intended receiver. However, the phase and amplitude of the forward scattered wave may be altered compared to the incident wave. The total effect of absorption losses and cumulative phase/amplitude changes from forward scattering contributes to the attenuation observed on the direct propagation path.

Bistatic scattering corresponds to the diversion of the radio wave in off-axis directions away from the transmitter-receiver link path. This can lead to power being scattered away that does not reach the intended receiver antenna, contributing to link degradation. Prior literature such as van der Zanden's research work in [59] has specifically examined bistatic rain scattering at mmWave frequencies. The relationship between wavelength, propagation medium characteristics, and particle size determines the regimes where forward scattering or bistatic scattering will dominate. For rainfall at mmWave frequencies,

where the wavelength approaches the drop size scale, significant bistatic scattering begins to occur in addition to attenuation. Therefore, a comprehensive model of propagation impairment by rain requires properly differentiating between the on-axis forward scattering contribution to attenuation versus the off-axis bistatic scattering. They investigated rain-induced bistatic scattering at 60 GHz and developed a comprehensive theoretical framework based on Mie scattering theory to calculate the bistatic scattering cross-sections of raindrops. The model took into account the raindrop size distribution, temperature, drop canting angles, and the complex refractive index of water at 60 GHz. Through simulations and experimental measurements, they demonstrated that bistatic scattering can significantly impact the received signal power, especially at larger scattering angles. The results showed that for a 60 GHz link with a path length of 1 km, the bistatic scattering contribution to the total signal power could reach up to 20% for a rainfall rate of 25 mm/h and a scattering angle of 60 degrees. This highlights the importance of considering bistatic scattering effects in addition to forward attenuation when modelling propagation impairments due to rain at millimetre-wave frequencies. Van der Zanden et al. also investigated the impact of different raindrop size distributions on the bistatic scattering cross-sections. They found that the contribution of different drop sizes to the total bistatic scattering varied significantly with the scattering angle. At smaller scattering angles, larger drops (e.g., 3-4 mm in diameter) dominated the scattering, while at larger angles, smaller drops (e.g., 1-2 mm) became more important contributors. Furthermore, they explored the influence of drop canting angles, which describe the orientation of the raindrops relative to the propagation direction. Their results demonstrated that the bistatic scattering cross-sections were sensitive to the canting angle distribution, particularly at larger scattering angles. This highlights the importance of accurately modelling the raindrop orientation and its variability in addition to the drop size distribution.

In the context of this research work, the general term scattering is used to refer specifically to the bistatic component that diverts signals away from the main link direction. This is distinguished from attenuation arising from both absorption and forward scattering along the direct transmitter-receiver path. Adopting terminology consistent with the wider literature helps delineate these distinct physical propagation mechanisms.

In FWA applications using the mDN, SNR may decrease at the received side due to un-

desirable interference caused by the scattering effect of raindrops. As a result, some of the transmitted electromagnetic energy may be scattered toward independent receivers, creating interference that needs to be carefully considered, especially in Non-Line-of-Sight (NLoS) scenarios, where scattered rays may act as the primary propagation paths. Properly accounting for scattering effects becomes essential to ensure the reliability and efficiency of mmWave FWA systems, particularly in challenging NLoS environments. A simplifying assumption in scattering models relies on approximating individual raindrops as homogeneous spherical particles and the incident radiation as a plane electromagnetic wave. Under these assumptions, the scattering behaviour can be analyzed through Mie scattering theory for larger droplets or Rayleigh scattering theory for droplets much smaller than the wavelength. The spherical raindrop approximation enables an analytical solution for the scattered radiation based on Maxwell's equations. However, real raindrops exhibit a range of non-spherical shapes depending on drop size as highlighted in subsection 2.3.8 for the literature review of previous work on scattering from non-spherical drops. Therefore, while computationally convenient, the spherical raindrop assumption neglects scattering effects from the distortions and flattening of large falling drops. More advanced computational techniques like the T-matrix or discrete dipole methods can account for non-spherical shapes. Nevertheless, the spherical approximation provides a useful baseline model for rainfall scattering, before adding additional physics. Rayleigh scattering is an approximation that represents scattering when the rain particle is substantially smaller than the radio wave's wavelength where the incident radio wave's energy is scattered with a radiation pattern corresponds to that of a dipole, and the quantity of energy scattered is proportionate to D^3/λ, where D is the raindrop diameter and λ is the wavelength. If the raindrop has the same diameter as the wavelength, the more sophisticated Mie scattering model is applied. Figure. 2.2 illustrates a visual comparison between Mie and Rayleigh scattering.

The cross-sections describe the far-field properties of the scattered radiation in terms of power, which are characteristics that are proportional towards the electromagnetic energy and are thus commonly expressed as cross-sectional areas that, when multiplied by the intensity of the incoming electromagnetic radiation, generate the appropriate power quantity. They are classified as Q_{sc} the scattering cross section which describes the total

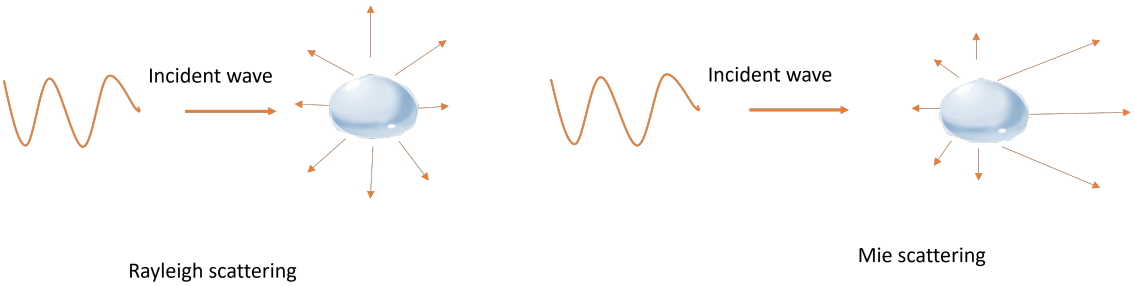

Figure 2.2: Mie and Rayleigh scattering pattern due to raindrops

power scattered in all directions by raindrops. Q_a, the absorption cross-section, defining the total power absorbed, and Q_{ext} extinction cross-section (equation 2.4.9), which emphasises the total attenuation of the forward incident signal caused by the raindrops. The studies referenced in [60; 61] offer insights into Mie scattering cross-sections, including equations for extinction, scattering, and absorption cross-sections, along with the calculation of Mie coefficients.

$$Q_{\text{ext}} = Q_{\text{sca}} + Q_{\text{abs}} \tag{2.4.9}$$

where:

$$Q_{\text{ext}} = \frac{\pi D^2}{x^2} \sum_{n=1}^{\infty} (2n+1)\Re(a_n + b_n) \tag{2.4.10}$$

and

$$Q_{sca} = \frac{\pi D^2}{x^2} \sum_{n=1}^{\infty} (2n+1)(|a_n|^2 + |b_n|^2) \tag{2.4.11}$$

Mie scattering coefficients a_n and b_n are complex functions of drop diameter, refractive index and wavelength. The x size parameter is defined as:

$$x = \pi D/\lambda \tag{2.4.12}$$

where λ is the wavelength mm and D is the drop diameter in mm.

2.5 Interference Due to Rain Scatter

Interference studies are conducted using practical communication systems immersed in a spatiotemporal rainfall intensity field, which can be generated either directly from data

or artificially constructed. In computing interference, variations in rainfall rate within the shared volume occupied by the transmitter and receiver antenna beams must be taken into account [62]. As raindrops radiate the electromagnetic wave in all directions, rain-induced effects can be observed not only in Line-of-Sight (LOS) or forward directions but also over a broad range of angles. This variability creates a scattering structure that is influenced by the ratio of wavelength to raindrop diameter and the Drop Size Distribution (DSD) in three dimensions. Consequently, when there exists a shared volume between interfering and interfered fixed links, it becomes essential to investigate rain-induced interference. As described in [63], the Bistatic Radar Equation (BRE) can be employed to calculate the ratio of received to transmitted power due to rain scattering (2.5.13).

$$\frac{P_r}{P_t} = \frac{\lambda^2}{4\pi^3} \int_V \frac{G_t G_r}{(r_t r_r)^2} \eta\left(\theta_s\right) A_{air} A_{rain} dV \tag{2.5.13}$$

where λ is the wavelength, G_t and G_r are directional gain functions for transmitter and receiver antennas, r_t and r_r are transmitter and receiver distances to scattering volume element dV, $\eta\left(\theta_s\right)$ is the Bistatic Scattering Cross Section (BSCS), A_{air} and A_{rain} are path attenuations due to atmospheric absorption and rain-induced scattering. BSCS η is given by equation 2.5.14:

$$\eta(\theta_s) = \int_0^\infty N(D)\sigma_{sca}(D)P(D,\theta_s)dD \tag{2.5.14}$$

where D is raindrop diameter, θ_s is the scattering angle, $N(D)$ is rain DSD, σ_{sca} is scattering cross section and P is scattering phase function.

P is the probability distribution of the scattered wave direction given by equation 2.5.15 and normalised so that integration across all angles yields unity:

$$P(\theta) = \frac{|S_1(\theta)|^2 + |S_2(\theta)|^2}{\pi x^2 Q_{sca}} \tag{2.5.15}$$

where $S_1(\theta)$ and $S_2(\theta)$ are scattering amplitude matrix elements as determined by the

Mie theory.

2.6 mmWave Rain Attenuation Measurement: A Survey

Several studies have been conducted on rain attenuation and scattering measurement campaigns, precipitation measurement, and prediction models. This section presents a literature survey on recent research conducted within mmWave frequency bands for point-to-point fixed links, considering different locations, link distances, frequencies, and transmission technologies, as cited in Table. 2.1.

When it comes to prediction, each model has its own set of input parameters and estimation techniques. Some works may be based on rainfall estimation rather than disdrometer datasets, while others may use limited inputs such as rainfall rate and temperature. Extended research has considered additional parameters such as DSD, the refractive index of water, and the number of drops to estimate rain attenuation over long-term measurements. These comprehensive approaches aim to improve the accuracy and reliability of rain attenuation predictions in mmWave fixed links.

Table 2.1: Rain attenuation measurements and prediction survey

Research work	Frequency (GHz)	Distance	Measurement period	Location	Ref
Measurement agrees with the ITU-R model of 99.99% of the time. When the rain rates are 31.9, 70.4, 94.5, and 108 mm/h, the maximum rain attenuations for 1.8 km are approximately 14.3, 33.6, 36.9, and 40.1 dB, respectively.	73.5	1.8 km	1 year	Malaysia	[64]
The results clearly show that including information on raindrop size improves prediction performance.	73 and 83	325 m	1 year	Milan, Italy	[65]
At 77 and 300 GHz, the computation of specific attenuation based on the ITU-R and Mie scattering with the Weibull distribution provide the best fit to the measured attenuation.	77 and 300	160 m	10 hours	Birmingham, UK	[66]
The data indicate that there is a 1.5–4.5 dB difference in the real and theoretical rain-induced signal attenuation using OFDM modulation.	23, 25, 28, and 38	3 km	1640 min	Beijing, China	[67]
A novel regression-based approach for attenuation prediction at 75 GHz was proposed.	38 and 75	100 m	3 years	Korea	[68]
Data have been analysed and compared to International Telecommunication Union Radiocommunication Sector (ITU-R) and DSD models	84	560 m	3 months	New Mexico	[69]

The ITU-R model underestimates attenuation on either an annual average and a worst-month statistics basis.	58	850 m	5 years	Czech	[70]
The study provided two novel methodologies for calculating specific attenuation when the rain rate exceeds 40 mm/h.	72 and 84	1.7 km	1.5 years	Albuquerque, US	[71]
A visibility and precipitation optical sensor captured the rain data. The observed rain attenuation was found to be consistent with the ITU-R P.838-3 model.	71 and 76	1 km	10 months	Molndal, Sweden	[72]
Individual year statistics showed significant year-to-year fluctuation. The best result was obtained when the ITU-R method was used with $R_{0.01}$	93	850 m	4 years	Praha, Czech	[73]
The worst month statistic obtained from the real measurements was lower than what was predicted by the ITU-R P.581-2 model.	26	1.3 km	1 year	Malaysia	[74]
Different wet antenna attenuation for varied rain rates, which indicated that the constant value of wet antenna attenuation used in some studies may overestimate the retrieved peak rain rates.	37.3-39.2	48-497 m	2 years	8 locations	[75]
Measured wet antenna attenuation showed 3 dB per antenna for a rain rate of 100 mm/h.	32	186-1810 m	2 years	Czech	[76]
Wet antenna effect, change of humidity level, and equipment stability would also impact the rain attenuation.	23, 25, 28, and 38	700 m	1640 min	Beijing, China	[77]

DSD model is used to quantify rain attenuation. DSD differs with climatic condition levels of pollution	57, 97, 135, and 210	500 m	1-3 years	Chilbolton and Singapore	[78]
Consistent alignment between the DSD attenuation model and the ITU-R R model for rainfall rate below 100 mm/h, with slight differences below 30 mm/h.	22, 23 and 31.4	Weather data	2 years	Tropical locations	[79]
Both the DSD model and the ITU-R model gave similar results for frequencies below 30 GHz with a maximum rainfall rate up to 30 mm/h in a tropical region.	10-100	Weather data	2 years	Tropical locations	[80]
Measurements from various instruments are combined to calculate the spatial distribution and rainfall intensity more accurately.	23, 38, 58	0.3–8.4 km	5 months	Switzerland	[81]
Theoretical calculations differ by several decibels from measurements.	32, 38	0.186–1.81 km	2 years	Czech	[82]

2.7 Summary

In the realm of future fixed link systems harnessing the potential of 5G millimetre wave frequency bands, a novel approach to service delivery emerges, akin to fibre networks but operating through short-range point-to-point transmission. This approach proves particularly valuable for distances below 300 meters, facilitating seamless connections between buildings or lampposts. In this chapter, we shed light on precipitation attenuation as the primary fade mechanism that significantly impacts the propagation of electromagnetic waves in these specific applications. Recent research endeavours have focused on investigating rain attenuation, conducting scattering measurement campaigns, analyzing precipitation data, and developing prediction models within the context of mmWave frequency bands for point-to-point fixed links. These studies span diverse locations, link distances,

frequencies, and transmission technologies, encompassing a comprehensive spectrum of scenarios.

Each prediction model utilizes specific input parameters and employs distinct estimation techniques. While certain studies rely on rainfall estimation or limited inputs like rainfall rate and temperature, others delve into more intricate factors such as Drop Size Distribution (DSD), the refractive index of water, and the number of raindrops to achieve more accurate estimates of rain attenuation over extended periods of measurement. These multifaceted investigations aim to enhance the understanding and predictability of rain-induced signal degradation in mmWave fixed links, paving the way for more reliable and efficient communication systems in challenging weather conditions.

Chapter 3

Fixed Link Measurement Experimental Setup

To evaluate the influence of precipitation on the targeted mmWave frequency bands, a series of measurements were carried out at 25.84 GHz, 77.54 GHz, and 77.125 GHz, encompassing diverse weather conditions, seasonal variations, and long-term datasets. The study employed Durham University's custom channel sounder fixed link, deployed on the rooftop, which facilitated the simulation of building-to-building transmission scenarios via both Line-of-Sight (LoS) links and side links. To ensure precise attenuation predictions, a highly dependable and accurate weather station was utilized throughout the experimentation process.

3.1 Weather Station

To relate the radio link to rain attenuation prediction and to evaluate precipitation statistics, a weather station is installed on the Durham University library roof located at Latitude: 54.768167 and Longitude: -1.573418 at 62 m above sea level. It is a $PWS100$ weather sensor illustrated in Figure. 3.1. It is a laser-based sensor capable of determining precipitation and visibility parameters for automatic weather stations including road weather and airport stations. Due to its advanced measurement technique and fuzzy logic algorithms, the PWS100 can determine each individual particle type from accurate size and velocity measurements and the structure of the received signal. The technical speci-

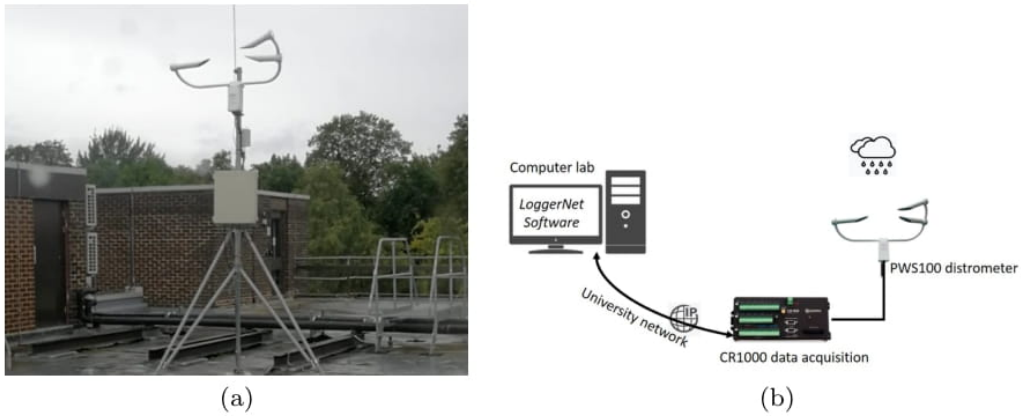

Figure 3.1: Weather measurement system installed on the roof of Durham University's library: (a) PWS100 weather station, (b) Block diagram.

fications of the station are listed in Table. 3.1.

Table 3.1: Technical specifications of the PWS100 weather station

Parameters	Specifications
Particle size	0.1 to 30 mm*
Size accuracy	±5% (for particles greater than 0.3 mm*
Particle velocity	0.16 to 30 m/s
Velocity accuracy	±5% (for particles >0.3 mm)*
Types of precipitation	drizzle, rain, snow grains, snowflakes, hail, ice pellets, graupel, and mixed
Rain rate intensity range	0 to 400 mm/h
Rain total accuracy	Typically ±10%

* PWS100 weather sensor manual note for the technical specs: *The accuracy figures quoted are for laboratory conditions with reference particles and visibility standards. In practice, the proportion of particles detected will fall off significantly below about 0.5 mm diameter*.

The PWS100 disdrometer covers a measurement area of 40 cm^2, and its operations are remotely controlled by a computer in the laboratory. Through the University's wireless network and CR1000 data acquisition system, data are stored at one-minute intervals via an Internet Protocol (IP) address. To accommodate various data types, the disdrometer features a sizable internal memory, partitioned into different buffers. One such buffer, the particle buffer, is dedicated to storing raw signal data captured from the detectors. The particle buffer has the capacity to hold data for 500 typical particles, and the processor can efficiently process these particles at a rate of 120 particles per second, under normal conditions. This processing speed effectively limits the maximum rainfall rates that the sensor can accurately measure. For most users, this limitation is not a concern, but it may be worth considering under specific circumstances. In situations where the rainfall rate surpasses 120 particles per second and persists over an extended period, the particle buffer may begin to fill up rapidly. If the rain rate remains above 120 particles per second for a sustained duration, the buffer could eventually run out of space, leading to the loss of some particles. The PWS100 disdrometer boasts outstanding measuring capabilities, providing a comprehensive set of outputs for each recorded minute. These outputs include the date and time of the measurement, the station status (indicating whether the equipment is functioning correctly or has encountered an error), power status, average visibility, average temperature, average humidity, precipitation intensity, precipitation accumulation, average rainfall velocity, average drop size, and information about various precipitation types such as drizzle, freezing drizzle, freezing rain, rain, snow grains, snowflakes, ice pellets, hail, and graupel. Moreover, the disdrometer offers detailed information about the Drop Size Distribution (DSD), with 300 bins and a 0.1 mm increment for each drop diameter, enabling a comprehensive characterization of the precipitation patterns.

3.2 Fixed Link Setup

The fixed link measurement system is based on Durham University channel sounder [83–86]. It consists of an experimental setup installed on the roof of the Engineering building located at Latitude: 54.767396, Longitude: -1.570390 at 65 m of sea level elevation. In Figure. 3.2, it is the link with a dark yellow dashed line connecting Tx (Transmitter Box)

and RX_D (Receiver Box - Direct link) and Tx to RX_S (Receiver Box - Side link).

In the course of our extensive literature review of my research work literature review and before starting to collect data for rain attenuation analyses, we have initiated an upgrade of the experimental setup. It involved the incorporation of a Phase Locked Loop (PLL) for the direct generation of the second IF at 12.92 GHz. This strategic modification allows for the integration of the IF generator within the Radio RF heads, thereby streamlining the configuration. Notably, this approach minimizes the intricacies associated with rain-induced impacts on inter-unit connections and mitigates the dependence on RF cables. Except for cables linking the rubidium standard reference clock to the PLL and the data acquisition cards, along with cables from the receivers' outputs, all components at each terminus of the link are consolidated within a singular weatherproof enclosure. Moreover, a pivotal upgrade involved the inclusion of a second receiver (Side Box Receiver) in the short link, facilitating the capture of scattered energy. Additionally, the integration of Filtronic RF heads has been installed for this research work to extend the measurement distance comprehensively. Simultaneously, endeavours have been directed toward refining system performance, coupled with an intensified data collection initiative achieved through the automation of data acquisition concurrent with meteorological measurements. These enhancements collectively contribute to enhancing the level of system efficiency and a more extensive dataset for analysis.

3.2.1 Direct Link

The direct link constitutes a short-range fixed link, employing Continuous Wave (CW) transmission, and operates over a Line-of-Sight (LoS) path length of 36 meters (represented by the horizontal yellow dashed line: Tx to RX_D as highlighted in Figure. 3.2(e).

The transmission configuration offers flexibility, allowing us to choose between CW for rain attenuation assessment or Wideband Frequency Modulated Continuous Wave (FMCW) for the estimation of narrow pulse distortion. The block diagram for CW transmission is depicted in Figure. 3.3. Within this setup, all RF boxes are equipped with Programmable PLL synthesizer ADF5355 boards, connected to an 80 MHz signal clock.

(a) Transmitter (b) Receiver-direct (c) Receiver-side (d) Filtronic transceiver

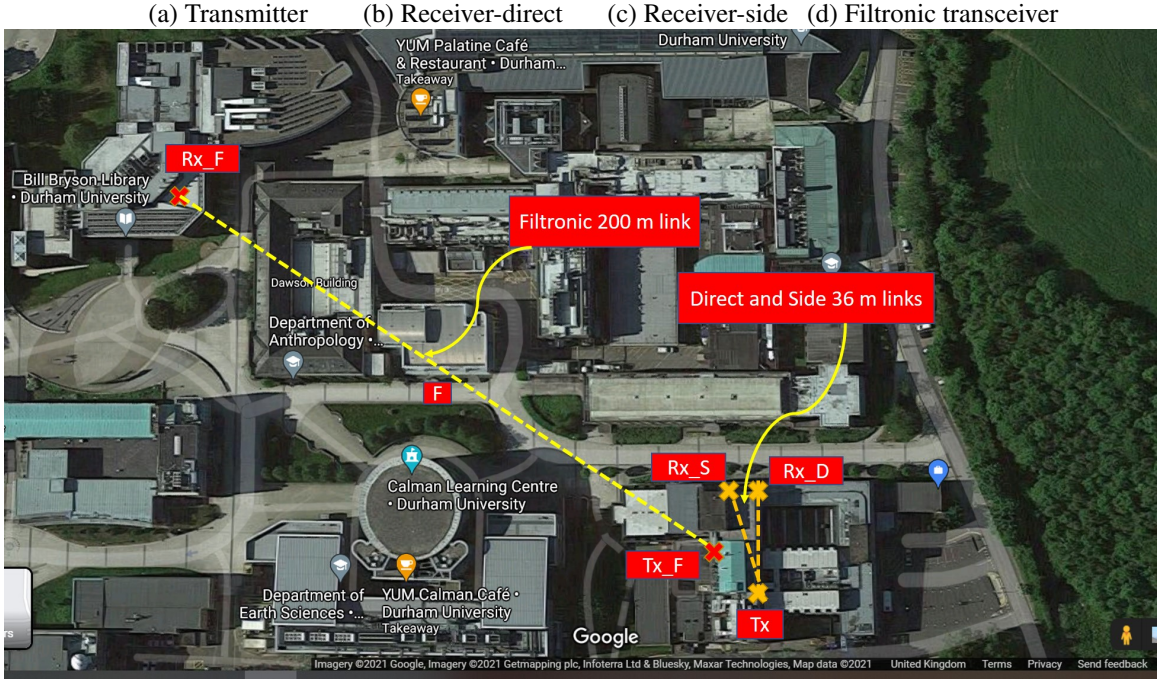

(e) Measurement location

Figure 3.2: Fixed link RF heads of the measurement setup and measurement location: (a) transmitter box for 36 m link (Tx), (b) receiver box for direct 36 m link (RX_D), (c) receiver box for side 36 m link (RX_S), (d) transceiver Filtronic box for 200 m link (RX_F), (e) measurement location - Durham University campus - Direct/Side links on the engineering department roof; Filtronic transceiver on the library roof.

The transmitter PLL output operates at 12.92 GHz. With the implementation of PLLs in my project and the reduction of cable connections, the diagram has been reinstalled. I reconfigured it to transmit the CW signal and receive the baseband signal from the receiver boxes as well and continuous monitoring takes place of the setup occurs after the technician completes the hardware installation. This signal is then fed to the RF heads, which consist of multiplexers and attenuators (see RF box scheme in Annex). The transmitted frequency is multiplied by 2 to achieve 25.84 GHz and by 6 for 77.54 GHz. For data acquisition, two data acquisition cards are utilized, connected to a 50 Hz trigger and

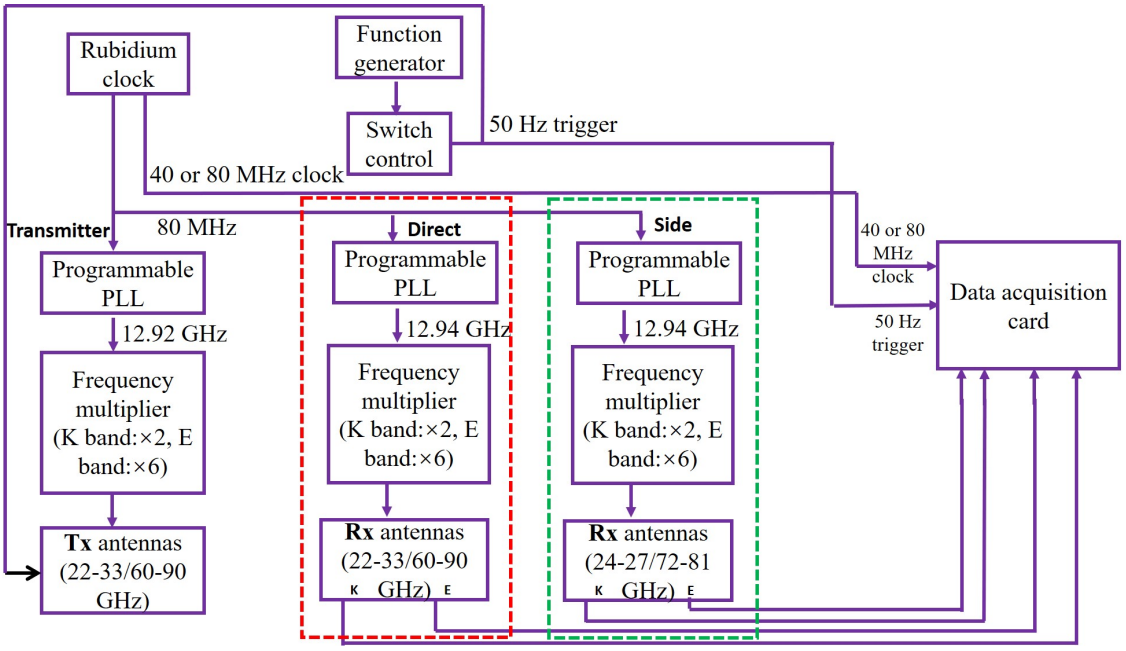

Figure 3.3: Block diagram of the direct and side fixed link measurement setup.

a 40 MHz clock. The 50 Hz signal is also linked to the transmitter box, facilitating the switching between vertical and horizontal polarization. The 40 or 80 MHz clock provides the sampling clock for the acquisition process. Regarding the receiver box, for 77.54 GHz, we employ two horn antennas with vertical and horizontal polarizations, with typical 25 dBi gain and a 48° 3dB-beamwidth. For the 25.84 GHz, a dual-polarized antenna is utilized, with a typical frequency range of 18-40 GHz, 15 dBi gain, and a 20° - 55° 3dB-beamwidth. To minimize wet antenna effects, all antennas are covered with radomes. At the receiver side, the PLL is programmed at 12.94 GHz, allowing for an offset frequency of 4 MHz and 12 MHz at 25.84 GHz and 77.54 GHz, respectively. Both the transmitter and receiver are positioned at a height of 1.90 meters, providing the required elevation for the link setup.

3.2.2 Side Link

The side link operates on Continuous Wave (CW) over a 36 m NLoS path length which is highlighted in Figure. 3.2, the link with the inclined dark yellow dashed line, i.e., Tx to Rx_S. The link relies on Non-Line-of- Sight (NLoS) reflected paths to receive the signal. Single vertical polarized antennas are used at 25.84 GHz and 77.54 GHz. The same configuration is provided as a direct link receiver box.

3.2.3 Filtronic Link

The third link in our experiment operates at a frequency of 77.125 GHz and spans a distance of 200 meters, connecting the Durham University Library roof (Latitude: 54.768167, Longitude: -1.573418) at an elevation of 62 meters above sea level to the engineering department roof. This link is visually represented in Figure. 3.2 by the light yellow dashed line denoting the path between TX_F and RX_F. To establish this link, we utilize commercial transceivers known as Filtronic Orpheus E-band modules, which operate within the 71-86 mmWave frequency band and utilize a 31 MHz RF Local Oscillator (LO) frequency step size. The baseband input power level for the transmitter falls within the range of -7.5 dBm to -17.5 dBm, and the baseband bandwidth is at least 750 MHz. The Filtronic Orpheus E-band modules are equipped with an Orpheus interface board, an NI USB-8451, and an electronic circuit power to supply the module. Once the modules are mated, they can be powered up using standard laboratory power supply units (-5V, +2.8V, +3.3V, +5.1V, +18V). The transmission and reception of baseband signals are facilitated through the SubMiniature version A (SMA) connectors.

For controlling the module, an NI USB-8451 is employed, utilizing the Filtronic Orpheus Graphical User Interface (GUI) software. The transceiver boxes are equipped with lens horn antennas, boasting a nominal gain of 39.3 dBi and a 1.6° 3dB beamwidth. Throughout this thesis, we figuratively refer to the 200 m Point-to-Point (PTP) link as the ”Filtronic link”.

Before installing the boxes for the Filtronic link, a Fresnel zone clearance check has been performed to ensure optimal signal transmission. This involved verifying that the Fresnel zone, which is an elliptical-shaped area between the antennas, remains clear of obstacles to minimize signal attenuation and interference. The lab technicians checked the terrain profile, considering factors such as terrain height, ground elevation, and any obstructions along the path. A visual inspection was conducted of the pathway between the engineering building roof and the library roof using binoculars and spotting scopes. There was no presence of any obstructing objects infringing on the radius cylinder surrounding the centre line between the antennas.

3.2.4 Experimental-setup link budget

The link budget equation serves as a tool to determine the feasibility and performance of a wireless link by balancing transmitted power against various losses encountered during propagation. Table 3.2 summarises the link budget for the experimental setups. The link budget equation is expressed as:

$$P_{RX} = P_{TX} + G_{TX} + G_{RX} - P_L - A_{TM} - L_{OT} \tag{3.2.1}$$

The received power P_{RX} depends on the transmitter power P_{TX}, antenna gains at the transmitter G_{TX} and receiver G_{RX}, and various losses in the system. The losses include free space propagation loss over distance P_L, atmospheric attenuation A_{TM} due to moisture, gases and rainfall, cable losses L_{cable}, and other losses L_{OT} from system stability factors, RF mismatches and connectors. The free space path loss P_L is calculated theoretically from the transmit and receive antenna separation distance and frequency:

$$P_{\mathrm{L}}(dB) = 20\log_{10}\left(\frac{4\pi d}{\lambda}\right) \tag{3.2.2}$$

where d is the distance between the transmitter and receiver in meters. λ is the wavelength of the signal in meters.

Meanwhile, cable losses depend on cable length and type. Typical coaxial cable provides around 0.1 dB of loss per meter length at mmWave bands, hence 4-6 dB estimates across long cable runs from antennas to backend hardware in the engineering roof and 1.8 dB in the library roof. Moreover, RF connectors and interfaces between cables or Printed Circuit Board (PCB) boards induce impedance mismatch losses up to 0.2 dB per connected pair. Hardware implementation also limited our system stability with thermal fluctuations in electronics on the order of ±0.05 dB over several minutes adding uncertainty. Lastly, despite shielding and grounding provisions Electromagnetic Interference (EMS) from background RF signals surrounding the receivers increase noise floor. Accounting for these RF implementation losses around 0.2-1 dB in the link budget is necessary. During the research work literature review and system upgrade, terminating unattenuated

ports properly, utilizing high-quality low-loss cables from reputable manufacturers, and maintaining good chassis grounding were implemented to improve results. The lab technician consolidated the aggregation of all RF components into singular outdoor shielded boxes in this system to help mitigate such cabling and interference concerns. Atmospheric loss A_{TM} varies depending on frequency, link distance and weather patterns.

Table 3.2: Link budget summary for the experimental measurement setups

Link	Freq. (GHz)	Pol.	RX Power (dBm)	RX Ant. Gain (dBi)	TX Ant. Gain (dBi)	Path Loss (dB)	Atm. Loss (dB)	Cable Loss (dB)	Other Loss (dB)	TX Power (dBm)	SNR (dB)
Direct Link	25.84	Co	-31	15	15	46.5	0.2	4	0.2	20	69
	25.84	Cross	-49	15	15	46.5	0.3	4	0.3	20	51
	77.54	Co	-49	25	25	59.8	0.4	4	0.4	20	51
	77.54	Cross	-65	25	25	59.8	0.5	4	0.5	20	35
Side Link	25.84	Co	-46	15	15	48.2	0.2	6	1	20	54
	25.84	Cross	-51	15	15	48.2	0.3	6	1	20	49
	77.54	Co	-42	25	25	62.1	0.4	6	1	20	58
	77.54	Cross	-59	25	25	62.1	0.5	6	1	20	41
Filtronic Link	77.125	Co	-45	39.3	39.3	92.3	0.6	1.8	1	18	55

3.3 Data Collection, Procedures, and Methodology

The data recording process is facilitated by a workstation equipped with two 14-bit two-channel data acquisition cards, as illustrated in Figure 3.4. To combine received signals from two frequency bands into a single channel of the data acquisition card for each received polarization, we utilize an offset frequency approach. Specifically, in the setup depicted in Figure 3.3, the 25.84 GHz co-polarization is combined with the 77.54 GHz co-polarization in channel 1 of data acquisition card number 1 for the direct link. Additionally, the 25.84 GHz cross-polarization is combined with the 77.54 GHz cross-polarization in channel 2 of data acquisition card number 1 for the direct link. For the side link, we employ channel 1 of data acquisition card number 2 to combine the 25.84 GHz and 77.54

GHz signals, while the remaining channel is allocated for the Filtronic box output. To ensure synchronization and accuracy, the sampling rate for all links is set at 80 MHz, with a 50 Hz trigger and a clock rate of 10 MHz connected to both data acquisition cards. In the case of the direct link, we generate four outputs for each band, encompassing vertical to vertical, vertical to horizontal, horizontal to vertical, and horizontal to horizontal. As for the side link, it produces vertical-to-vertical and horizontal-to-vertical outputs, while the Filtronic link offers linear polarization.

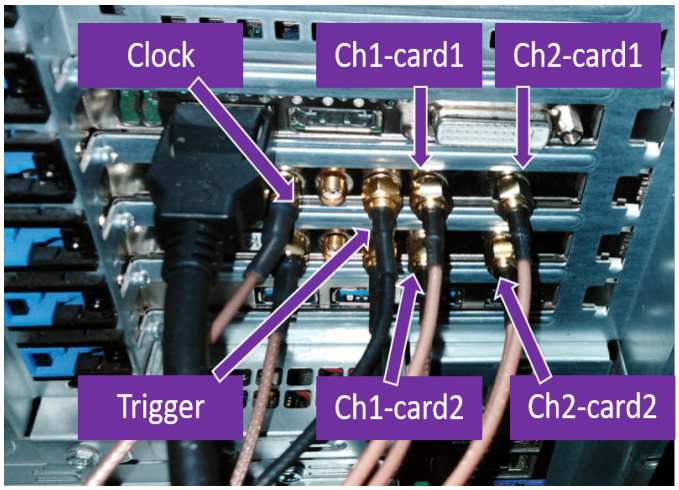

Figure 3.4: Two data acquisition cards connected to the workstation with two-channel 14-bit.

It is essential to mention that a separate workstation is employed for disdrometer data collection, which is synchronized with the radio data workstation to facilitate seamless coordination between the various measurement processes which are Network Time Protocol (NTP) synchronized.

3.3.1 Link Data

The methodology for conducting long-term measurements, as illustrated in the flow chart presented in Figure 3.5, consists of several key steps within the scope of the PhD thesis research. Initially, the PLLs of all RF boxes are programmed using the Ethernet cable and specific software, such as ADF4355 software for direct and side link boxes and OrpheusGUI for Filtronic boxes. Following the setup, the system is configured to operate in CW long-term transmission mode, while the workstation is programmed to autonomously record data. The data recording process is triggered when precipitation events occur. The

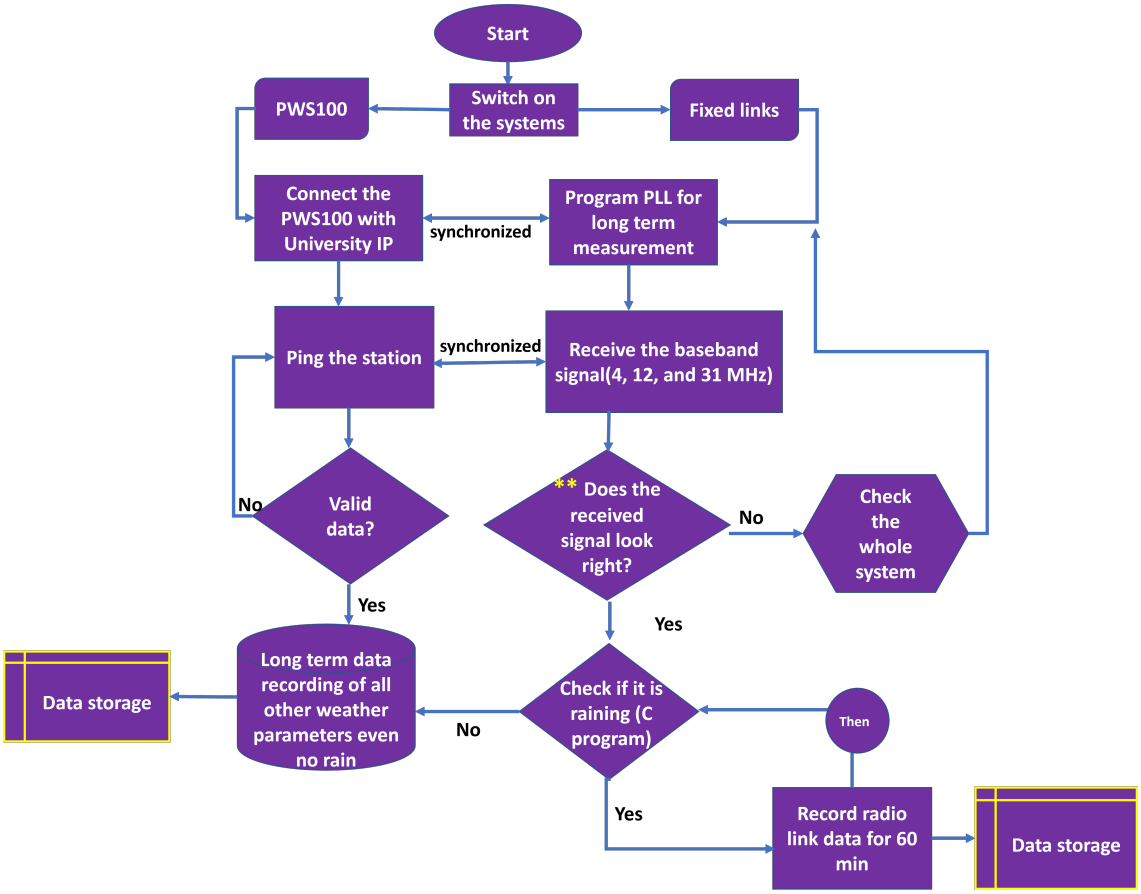

Figure 3.5: Flow chart of the data collecting methodology for the fixed link system and the weather station.

system detects the onset of precipitation by monitoring the precipitation rate, such as a threshold value of 0.1 mm/h. Upon detecting the first rain event, the data acquisition card initiates the recording of fixed link data and concurrently collects precipitation data for a duration of 60 minutes. At the end of the one-hour radio data recording period, the program conducts a real-time check to ascertain whether precipitation, such as rain, snow, drizzle, hail, or ice pellets, is still ongoing. If the precipitation persists, the data recording continues for an additional 60 minutes to ensure comprehensive data capture. Conversely, if the precipitation has ceased, the workstation terminates the recording process while remaining in communication with the weather station to monitor for future precipitation events. Subsequently, the recording process is repeated as necessary, thereby creating an iterative cycle that operates throughout the year. This approach enables the continuous collection of weather data alongside the fixed link measurements, facilitating a comprehensive and long-term analysis.

** The received signal checks before proceeding with data collection:

- Frequency check - Check if the received signal frequency matches the expected transmitted frequency using the Fourier transform. An example of an RF box signal stability test at 12.92 GHz and frequency check is highlighted in Annex C3 Figure. C.4.

- Power level check - The received power should match the expected transmitted power, taking into account any path loss effects. This is measured using the power meter.

- Phase noise check with the spectrum analyzer - This quantifies noise and instability in the carrier phase. Lower phase noise indicates a more stable frequency source at the transmitter.

- Spectral purity check with the spectrum analyzer - The signal should not contain unintended frequency components outside the main carrier frequency.

Real-time data recording takes place at precise one-minute intervals, and the recorded data are subsequently analysed using the Fast Fourier Transform (FFT) technique. The frequency multipliers in both the transmitter and receiver result in a 1 MHz offset in the first Intermediate Frequency (IF). This leads to frequency offsets of 4 MHz, 12 MHz, and 31.25 MHz at the output of the receiver for the 25.84 GHz, 77 GHz, and 77.125 GHz bands, respectively. The analysis focuses on identifying signal peaks at those specific frequencies highlighted in Figure 3.6. The characteristics of these particular peaks are meticulously documented because they correspond to the frequencies of interest - the original transmitted signals. These selected signal peaks are meticulously scrutinized and depicted. Each peak is thoroughly examined to measure parameters including the precise peak frequency and any deviation from expected values, the peak amplitude which indicates received signal strength, the -3dB bandwidth revealing signal purity, and the peak shape and symmetry providing insight on distortion. Spectral purity is evaluated by checking for any unwanted signal peaks or sidebands around the main frequencies. These rigorous quantified metrics enable comprehensive scrutiny of the peak properties.

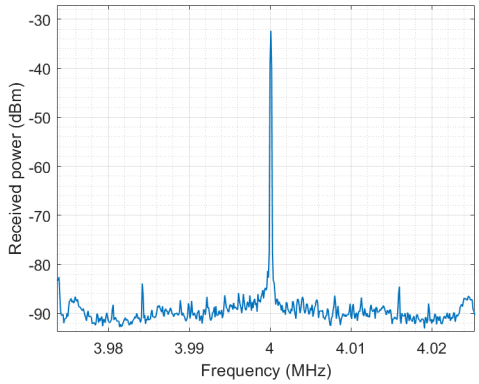

(a) 25.84 GHz

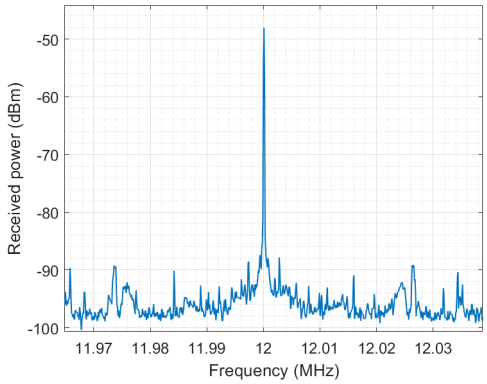

(b) 77.54 GHz

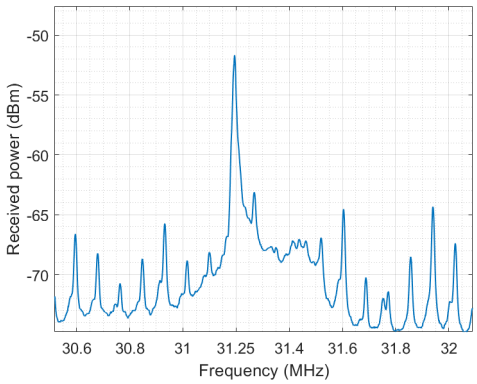

(c) 77.125 GHz-Filtronic link

Figure 3.6: Sample of the signal peak of 4, 12, and 31 MHz for the three IF bands, (a) 25.84 GHz, (b)77.54 GHz, (c) 77.125 GHz.

Each minute of the received signal data is meticulously chosen and synchronized with the corresponding weather data to ensure accurate data pairing and analysis. The received power data are further classified into co-polarization and cross-polarization categories for both the direct and side links of K and E bands (Kco/Kcro; Eco/Ecro), enabling a comprehensive assessment of the signal characteristics. Remote management of the three short-range links and the weather station is facilitated through the university's internet network, ensuring seamless and efficient operation. This remote control mechanism plays a vital role in data accuracy as it promptly detects any errors or system failures, thereby enhancing the reliability and availability of data. The radio link data availability rate achieved 85%, attesting to:

- Robust setup - Such a high availability indicates the monitoring setup including the instruments, data acquisition hardware, and software is robust. The system is able to continuously collect data over long periods with minimal downtime or failures

as it is lab engineering customised not industrial.

- Effective remote monitoring - A high uptime implies the remote monitoring mechanisms that allow operators to detect and troubleshoot any issues with the setup are effective. Active remote monitoring during the year and while the University is closed while maintaining access to the system enables prompt responses to any problems, reducing data loss.

- Challenging conditions - The monitoring location is subject to outdoor weather and environments. Maintaining over 85% availability despite these conditions is noteworthy.

- Statistical significance - The longer the monitoring duration, the more statistically significant the dataset is. High availability ensures large, continuous datasets maximizing statistical robustness.

The collected data, including the recorded radio signals and weather information, is stored on a minute-by-minute basis, ensuring that no valuable data are lost and enabling detailed post-processing and analysis. This meticulous data collection and management process, in combination with the comprehensive analysis methods, provides valuable insights into the behaviour of the fixed link systems under various weather conditions and long-term environmental effects.

The long-term datasets obtained from the measurements are categorized into two groups for analytical purposes: minutes with rainfall occurring, and minutes without rainfall deemed ”clear sky” conditions. To accurately discern and quantify the attenuation attributable solely to rainfall, stable received signal power data obtained during clear sky periods devoid of precipitation serve as a reference baseline representing the nominal attenuation level. These clear sky baseline periods, while nominally free of rainfall, may transpire during both daytime and nighttime hours, and need not be strictly cloudless so long as observable rainfall is absent. By classifying the datasets into rainy versus clear sky minutes and selecting stable signals from rain-free periods as the baseline reference, the comparison of attenuation levels between these rainy and clear-sky groups enables isolation of the attenuation impacts directly attributable to the intervening rainfall.

The focus of the thesis is on classifying the mmWave fixed link radio data and precipitation statistics for attenuation prediction into two distinct categories: yearly and seasonal. The yearly category employs available weather statistics data to predict rain attenuation using appropriate models. This approach allows for an overarching view of the attenuation patterns throughout the entire year. On the other hand, the seasonal category relies on fixed radio link data collected during specific periods across different seasons. Several factors, such as system upgrades, recording failures, data collection gaps, exclusion of insignificant hours on clear days, equipment maintenance or refurbishment, and any lockdown periods affecting access to the setup, are taken into account during the analysis. Given these factors, achieving complete radio data collection for the entire 365-day year can present challenges.

Table 3.3 presents the comprehensive fixed link measurements conducted between November 2019 and June 2021, including instances of no rain hours and days. Notably, the installation of the 200 m link was completed in October 2020. To ensure the accuracy of

Table 3.3: The total amount of datasets collected throughout the rain attenuation study's measurement campaign.

Dates		Number of minutes (For each link)	Link type
Nov-19		6000	D+S
Dec-19		18832	D+S
Jan-20		6360	D+S
Feb-20		4140	D
Mar-20		13620	D
Sep-20	Start of automatic record:	1980	D+S
Oct-20		9453	D+S
Nov-20		5451	D+S+F
Dec-20		10915	D+S+F
Jan-21		13370	D+S+F
Feb-21		9286	D+S+F
Mar-21		1348	D+S+F
Apr-21		921	D+S+F
May-21		2818	D+S+F
Jun-21		254	D+S+F
Total		104748	D: Direct S: Side F:Filtronic

rain attenuation modelling, minutes associated with equipment transient behaviour, power

fluctuations, atmospheric attenuation, equipment icing, high humidity levels, and strong wind conditions are carefully excluded from the analysis. The estimation of attenuation is based on the utilization of the best-measured data sets, ensuring that the most stable signal strength for each link is considered. By meticulously classifying the data into rainy and clear sky minutes and employing a rigorous exclusion process for factors that might introduce uncertainties, the study aims to provide comprehensive and reliable predictions of rain attenuation in mmWave fixed link systems. The combination of yearly and seasonal analyses offers valuable insights into the behaviour of the system under various weather conditions, enabling a deeper understanding of the environmental effects on the fixed links' performance.

3.3.2 Rain Data

The raw data from the PWS100 weather station is stored locally on the device in a .dat file format which contains binary data. This raw data is then ingested and pre-processed using Matlab script (Appendix A.1) that implements cleaning and conditioning procedures including parsing the binary format, removing invalid values, splitting data into numeric and cell columns, concatenating the data from all files into variables, and smoothing temporally. This multi-step data wrangling process converts the raw minute-by-minute weather measurements into a processed dataset with consistent formatting. The processed weather data can then be readily analyzed to generate weather specifications for each column (a sample of weather data is included in Appendix B. 4).

3.3.3 Processed Datasets

The first two channels of the data acquisition card are dedicated to recording data for the direct link outputs, while the second card is used for the side and Filtronic links. The recorded data are stored in binary format for each minute, with a sampling rate of 80 Msamples/sec. A Matlab code is utilized to extract raw data and convert it to received signal strength in -dBm, which is then saved as a ".mat" file with the corresponding date and time.

For rain attenuation measurement, clear sky days are taken as a reference with 0 dB

attenuation, and only stable signals observed over an extended period are considered for accuracy and reliability. The process of measuring attenuation involves normalizing the measured values to a reference power level obtained immediately before the onset of rain to assess the impact of rain on signal quality over time. The attenuation in Decibels (dB) is determined using the formula in equation 4.14:

$$\text{Attenuation (dB)} = 10 \times \log_{10}\left(\frac{P_{\text{ref}}}{P_{\text{meas}}}\right) \tag{3.3.3}$$

where P_{ref} represents the reference power level before the rain event (in dBm), and P_{meas} represents the measured power level during the rain event (in dBm). Normalizing the measurements to the reference power level P_{ref} obtained before the rain event minimizes the influence of long-term system drifts. Instead of relying on absolute power levels, which can gradually fluctuate over time, this approach calculates the SNR relative to a baseline P_{ref}. Any decrease in power P_{meas} compared to P_{ref} directly reflects the attenuation caused by the presence of rain. By adopting this normalization technique, the reported rain attenuation values specifically capture the impact of rain events on signal quality.

Any erroneous or invalid data points are identified and excluded from the analysis and rain attenuation calculation. Instances of such data anomalies may arise from issues such as a loose cable or a faulty connector on an RF box, problems in the cables linking the RF box output to the workstation, or potential malfunctions in the data acquisition cards. These anomalies could result in inaccuracies being recorded, visible as spikes or erratic fluctuations in the data. Similarly, inaccuracies in the analogue-to-digital conversion hardware of the data acquisition cards or software drivers during data acquisition can lead to sudden signal drops as observed in Figure. 3.8, i.e., invalid minutes or spikes from the instruments. Such errors may introduce distortions or gaps in the collected data, impacting the overall accuracy and reliability of the acquired information. The invalid data could come from temporary loss of power or synchronization signals used to drive data acquisition which could lead to signal drops without rain. Examples of received signals at 77.54 GHz and 25.84 GHz for the direct link are depicted in Figures 3.7 and 3.8, respectively. The highlighted example illustrates a clear-sky received signal with a sudden drop observed

due to issues raised previously. Investigations and end-to-end testing of the link received signal revealed that a faulty connector to the data acquisition card caused the abrupt signal drop. To compute the measured loss, the received signal during a rainy event is compared with a reference signal from a period without rain, taken from the same measurement period. Care is taken to ensure that the reference signal is not too distant or too close to the rain event (15 min clear sky before the rain event occurs), as antenna wetness or icing could impact the rain attenuation analysis.

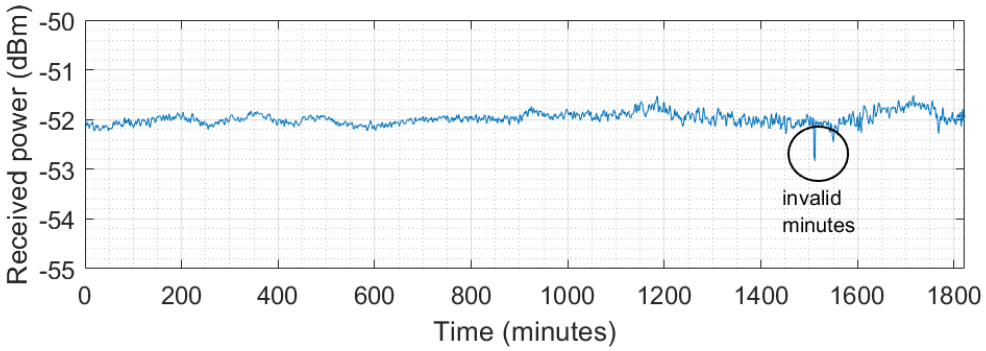

Figure 3.7: Example of received signal strength includes invalid and removable minutes at 77.54 GHz.

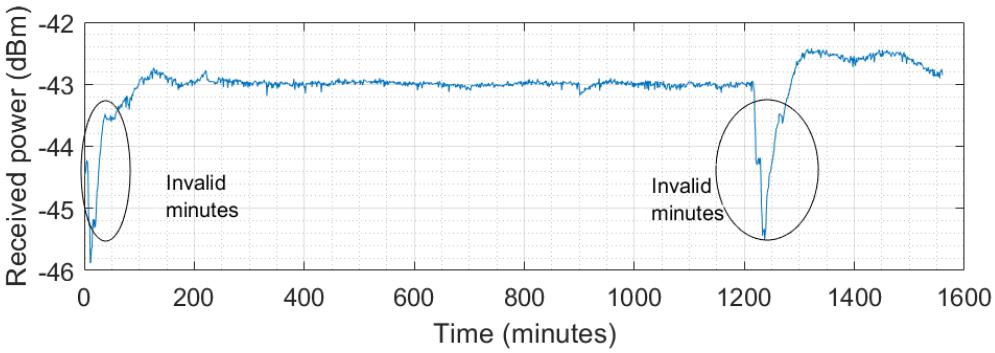

Figure 3.8: Example of received signal strength includes invalid and removable minutes at 25.84 GHz.

3.3.4 Measurement Uncertainty and Error

The accuracy of the measurements conducted using the experimental setup depends on various factors that contribute to uncertainty and imprecision. To quantify these errors and ensure the validity of the collected data, a thorough analysis of the measurement uncertainty is necessary. The main sources of uncertainty include:

- Resolution of the data acquisition system: The data acquisition cards have a resolution of 14 bits, corresponding to a quantization step size of around 0.006 dB at the power levels measured in the experiments. This quantization of the analogue signal introduces quantization errors up to ±0.006 dB due to rounding of the digital values.

- Drift in power level measurements: Even under clear sky conditions, slight variations in the received power are observed over time. These drifts are caused by factors like thermal fluctuations in the electronics and antenna movements due to wind and mechanical vibrations. Based on long-term observations, the drift can lead to fluctuations up to ±0.05 dB in the received power over short time scales on the order of minutes. When using a reference power level to calculate rain attenuation, these drifts directly translate to errors in the final attenuation values.

- Alignment errors: Imperfect antenna alignment and variation in antenna radiation patterns over time can also lead to changes in received power. Even with careful initial alignment that has been carried out by the technicians, factors like strong winds can misalign the antennas over longer periods. Regular alignment checks and adjustments have been performed to minimize this source of error.

- Accuracy limits of weather instrumentation: The precipitation measurement devices, PWS100 disdrometer, have inherent accuracy limits that propagate into the final attenuation calculations. As per the PWS100 specifications, these accuracy limits are around ±5% for particle size measurements above 0.3 mm diameter, ±5% for velocity measurements above 0.3 mm, and ±10% for rainfall rate cumulative measurements.

The overall measurement uncertainty can be calculated by taking the Root-Sum-of-Squares (RSS) of the individual error contributions:

$$U = \sqrt{\sum_{i=1}^{N} U_i^2} \tag{3.3.4}$$

where U_i represents each uncertainty component mentioned above and N is the number of components. Based on the above factors, this results in a total uncertainty of around ±0.12

dB in the attenuation measurements from the setup, plus the weather station PWS100 accuracy limits provided above for the rain measurement.

3.4 Summary

As highlighted in this chapter, the research work is founded on robust and reliable measurements, which encompass realistic precipitation statistics from the weather station PWS100 and mmWave data from the channel sounder fixed links. The data are obtained through the deployment of a highly accurate weather station at the scientific site, along with experimental mmWave fixed link setups operating at various frequency bands, specifically 77.54 GHz, 25.84 GHz, and 77.125 GHz. These fixed links include a 36 m direct path and side path links, as well as a 200 m point-to-point link operating at 77.125 GHz. For each link, the most reliable and best-measured data sets, as well as the most stable signal strength, are employed for estimating the rain attenuation. This approach ensures the accuracy and validity of the obtained results.

Considerable endeavours were undertaken to establish a stable experimental setup capable of delivering high-quality data. PLLs were installed on all RF boxes to minimize cable lengths. Data acquisition cables were upgraded to high-quality connectors with robust weatherproofing. The boxes and internal components were weatherproofed with filters added to reduce noise. Remote monitoring was taking place to rapidly identify and resolve any system failures, reducing data gaps. The weather station was configured to automatically trigger the recording of radio data during rain events. Continuous maintenance procedures were instituted, including coordination with technicians, to sustain data integrity. A new 200 m extended link was installed to enable comparative rain attenuation analysis. The meticulous measurements and system hardening ensured the robustness required for accurate rain attenuation modelling.

The subsequent chapter presents a comprehensive and thorough attenuation prediction, leveraging both theoretical models and statistical precipitation data. By combining these two essential components, the research aims to provide a comprehensive understanding of rain attenuation in mmWave fixed link systems.

Chapter 4

Precipitation Statistics and Rain Attenuation Prediction

4.1 Introduction

Rain attenuation constitutes a significant factor that demands consideration in the design of 5G fixed short-range point-to-point communication links. It pertains to the impact of rain on radio waves, and its influence encompasses multiple parameters that are crucial inputs, such as temperature, humidity, drop size distribution, terminal velocity, and shape of the raindrops [87]. To address this complex phenomenon, various models have been developed, leveraging statistical weather data to serve as system inputs applicable to diverse regions worldwide. These models aim to overcome the limitations of radio link data and frequencies by taking into account a wide array of parameters, including frequency, rain rate, drop size distribution (DSD), velocity, temperature, and water permittivity. This chapter focuses on the analysis and presentation of precipitation statistics on an annual basis, utilizing data gathered from the PWS100 weather station. Subsequently, these statistical insights are incorporated into rain attenuation prediction models to achieve accurate and reliable modelling predictions. The chapter outlines the precipitation statistics for the measurement period concerning this thesis and details their integration into the rain attenuation prediction models, drawing from the meteorological data sourced from the weather station. By understanding and incorporating these statistical parameters, the research aims to enhance the prediction and assessment of rain attenuation in mmWave

fixed link systems, thus contributing to the advancement of 5G communication technologies.

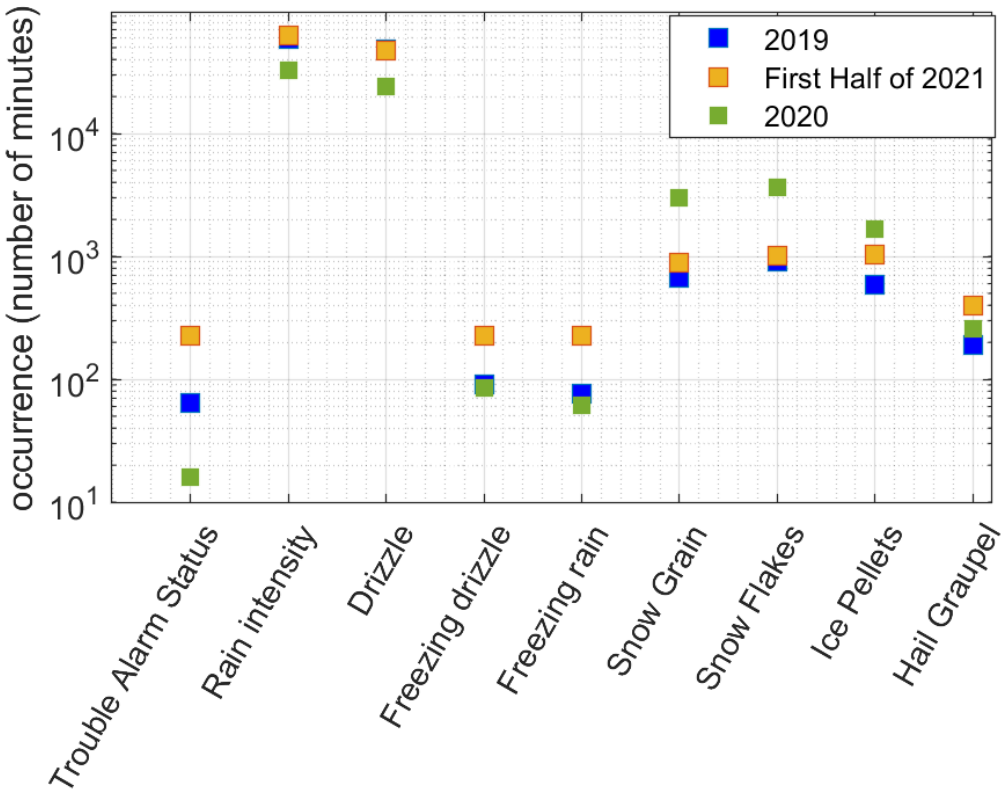

Figure 4.1: The total number of occurrences (minutes) for all types of precipitation recorded.

4.2 Weather Measurement Data

4.2.1 Precipitation Occurrences

The weather station offers minute-by-minute precipitation data. The system can output visibility and precipitation-related weather codes such as those detailed in World Meteorological Organisation (WMO) code. The data output in the .txt file comprises average visibility, humidity, temperature, rain intensity, rain accumulation, average fall velocity, snow grain, snowflakes, ice pellets, drizzle, hail, graupel, and DSD bin values (0.1 mm increment per value) up to 30 bins. As indicated in Figure. 4.1, nearly 1000 days of weather data were evaluated for the statistics on this phase of prediction. A total of 154,874 minutes occurrences have been reported for rainfall events (107 days) and

136,151 occurrences of other particles, i.e., drizzle, freezing drizzle, freezing rain, snow Grain, snowflakes, ice Pellets, hail, and graupel. 2020 shows the lowest in terms of rain intensity occurrences compared to 2019 and the first half of 2021 and the highest occurrences in terms of other particles such as snow and ice pellets. Drizzle particles drop almost as frequently as rain and the same is truly the case for snow particles of all sorts. Overall observation shows that over the measurement period, the statistics weather data availability is 95 % (from PWS100 weather station).

4.2.2 Rainfall Events

Figure. 4.2 shows the Complementary Cumulative Distribution Functions (CCDFs) of the yearly rain intensity in mm/h that is exceeded for the given probability. For most of the measurement data period, the maximum rain intensity is less than 28 mm/h. Occasional rain events above 30 mm/h take place.

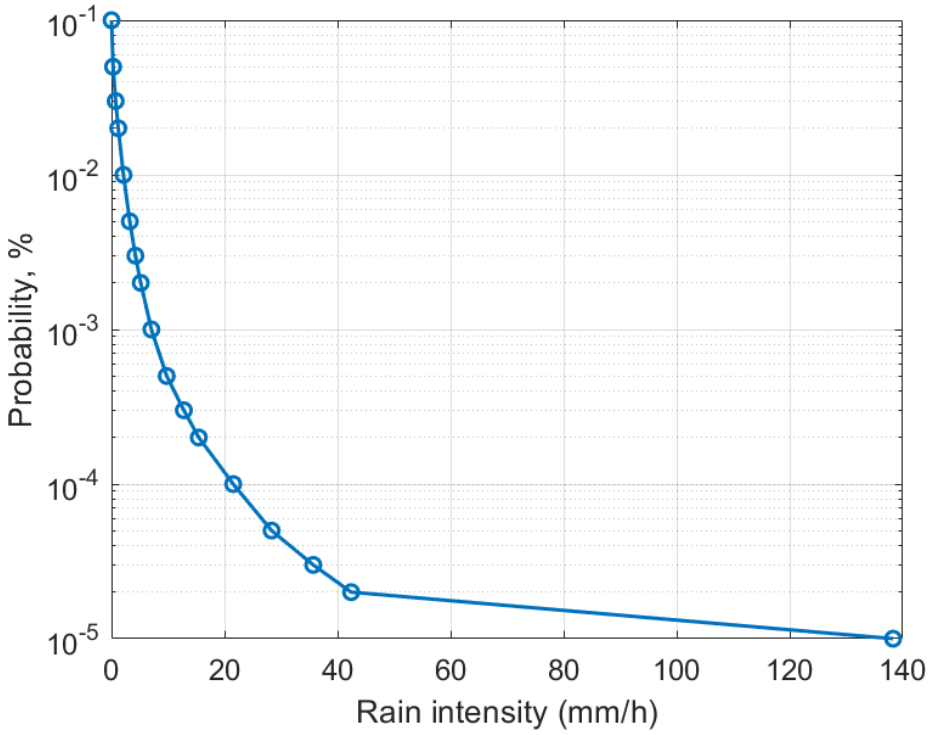

Figure 4.2: Yearly rain intensity CCDF.

Figure. 4.3 presents the total count of rain events and the corresponding duration of these events. It is observed that as the rain intensity increases, the total number of rain events

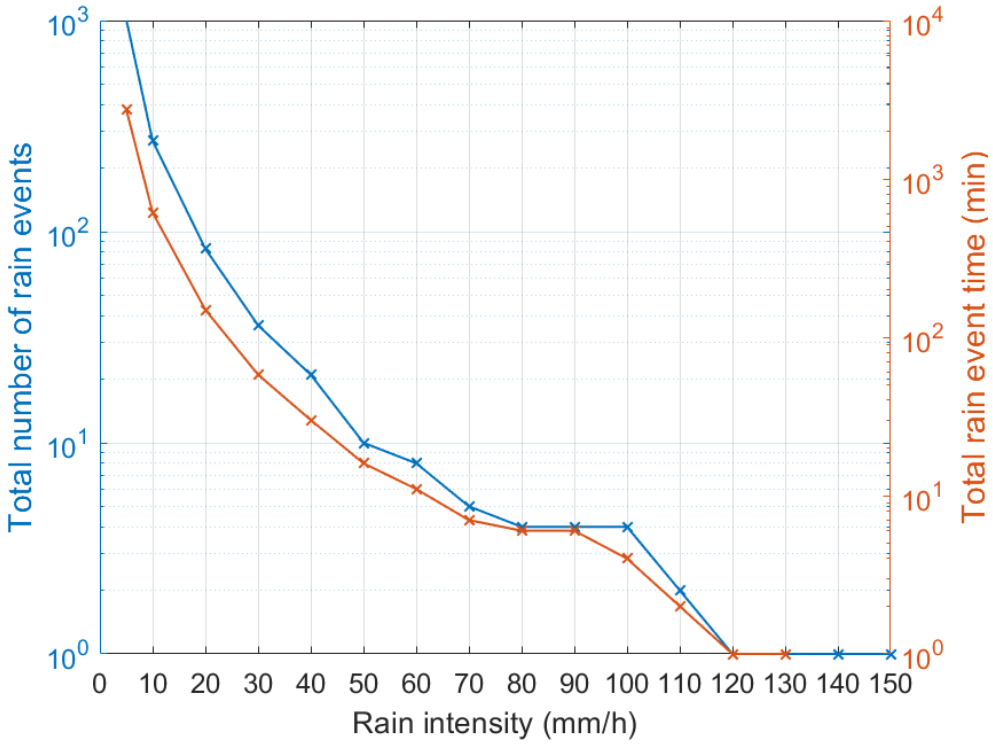

Figure 4.3: Total number of rain events and total rain event time.

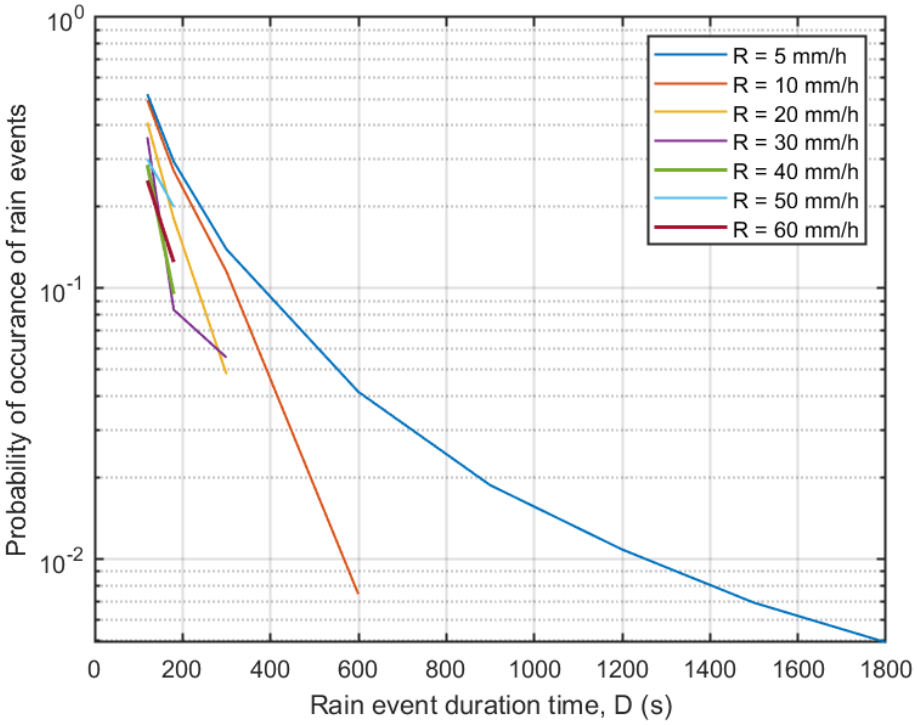

Figure 4.4: Probability of occurrence of rain events.

and the overall duration of these events tend to decrease. In Figure 4.4, the probability of rain events lasting longer than a specified duration (D) is depicted based on the rain rate (RR) being greater than a certain threshold. As both the rain intensity and the duration of rain events increase, the probability of such events occurring decreases, with a pronounced reduction for instances of very heavy rainfall. The threshold for light and moderate rainfall events is identified to be greater than 10 minutes, whereas, for heavy rainfall and beyond, it falls within the range of 2.5 to 6.5 minutes. The figures reveal a relatively even distribution of occurrences and the number of events across various durations and accumulated rainfall, facilitating the establishment of appropriate boundaries. This observation can be explained by examining the rain formation process.

Rainfall is classified into three main types: convective, stratiform, and orographic rain, which are further categorized based on intensity as light, moderate, heavy, very heavy, and torrential rainfall. Convective rainfall results from the rising of warm air from the ground due to solar heating. As the warm air ascends and cools, it condenses, leading to the formation of clouds at the condensation or dew point. This process often leads to torrential downpours, accompanied by thunder and lightning. Such intense rainfall is more common in warmer regions and tends to be brief and localized, as evident in our disdrometer measurements during the summer period, where rain intensity exceeds 50 mm/h but typically lasts only for a minute. Orographic rain occurs in regions with abrupt changes in terrain elevation, such as mountains or cliffs. On the other hand, stratiform rain occurs when there is a forced upward movement of air, resulting in less intense rainfall but with broader coverage. This type of rain is more dominant in our measurement location, Durham County, England, where stratiform rain is more prevalent than convective rain. The data collected throughout the measurement period indicates that up to 90% of the recorded rainfall is of light intensity, while heavy rainfall events are more seasonal in nature.

One significant rainfall parameter to be considered is the temporal correlation which is important for understanding how the intensity of rain at a certain site varies over time because rainfall events are variable in time [88] and as mentioned in [88], higher attenuation values may occur within very heavy rainfall with short duration. The temporal correlation function is described by equation 4.2.1:

$$\rho = \frac{\mathrm{cov}\left(rr_{t_1}, rr_{t_2}\right)}{\sqrt{\sigma_1 \sigma_2}} \tag{4.2.1}$$

where rr_{t_1} and rr_{t_2} are the point rain rate at two different times t1 and t2. σ is the standard deviation of the same location. The time instances for which the correlation is calculated are t1 and t2.

The rain intensity can vary within a 1 minute period, especially for convective rainfall which tends to be intense but short-lived. The 1 minute average intensity may not capture the peak intensities that occur, which could explain why some heavy/torrential rain events last only 1-2 minutes – the peak intensity may have been much higher than the 1 minute average. Higher temporal variation in intensity also means the temporal correlation will decrease more rapidly with increasing time difference. Rapid changes in intensity can lead to higher rain attenuation, especially if the peak intensities are not captured by the 1-minute averages. The probability distributions and duration statistics could also change if sub-minute intensities are considered instead of 1-minute averages. For example, the probability of very heavy (>50 mm/h) 1-minute rain may be low, but the probability of such high sub-minute peak intensities could be higher. The dynamics of rain cell movement and development can lead to intensity fluctuations within the 1-minute scale as well, driving intensity changes not captured by longer averaging times. In summary, sub-minute intensity fluctuations, especially for convective rain, are important to consider alongside the 1-minute averages when analyzing temporal rainfall statistics and rain attenuation. Higher temporal resolution data could provide additional insights.

4.3 Drop Size Distribution

In both meteorology and microwave wireless communication, the Drop Size Distribution (DSD) holds paramount importance [89]. Its study and modelling date back to as early as 1943 [90; 91]. The DSD refers to the probability density of finding raindrops with equivalent volumetric diameter D in a given unit volume (N is the quantity symbol). This distribution is closely linked to the rainfall velocity, and in turn, it influences the rain rate. It is worth noting that a universal DSD applicable across all regions is not achievable due to its variability between different climatic zones. The DSD exhibits distinct characteris-

tics in various regions, such as tropical, dry, polar, continental, and coastal areas [92]. This regional variability in DSD underscores the significance of taking into account the specific meteorological conditions and local climate when analyzing and modelling rainfall characteristics. In summary, the Drop Size Distribution plays a crucial role in understanding rainfall behaviour and its impact on microwave wireless communication systems. Its varied nature across different regions necessitates tailored approaches to DSD modelling, considering the unique weather patterns and geographical features of each location.

4.3.1 DSD Models

Because of their consistent alignment with the usual drop size distribution shape in the majority of experimental data, the Exponential and Gamma distributions are the most commonly used analytical approximations of the DSD. By fitting empirical data by Marshall and Palmer [89], they were able to construct a negative exponential distribution. It is used in the form given by the following equation 4.3.2:

$$\mathrm{N(D)} = \mathrm{N_0} \exp(-\lambda \mathrm{D}) \tag{4.3.2}$$

where $\mathrm{N_o}$ is an intercept parameter and is constant for all Rainfall Rate (RR) in mm/h and λ is the distribution slope parameter in mm^{-1} and is determined as a function of RR. D is the drop diameter in mm.

$$\lambda \approx a * RR^b \tag{4.3.3}$$

where b= -0.21. For various rainfall types [93], these parameters are given in Table. 4.1.

Table 4.1: Exponential distribution model parameters

Rain type	$\mathrm{N_o}$ (mm^{-1} m^{-3})	λ (mm^{-1})
Thunderstorm or shower	1400	$3\mathrm{R}^{-0.21}$
Continuos rain	7000	$4.1\mathrm{R}^{-0.21}$
Drizzle	30000	$5.7\mathrm{R}^{-0.21}$
Average rain	8000	$4.1\mathrm{R}^{-0.21}$

The gamma model is given by equation 4.3.4 and its parameters in Table. 4.2:

$$\mathrm{N(D)} = \mathrm{N_0 D^{\mu}} \exp(-\lambda \mathrm{D}) \tag{4.3.4}$$

N(D) is the number of drops per unit volume per drop diameter interval (dD). Its unit is $\mathrm{m^{-3}\ mm^{-1-\mu}}$.

$\mathrm{N_0}$ is the intercept parameter of DSD. Its unit is $\mathrm{m^{-3}\ mm^{-1-\mu}}$. λ ($\mathrm{mm^{-1}}$) is the slope parameter. μ is shape of the DSD.

Table 4.2: Gamma distribution model parameters

Rain type	$\mathrm{N_o}$	λ	μ
Convective	$6.29\mathrm{e}5\mathrm{R}^{-0.416}$	$8.35\mathrm{R}^{-0.185}$	3
Stratiform	$2.57\mathrm{e}4\mathrm{R}^{0.012}$	$5.5\mathrm{R}^{-0.129}$	3

The Weibull raindrop distribution is obtained only from the raindrop production process, and it may perfectly capture the distribution of raindrops of varying sizes. The model is given by equation 4.3.5

$$N(D) = N_0 \frac{\eta}{\sigma} \left(\frac{D}{\sigma}\right)^{\eta-1} \exp\left[-a\left(\frac{D}{\sigma}\right)^{\eta}\right] \tag{4.3.5}$$

where these parameters are commonly proposed by Sekine [94]: $N_0 = 1000, \eta = 0.95R^{0.14}$, $\sigma = 0.26R^{0.42}$, $a = 1$.

The lognormal distribution is given by equation 4.3.6:

$$N(D) = \frac{N_t}{\sqrt{2\pi}\ln\sigma_g D} \exp\left[\frac{-\ln^2(D/D_g)}{2\ln^2\sigma_g}\right] \tag{4.3.6}$$

where N_t is the total number of drops $\mathrm{m^{-3}}$, D_g is the geometric mean diameter and σ_g is the standard geometric deviation, which can be defined by:

$$\ln(D_g) = \overline{\ln D} \tag{4.3.7}$$

and

$$\ln^2(\sigma_g) = \overline{(\ln D - \ln D_g)^2} \tag{4.3.8}$$

4.3.2 DSD Measurement

Various methodologies are employed for DSD measurements, including photographic techniques and more modern automated disdrometers utilizing laser-based measurements. Each disdrometer has its limitations, with a minimum detectable drop size and a maximum measurement size, potentially impacting the accuracy of the results. Moreover, the small collection area of each disdrometer can lead to noisy drop counting, particularly for larger drops. Additionally, during intense rainfall, optical disdrometers may encounter challenges as one drop might be obscured by another, affecting the readings.

In this research, the laser-based PWS100 disdrometer, as described in the previous chapter, is utilized due to its high measurement accuracy. The disdrometer records 300 values of the number of particles within a diameter range of 0.1 to 30 mm, with a particle size bin of 0.1 mm. Additionally, the average velocity of all particles is recorded, providing valuable information for DSD calculations. The DSD measurements obtained from the PWS100 disdrometer are calculated using $N(D_i)$ in equation 4.3.9 which contribute to the precise estimation of rain attenuation and its modelling for microwave communication applications.

$$N(D_i) = \sum_j \frac{n\left(D_i, v_j\right)}{v_j} \cdot \frac{1}{S \cdot \Delta t \cdot dD_i} \tag{4.3.9}$$

where $S = 40$ cm^2 is the measurement surface of the laser beam of the PWS100 disdrometer, $\Delta t = 60$ s is the integration time, $n\left(D_i, v_j\right)$ is the number of particles registered within the classes with mean diameter D_i(mm) and mean speed v_j(m/s), dD_i(mm) is the class width associated with the diameter D_i. Rain drops with diameters less than 9.5 mm are classified as 23 bins to calculate the DSD values. Appropriate unit conversions are implemented to deliver the result in $\left(\mathrm{m}^{-3}\ \mathrm{mm}^{-1}\right)$.

As the velocity of each particle is not recorded, the theoretical relationship between the terminal fall velocity and the drop diameter is adopted for DSD computation. Specifically,

the following relation (equation 4.3.10) is used to calculate the rainfall velocity:

$$v(D_i) = \begin{cases} 3.78 D_i^{0.67}, D_i < 0.8 \\ 9.65 - 10.3 e^{-0.6 D_i}, D_i \geq 0.8 \end{cases} \tag{4.3.10}$$

which is a combination of two widely used equations to achieve a non-negative and monotonic relation between drop diameter and the terminal fall velocity [95; 96]. The equation for calculating rainfall velocity ($v(D_i)$) employs two distinct regimes based on the drop diameter (D_i). The first regime ($D_i < 0.8$) represents smaller raindrops where viscous forces dominate, leading to a power-law relationship ($D_i^{0.67}$) between drop size and fall velocity. In contrast, the second regime ($D_i \geq 0.8$) accounts for larger raindrops where gravitational forces prevail, resulting in an exponential decay function ($e^{-0.6 D_i}$) that models the saturation effect as drop size increases. By combining these regimes, the equation ensures a smooth and continuous transition in the relationship between drop diameter and terminal fall velocity, enabling accurate computation of the DSD essential for rainfall measurement and modelling.

As we mentioned before, the disdrometer contains 300 bin values for drop size distribution (0.1 mm increment per value). It can determine the number of drops per bin, and the output raw data generates the number of drops for each bin (the number of drops is classified for each drop diameter type). The PWS100 determines each individual particle type from an accurate measurement of the particle size. For every minute and for each bin, the following steps are used for the estimation of the average DSD from the rain rate and the number of drops using equation (4.3.9):

- The disdrometer measurements' integration time intervals are classified into rain rate classes, such as 5 mm/h and 20 mm/h.
- The disdrometer bin size classes are reorganised according to the bin size classes (0.1 mm, 0.2 mm.... 30 mm) for each long-term mean (that is, for each rain rate class).
- The (long-term mean) drop count in each bin size class is divided by the instrument's measuring area (40 cm^2) and column height (integration time multiplied by

the mean fall velocity of the bin's mean diameter). As a result, the long-term mean drop counts per unit volume are calculated.

- Drop counts per unit volume are divided by bin size class width to produce the appropriate distribution density in each bin size class.

Appropriate unit conversions are then applied to obtain the result in $(\mathrm{m}^{-3}\ \mathrm{mm}^{-1})$ since the above-outlined steps yield the commonly known drop size distribution (DSD), in units of $1/(m^3 mm)$.

Figure. 4.5 shows the average rain DSD overall rain bins. During the measurement period, the DSD attains its peak within the 0.125 - 2 mm range.

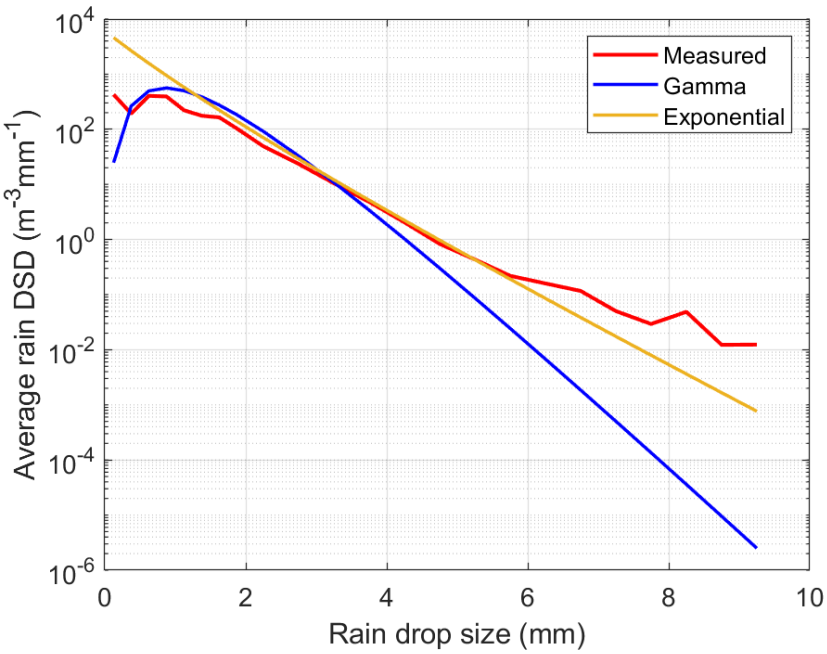

Figure 4.5: Average rain DSD overall rain intensities using disdrometer data, Gamma, and Exponential model.

Figures. 4.6 and 4.7 illustrate the rain DSD under varying rain intensities, and the measured DSD compared to the rainfall rate across the four seasons throughout the year, respectively. The measured DSD data indicates that larger raindrops, from 3 to 8 mm in diameter, are frequently observed during light to moderate rainfall intensities up to 10 mm/h. Fitting an exponential distribution model to the measured DSD shows close conformance for drop diameters below 4 mm acrosslight and moderate rainfall. However, the deviation between the Gamma DSD model and measurements emerges for drop sizes exceeding 4 mm. Specifically, Figure 4.6a illustrates that the frequency of drops with diameters between 4-8 mm tends to be higher in the measured DSD compared to the Gamma model in Figure 4.6b. This is evidenced by the broader ”shoulder” of the measured DSD curve in the 4-8 mm range.

Consequently, using the Gamma model for rain attenuation calculations may lead to overestimation in this interval, resulting in higher attenuation values. The data further reveals that very heavy rainfall leads to higher DSD values in the range of 0.1-1.8 mm, which is more closely matched by the Gamma model. On the other hand, light and moderate rainfall consistently agree well in terms of DSD values across all rain diameters. The exponential DSD model appears more suitable given the large volume of data, but for very large raindrop sizes, there is increased uncertainty between the models and the measured DSD. Given the high capability of the PWS100 disdrometer in measurement and the diverse datasets available, the measured DSD data is deemed suitable for rain attenuation modelling, which will be the focus of the subsequent sections. Histograms of N, representing the number of raindrops within specific diameter ranges, were determined for different seasonal rainfall rates: autumn, winter, spring, and summer. An overall increase in N values is observed with an increasing rain rate, particularly during the winter period. However, for the remaining seasons, the distributions do not follow a clear trend with rainfall intensity. Considerable variation is observed for light and moderate continuous rainfall rates, particularly those below 10 mm/h. For instance, in the winter season, during rainfall intensity of up to 2 mm/h and steady rainfall, N reaches its maximum of 2030 m^{-3} mm^{-1}. In contrast, during the summer season with a rainfall rate of 40 mm/h, N is recorded as 427 m^{-3} mm^{-1}. The concentration of raindrops is higher during moderate and light rainfall in winter and is subject to increased variation in spring and summer.

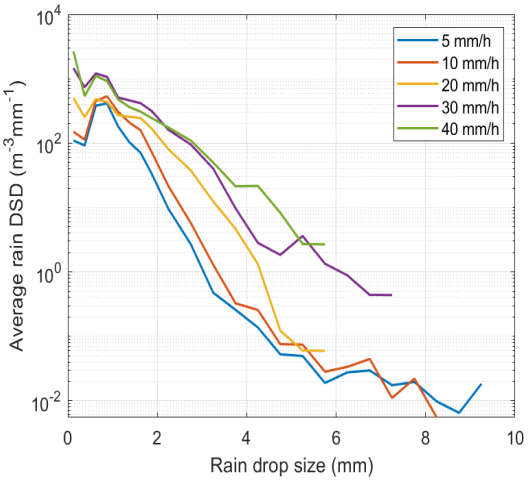

(a) *Measured DSD disdrometer data.*

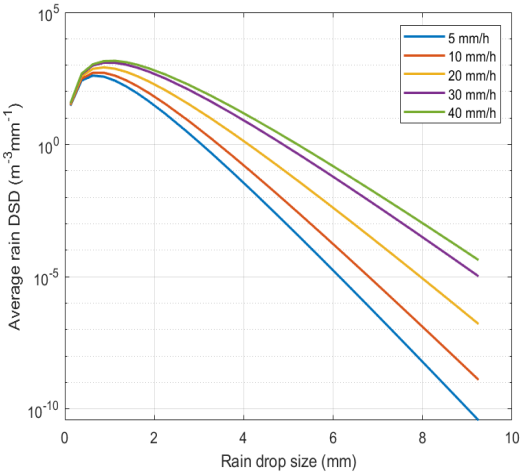

(b) *DSD Gamma model.*

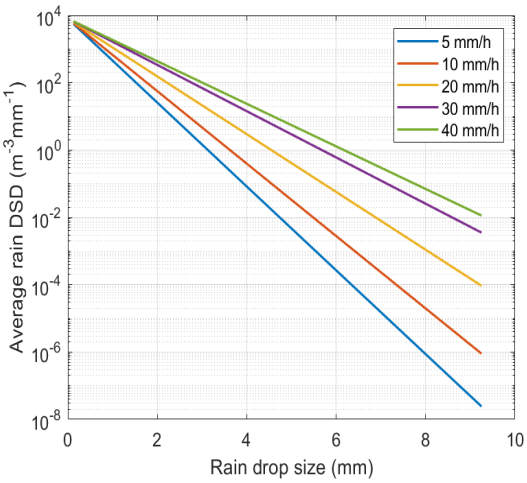

(c) *DSD Exponential model.*

Figure 4.6: Rain DSD under different rain intensities.

This distribution may be influenced by factors such as wind speed, temperature, humidity, or the variability of rainfall in time and space.

4.4 Complex Refractive Index of water

Water poses an intriguing challenge for the comprehensive application of classical electromagnetic theory. Utilizing the complex refractive index, expressed in Equation 4.4.11

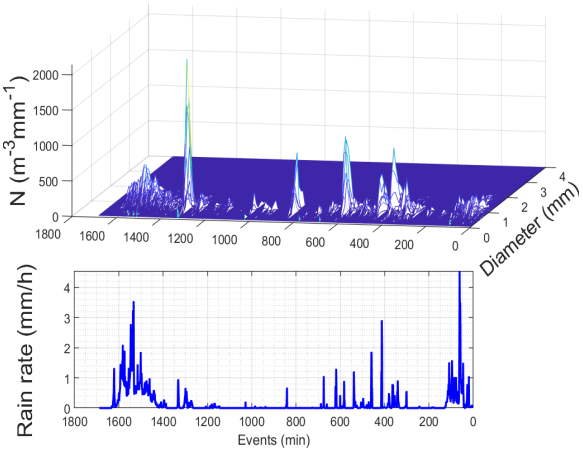

(a) *Autumn season.*

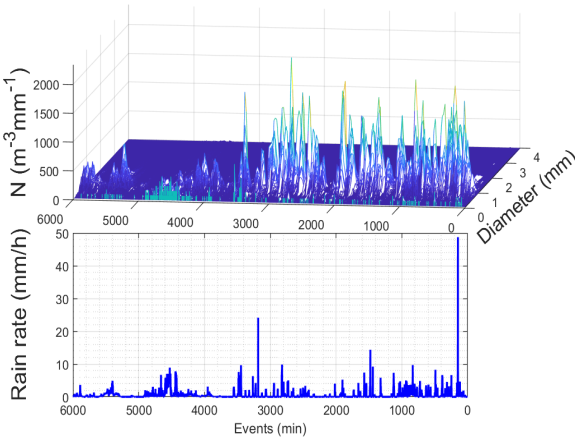

(b) *Winter season.*

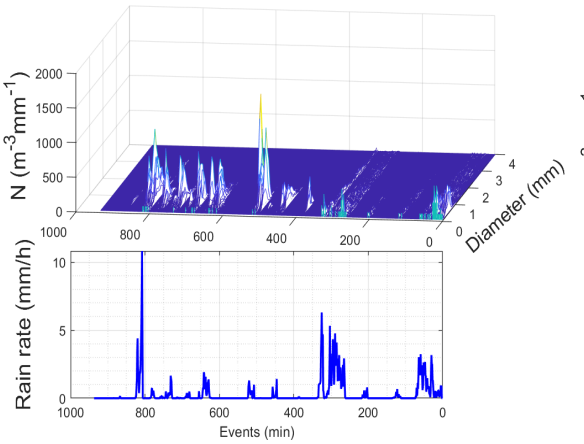

(c) *Spring season.*

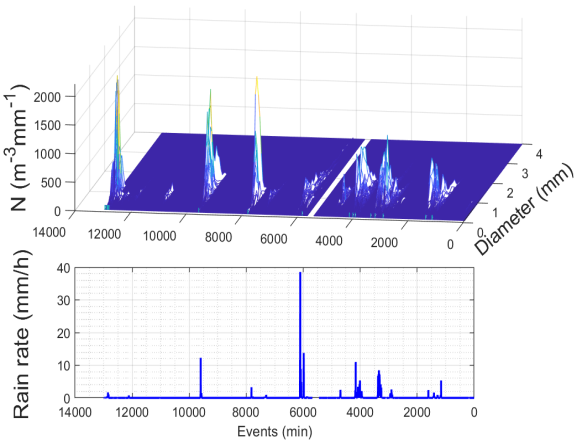

(d) *Summer season.*

Figure 4.7: Measured DSD versus rainfall rate within four seasons along the year.

as a function of wave number, is a method employed to analyze its optical properties [34].

$$N(v) = n(v) + ik(v) \tag{4.4.11}$$

where the wave number, v, is defined as the inverse of the wavelength, and has units of cm^{-1}. $N(v)$ can be calculated as a function of a variety of optical properties such as reflectance, transmittance, emittance, and Mie scattering parameters at any spectral location.

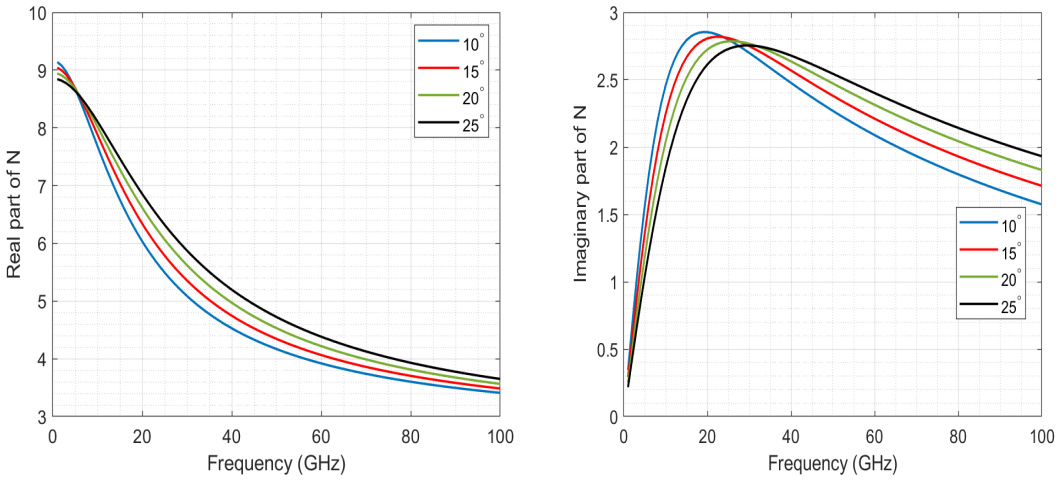

(a) *Real part.* **(b)** *Imaginary part.*

Figure 4.8: Complex refractive index of water.

Figure. 4.8 shows the variation of the real part of the refractive index of water versus frequency up to 100 GHz within four examples temperature: 10, 15, 20, and 25°. It is noticed a smooth constant of n_r above 40 GHz. While a sinusoidal variation of the imaginary part n_i. Ultimate measurements reveal that when frequency increases, the refractive index of water decreases for all temperature levels.

As discussed in the previous sections, the complex refractive index of water is a key parameter governing its interaction with electromagnetic waves as well as the DSD measurement. In the following section, we review empirical and physics-based models that have been developed to predict rain attenuation. These models relate measurable weather parameters like rainfall rate, drop size distribution, and path length to the expected attenuation. Their successful application depends on appropriate tuning and validation using real-world propagation measurements. However, the availability of such measurements is geographically limited. Therefore, generalized models are needed to provide rain attenuation estimates across diverse locations and frequencies.

4.5 Rain Attenuation Prediction

Studies discussed in [97] have explored various empirical, physical, and compound nature-based models for predicting rain attenuation. One of the crucial aspects in developing such

a model is identifying its parameters, including rain rate, temperature, water permittivity, path length, rainfall velocity, and raindrop size distribution. Among these factors, rainfall rate and path length are commonly considered in most models. However, it is important to note that the availability of propagation measurements is limited to only a few locations worldwide and for a restricted number of frequencies. Therefore, direct application of these insights to all locations is not feasible. As a result, multiple attenuation models based on physical data and weather parameters have been developed to provide appropriate inputs for communication system margin calculations in diverse locations.

Rain attenuation plays a vital role in channel modelling for reliable wireless radio links, especially in FWA applications, where maintaining non-outage links is essential. Possessing a precise rain attenuation model for mmWave fixed links is of paramount importance to prevent the miscalculation of transmission and receiving system parameters, including antenna gain, power, azimuth, polarization type, and amplifiers. Furthermore, the significance of improving existing rain attenuation models for mmWave short-range fixed links lies in enhancing the accuracy of predictions, optimizing system performance, and ensuring reliable communication under various weather conditions. Additionally, raindrops can cause significant interference between neighbouring links due to the scattering effect, as depicted in the use-case previously highlighted in Chapter Two in Figure. 2.1. This interference poses significant challenges to spectrum management and regulation for relevant authorities. In [3], the rain attenuation modelling took into account polarization angle, frequency, station height, precipitation rate, elevation angle, and latitude. On the other hand, [98] considered variables such as temperature, path length, frequency, precipitation rate, wetness, wind speed, wind direction, and visibility for frequencies above 10 GHz. Furthermore, the analyses in [99] classified rain attenuation models into five categories:

- The fade slope model where the rain attenuation slope versus the time data using a precise experimental setup was created.
- The empirical model is based on experimental data findings instead of a selection of relevant input-output correlations.
- The physical model is based on certain analogies between the formulation of the

rain attenuation model and the real structure of rainfall.

- The statistical model relies on a statistical analysis of meteorological and infrastructure data, and the final model is generated in most cases using regression analyses.
- The optimization model, where input parameters are generated through optimization by some of the other elements that impact the rain attenuation

Table 4.3: Classification of rain attenuation models that have been highlighted in [3]

Fade Slope	Empirical	Optimization	Statistical	Physical
Andrate [100]	Garcia [101]	Livieratos [102]	ITU-R P.530-17	Crane T-C [103]
Chebil [104]	Crane [105]	Pinto [106]	Singh [107]	Ghiani [108]
	Mello [109]			Capsoni [110]
	Moupfouma [111]			
	Abdulrahman [112]			
	DaSilva [109]			
	Budlal [113]			

A summary of rain attenuation models is listed in Table. 4.3. For most of these models path length, frequency, and rain rate are common input parameters. Crane and Andrade's models are well known for suitability for short-range links between 7 and 137 GHz at 500 m path length into the Andrade model and 300 m for the Crane model between 26 and 75 GHz.

4.5.1 Estimation Models Used Through This Research Work

4.5.1.1 Da Silva-Unified

The model uses a semi-empirical method for rain attenuation prediction in Earth-Space and terrestrial links using rain rate distribution [114]. The attenuation for given path-length d is given by equation 4.5.12:

$$\mathrm{A} = \gamma \cdot \mathrm{d_{eff}} \tag{4.5.12}$$

where

$$\gamma = \mathrm{k}\,(\mathrm{R}_{0.01})^{\alpha} \tag{4.5.13}$$

and

$$\mathrm{d_{eff}} = \frac{\mathrm{d}}{1 + \mathrm{d}/\mathrm{d_0}\,(\mathrm{R_{0.01}})} \tag{4.5.14}$$

where $\gamma(\mathrm{dB/km})$ is the specific attenuation. $R_{0.01}$ is the rain rate exceeded at 0.01%. The rain attenuation model employs a simulation technique where an equivalent cell with uniform rainfall rate and length $d0$ is randomly placed in the great circle plane to account for the influence of non-uniform rainfall along the propagation path. In the case of uniform distribution of rainfall, the effective length is considered to be the actual effective path length between the transmitter (TX) and receiver (RX). This approach was proposed because rainfall is typically not uniformly spread over the entire radio path length. Thus, calculating rain attenuation solely based on the actual path length can lead to inaccurate results.

To address this, the model takes into account the horizontal uniformity of rainfall and defines the effective route length of the communication connection between the TX and RX. This effective path length ($\mathrm{d_{eff}}$) represents the average length of the intersection between the equivalent cell and the propagation path. The diameter of the equivalent cell, denoted as $d0$, is determined empirically from experimental data and depends on the region's long-term point rainfall rate. Da Silva proposed an exponentially declining function of the point rainfall rate R (mm/h) in the model to calculate $d0$.

For link path lengths below 1 km, the model suggests the use of correction factors for rainfall distribution larger than 1 to enhance the accuracy of the method. In this context, the empirical expression $\mathrm{R_{effT}}$ is introduced to correct R as defined in equation 4.5.15:

$$\mathrm{R_{eff}} = 1.74\mathrm{R}^{0.786+0.197/\mathrm{d}} \tag{4.5.15}$$

while d_0 is given by:

$$\mathrm{d_0} = 125 \cdot \mathrm{R}^{-0.33} \tag{4.5.16}$$

4.5.1.2 Crane Model

The Crane model (equation 4.5.17), described in [105], utilizes geophysical measurements of point rain rate statistics, horizontal rainfall structure, and vertical temperature

structure of the atmosphere. This approach allows for the establishment of rain distribution both globally and within the United States through detailed rain distribution maps. With the help of these maps, one can estimate the rain rate distribution. The model also provides a way to simulate the attenuation for a given path length 'd'.

$$A\left(R_p, D\right) = kR_p^{\alpha}\left[\frac{e^{u\alpha D}-1}{u\alpha}\right] \tag{4.5.17}$$

where u, b, c, de are parameters given by:

$$u = \frac{\ln\left[be^{cd}\right]}{d}, \quad d \text{ in km} \tag{4.5.18}$$

$$b = 2.3R^{-0.17}, \quad R \text{ in mm/h} \tag{4.5.19}$$

$$c = 0.026 - 0.03\ln R \tag{4.5.20}$$

$$d = 3.8 - 0.6\ln R \tag{4.5.21}$$

4.5.1.3 ITU-R P.530-3

The ITU-R P.838-3 model, given by equation 4.5.23, calculates a relationship that may be used to estimate rain attenuation. Despite its simplicity, the empirical connection presented was theoretically and empirically validated:

$$\gamma = kR^{\alpha} \tag{4.5.22}$$

where R is the rain rate (mm/h), k and α are model parameters dependent on the frequency f, and γ is the specific attenuation in dB/km.

The total attenuation for a specific distance depends on the effective path length d_{eff}, between the Tx and Rx antennas as:

$$A = \gamma d_{eff} \tag{4.5.23}$$

where the effective path length, d_{eff}, of the link is obtained by multiplying the actual path length d by a distance factor r.

In ITU-R P.530-17 the distance factor is given as:

$$r = \frac{1}{0.477 d^{0.633} R_{0.01}^{0.073\alpha} f^{0.123} - 10.579(1 - exp(-0.024d))} \tag{4.5.24}$$

where $R_{0.01}$ is the rain rate exceeded for 0.01% of the time (with an integration time of 1 min).

4.5.1.4 Budalal

The model defined in [113] concentrates on the prediction of rain attenuation over mmWave frequencies for a short-range path (less than 1 km). The model proposed a correction increment factor $I_{f\gamma}$ for the distance factor to improve the ITU-R P.530-17 is given below in equations 4.5.25 and 4.5.26:

$$I_{f\gamma} = \left[\frac{1}{1.77 d^{0.77} R_{0.01}^{-0.05}} \right] \text{ for f} \leq 40 \text{ GHz and } d < 1 \text{ km} \tag{4.5.25}$$

$$I_{f\gamma} = \left[\frac{1}{0.477 d^{0.633} R_{0.01}^{0.073} f^{0.123}} \right]^2 \text{ for f}>40 \text{ GHz and } d < 1 \text{ km} \tag{4.5.26}$$

4.5.1.5 UK (2003 RAL)

The ITU-R model was proposed to be modified in [115], where the distance factor is given by:

$$r = \frac{d}{0.874 + 0.0255 \cdot (R^{0.54} - 1.7) \cdot d^{0.7}} \tag{4.5.27}$$

4.5.1.6 DSD

Rain attenuation may also be predicted using the DSD model.

$$\gamma = 4.343 \times 10^3 \int_0^\infty \delta_{ext}(D) N(D) dD \tag{4.5.28}$$

where γ is the specific attenuation in dB/km, $\delta_{ext} = \pi(\frac{D}{2})^2 Q_{ext}$ is the extinction cross section (m^2) for water drops of diameter D (mm), and $N(D)$ is the drop size distribution value ($m^{-3}mm^{-1}$) at diameter D. The extinction efficiency Q_{ext} can be calculated from Mie scattering or Rayleigh scattering theory depending on the size parameter $x = \pi D/\lambda$, where λ is the wavelength.

The extinction efficiency Q_{ext} can be calculated from Mie scattering or Rayleigh scattering theory depending on the size parameter $x = \pi D/\lambda$, where λ is the wavelength. For Mie scattering, the extinction efficiency is calculated as:

$$Q_{ext} = \frac{2\pi}{x^2} \sum_{n=1}^{\infty} (2n+1) \operatorname{Re}\{a_n + b_n\} \tag{4.5.29}$$

$$a_n = \frac{\psi_n'(mx)\psi_n(x) - m\psi_n(mx)\psi_n'(x)}{\psi_n'(mx)\xi_n(x) - m\psi_n(mx)\xi_n'(x)} \tag{4.5.30}$$

$$b_n = \frac{m\psi_n'(mx)\psi_n(x) - \psi_n(mx)\psi_n'(x)}{m\psi_n'(mx)\xi_n(x) - \psi_n(mx)\xi_n'(x)} \tag{4.5.31}$$

where ψ_n and ξ_n are the Riccati-Bessel functions which can be expressed using spherical Bessel functions of the first kind and third kind as:

$$\psi_n(x) = \sqrt{\frac{\pi x}{2}} J_{n+\frac{1}{2}}(x) \tag{4.5.32}$$

$$\xi_n(x) = \sqrt{\frac{\pi x}{2}} H^{(2)}_{n+1/2}(x) \tag{4.5.33}$$

In this section, rain attenuation models were discussed. Now, the focus shifts to applying these models to make predictions of rain attenuation on a yearly basis. Measured disdrometer data is utilized to provide inputs to the attenuation models, enabling analysis of the expected attenuation behavior over short-range fixed links across desired frequency bands annually. This analysis provides a comprehensive perspective of rain attenuation under different rainfall conditions over an extended period. Further investigations are warranted to understand the factors influencing differences between model predictions, which can ultimately help improve rain attenuation estimation accuracy.

4.5.2 Prediction of Specific Attenuation from Annual Data

In this section, the attenuation will be computed on a yearly basis, providing a comprehensive perspective of the predicted attenuation behaviour for the specific attenuation (dB/km) over short-range fixed links in the desired frequency bands. The calculated attenuation will be mapped against the measured disdrometer precipitation throughout the year using the discussed models in the previous part. The calculations presented here pertain to the time period from January 2019 to June 2021. The specific attenuation calculation in dB/km is limited to the ITU and DSD models, as most rain attenuation models in dB/km are based on the empirical equation kR^{α}. These models differ in terms of introducing path length in dB. Figure 4.9 illustrates the CCDFs of the calculated attenuation for the two selected frequencies over a period of two and a half years using the ITU-R and DSD models.

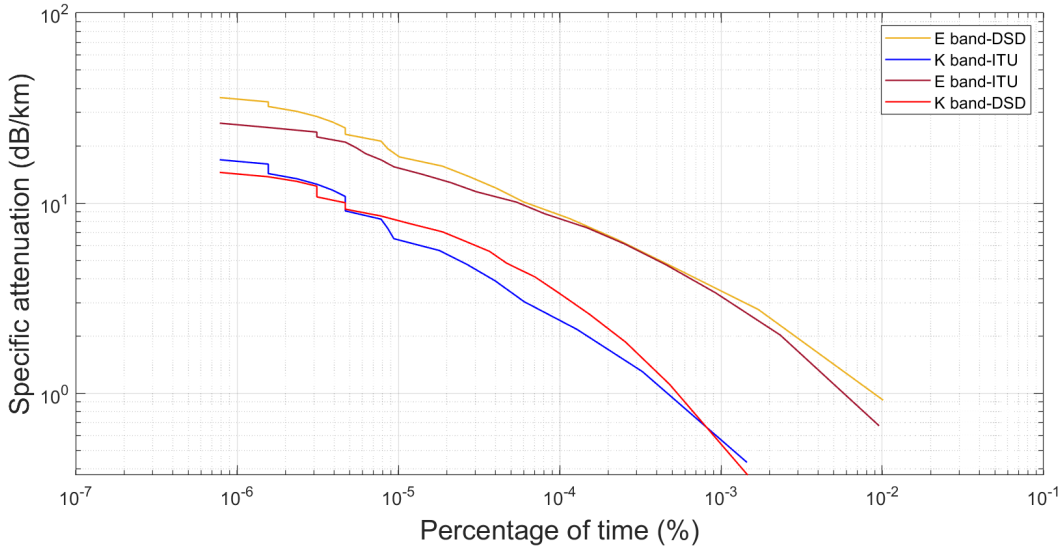

Figure 4.9: Cumulative distributions of rain specific attenuation.

It is widely recognized that the ITU model requires fewer input data, while the DSD model relies on an extensive range of disdrometer data and inputs, allowing for accurate and precise computations. The models show close alignment, with only slight differences observed for higher attenuation values at lower time percentages. The attenuation reaches its lowest value of 1 dB/km for time percentages greater than 0.1%, and its highest value of 10 dB/km for time percentages less than 0.001%.

Figures 4.10 and 4.11 provide a more detailed analysis of the variation in rain attenuation throughout the measurement period. It is observed that the ITU model yields somewhat higher values than the DSD model for higher frequencies (77.54 GHz) and heavy rain rates exceeding 15 mm/h. The models show the closest alignment at 25.84 GHz across the range of rainfall events measured. The RMSE between the ITU and DSD models at 25.84 GHz is 0.87 dB, compared to 2.34 dB at 77.54 GHz across the observed rain rates. The correlation coefficient between the model predictions is 0.94 at 25.84 GHz and 0.89 at 77.54 GHz. This suggests a very strong positive correlation between the models at both frequencies, with slightly better alignment at the lower frequency.

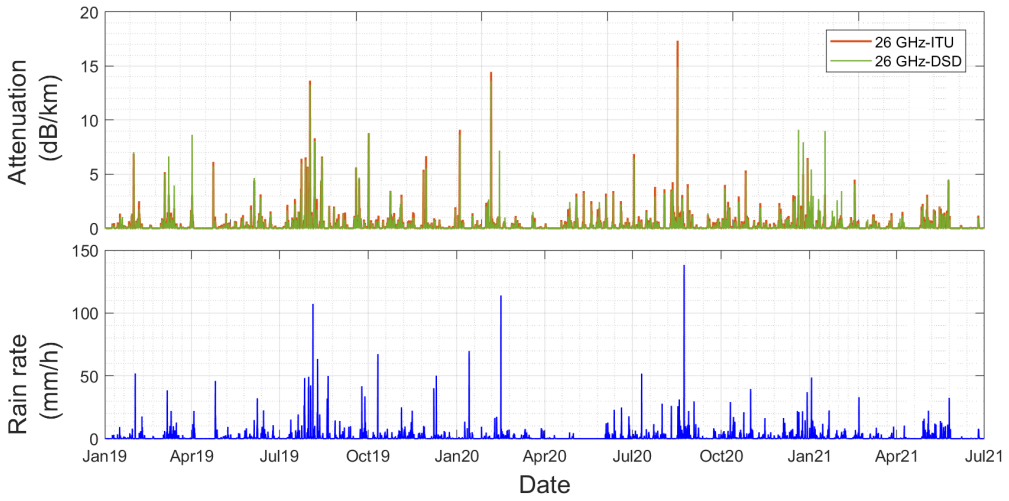

Figure 4.10: Calculated specific attenuation for 25.84 GHz.

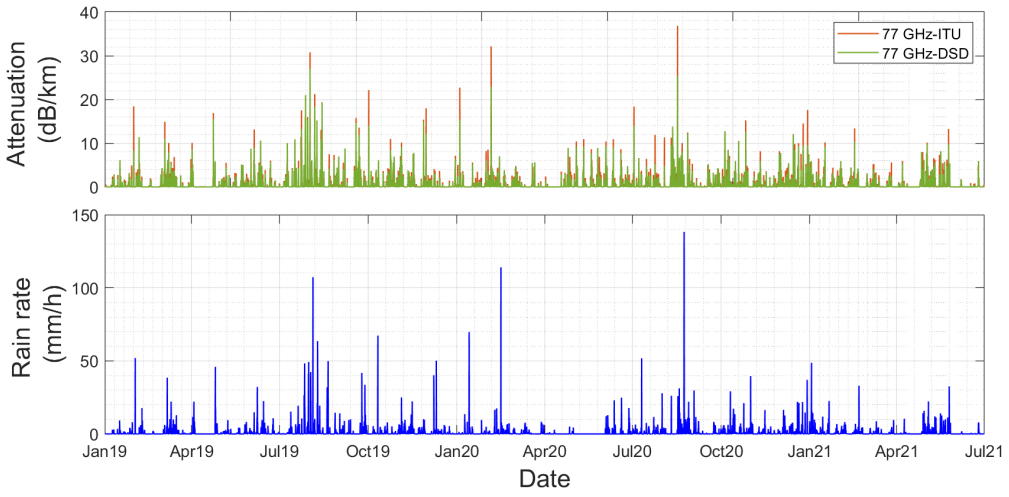

Figure 4.11: Calculated specific attenuation for 77.54 GHz.

Specifically, at 77.54 GHz, the difference in attenuation reaches 10 dB/km for rain intensities up to 110 mm/h, while it is 2 dB/km for rainfall below 20 mm/h. For example, at 77.54 GHz and medium rainfall rates below 20 mm/h, the ITU prediction is 33% higher than the DSD model, and this difference increases to over 50% for extremely heavy rainfall exceeding 50 mm/h. The disparities between the DSD and ITU models prompt further investigation, which is performed on various parameters, including the extinction cross-section σ_{ext}, diameter D of raindrops, number of recorded drops N, the complex refractive index of water, and the contribution of raindrop diameter and velocity towards the specific attenuation. This detailed analysis aims to better understand the factors influencing rain attenuation and to address the discrepancy between the DSD and ITU models. Further investigations will shed light on the underlying mechanisms and help improve the accuracy of rain attenuation predictions.

In this research work, the interaction between raindrops was assumed to be negligible. However, in [116], it was found that when drops become larger than 5 mm, they undergo collision and interaction with other drops, leading to unsteady behaviour and potential collapse due to their forces. For Mie theory calculations, it is assumed that raindrops are spherical, which is not always the case in real rainfall events. In reality, smaller drops (less than 2 mm) tend to be close to spherical, while larger drops take an oblate form flattened at the bottom due to underlying forces as presented in Figure. 4.12 [2].

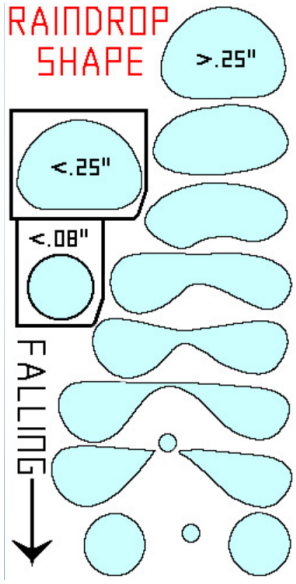

Figure 4.12: Raindrop shape through rainfall event (Image from [2]).

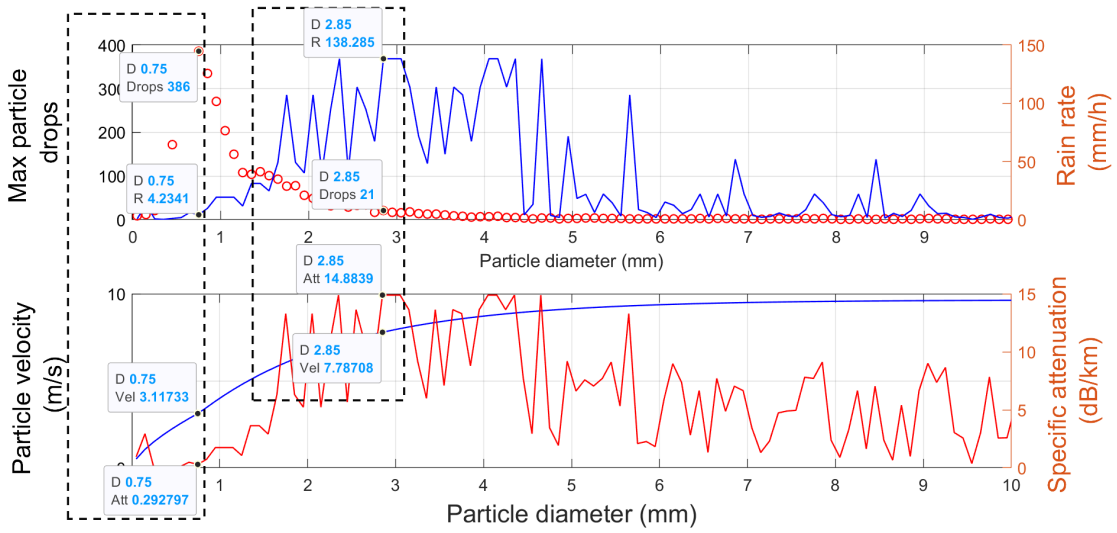

Figure 4.13: Particle velocity and attenuation variation versus its diameter and the number of maximum drops for each particle type.

There is a notable variety and irregularity in the relationship between raindrop velocity, the number of drops, rainfall intensity, and attenuation. Figure 4.13 provides a detailed example of this relationship. The attenuation is computed based on the recorded weather data, allowing us to determine the quantity and type of drops observed within a specific time frame. This enables us to designate the prevalent drops during each measurement interval for every particle diameter bin. For instance, a raindrop with a size of 2.85 mm and a relatively low number of drops (21) results in the highest attenuation value of 14.88 dB/km. Even with a lower proportion of drops, the attenuation reaches its maximum, but only during very heavy rainfall, reaching up to 130 mm/h, where the raindrop velocity approaches 7.78 m/s. On the other hand, for smaller raindrops, e.g., those with a size of 0.75 mm, a rain rate of 4.23 mm/h, and a higher number of drops (386 drops), but with a fall velocity of 3.11 m/s, the attenuation is much lower at 0.29 dB/km. From this analysis, it is evident that rainfall intensity is the primary contributor to specific maximum attenuation variation. To elaborate, let's examine the example of a raindrop with a size of 2.85 mm. With a relatively low number of just 21 drops, this results in the highest attenuation value of 14.88 dB/km. This maximum attenuation occurs despite the low drop count, but it corresponds to very heavy rainfall of up to 130 mm/h, where the raindrop velocity is quite high at 7.78 m/s. In contrast, smaller 0.75 mm raindrops with a higher drop count of 386 at a lower rain rate of just 4.23 mm/h have a lower fall velocity of 3.11 m/s. Consequently, the attenuation is much lower at 0.29 dB/km, even with more drops. When the drops are smaller and the rainfall is of medium intensity, a larger number of droplets has little to no impact on the specific attenuation. In contrast, during heavy rainfall with larger raindrops, the attenuation is strongly affected by both the number of drops and their fall velocities. The intricate interplay between these factors results in the observed irregularities and complexities in the specific attenuation patterns. The fall velocities is given by equation 4.5.34 and 4.5.35:

$$v(D_i) = 3.78 D_i^{0.67}, D_i < 0.8 \tag{4.5.34}$$

$$v(D_i) = 9.65 - 10.3 e^{-0.6 D_i}, D_i > 0.8 \tag{4.5.35}$$

The DSD measurement is susceptible to various environmental factors, with wind being one of them. Studies such as [117–120] have highlighted the impact of wind on disdrometer measurements. The horizontal component of the wind is generally not a major concern because it does not directly affect the fall velocity of raindrops. However, vertical turbulence becomes more significant with increasing wind speed. Turbulence in the updrafts and downdrafts can influence the real fall speed of particles, making the assumption that raindrops are falling at their terminal velocity incorrect. As a result of these velocity discrepancies caused by turbulence, the observed momentum and, consequently, the assigned size bin of the drops can be both overestimated and underestimated to some extent. This may introduce inaccuracies in the DSD measurement. The impact of wind on the disdrometer is more pronounced for tiny drops with low terminal velocities. These inaccuracies in the DSD measurements due to wind-induced turbulence can lead to challenges in accurately characterizing the raindrop size distribution, especially for small drops. Researchers need to consider and account for these environmental factors when interpreting disdrometer data and analyzing the DSD to ensure more reliable results.

4.5.3 Prediction of Short-Range Fixed Link Attenuation from Seasonal Data

In this section, the predicted attenuation in dB is examined for short-distance fixed links at 36 m and 200 m, serving as a reference for comparison with the measured data in the next chapter.

Figure 4.14 illustrates how the attenuation evolves in relation to the rain rate in mm/h. The attenuation values are determined at one-minute intervals, but they appear scattered randomly over time, necessitating fitting for each level of rain intensity. For rainfalls below 40 mm/h, both frequencies at the 36 m link show a correlation between the prediction models, with these values being doubled for the 200 m link. However, when the rainfall exceeds the threshold of 5 mm/h, the rain attenuation increases further with the rise in rain intensity. It is worth noting that we implemented the computed distance factor within the ITU-R model, without restricting it to the conventional r=2.5.

The data reveal a significant variation in rain attenuation with the rain rate, as predicted

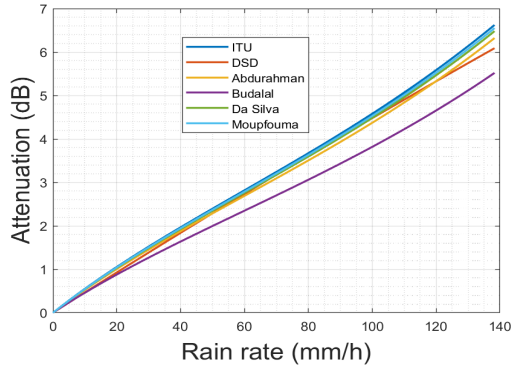

(a) *25.84 GHz vertical d=36 m.*

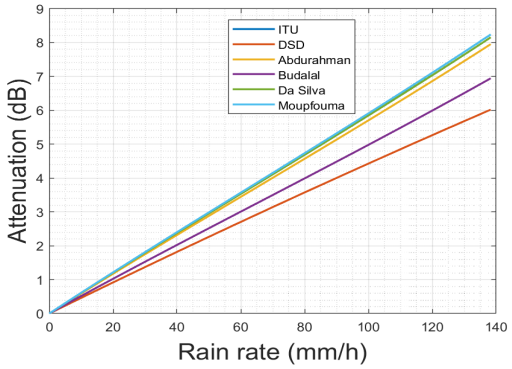

(b) *25.84 GHz horizontal d=36m.*

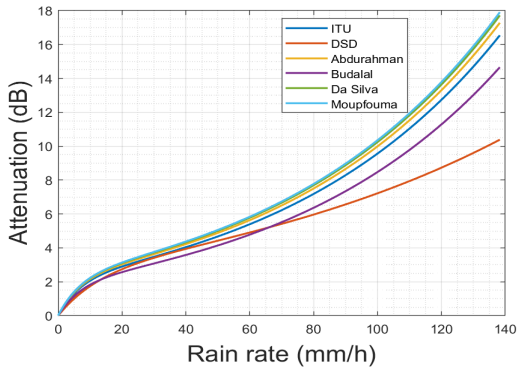

(c) *77.54 GHz vertical d=36m .*

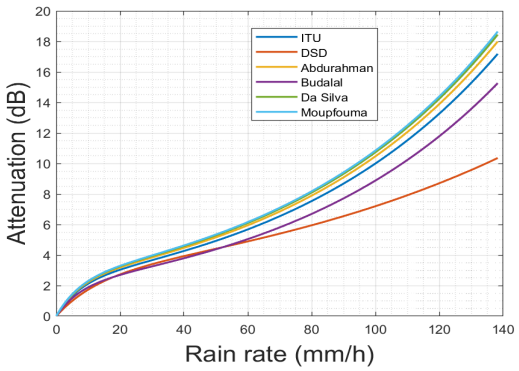

(d) *77.54 GHz, horizontal d=36m.*

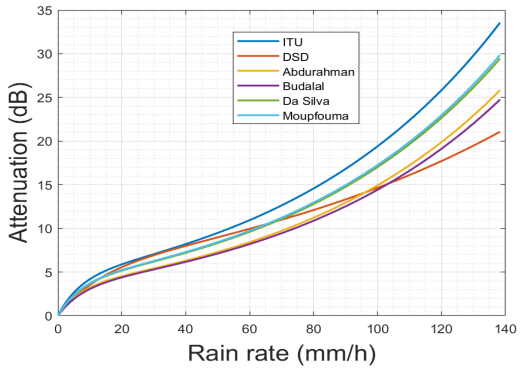

(e) *77.125 GHz, vertical d=200m.*

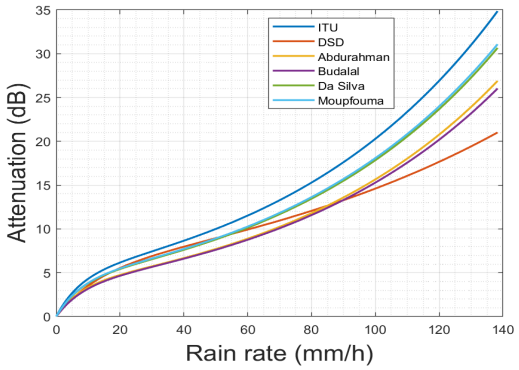

(f) *77.125 GHz, horizontal d=200m.*

Figure 4.14: Predicted rain attenuation versus rain intensity.

by all the models employed. For a percentage of time exceeding 0.01%, the attenuation reaches 1.50 ± 0.15 dB at 25.84 GHz based on the rain gauge measurements, which have a typical accuracy of ±10% for total rainfall as per the rain gauge specifications. During light rainfall, the link demonstrates a maximum attenuation of 0.06 ± 0.01 dB and 0.38 ± 0.05 dB at K and E bands, respectively, as measured by the weather station data which has

a ±0.50 dB calibration uncertainty according to the manufacturer. For heavy rainfall of up to 20 ± 2.00 mm/h based on the tipping bucket rain gauge measurements, which have ±10% volumetric accuracy, the attenuation reaches 0.83 ± 0.10 dB and 2.68 ± 0.20 dB at K and E bands, respectively. The raindrop size distribution was measured with the PWS100 disdrometer having ±5% diameter measurement accuracy above 0.3 mm diameter based on its specifications. However, the 200 m link shows somewhat higher attenuation values. For a percentage of time that exceeds 0.01%, the attenuation is in the range of 3.02 - 6.29 dB.

4.6 Summary

This chapter conducted a comprehensive analysis of three years of disdrometer weather data. The summary findings are highlighted in Table. 4.4. Focusing statistically on 95% of the available data, the examination revealed that the overall measurement period predominantly experienced rainfall intensity lower than 28 ± 2.8 mm/h according to the disdrometer measurements, which have a rainfall intensity accuracy of ±10% as per the specifications. Analysis of the rainfall events showed the number of occurrences was evenly distributed across a wide range of event duration. The accumulated rainfall volumes had an uncertainty of ±0.50 mm based on the tipping bucket rain gauge precision limits. The DSD measurements, with ±5% drop sizing accuracy, indicated the dominant raindrop diameter fell within 0.13-2 ± 0.1 mm for most events. Further replicated measurements across diverse locations could better quantify the rainfall characteristics and refine the uncertainty ranges.

Moving on to DSD modelling, the exponential model showed alignment with the measured DSD, indicating its suitability in characterizing the drop size distribution accurately within ±5% based on disdrometer sizing uncertainty. The diversity in disdrometer data proved advantageous in terms of seasonal distribution, particularly during the winter season when rain intensity tends to increase up to ±10% from the annual mean according to the disdrometer intensity measurements with ±10% accuracy. Moreover, the dispersion of raindrops remained largely unaffected by occasional occurrences of very heavy rain rates exceeding 25 ± 2.5 mm/h, mainly observed during the summer season with ±5%

uncertainty in event detection based on the disdrometer specifications.

Table 4.4: Summary of the rain attenuation findings using disdrometer data and ITU & DSD models

Summary	Key Findings
Rain attenuation	Rain attenuation increases with rainfall intensity. Maximum attenuation observed at 25.84 GHz is 1.50 ± 0.15 dB during light rainfall and 0.83 ± 0.10 dB during heavy rainfall.
Raindrop Size Distribution (DSD)	Raindrop diameters primarily fall within 0.13-2 ± 0.1 mm.
Analysis of rainfall events	Predominantly, rainfall intensity is lower than 28 ± 2.8 mm/h.
DSD modelling	Exponential model shows alignment with measured DSD within ±5%.
Estimation of rain attenuation	Attenuation ranges from 1 ± 0.1 dB/km to 10 ± 1 dB/km. Variations between the ITU and DSD models for heavy rain events surpassing 20 ± 2 mm/h.
Impact of raindrop diameter	Raindrops with diameters of 1-2 ± 0.1 mm contribute to maximum attenuation values, especially at higher frequencies.
Attenuation variation with rain rate	Steady increase in attenuation observed with rising rain rate, particularly after surpassing the 5 ± 0.5 mm/h threshold.

Notes
Weather data measurements from the PWS100 station were utilized, with a typical accuracy of ±10% for total rainfall and ±5% sizing accuracy.

For the estimation of rain attenuation, we employed long-term disdrometer data and various rain attenuation models. The calculations highlighted that the attenuation reached its lowest value of 1 ± 0.1 dB/km when time percentages exceeded 0.1%, and its highest value of 10 ± 1 dB/km when time percentages dropped below 0.001%. When comparing the ITU and DSD models for attenuation prediction, we observed consistent alignment at 25.84 GHz. However, at 77.54 GHz, especially during very heavy rainfall, the specific attenuation exhibited larger discrepancies between the DSD and ITU-R models. Notably, the analysis revealed non-uniformity between the models for heavier rain events exceeding 20 ± 2 mm/h according to tipping bucket rain gauge accuracy. Further measurements are needed to quantify the sources of variation between models.

Additionally, the study of raindrop diameter showed that raindrops within the range of 1-2

± 0.1 mm contributed to the maximum attenuation values at 77.54 GHz for most rainfall events. As for rainfall intensities higher than 20 ± 2 mm/h based on tipping bucket rain gauge accuracy, the specific attenuation reached noteworthy figures of 15 ± 1 dB/km and 28 ± 3 dB/km for 25.84 GHz and 77.54 GHz, respectively, within the diameter range below 2 ± 0.1 mm measured by the disdrometer with ±5% sizing accuracy. When examining the attenuation values for the 36 m and 200 m links obtained from datalogger readings with ±10% measurement error, we observed a steady increase in attenuation with the rise in rain rate, particularly after the threshold of 5 ± 0.5 mm/h was surpassed according to the tipping bucket rain gauge precision limits. Further measurements are required to improve the precision of the determined attenuation values.

In summary, this chapter has revealed important insights into how rain attenuation relates to rainfall characteristics and specific frequency bands using prediction models.

Chapter 5

Fixed Link Measurement for Direct and Side Link

5.1 Introduction

Rainfall attenuation significantly influences the design of short-range fixed links, especially those under 300 m, for FWA 5G applications. This impact is particularly notable at frequencies exceeding 10 GHz, such as in fixed wireless access deployments. These deployments aim to offer a cost-effective means of delivering high-speed internet, comparable to fibre, through 5G mmWave. This technology extends its reach from urban to rural locations, catering to homes and businesses globally. System planning and deployment working in higher frequency bands present a significant challenge in resolving the balance between bandwidth availability and rain attenuation challenges.

This chapter incorporates radio measurement data to assess real rain attenuation for direct and side links using the fixed link experimental setup and weather station described in Chapter Three, which will be evaluated using models for the chosen frequency bands and other frequencies using a frequency scaling mechanism. The chapter assesses the attenuation for 25.84 GHz and 77.54 GHz over the measurement period of November-December 2019, January-March 2020, September-December 2020, and January-June 2021. The data does not cover the entire period for each month since only rainy hours and hours before and after rainfall are utilized for attenuation reference. The analysis includes the effec-

tiveness of the path distance factor as well as the effect of antenna wetness and raindrop diameter.

5.2 Direct link Measurement and Analysis

5.2.1 Received Signal

To gain a better understanding of the various processes that lead to mmWave short-range link attenuation, the analysis is based on the raw received signal in dBm against meteorological data obtained through long-term measurements for the first 36 m direct link. The received signal data for the periods from November 2019 to March 2020 (rain events only) and from September 2020 to June 2021 (including snow events) are outlined in Figure. 5.1 and 5.2, respectively. It should be noted that measurements during this timeframe may include intermittent periods due to setup upgrades, department closures during lockdowns, or clear sky days.

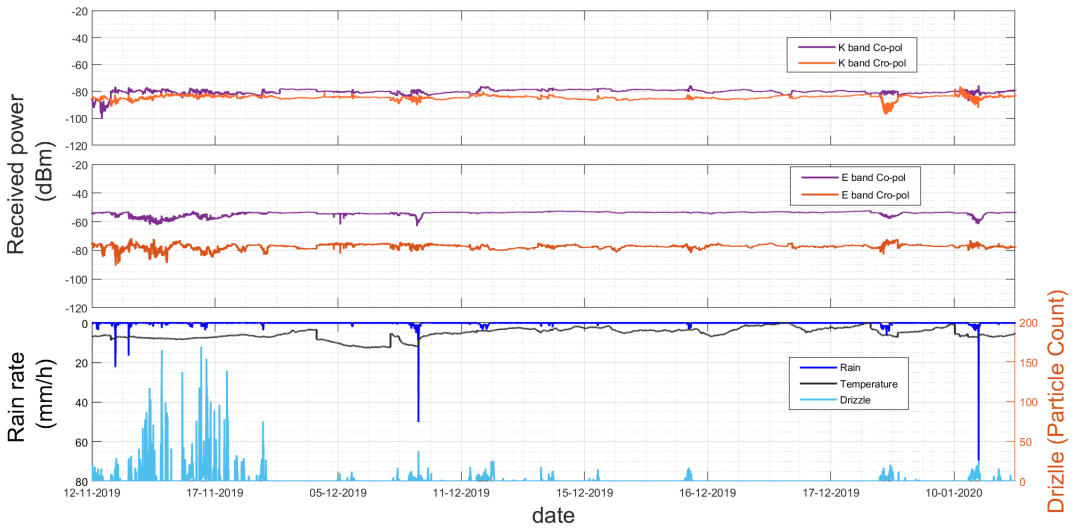

Figure 5.1: 36 m direct link received signal for K and E bands at co-polarization and cross-polarization between November 2019 and March 2020.

The observations indicate that the signal strength follows the trend of rain events, although not necessarily in a straightforward manner. For example, with a moderate rainfall rate of 10 mm/h, the signal power experiences a reduction compared to instances of very heavy rainfall. This is particularly shown in the case of cross-polarization, as illustrated

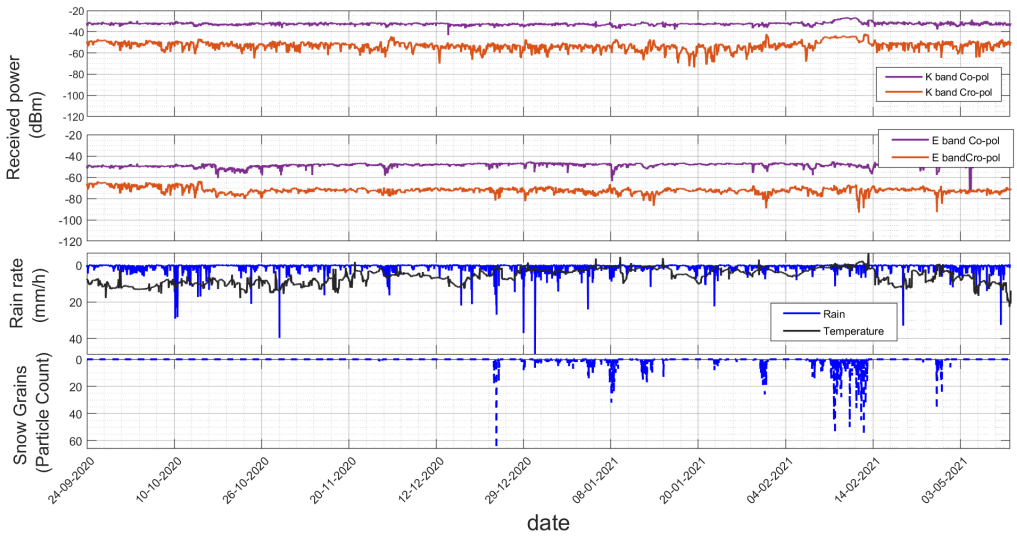

Figure 5.2: 36 m direct link received signal for K and E bands at co-polarization and cross-polarization between September 2020 and June 2021.

in the example of 07-11-2019 in Figure 5.2. Variations in received power between the two periods are also evident, which can be attributed to system upgrades and changes in components.

The analysis involves examining several sample events from the datasets to gain clarity into the separate phenomena contributing to the mmWave link attenuation signal. The aim is to understand the impact of individual factors that cause attenuation. The investigation begins with the performance of simple attenuation mechanisms and then explores dense and mixed precipitation scenarios. Additionally, the study looks at how temperature and wet antennas, such as those generated by drizzle accumulation, affect the signal, as well as the effects of raindrop contribution range and diameter types. Furthermore, the analysis explores several currently unexplained aspects and provides examples of various phenomena occurring together. By delving into these diverse scenarios, the goal is to unravel the complexities surrounding mmWave link attenuation and enhance the understanding of this critical aspect in wireless communication.

5.2.2 Correlation Between Rainfall Events and the Received Signal

The time series of rainfall rate and rain attenuation are depicted in Figure. 5.3, showcasing five diverse rainfall events with varying durations that lead to different aspects of

signal attenuation. One notable observation is that even with heavier rainfall, the signal strength does not experience a sudden drop, whereas continuous rainfall with moderate rain intensity leads to more significant degradation.

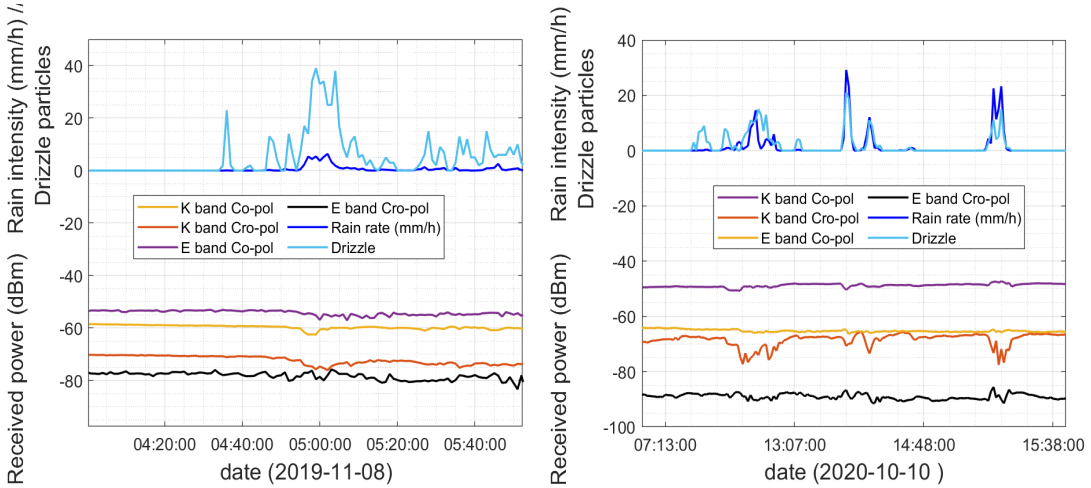

(a) *02 November 2019.* **(b)** *10 October 2020.*

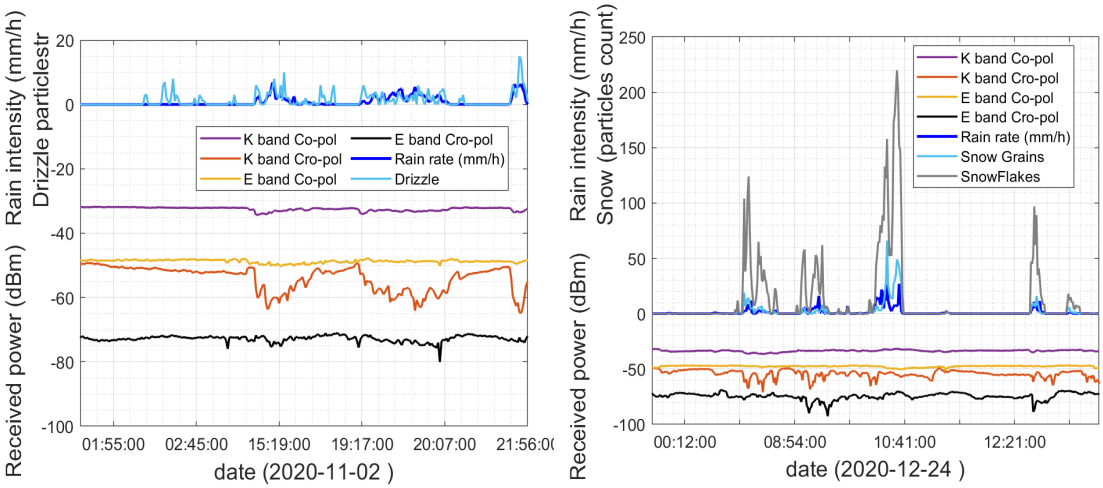

(c) *02 November 2020.* **(d)** *24 December 2020.*

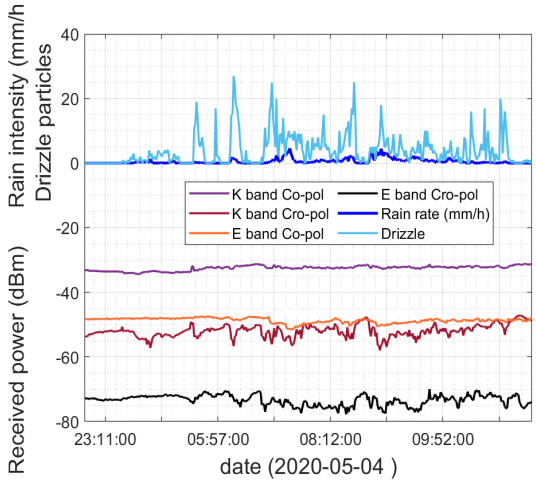

(e) *04 May 2021.*

Figure 5.3: The received signal mapped against different rainfall events examples.

For instance, on 10-Oct-2020 around 13:17, a heavy rainfall event lasting approximately 4 minutes with an intensity of 27.5 to 30.5 ± 1.5 mm/h was observed, resulting in a temporary decrease in the signal that recovered once the rainfall concluded. In contrast, continuous rainfall exceeding 120 minutes at an intensity below 4.75 to 5.25 ± 0.25 mm/h leads to substantial signal degradation, recovering after about 20 minutes. The 25.84 GHz cross-polarized signal appears more sensitive to such long-duration, low-intensity rain between 28.5 and 42 minutes. However, the 77.54 GHz cross-polarized signal promptly degrades and swiftly recovers to its original state when rain intensity declines to 1.9 to 2.1 ± 0.1 mm/h. On 02-Nov-2020 example, two continuous rainfall events occurred around 03:25 seconds and 20:07, separated by 30 rain-free minutes, while drizzle continued throughout the day. Here, the 25.84 GHz cross-polarized signal exhibited noticeable losses, declining by 1.9 to 2.1 ± 0.1 dB from an initial -50.89 dBm as intensity fell below the 5.4 ± 0.3 mm/h threshold, reaching -62.6 to -65.4 dBm. Gradual recovery occurred for rain rates of 2.66 to 2.94 ± 0.1 mm/h down to 0.49 to 0.55 ± 0.03 mm/h, but full recovery took around 4 minutes after rainfall ceased. A summary of the above observations is highlighted in Table. 5.1:

Table 5.1: Summary of key findings of the received signal against different rainfall events for 36 m direct link

Date	Event Summary	Observations
10-Oct-2020	Heavy rainfall for ∼4 min, intensity 27.5-30.5 mm/h	Temporary signal decrease, recovered after rain
02-Nov-2020	Continuous rainfall >120 min, intensity $\leq 4.75 - 5.25 mm/h$	Substantial signal degradation, 20 min recovery
02-Nov-2020	2 rainfall events ∼03:25 and ∼20:07, 30 min apart	25.84 GHz cross-pol signal losses, gradual recovery
24-Dec-2020	Mixed snow & rain event, peaked at 57-63 flakes, 5.7-6.3 mm/h	77.54 GHz cross-pol signal dropped by 3.8 to 4.2 ± 0.2 dB as precipitation peaked. The signal continued degrading despite the event ending at 14.25 to 15.75 ± 1 dB after the 4-minute event.

Comparatively, the 77.54 GHz cross-polarized signal behaved analogously for mixed snow and rain. For instance, on 24-Dec-2020 around 08:54, an event started at -75.19 dBm, dropping by 3.8 to 4.2 ± 0.2 dB as precipitation peaked at 57 to 63 ± 3 snowflakes

and 5.7 to 6.3 ± 0.3 mm/h rain. The signal continued degrading at this level, and even after the 4-minute event, it gradually declined an additional 14.25 to 15.75 ± 1 dB despite halted precipitation. This post-event attenuation may be linked to antenna icing or wetness before signal restoration when rainfall resumed 2 minutes later. Further mixed events produced comparable signal losses when snow ceased and 15.2 to 16.8 ± 1 mm/h rain caused additional 4.75 to 5.25 ± 0.25 dB attenuation, reversing the earlier post-snow signal decrease. In multivariate time series, such statistical variations could introduce nonlinear artefacts, warranting deeper investigation using DSD methods in this thesis research.

5.2.3 Rain Attenuation Measurement

5.2.3.1 Measured Data

Rain attenuation measurements are the next step in the data analysis process. Samples were taken from various periods throughout the year, with a focus on repeated events to calculate attenuation. We carefully selected the most frequently occurring events to measure the attenuation, specifically choosing dominant rainfall types and instances where signal losses were evident due to rainfall. Notably, long-duration rainfall was excluded as it tends to overestimate attenuation levels when compared to predicted values using models. The prediction models independently utilize rain intensity per minute and rain event time duration. For instance, a study in [121] highlights the performance evaluation of these models at GSM network locations. This research suggests that considering specific characteristics of rainfall, such as duration, is crucial for accurate attenuation predictions. Furthermore, the investigation into terrestrial rain attenuation models emphasizes the need for a comprehensive understanding of rain characteristics. The study explores existing models and underlines the importance of tailored models that consider factors like rain intensity per minute and event time duration, supporting the decision to exclude long-duration rainfall for better prediction accuracy [122]. The models are designed based on certain assumptions about the behaviour of rainfall, such as its intensity, duration, and spatial distribution. Long-duration rainfall events, however, might introduce complexities that challenge these assumptions. The extended duration could lead to variations in rainfall intensity, temporal patterns, and spatial distribution, aspects that may not

align with the simplified representations within the models. As a result, the theoretical foundation of the models may be strained when applied to prolonged rainfall scenarios, potentially leading to inaccuracies in predictions.

Table. 5.2 summarises the initial observations for different rainfall events. In scenarios of a maximum rain intensity of 40 ± 2 mm/h, the observed attenuation at 25.84 GHz cross-polarization is 2.40 ± 0.12 dB and 1.90 ± 0.10 dB for co-polarization. During light rainfall events with an intensity of 2 ± 0.1 mm/h, attenuation values are 0.26 ± 0.03 dB for cross-polarization and 1.44 ± 0.07 dB for co-polarization, respectively. Considering the drift in power level measurements, fluctuations in received power over time could also affect attenuation values. At 77.54 GHz, the maximum attenuation reaches 2.65 ± 0.13 dB for co-polarization when the rainfall rate is approximately 29 ± 1.5 mm/h, and it rises to 4.72 ± 0.47 dB for cross-polarization when the rainfall rate is below 5 ± 0.25 mm/h. These findings highlight the importance of understanding and mitigating sources of uncertainty to ensure the reliability of attenuation measurements.

Table 5.2: Preliminary observations: Summary of attenuation measurements for different rainfall events at 36m direct link

Rain Intensity (mm/h)	Frequency (GHz)	Attenuation (dB)
40 ± 2	25.84	Cross-Polarization: 2.40 ± 0.12 Co-Polarization: 1.90 ± 0.10
2 ± 0.1	25.84	Cross-Polarization: 0.26 ± 0.03 Co-Polarization: 1.44 ± 0.07
29 ± 1.5	77.54	Co-Polarization: 2.65 ± 0.13
Below 5 ± 0.25	77.54	Cross-Polarization: 4.72 ± 0.47

Interestingly, these findings indicate that attenuation does not always strictly follow the trend of rain rate, suggesting the presence of other factors influencing reported attenuation, aside from rain intensity. As a result, further analysis is needed to explore these factors and compare the results against predicted values. Before proceeding with this investigation, we first relate the measurements to the ITU-R model. For short links, it was recommended to apply a maximum value of 2.5 for the distance factor. This step will help establish a comprehensive understanding of the relationship between the measured data and the ITU-R model predictions, providing valuable insights for the subsequent analysis.

5.2.3.2 Distance Factor Examination

Rain attenuation predictability is crucial for short-range mmWave terrestrial links in the context of signal strength prediction and link budget considerations for 5G systems and beyond. The ITU-R P.530-17 model is widely used for frequencies below 100 GHz and path lengths up to 60 km, primarily in temperate regions. The distance factor, denoted as r, is experimentally determined based on long-range experimental data. According to the model, r should not exceed 2.5, and if it does, it is set to 2.5 [123–125]. However, studies analyzing observed attenuation on terrestrial links with lengths below 1 km and frequencies of 26 and 38 GHz found inconsistencies with the distance factor restriction [126]. This restriction led to underestimating measured attenuation compared to the predictions made using the ITU-R P.530-17 model. As a result, an increment factor was introduced to address this issue and was validated with measurements from different frequencies and short-path lengths, both below and above 40 GHz [127–130].

In light of these findings, a detailed analysis is being conducted to evaluate the suitability of the distance factor restriction of 2.5 for our 36 m short-range link and the 200-meter link. Figures 5.4 to 5.7 present a comprehensive comparison of measured attenuation against the predicted values using the ITU model for both cases. The first case involves calculating attenuation without applying the distance factor constraint, while the second case applies a maximum limitation of 2.5. The results indicate that the overestimation between measured and predicted attenuation increases with higher rain rates due to the assignment of the distance factor threshold. However, for the 36 m short-range link, the distance factor values decrease as rainfall increases. For instance, for a given $R_{0.01}$ of 10 mm/h, the distance factor starts with a maximum value of 2.87 and 2.54 for K and 77.54 GHz, respectively, for the 36 m path link. The values then decrease until the link distance reaches 300 m, becoming stable in the range of 1.5 - 2.81. For the path length of 36 m, the maximum value of the distance factor is found to be incompatible.

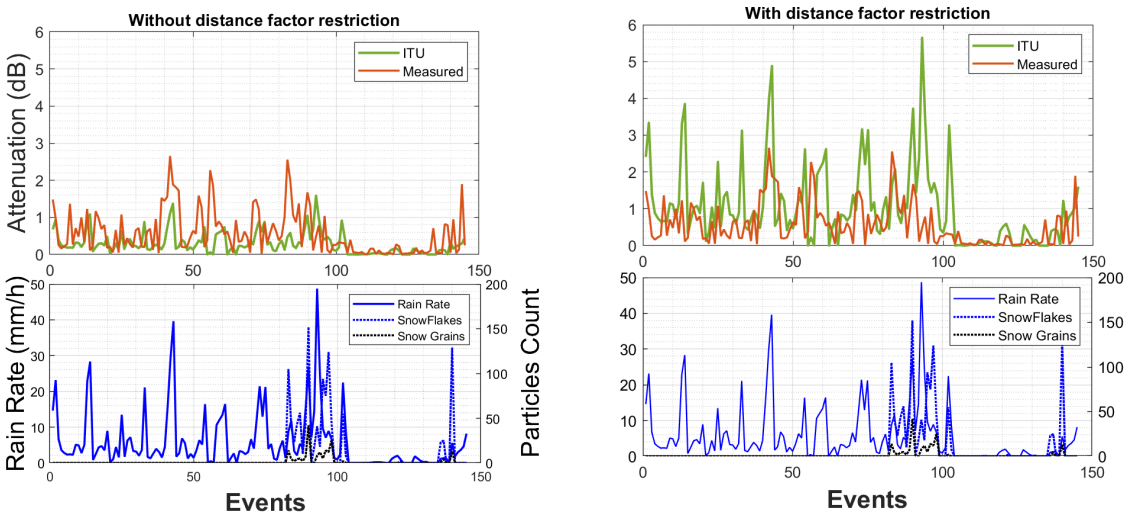

Figure 5.4: The measured attenuation vs the predicted attenuation with and without using the maximum distance factor restriction of 2.5 for 77.54 GHz co-polarization.

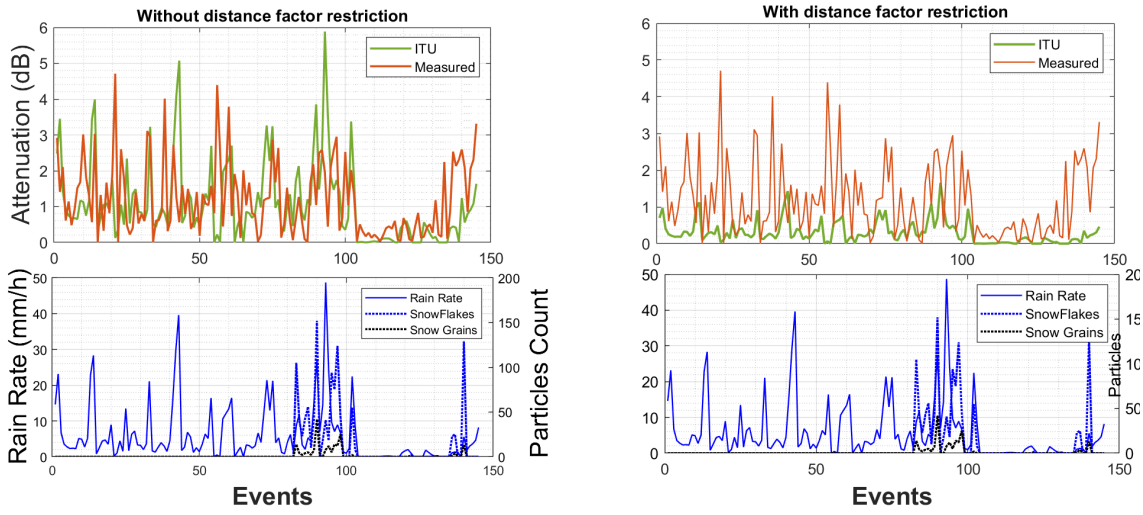

Figure 5.5: The measured attenuation vs the predicted attenuation with and without using the maximum distance factor restriction of 2.5 for 77.54 GHz cross-polarization.

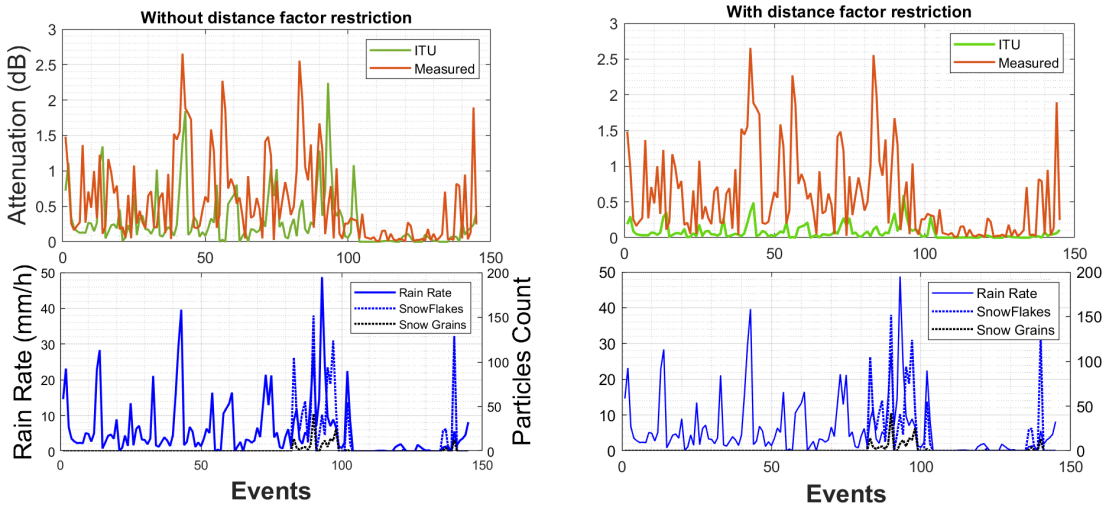

Figure 5.6: The measured attenuation vs the predicted attenuation with and without using the maximum distance factor restriction of 2.5 for 25.84 GHz co-polarization.

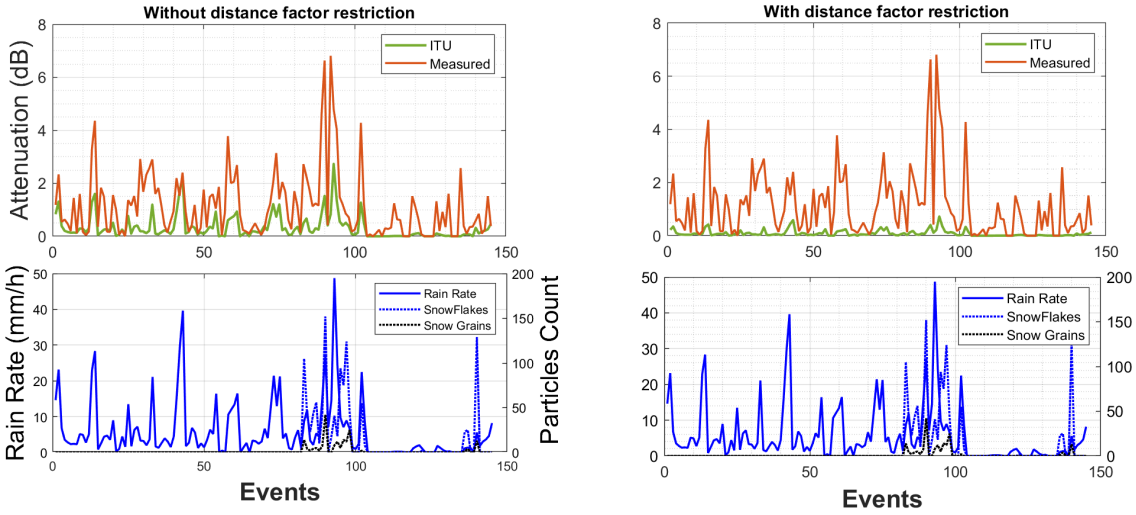

Figure 5.7: The measured attenuation vs the predicted attenuation with and without using the maximum distance factor restriction of 2.5 for 25.84 GHz cross-polarization.

In summary, the study highlights the significance of rain attenuation predictability for mmWave terrestrial links and raises questions about the adequacy of the distance factor restriction in the ITU-R model, especially for short-range links. The analysis aims to provide valuable insights for improving attenuation predictions and optimizing the performance of mmWave communication systems. The forthcoming analysis will incorporate the aforementioned findings, and for subsequent evaluations, we will utilize the computed distance factor value from the measurements, which might exceed 2.5. By removing the

maximum value limitation, the measured data will be compared against the predicted values for a more comprehensive analysis of rain attenuation. This approach will allow us to explore additional factors that may influence attenuation, such as droplet diameter, antenna wetness, humidity, and temperature, thereby gaining further insights into the accuracy of the prediction models. Through this process, we aim to enhance our understanding of the various factors impacting rain attenuation and improve the reliability of the attenuation predictions.

5.2.3.3 Measured and Predicted Attenuation

Figure. 5.8 displays the cumulative distribution functions of the measured attenuation. At 25.84 GHz cross-polarization, the attenuation values are higher than expected, with a difference of up to 1.33 dB observed at a cumulative probability of 0.8. However, at 77.54 GHz cross-polarization, the measured attenuation aligns well with the predicted values. This alignment is evident in a close correspondence between the measured and expected attenuation values (95%). For 25.84 GHz co-polarization, the measured attenuation matches the expected values for attenuation levels below 0.3 dB and above 1.4 dB, a deviation of 10% is observed within this range, indicating a moderate level of inconsistency. On the other hand, co-polarization at 77.54 GHz exhibits correlation for extremely low attenuation levels, below 0.05 dB. These observations indicate that there are discrepancies in the measured attenuation values, particularly for cross-polarization at 25.84 GHz. However, at other frequency and polarization combinations, the measured and expected attenuation demonstrate a better correlation. Further analysis and investigation are needed to understand the reasons for the discrepancies and improve the accuracy of the attenuation predictions.

Mixed precipitation is common during winter measurements, where a single rainfall event may consist of raindrops, snow grains, snowflakes, ice pellets, and drizzle, especially when the temperature falls below 5 degrees. For instance, the rainfall event on 24 December 2020, as illustrated previously in Figure 5.3, represents such a scenario. However, in the analysis of rain attenuation presented in Figure 5.8, this type of mixed precipitation event is not considered. The reason is that the DSD model cannot be applied during such mixed events, as they comprise a combination of raindrops, snow, ice, and

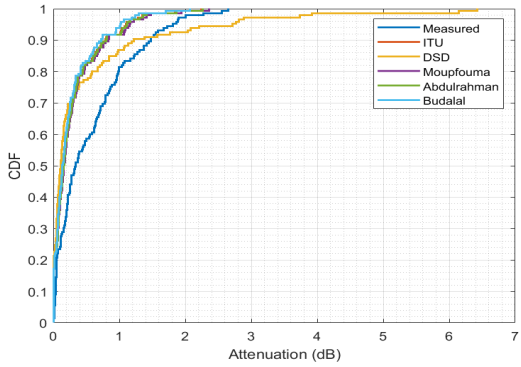

(a) *25.84 GHz co-pol d=36 m.*

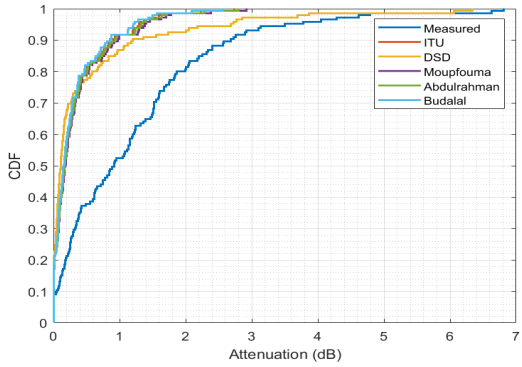

(b) *25.84 GHz cross-pol d=36m.*

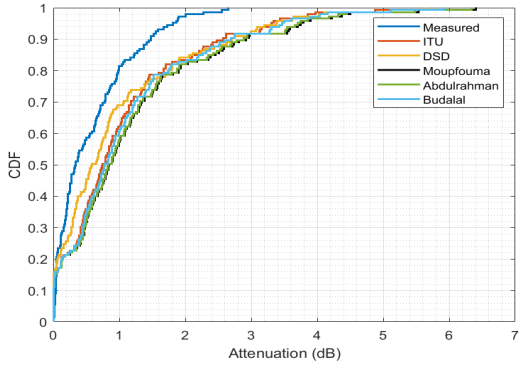

(c) *77.54 GHz co-pol d=36m .*

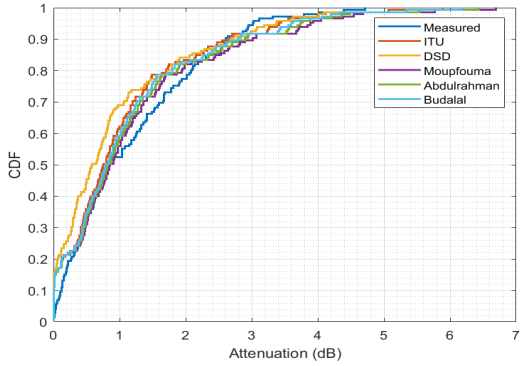

(d) *77.54 GHz, cross-pol d=36m.*

Figure 5.8: CDFs of measured and modeled rain attenuation for direct link.

hail. To ensure measurement accuracy and focus on investigating rain attenuation, we exclude these mixed events from the samples shown in Figure 5.8.

5.2.4 Exceedance Probability

Figure 5.9 presents the exceedance probability curves for the measurement period. These curves illustrate the probability, represented as a percentage of the time, that a certain rain rate and attenuation would be recorded or exceeded. At 25.84 GHz, the link shows a maximum attenuation value of 2.73 dB with a 0.68% exceedance probability, corresponding to a rainfall intensity of 48 mm/h. On the other hand, at 77.54 GHz, the maximum attenuation reaches 5.88 dB for the same exceedance probability and rainfall intensity of 48 mm/h. However, at a rain intensity of only 1 mm/h, the attenuation values are significantly lower, measuring 0.01 dB and 0.10 dB for 25.84 GHz and 77.54 GHz, respectively, with an exceedance probability of 82%.

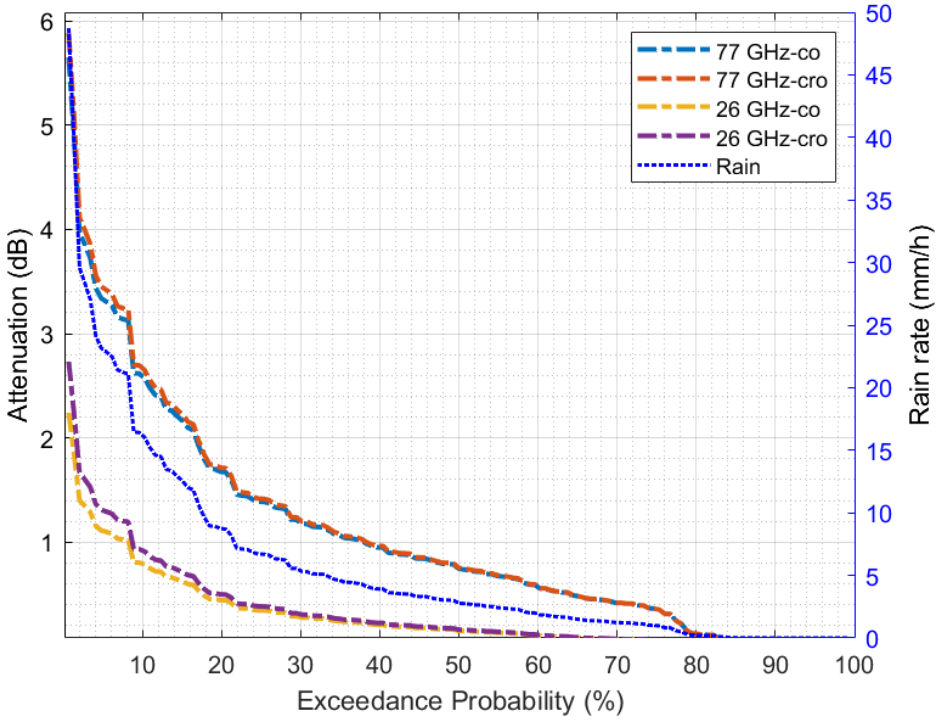

Figure 5.9: Rain attenuation exceedances measurements.

Table 5.3: Rain rate and attenuation measurement for the given exceedance in% during the measurement period

Exceedance	0.001%	0.002%	0.003%	0.005%	0.01%	0.02%	0.03%	0.05%	0.1%
Rain rate (mm/h)	69.76	50.15	42.47	33.01	29.57	22.55	17.3	13.34	8.79
Attenuation (77.54 GHz Co pol) dB	5.06	4.38	4.22	4.01	3.48	3	2.63	2.12	1.6
Attenuation (77.54 GHz Cross pol) dB	7.83	6.18	5.48	4.57	4.23	3.48	2.88	2.4	1.82
Attenuation (25.84 GHz Co pol) dB	3.11	2	1.85	1.83	1.32	1.02	0.74	0.59	0.37
Attenuation (25.84 GHz Cross pol) dB	4.05	2.92	2.48	1.93	1.73	1.33	1.02	0.79	0.52

The overall analysis reveals that probabilities of exceeding 70% occur when the rain rate is below 1.25 mm/h, coupled with measured attenuation less than 0.42 dB at 77.54 GHz and 0.07 dB at 25.84 GHz. Table 5.3 provides further details on rain attenuation and rain intensity exceedance at p% for the two frequency bands. For a link availability of 99.99% within the 36 m point-to-point short-range link, the rain fade margin ranges from 3 dB to 3.48 dB for 77.54 GHz and from 1.02 dB to 1.73 dB for 25.84 GHz, with a corresponding rain intensity of 29.57 mm/h. The application of these measurement results indicates that, for a link availability of 99.99% throughout the year, February records the highest rain attenuation values, while the lowest values are observed in September. By considering the exceedance probability and rain attenuation values, we can gain valuable insights into the performance of the link under various weather conditions, which is crucial for reliable

communication systems in different climates.

The comparison between the rain attenuation computed using the ITU and DSD models, which are developed using empirical models, rain intensity, and Mie theory, is assessed in relation to the rain attenuation obtained from actual measurement datasets. To evaluate the performance of the rain attenuation prediction models, we employ the Root Mean Square Error (RMSE), as expressed in equation (5.2.1), as described in [131]. The RMSE serves as a metric to measure the accuracy of the models in predicting rain attenuation. By calculating the RMSE, we can determine how well the predicted values align with the actual measured data, and thus, ascertain the effectiveness of the prediction models in estimating rain attenuation under various conditions. This analysis helps to validate the reliability of the models and gain confidence in their ability to provide accurate predictions for rain attenuation in different scenarios.

$$RMSE = \sqrt{\frac{\sum_{i=1}^{N} \left(Att_{meai} - Att_{prdi}\right)^2}{N-1}} \tag{5.2.1}$$

where Att_{meai} is the measured rain attenuation value, Att_{prdi} represents the predicted rain attenuation value from the models and N is the total number of rain attenuation measurements considered (samples). Table 5.4 presents the RMSE values for the given frequency bands, which serve as indicators of the prediction efficiency of the models concerning both rain rate and rain attenuation.

Table 5.4: Comparison of RMSE values for the ITU and DSD models

	Kco (25.84 GHz co-polarisation)	Kcro (25.84 GHz cross-polarisation)	Eco (77.54 GHz co-polarisation)	Ecro (77.54 GHz cross-polarisation)
RMSE_ITU (dB)	0.0144	0.0069	0.0925	0.1398
RMSE_DSD (dB)	0.0037	0.0084	0.1091	0.1267

The validation results with the DSD model for the 25.84 GHz band in co-polarization demonstrate the lowest RMSE value compared to the ITU-R model and the 77.54 GHz band. Conversely, for the cross-polarization at 77.54 GHz, the ITU model exhibits the

lowest RMSE value. These findings align with the results observed in the cumulative distribution functions (CDFs) analysis. The RMSE values provide insights into how well the prediction models perform in estimating rain attenuation and rain rate, offering a measure of the accuracy of their predictions. The lower the RMSE value, the closer the predicted values are to the actual measured data, indicating higher prediction accuracy. By evaluating the RMSE values for different frequency bands and polarizations, we can determine which prediction model performs best under specific conditions, further enhancing our understanding of the models' capabilities and limitations. The diverse distribution of attenuation values in the highlighted measured and predicted attenuation results (DSD and ITU) in both subsections 4.6 and 5.2.3.3 suggests variability. This variability can be attributed to several underlying factors. Firstly, the assumption made by Mie's theory, which considers raindrops to be perfectly spherical, may not always hold true in real-world rain events. In actuality, raindrops can take on different shapes and sizes, leading to deviations between the model's predictions and the actual measured attenuation values. Another influencing factor is the impact of severe weather conditions on the accuracy of the disdrometer data used in the DSD model. Adverse weather conditions can affect the performance of the disdrometer, resulting in potential inaccuracies in data collection, and consequently, the DSD model may overestimate the measured attenuation in certain instances. At lower rain rates, windy conditions can disrupt the propagation of mmWave signals, causing fluctuations in the measured attenuation levels. The presence of strong winds can interfere with the signal's path to the receiver, affecting the overall attenuation values. Moreover, the variations in humidity and temperature across different spatial and temporal locations also play a role in influencing the datasets' points. While the calculations might utilize average yearly temperature values and neglect humidity fluctuations, in reality, these environmental parameters can fluctuate significantly and influence the observed attenuation values.

Additionally, the non-uniform distribution of raindrop sizes and the occurrence of rain events across both space and time contribute to the diverse range of data points. The variations in raindrop distributions, particle sizes, rainfall speeds, and particle speed all impact the attenuation values recorded during different rainfall events. To address the complexity of these factors and their effects on measured attenuation, an extensive study

has been undertaken to investigate the influence of drop diameter and the impact of wet antennas on the attenuation data. The goal is to gain deeper insights into the underlying mechanisms and refine the prediction models, ultimately enhancing their accuracy and robustness under diverse environmental conditions. This comprehensive analysis aims to contribute to a more reliable understanding of rain attenuation in mmWave communication systems and improve their performance in real-world scenarios.

5.2.5 Raindrops Diameter vs Attenuation

The measured attenuation data exhibits a wide range of values that deviate from the predicted values, prompting a thorough analysis of the factors influencing attenuation. To better understand the contribution of raindrop diameter and the dominant number of drops to the overall attenuation, a comprehensive case study was conducted. Comparisons were made between the drop diameters of dominant events and all events. The detailed description of each raindrop's contribution to the measured attenuation (in dB) for various rainfall events is presented in Figure. 5.10. At 77.54 GHz, for light and moderate rainfall, raindrops in the range of 0.2-2 mm consistently contribute to the total attenuation. For instance, at a rainfall intensity of 1.03 ± 0.1 mm/h, the attenuation for 77.54 GHz co-pol reaches a maximum of 0.32 ± 0.12 dB, where raindrops with a diameter of 1.25 ± 0.0625 mm (±5% accuracy) make a significant contribution with around 130. In the case of heavy rainfall up to 16 ± 1.6 mm/h and 517 drops, the attenuation reaches 3.03 ± 0.12 dB, with the same drop diameter of 1.25 ± 0.0625 mm contributing significantly to the overall attenuation. However, during very heavy rainfall events with an intensity higher than 20 ± 2 mm/h for both 26 and 77.54 GHz, most raindrop types contribute consistently to the maximum measured attenuation of up to ±0.12 dB uncertainty.

At 25.84 GHz, for most rainfall events with light, heavy, and very heavy rainfall, all raindrops contribute uniformly, resulting in no substantial variance in attenuation concerning raindrop diameter of up to ±0.0625 mm. However, for moderate rainfall with an intensity of 3 ± 0.3 mm/h, raindrops with a diameter of 3.05 ± 0.1525 mm become the major contributors, leading to a maximum attenuation of 0.22 ± 0.12 dB. On the other hand, for heavy and very heavy rainfall events at the same frequency band with intensities up to 16

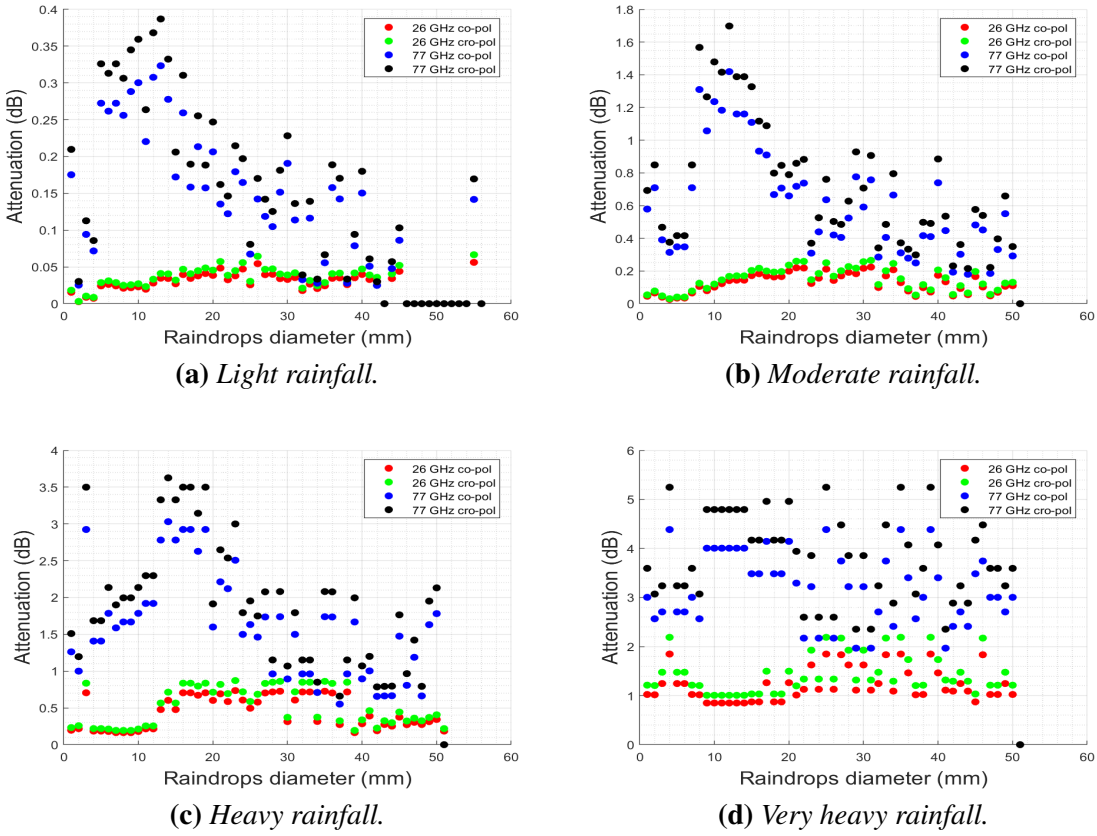

(a) *Light rainfall.* **(b)** *Moderate rainfall.*

(c) *Heavy rainfall.* **(d)** *Very heavy rainfall.*

Figure 5.10: Measured rain attenuation versus raindrops diameter for light, moderate, heavy, and very heavy rainfalls.

± 1.6 mm/h, raindrops in the range of 0.1-0.7 mm contribute significantly to the overall attenuation of up to ±0.12 dB uncertainty. Interestingly, for most rainfall events, the highest attenuation is observed when the raindrop size is less than 2 ± 0.1 mm, while larger droplets above 2 mm have a relatively insignificant contribution to attenuation within the measurement uncertainty of ±0.12 dB. This size distribution of raindrops falling within the range of less than 2 mm appears to align with reasonable limits for spherical raindrops, as outlined for both frequency bands. Based on these analyses, higher attenuation values up to ±0.12 dB uncertainty are influenced by a higher number of dominant diameter raindrops, especially for heavy rainfall events with raindrop diameters below 2 ± 0.1 mm.

These findings shed light on the intricate relationship between raindrop diameter, rain intensity, and measured attenuation, providing valuable insights for optimizing mmWave communication systems in varying weather conditions and improving the accuracy of attenuation prediction models.

5.2.6 Rainfall Velocity and Attenuation

Figure. 5.11 presents a comprehensive analysis of the measured attenuation in relation to the rainfall velocity (in m/s) for various rainfall events recorded during the measurement period, using data collected by the PWS100 disdrometer. Notably, for the 77.54 GHz co-pol, the trend of velocity does not consistently follow the attenuation pattern. For instance, at a velocity of 29.57 m/s, the maximum attenuation value reaches 2.6 dB, but when the velocity decreases to 4.5 m/s, the attenuation is within the range of 1.89 dB. Interestingly, it has been observed that at attenuation levels less than 1 dB, the velocity tends to exhibit an increasing pattern with attenuation. On the other hand, for most occurrences at 25.84 GHz for cross-pol, the attenuation rises with increasing rainfall velocity, more so than the co-pol. This factor could potentially contribute to the already observed highest rain attenuation levels at 25.84 GHz. The analysis of attenuation with respect to rainfall velocity provides valuable insights into the complex interplay between these factors, highlighting the need for further investigation to optimize mmWave communication systems for varying weather conditions and refine the prediction models for better accuracy.

5.2.7 Temperature Effect

The investigation of temperature and its impact on attenuation variation is a crucial element in our study. Our measurements were conducted across different periods of the year, covering four seasons, to monitor the measured attenuation at various temperatures and observe how the attenuation behaves concerning these variable parameters. Figure. 5.12 showcases the temperature variation throughout the measurement period (November 2019 and June 2021), with a maximum temperature of 22.71°C (T_{max}) and a minimum of -6.76°C (T_{min}), while the mean temperature stands at 6.48°C (T_{mean}). The temperature pattern shows relatively stable variations across the seasons, indicating normal temperature fluctuations.

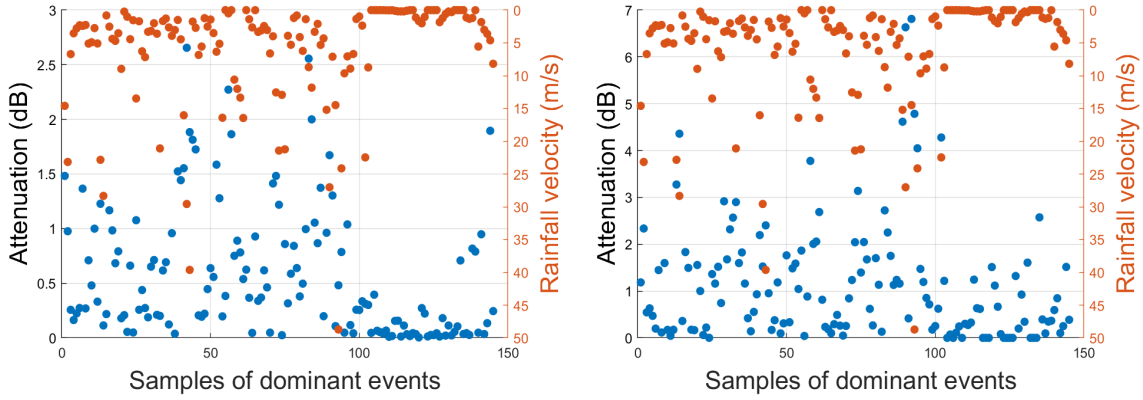

(a) *25.84 GHz co-pol.* **(b)** *25.84 GHz cro-pol.*

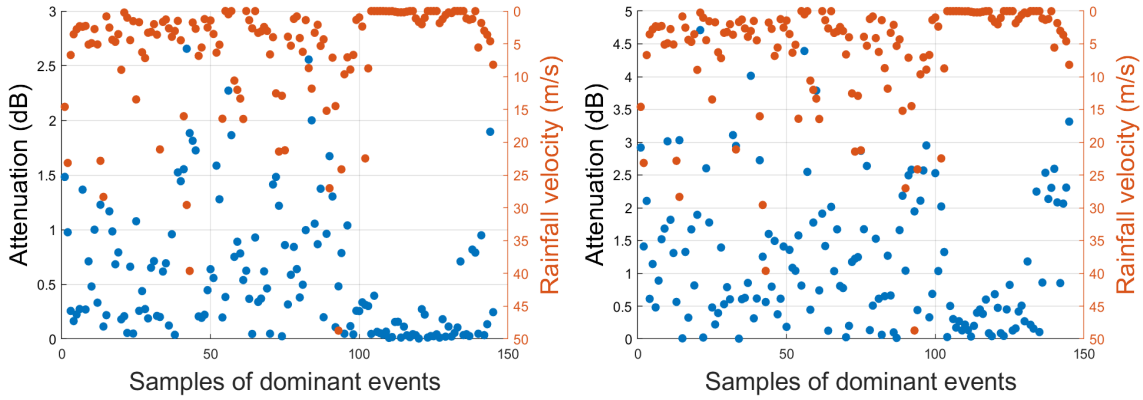

(c) *77.54 GHz co-pol.* **(d)** *77.54 GHz cro-pol.*

Figure 5.11: Measured rain attenuation versus measured rainfall velocity at 77.54 GHz and 25.84 GHz at 36 m direct link.

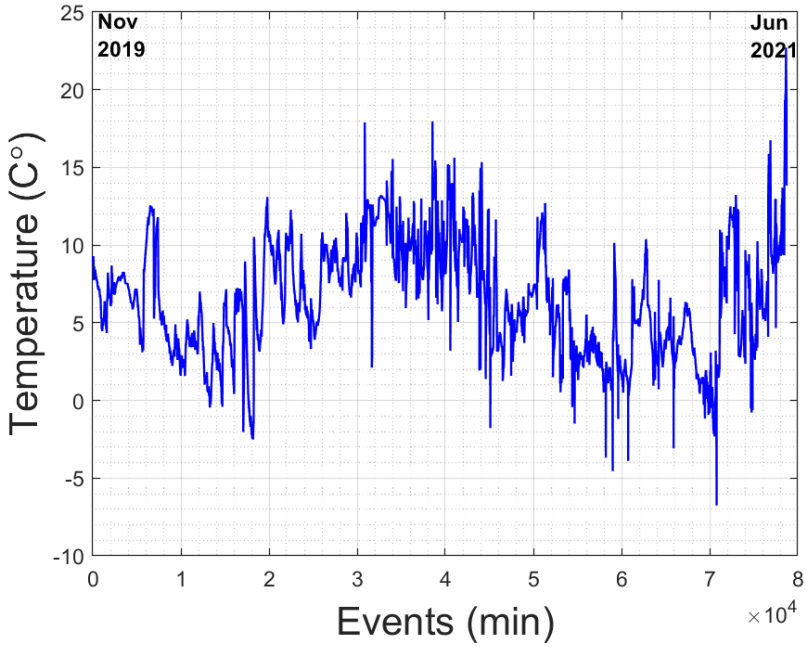

Figure 5.12: Measured temperature through the measurement period.

Table 5.5: Attenuation variation in terms of temperature within different rainfall types

Temperature	T_max				T_min				T_mean			
Rainfall	Light	Moderate	Heavy	Very Heavy	Light	Moderate	Heavy	Very Heavy	Light	Moderate	Heavy	Very Heavy
25.84 GHz co-pol (dB)	0.06	0.24	0.76	0.06	0.06	0.24	0.75	0.06	0.06	0.24	0.73	0.06
25.84 GHz cro-pol (dB)	0.07	0.28	0.90	0.07	0.07	0.29	0.89	0.07	0.07	0.28	0.87	0.07
77.54 GHz co-pol (dB)	0.36	1.41	2.99	0.36	0.34	1.41	3.08	0.34	0.35	1.42	3.03	0.35
77.54 GHz cro-pol (dB)	0.43	1.68	3.57	0.43	0.41	1.69	3.68	0.41	0.42	1.70	3.63	0.42

To gain a deeper understanding, Table. 5.5 provides a comprehensive overview of attenuation values in dB for each of the three temperature levels. Notably, for both polarizations at 25.84 GHz, the temperature appears to have a minimal noticeable impact on attenuation for most rainfall events, except during heavy rainfall, where the attenuation fluctuates by 0.01 dB with temperature changes. In the case of 77.54 GHz, slight variations ranging from 0.01 to 0.06 dB are observed for the four rainfall categories when the temperature changes.

However, the most noteworthy observation is when the temperature drops from 22°C to -6°C, resulting in a slight increase in attenuation, reaching a maximum step of 0.06 dB for moderate and severe rain events. This finding indicates that lower temperatures may contribute to slightly higher attenuation levels, especially for specific rainfall conditions. This can be attributed to several factors. Firstly, at temperatures below freezing, more supercooled raindrops can exist without freezing, leading to increased scattering losses. Secondly, partial freezing results in mixed-phase hydrometeors, including graupel and ice pellets. These, when combined with liquid drops, contribute to higher diffuse scattering attenuation, even in the presence of lower liquid water content. Thirdly, cold rainfall events often exhibit dynamic frontal boundaries and atmospheric conditions, sustaining increased precipitation density and depth over longer durations, thereby enabling greater accumulation of attenuation effects. Lastly, wet icy accretion can temporarily coat antenna equipment before melting, a phenomenon not observed in warmer conditions, momentarily elevating diffuse scattering and reflection losses. So, the intricate microwave interactions with cold rainfall around the freezing mark, allowing for mixed-phase conditions and dynamic storm dynamics, may elucidate this association between lower temperatures and signal attenuation levels.

By closely monitoring the measured attenuation at different temperature levels, we can gain insights into the influence of temperature on attenuation variation, allowing for better predictions and adjustments to mmWave communication systems in diverse weather

conditions. Further analysis will be carried out to establish a more comprehensive understanding of the relationship between temperature and attenuation in future research.

These analyses of the temperature's influence on total attenuation yielded interesting findings. The results indicate that temperature has a minimal impact, contributing only 0.06 dB to total attenuation in the E band when temperatures decrease from the maximum value to the minimum value within light/moderate rainfall events. Specifically, this effect accounts for approximately 1.5% at 77.54 GHz and 0.5% at 25.84 GHz. These results demonstrate that temperature variations have a negligible effect on attenuation levels during such rainfall conditions at the respective frequency bands.

5.2.8 Wet Antenna Effect

When the receiver antennas in our propagation experimental setup become wet, it leads to antenna wetness, as exemplified by the horn antennas installed with the fixed link experimental setup (see Figure. 5.13). Antenna wetness contributes to its own attenuation [132]. Studies have shown that wet antenna loss can be a significant factor in increasing measured attenuation compared to estimated models at 25.84 GHz, with wet antenna testing resulting in losses in the range of 0.4–3 dB [133]. Additionally, wet antenna effects have

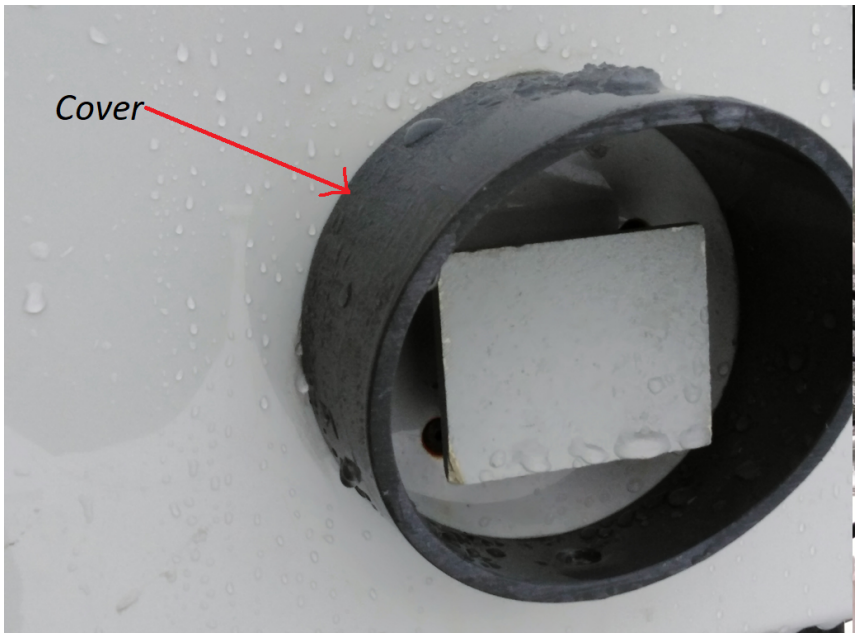

Figure 5.13: Antenna wetness of the experimental setup.

been found to considerably contribute to overall attenuation, especially when evaluating shorter links [134]. For instance, in a study involving eight short-range commercial links operating at frequencies of 37.3–39.2 GHz, the wet antenna effect reached a maximum of 2.8–5.3 dB for heavy rainfall events and 1.5–2.0 dB for light rainfall [134]. As future networks are expected to rely increasingly on E-band-based communication links, it is crucial to consider wet antenna effects as an actual attenuation source when calculating link budgets and designing fading margins [134; 135]. Therefore, it has been proposed that future updates of the ITU-R 838.3 recommendation should include a set of nominal values for different frequencies, polarizations, and locations to account for wet antenna effects [135].

To identify an appropriate model based on our current measurements, we extract the total attenuation (A_m) from the measurement data and apply the ITU model to estimate the rain attenuation (A_i). Subsequently, we obtain the attenuation induced by the wet antenna through the following equation 5.2.2:

$$A_w = A_m - A_i \tag{5.2.2}$$

The antenna attenuation A_a is a proportion of the overall measured attenuation A_m at any given moment. As detailed in [132], A_a size is less than A_m and must also be less than the maximum antenna attenuation measured in the simulated rain experiments. The model used to estimate the Wet Antenna Effect (WAE) is provided in equation 5.2.3 [132] as:

$$A_a = C\left(1 - e^{-dA_m}\right) \tag{5.2.3}$$

where C is the highest value of measured antenna attenuation in the simulated rain experiments, and d is a parameter to be calculated from those experiments' measurements and fitting results. Figure. 5.14 illustrates the relationship between the measured attenuation and the wet antenna attenuation, focusing on peak rain rates and measured attenuation. To ensure the antennas were completely wet, we selected continuous rainfall events lasting between 15 to 60 minutes, excluding short-lived rain occurrences lasting less than 15

minutes. The chosen time period was based on direct observations of the experimental setup located on the rooftop, where we had access to RF heads and could observe the antennas during precipitation events over an extended period. In this research project, wind direction hasn't been included as a factor. It is worth noting that wind direction can potentially influence antenna wetness, as it may affect the airflow around the antenna and subsequently impact moisture accumulation. Studies such as those in [136; 137] showed in their work that wind direction impacts the spatial non-uniformity of moisture on antennas where both studies underscore the importance of comprehensively assessing environmental variables in understanding antenna wetness effects on signal attenuation. However, for the scope of our study, we focused solely on other variables such as rainfall intensity, temperature, and humidity while the measurement setup doesn't enable wind measurement.

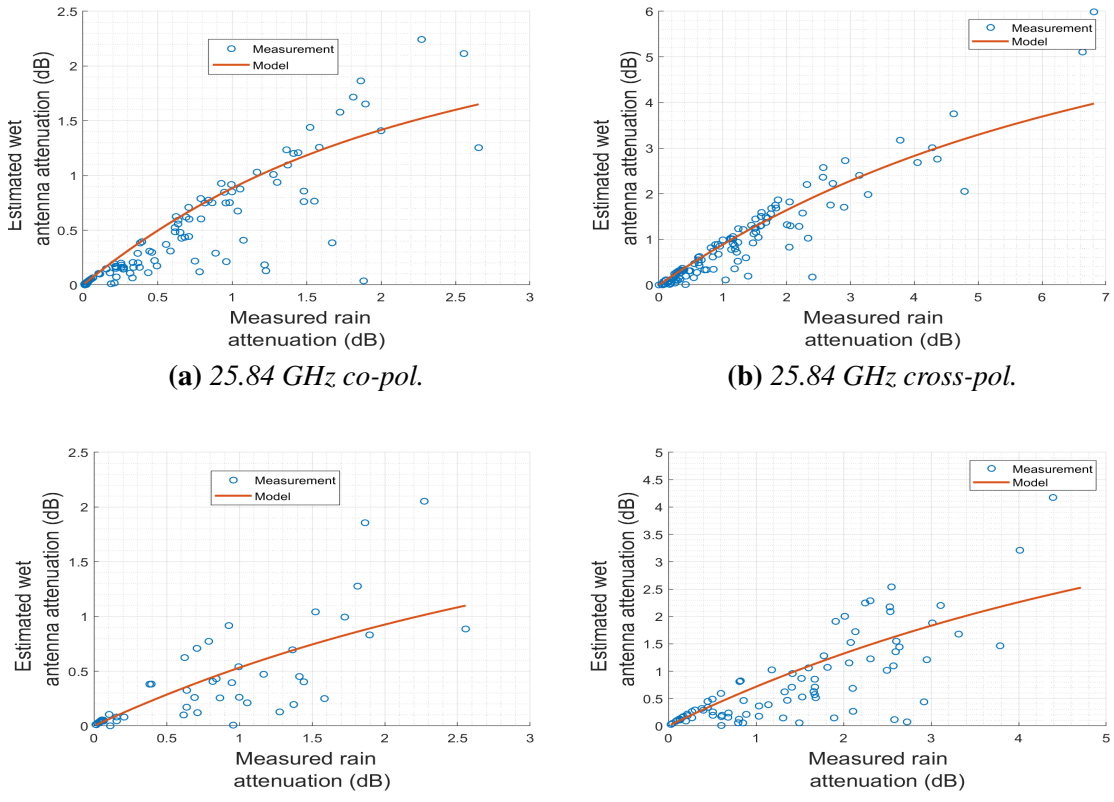

(a) *25.84 GHz co-pol.* **(b)** *25.84 GHz cross-pol.*

(c) *77.54 GHz co-pol.* **(d)** *77.54 GHz cross-pol.*

Figure 5.14: Relationship between measured rain attenuation and the estimated wet antenna attenuation.

The C values calculated were 2.24 dB, 5.98 dB, 2.05 dB, and 4.58 dB for 25.84 GHz

co-polarization, 25.84 GHz cross-polarization, 77.54 GHz co-polarization, and 77.54 GHz cross-polarization, respectively. Table. 5.6 provides a breakdown of the additional attenuation caused by wet antennas as a percentage of the total attenuation for the direct short link (36m). Antenna wetness has a notable impact on 25.84 GHz cross-polarization during light rainfall, but as rainfall intensity increases, this percentage decreases significantly, especially at 77.54 GHz with the same polarization. Among all rainfall conditions, 77.54 GHz co-polarization experiences a more pronounced effect from antenna wetness compared to 25.84 GHz co-polarization. Snow is found to be the main contributing factor to the increased attenuation caused by wet antennas in total attenuation. Overall, during rainy events, the maximum antenna wetness can achieve ranges from 0.6 dB to 1.8 dB for 25.84 GHz (both polarizations) and from 0.53 dB to 1.93 dB for 77.54 GHz (both polarizations). This highlights the exponential increase of WAE with rainfall, indicating a poor correlation with rainfall intensity. Within snowy events, snow grains and flakes remain the major contributors to antenna wetness, with values ranging from 0.1 dB to 1.22 dB, 0.27 dB to 3.05 dB, 0.24 dB to 0.49 dB, and 0.83 dB to 1.04 dB for 25.84 GHz co-polarization, 25.84 GHz cross-polarization, 77.54 GHz co-polarization, and 77.54 GHz cross-polarization, respectively. These significant values should not be used to inflate the predictions of rain attenuation. Significant reductions in attenuation due to wetness were evaluated in a previous study within our group, reported in [138], after covering the Tx/Rx antennas with randoms and waterproof plates. However, it is worth noting that during light rainfall lasting for a long duration, the wetness of the antennas' radomes may cause further attenuation, as mentioned in prior research [138].

Table 5.6: Percentage of the additional attenuation caused by the wet antennas of the total attenuation for 36 m direct link

	2 mm/h	10 mm/h	20 mm/h	Snow
25.84 GHz co-pol	33%	30%	26%	76%
25.84 GHz cro-pol	80%	44%	51%	77%
77.54 GHz co-pol	40%	35%	35%	45%
77.54 GHz cro-pol	73%	39%	10%	53%

The extra covers, i.e., highlighted in Figure. 5.13 do not effectively mitigate the wet effect, particularly during prolonged rain in colder seasons, as drying takes longer. Furthermore,

the measurement data concerning antenna wetness have been influenced by frozen rain and the buildup of snow.

5.3 Frequency Scaling for Rain Attenuation Direct Link

The limited availability of long-term rain attenuation data has led to the utilization of the frequency scaling technique, which allows for a reasonable estimation of attenuation statistics at a specific frequency using measurements obtained at another frequency [139]. This technique proves beneficial when separate frequency propagation occurs during the same rainfall event. Previous research, as reported in [140] and [141], has classified the frequency scaling for rain attenuation into three categories: ratio-based, non-ratio, and composite models. The ratio-based model focuses on scaling attenuation statistics that remain static and are not in real-time. It takes frequency as a parameter and is defined in equation 5.3.4 (ITU-R P.530-18):

$$A_2 = A_1 \left(\Phi_2/\Phi_1\right)^{1-H(\Phi_1,\Phi_2,A_1)} \tag{5.3.4}$$

where:

$$\Phi(f) = \frac{f^2}{1+10^{-4}f^2} \tag{5.3.5}$$

and

$$H\left(\Phi_1,\Phi_2,A_1\right) = 1.12\times10^{-3}\left(\Phi_2/\Phi_1\right)^{0.5}\left(\Phi_1 A_1\right)^{0.55} \tag{5.3.6}$$

A_1 and A_2 are the equiprobable values of the excess rain attenuation at frequencies f_1 and $f_2(\mathrm{GHz})$, respectively. The Statistical Attenuation Ratio (SAR) based models use frequency as well but implement attenuation models such as the DSD model.

Real attenuation measurements at 25.84 GHz and 77.54 GHz are being used to perform frequency scaling for rain attenuation in additional frequency bands. The World Radiocommunication Conference 2019 identified several mmWave frequency bands (24.25-27.5 GHz, 37-43.5 GHz, 45.5-47 GHz, 47.2-48.2 GHz, and 66-71 GHz) for potential allocation for International Mobile Telecommunications (IMT-2020) for 5G applications,

along with 71-81 GHz for non-geostationary fixed-satellite services [142]. Moreover, early 5G FWA providers worldwide have adopted mmWave frequency bands such as 24.5-29.5 GHz and 37-43.5 GHz for possible deployment [143].

The frequency scaling method, based on the ITU-R P.530-18 model, provides a standardised approach for estimating rain attenuation at various frequencies using a reference set of observations at a single baseline frequency. This method takes advantage of the fact that rain attenuation increases with frequency, which is consistent with accepted electromagnetic scattering concepts and models. The primary assumptions are that the rain medium has a power-law dependence on frequency and that the connection between attenuation and rainfall rate is constant over important frequency ranges. In this study, we reduced potential variability from those factors by replicating identical conditions, including the same 36 m path length and weather events, for measurements at 25.84 GHz and 77.54 GHz. This increased the applicability of the ITU-R scaling standard to those two frequencies. Because the model is only formally described up to 55 GHz, we carefully used the 25.84 GHz data as a reference point to scale up to higher frequencies of interest ranging from 28 GHz to 81 GHz. Figures. 5.15 and 5.16 demonstrate the CDFs of attenuation values using the frequency scaling method. It is important to note that the scaling was carried out for the same path length of 36 m and under identical weather conditions, taking into account the impact of antenna wetness. This ensured the recreation of identical measurements for 25.84 GHz and 77.54 GHz, thus minimizing measurement errors and other effects on rainfall attenuation. As the ITU-R model is applicable only within the frequency range of 7-55 GHz, we used the 25.84 GHz data to scale into frequencies of 28 GHz, 39 GHz, 46 GHz, 60 GHz, and 81 GHz for both polarizations. Across all frequencies, cross-polarization shows higher attenuation than predicted for values below 10 dB. For instance, at 39 GHz co-polarization, during very heavy rainfall of 29.57 mm/h, the attenuation reaches 5.21 dB.

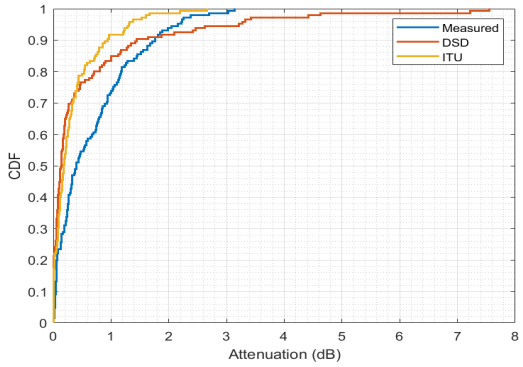

(a) *28 GHz co-pol d=36 m.*

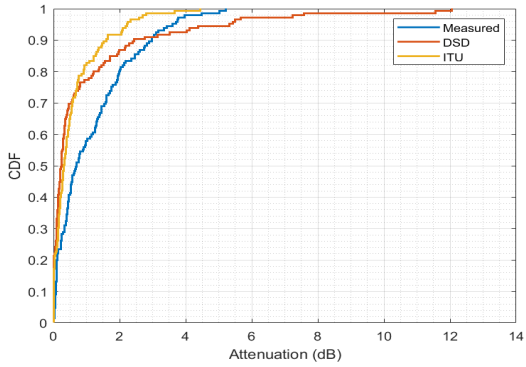

(b) *39 GHz co-pol d=36m.*

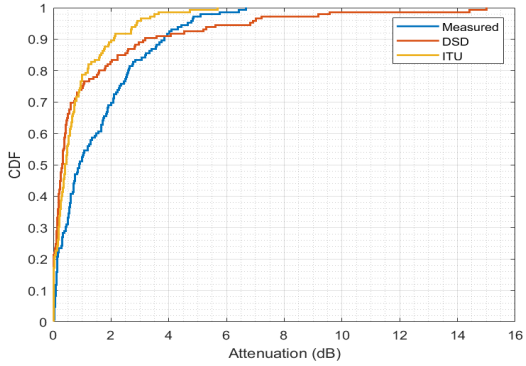

(c) *46 GHz co-pol d=36m .*

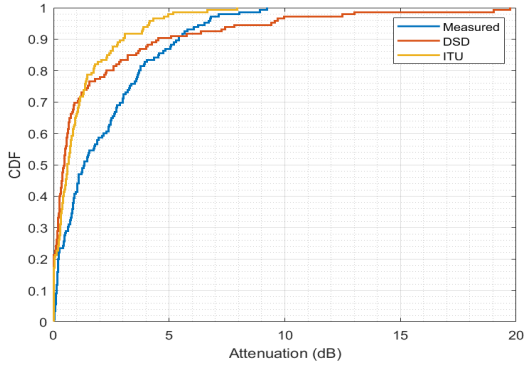

(d) *60 GHz co-pol d=36m.*

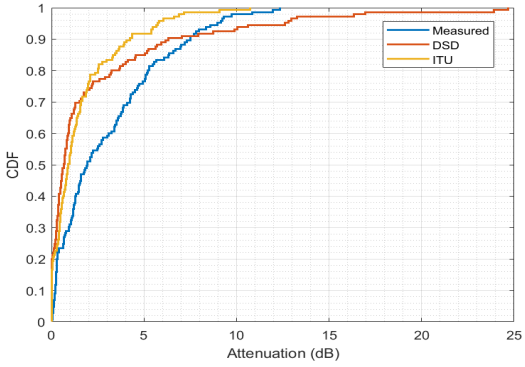

(e) *81 GHz co-pol d=36m.*

Figure 5.15: Cumulative distributions of measured rain attenuation mapped against the predicted using frequency scaling method for direct 36 m link co-pol.

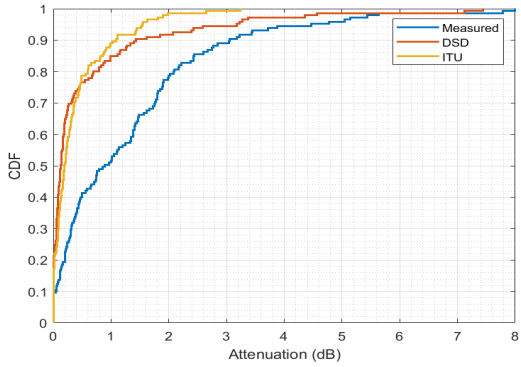

(a) *28 GHz cross-pol d=36 m.*

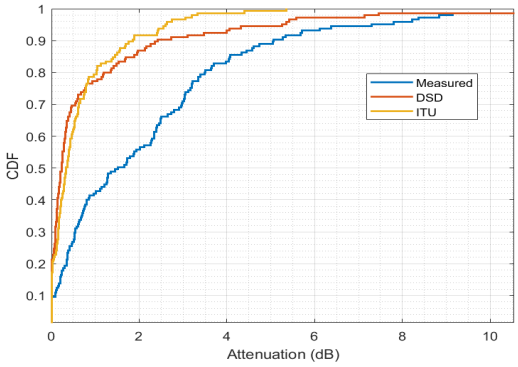

(b) *39 GHz cross-pol d=36m.*

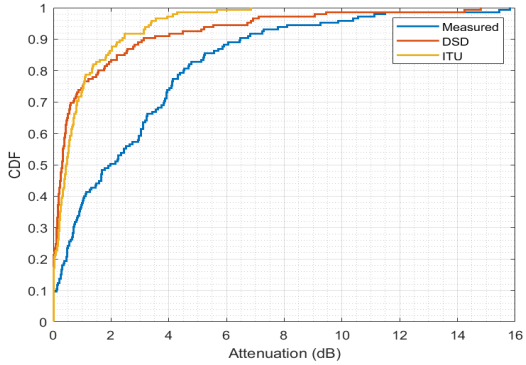

(c) *46 GHz cross-pol d=36m .*

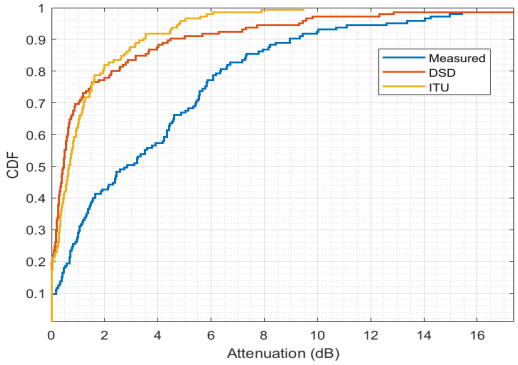

(d) *60 GHz cross-pol d=36m.*

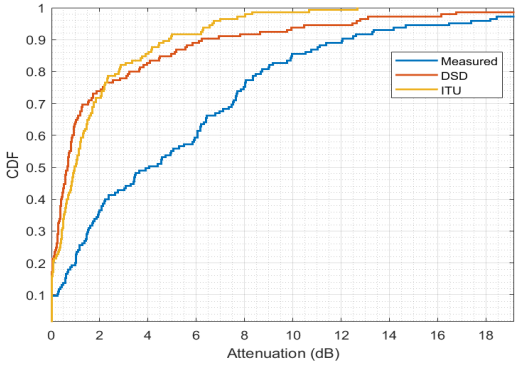

(e) *81 GHz cross-pol d=36m.*

Figure 5.16: Cumulative distributions of measured rain attenuation mapped against the predicted using frequency scaling method for direct 36 m link cross-pol.

5.4 Side Link Measurement and Analysis

5.4.1 Received Signal

The received signal from the side 36 m link between November 2019 and March 2020 (Figure. 5.17) and between September 2020 and June 2021 (Figure. 5.18) exhibits higher

signal losses for most of the measurement points during rainfall events, as the side link relies on reflected Non-Line-of-Sight (NLoS) paths. Raindrop scattering mechanisms influence the reported attenuation in this setup. It should be noted that while the dataset incorporates extensive long-term measurements gathered continuously over multiple months, received signal power profiles exhibit noticeable step changes between certain periods. These discontinuities arise due to necessary upgrades and alterations to the measurement system hardware implemented intermittently over the year-long observation window

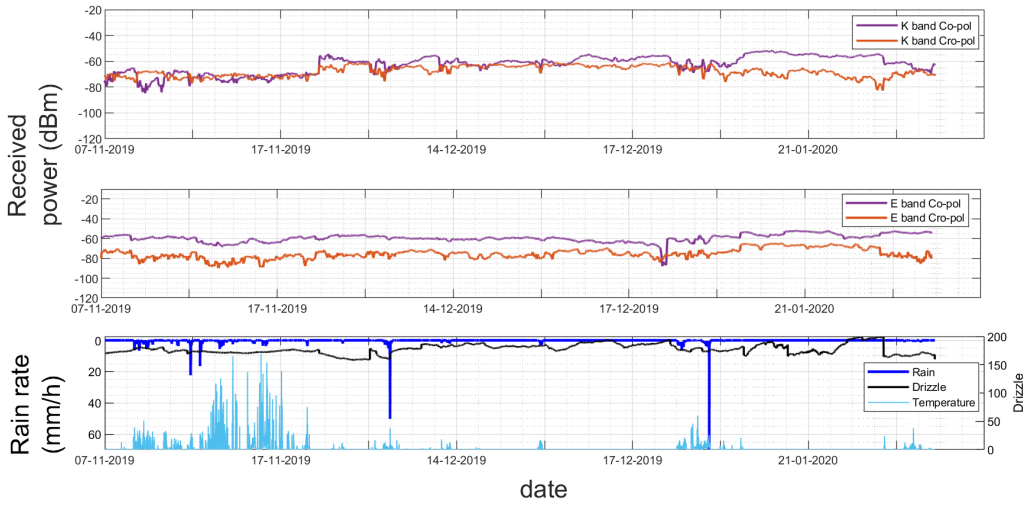

Figure 5.17: 36 m side link received signal for K and77.54 GHz at co and cross polarisation between November 2019 and March 2020.

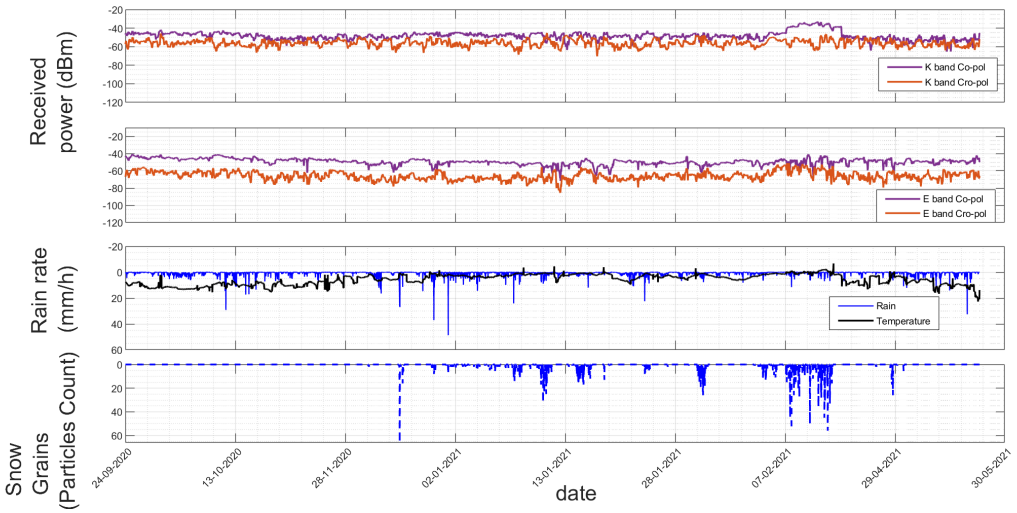

Figure 5.18: 36 m side link received signal for 25.84 GHz and 77.54 GHz at co and cross polarisation between September 2020 and June 2021.

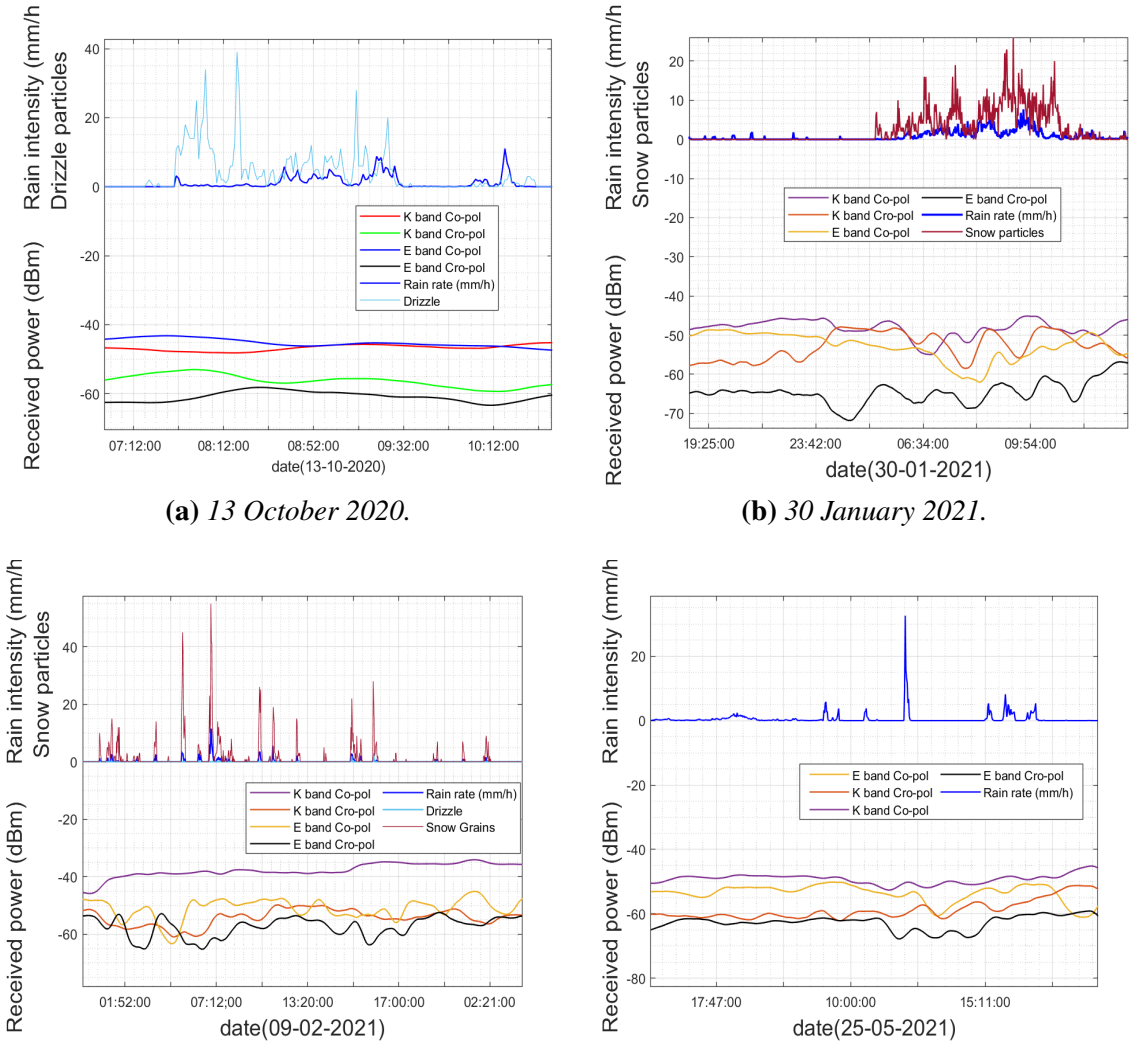

(a) *13 October 2020.* **(b)** *30 January 2021.*

(c) *09 February 2021.* **(d)** *25 May 2021.*

Figure 5.19: Measured rain attenuation within different rainfall events for side link.

At both 25.84 GHz and 77.54 GHz, cross-polarization exhibits greater signal fall than co-polarization. Interestingly, in some rainfall events, the signal strength increases due to raindrop scattering effects. Since the side link relies on NLoS paths, the signal strength during precipitation occurrences is variable and unpredictable, not following a consistent trend with rainfall events. This behaviour is evident in Figure. 5.19, where the link is strongly affected by snowfall occurrences rather than rain. Examples from different measurement periods, such as 13 October 2020, 30 January 2021, 09 February 2021, and 25 May 2021, demonstrate the variation in the received signal.

The 25.84 GHz co-polarization signal strength generally follows the precipitation pat-

tern in these examples. However, for 77.54 GHz cross-polarization, the signal may drop by 10 dB during snowfall events and may not recover due to scattering, while moderate rainfall events can cause the signal to increase. For instance, during rainy events on the 25th of May 2021 without drizzle, ice pellets, or snow, the received power at 77.54 GHz cross-polarization is -62.14 dBm on a clear sky minute before the rain event. When rainfall occurs with 5 mm/h intensity, the received power slightly increases by 1.5 dB. It is important to note that signal losses in NLoS paths cannot always be solely attributed to rainfall, as severe rainfall may cause significant scattering effects from raindrops and gaseous molecules, leading to interference problems. Therefore, evaluating potential signal loss through NLoS paths is crucial during the planning and installation process of such transmission systems [144].

5.4.2 Measured Rain Attenuation Empirical Distribution Function

Rain attenuation for the side link has been measured using dominant and repeating rainfall episodes and then overlaid with predicted values as highlighted in Figure. 5.20. A comparison between the side link and the direct link reveals distinctive aspects in terms of attenuation levels. At the 25.84 GHz frequency band, co-polarization exhibits a maximum attenuation value of 4.39 dB during heavy rainfall events of approximately 26 mm/h. The measured values are higher than the predicted ones when the attenuation reaches the 2 dB threshold. On the other hand, cross-polarization shows a maximum attenuation value of 7.13 dB for moderate rainfall events with an intensity of 10 mm/h and exhibits higher losses compared to the modelled values. For the 77.54 GHz frequency band, co-polarization reaches a maximum attenuation of 6.5 dB during very heavy rainfall with an intensity of 32 mm/h, while cross-polarization exhibits a maximum attenuation of 9.87 dB for rainfall events of 37 mm/h without snow. These higher values and fluctuations in the side link's attenuation need to be further examined, similar to the direct link, but not limited to attenuation alone. The ongoing analysis includes investigating link performance and scattering-induced interference between short-range fixed links, which can cause outages and loss in received power [144].

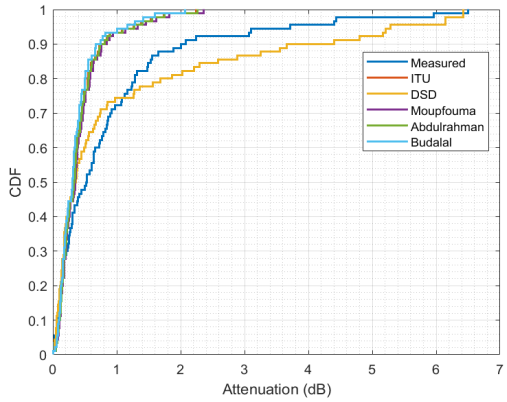

(a) *25.84 GHz vertical d=36 m side link.*

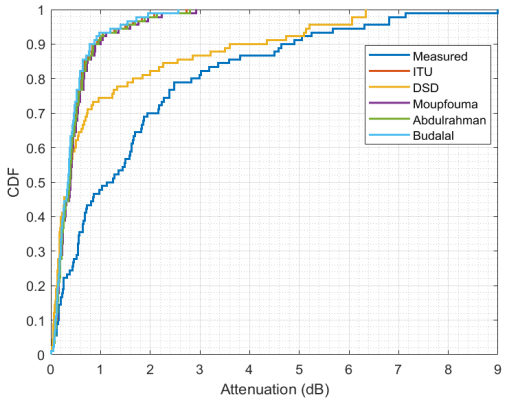

(b) *25.84 GHz horizontal d=36m side link.*

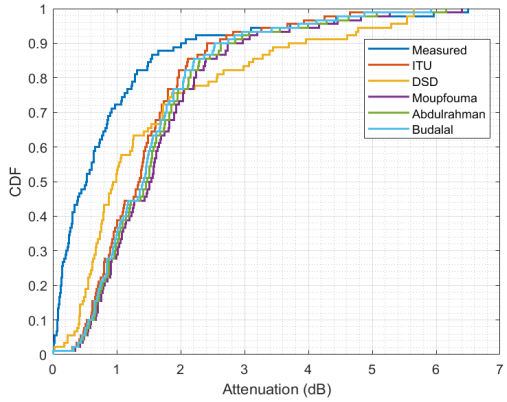

(c) *77.54 GHz vertical d=36m side link .*

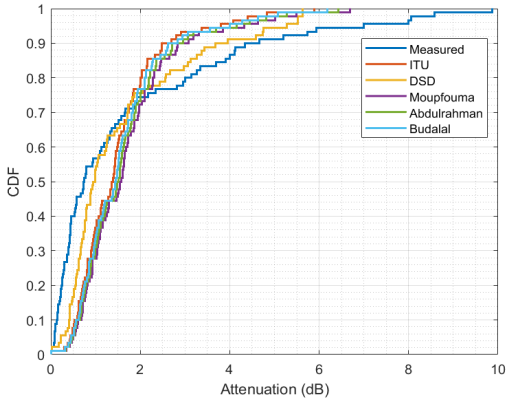

(d) *77.54 GHz, horizontal d=36m side link.*

Figure 5.20: Measured rain attenuation versus rain intensity for side link.

5.5 Link Performance and Scattering Induced Interference Measurement

5.5.1 Link Performance

The established links in our experimental setup, previously described in Chapter 3 and detailed in the Direct and Side measurement sections of this chapter, include the transmission from the transmitter (T_X) to the receiver (RX_D) via a LoS path, commonly known as the direct link. This direct link experiences signal degradation due to absorption and scattering losses induced by precipitation in the propagation environment. As well, it includes the second receiver (RX_S) operates in close proximity to the direct link path, but outside it, aiming to gather data through a non-line-of-sight (NLoS) channel, where the

signal scatters away from the direct path. Both links are influenced by several factors, including the effects of rainfall-induced signal degradation and gaseous attenuation. These factors collectively influence signal strength and quality, making it imperative to analyze and understand their impact on the overall performance of the communication system. Proper consideration and analysis of these factors are vital for optimizing link design and ensuring reliable data transmission. The link gain for the LOS channel is computed by separating it into two parts: divergence attenuation and atmosphere attenuation [145]. Divergence attenuation refers to the free-space propagation loss that occurs as an electromagnetic wave expands in space from a transmitting antenna. As the wavefront spreads out over a distance, the power density reduces due to spatial divergence. The divergence attenuation is given by:

$$G_D = 4A/\left(\pi d^2 \alpha_A^2\right) \tag{5.5.7}$$

where α_A is the full divergence angle of the transmitter (T_x). A is the effective receiving area of R_{X1}. So the divergence gain or loss depends on how collated or focused the Tx antenna beam is. More divergent beams will spread faster, reducing power density at the receiver. This geometric dilution quantifies signal decay over a line-of-sight channel where no obstructions or scattering occurs.

The atmospheric attenuation is given by:

$$G_A = \exp\left(-\alpha_{atm} d\right) \tag{5.5.8}$$

where $\alpha_{atm} = \alpha_t + \alpha_g$ is the atmospheric attenuation coefficient. α_g is the gaseous attenuation by air. α_t is the precipitation (rainfall, snow grain snowflakes) attenuation. We can calculate the overall direct link gain by combining atmospheric and divergence attenuation.

$$G_{\text{Los}} = G_A G_D = \frac{4A \exp\left(-\alpha_{atm} d\right)}{\pi d^2 \alpha_A^2} \tag{5.5.9}$$

For the side link introduced by the scattering effect, we use the single scattering model described in [146] to measure the gain link. The link geometry and mechanism are exhib-

ited in Figure. 5.21(b). Tx is set to be at the origin coordinate (0, 0), Rx1 is at (36 m, 0),

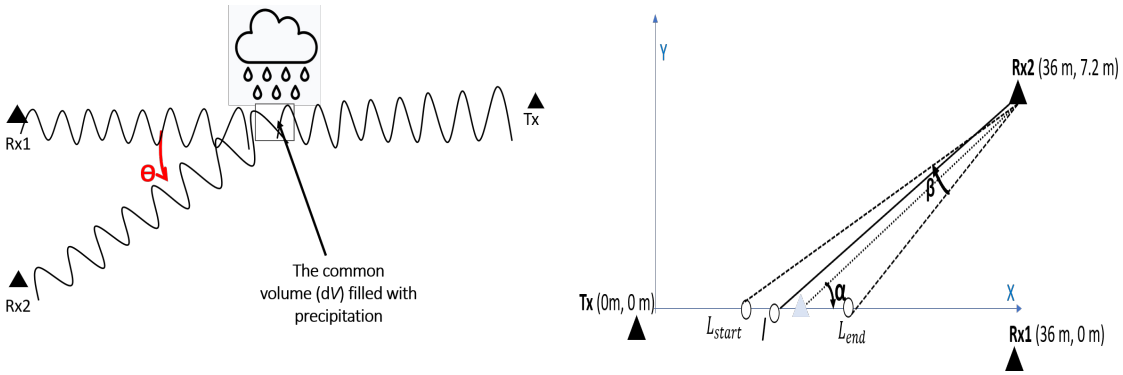

(a) *Geometry of Rain Scatter.*

(b) *Shematic Geometry of the direct (LoS) and side (NLoS) links (Not to scale).*

Figure 5.21: Direct and side link experimental setup: (a) Geometry of Rain Scatter, (b) Coordinate Geometry of the direct (LoS) and side (NLoS) links.

and Rx2 is set at (a=36 m, b=7.2 m). The gain calculation is described and well detailed in [147] is given by:

$$G_{\text{NLoS}} = \int_{L_{start}}^{L_{end}} \Omega(l) p(\mu) \alpha_{atm} \exp\left\{-\alpha_{atm}\left[l + \sqrt{(a-l)^2 + b^2}\right]\right\} dl \tag{5.5.10}$$

where l is the transmission path before the first scattering. $\Omega(l)$ is the solid angle from the receiving area to the scattering point (l; 0):

$$\Omega(l) = \frac{A}{[(a-l)^2 + b^2]^{3/2}} \frac{(a-l) + b\tan\alpha}{\sqrt{1+\tan^2\alpha}} \tag{5.5.11}$$

L_{start} and L_{end} represent the lower and upper integration limits for the path length l before the first scattering point as part of computing the non-line-of-sight link gain. Specifically, L_{start} is the minimum (closest) possible path length to the scattering point. This is constrained by the geometry of receiver antenna beamwidth covering an area defined by angle $\alpha - \beta/2$. L_{end} is the maximum (farthest) possible path length to the scattering point. This is constrained by the geometry of receiver antenna beamwidth covering an area defined by angle $\alpha + \beta/2$. So, L_{start} and L_{end} provide the lower and upper limits of where the first scattering point can be located, based on the antenna field of view and total link span. This sets the bounds for numerical computation of the NLoS gain overall potential scattering

paths. They are given as follows:

$$\begin{aligned} L_{\text{start}} &= \min\left\{\max\left\{a-\frac{b}{\tan(\alpha-\beta/2)},0\right\},d\right\} \\ L_{\text{end}} &= \min\left\{\max\left\{a-\frac{b}{\tan(\alpha+\beta/2)},0\right\},d\right\} \end{aligned} \tag{5.5.12}$$

where α and β represent the pointing angle and the full angle of field of view, respectively, and μ is the cosine of scattering angle in $(l,0)$, which is given by:

$$\mu(l) = \frac{a-l}{\sqrt{(a-l)^2+b^2}} \tag{5.5.13}$$

One significant element that defines the potential distribution of the scattered wave direction is the scattering phase function $P(D,\theta_s)$. It allows determination of how much incident power gets scattered at each direction θ_s based on particle sizes and dielectric properties. Analyzing this distribution provides insight into the optimal receive antenna pointing angle. It is given by:

$$P(\theta) = \frac{|S_1(\theta)|^2+|S_2(\theta)|^2}{\pi x^2 Q_{sca}} \tag{5.5.14}$$

where $S_1(\theta)$ and $S_2(\theta)$ terms are elements of the scattering amplitude matrix given by the Mie theory. θ_s is the scattering angle, $N(D)$ is the measured raindrops distribution. According to [147], α the pointing angle is optimal when $\alpha < \pi/2-\beta/2$. For maximum received signal power via scattering, the receive antenna should point slightly away from the direct transmitter-receiver azimuth angle by at least half the antenna beamwidth $\beta/2$. This ensures significant scattered signal aggregation within the receiver field of view.

The maximum link gain G_N^* of side link paths and full-angle β can be reached by selecting the following optimal pointing angle,

$$\alpha^* = \arctan\frac{y}{x}+\beta/2$$

The second receiver for the side link is positioned horizontally at a distance of 7.2 meters from the first receiver. The atmospheric visibility plays a crucial role in the link's performance, affecting the gains of both the direct (LoS) and scattered (NLoS) links. The

PWS100 disdrometer utilized for weather monitoring records the visibility conditions across the propagation path. Quantified visibility data is reported on a per-minute basis with an accuracy of ±10% up to a maximum range of 20 Km. Analysis of the cumulative distribution of measured visibility over the course of the long-term measurement campaign provides insights into attenuation link dynamics. As presented in Figure. 5.22, the assessed visibility spans an extensive dynamic range from 100 meters to beyond 15 Km over the measurement timeline. However, probability distribution highlights that despite periods of heavy precipitation-induced fading, the likelihood of very low visibility below 300 meters remains low at approximately 10%. Instead, the distribution skews towards high visibility with median and mean values of 10 kilometres and 11.59 kilometres respectively. This corresponds to attenuation through fog, haze or moderate rains for the majority of link conditions. In summary, while the disdrometer quantified visibility fluctuates substantially from below 100 meters to above 15 kilometres based on weather, the probabilistic likelihood favors milder attenuation environments. Quantifying these trends helps characterize average link availability and interpret measured attenuation compared to precipitation maps. Further statistical correlation between attenuation and quantified low visibility events would prove beneficial.

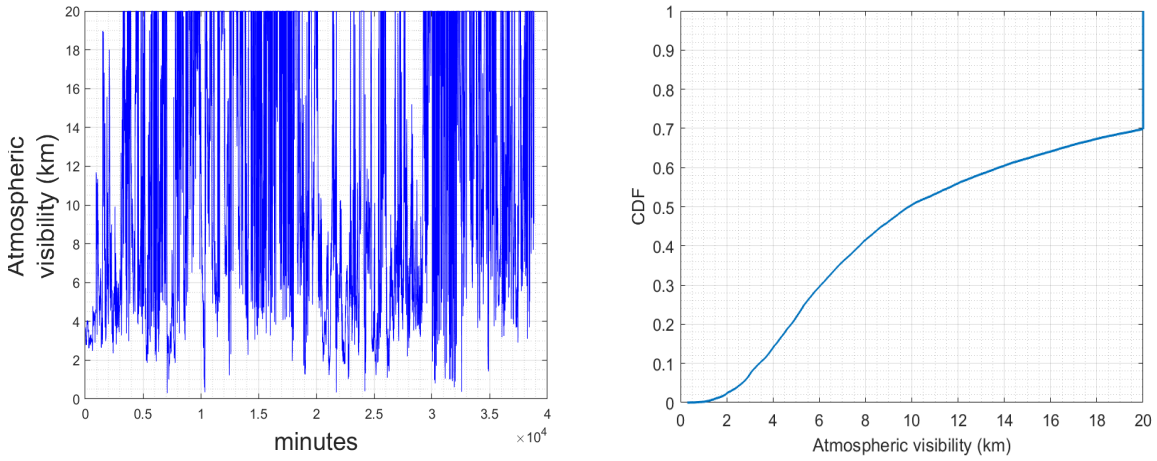

(a) *Measured visibility.* **(b)** *CDF.*

Figure 5.22: Visibility measurement: (a) visibility of each event, (b) CDF.

The link gains for both the direct and scattered links are calculated and reported in Figure. 5.23. When the visibility drops below 2 kilometres, the NLoS link gain tends

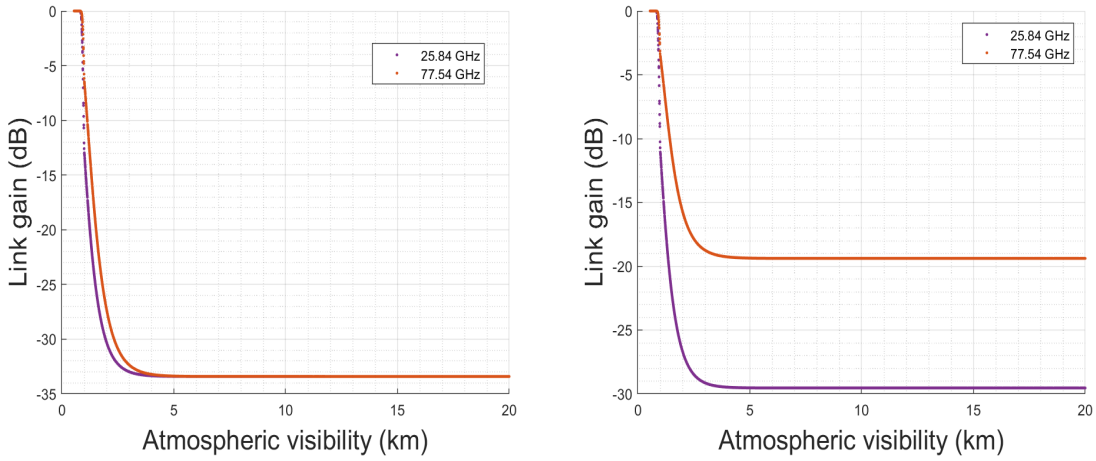

(a) *LoS direct link link.* **(b)** *NLoS side link.*

Figure 5.23: Link gain of the direct (LOS) and side (NLoS) link versus the atmospheric visibility.

to decrease, indicating that lower visibility conditions have a detrimental effect on the signal strength of the scattered link. On the other hand, when the visibility exceeds 1.5 Km, the gain for the NLoS link at 25.84 GHz significantly increases. However, there is no substantial difference in gains between the frequency bands for the LoS direct link. These findings are consistent with our previous observations on attenuation results, where the 25.84 GHz frequency band exhibited higher attenuation values compared to the 77.54 GHz frequency band in the side link.

It is important to note that the higher signal loss experienced by the LoS link in rainy conditions and the higher scattered power for the NLoS path in the side link increases the probability of interference as rain intensity increases. However, in the case of higher visibility, the received signal in the direct link is significantly higher than the received signal in the side link, given the very short distance between the two receivers. As the distance between the receivers increases, minimal interference may occur due to raindrop scattering. Therefore, careful consideration and measurement of scattering effects are crucial when assessing the performance of the communication system in these conditions.

5.5.2 Scattering Measurement

In the context of rain-induced interference, the scattered power can be considered as the power that is scattered within the overlapping volume of a transmitter and a nearby re-

ceiver (5.21(a)). Only scattering within this common volume is considered in the first-order multiple scattering approximations, while scattering that occurs throughout the trajectory from the transmitter to the beam junction and then to the receiver is treated as lost power and is included in extinction along with absorption [148]. To gain a better understanding of this phenomenon, it is essential to investigate the Bistatic Scattering Radar Equation (BSRE).

The methodology for modelling the Bistatic Scattering (BS), whether single-scattering or multiple-scattering, depends on the wavelength, size, and number density of the scatterers (raindrops). In the single-scattering regime, the incident wave weakly interacts with only a few other scatterers before reaching the scatterer of interest. The incident wave is primarily the direct wave from the source for each scatterer, and interactions with other scatterers have a relatively minor impact. However, as the number density of scatterers increases or the strength of scattering intensifies (which can happen at higher frequencies), multiple scattering may become more significant [149–151].

The Bistatic Radar Equation (BRE) given in equation 5.5.15 is be used to describe the correlation between the physical processes that cause scattering and the resulting coupling and interference. This equation helps to quantify the scattered power and its effect on the communication system when rain is present. By considering both single-scattering and multiple-scattering regimes, it becomes possible to assess the impact of rain-induced interference on the link performance and communication reliability.

$$\frac{P_r}{P_t} = \frac{\lambda^2}{4\pi^3} \int_V \frac{G_t G_r}{(r_t r_r)^2} \eta\left(\theta_s\right) A_{air} A_{rain} dV \tag{5.5.15}$$

where λ is the wavelength, G_t and G_r are directional gain functions for transmitter and receiver antennas, r_t and r_r are transmitter and receiver distances to scattering volume element $dV, \eta\left(\theta_s\right)$ is the BSCS, A_{air} and A_{rain} are path attenuation due to atmospheric absorption and rain-induced scattering. This equation would be used to determine the coupling between two antenna beams that occupy a shared volume filled with scatterers. BSCS η in the bistatic radar equation depends on the scattering properties of raindrops and their size distribution and can be calculated by integrating over all drop sizes as de-

scribed in equation 5.5.16:

$$\eta(\theta_s) = \int_0^{\infty} N(D)\sigma_{sca}(D)P(D,\theta_s)\,dD \tag{5.5.16}$$

where D is the drop diameter, θ_s is scattering angle, $N(D)$ is raindrop size distribution (DSD), σ_{sca} is the scattering cross section and $P(D,\theta_s)$ is the scattering phase function which describes the probability distribution of the scattered wave direction. Cross section and phase function are calculated using Mie theories and DSD is fitted to real measured DSD data. Provided that the raindrops are homogeneous spherical particles with known diameters, distribution, refractive index of water, temperature, and humidity from the weather station measurement, we should utilise the Mie scattering theory to obtain an accurate and reliable solution for the scattering characteristics of a single sphere. Extinction cross-section, scattering cross-section and absorption cross section is calculated using Mie parameters as noted in Equations 2.4.9, 2.4.10, and 2.4.11.

Typically, the phase function is normalized so that integration across all angles returns unity. Figure. 5.24 presents the normalized phase function as a function of scattering angle for 25.84 and 77.54 GHz for different raindrop diameters. The scattering phase function, or phase function, gives the angular distribution of signal intensity scattered by raindrops at the given frequency wavelengths.

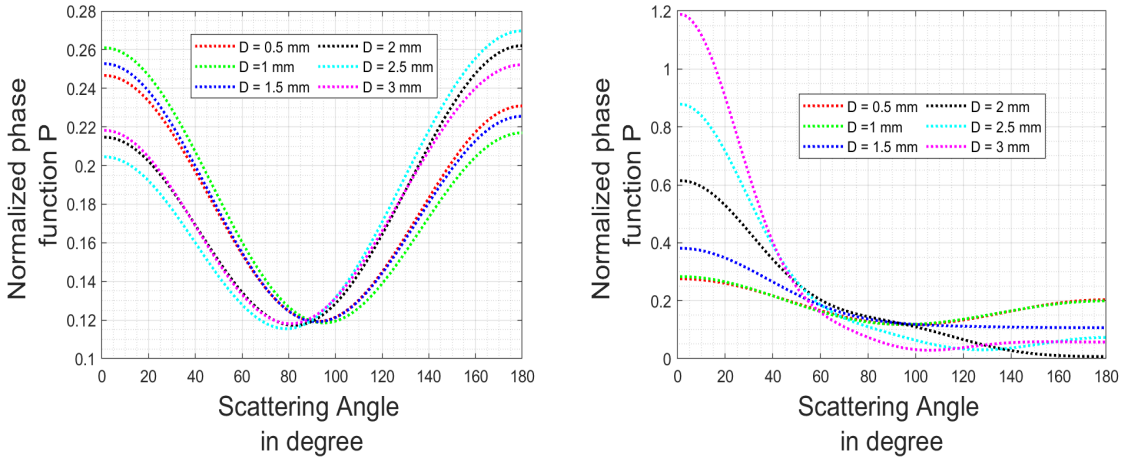

(a) *25.84 GHz.* **(b)** *77.54 GHz.*

Figure 5.24: Normalized scattering phase function $P(\theta)$ at (a) 25.84 GHz and (b) 77.54 GHz.

The figures show that at the 25.84 GHz frequency band, the Mie theory solution approximates more Rayleigh-type scattering for all raindrop's diameters while 77.54 GHz is more forward-oriented, especially for raindrops below 1.5 mm. The scattered energy is more forward-oriented for drops equal to or above 2 mm in diameter. For 25.84 GHz, the raindrop's diameter equal to or below 1.5 mm scatter more energy below 60° scattering angle. It should be noted that the refractive index of water has been calculated using the average measured temperature 6°.

Figures. 5.25 and 5.26 represent the normalized the Bistatic Scattering Cross Section (BSCS) for 77.54 GHz, and 25.84 GHz, respectively for different rainfall events (1, 5, 10, 20, 30, 40 mm/h) for raindrops with diameters ranging from 0.5 mm to 3 mm owing to the fact that the most of raindrops belong to this range from the previous measurement. The Bistatic Scattering (BS) function is used to quantify the predicted magnitude of the signal that will be detected by the receiver. This is significant for assisting with system design and performing engineering performance assessments (such as signal-to-noise ratio and total uncertainty measurement) for short-range fixed links. Furthermore, it is relevant to examine the behaviour of the bistatic scattering process and evaluate the sensitivity of bistatic measurements to Earth surface parameters.

The analysis of bistatic scattering for rain-induced interference was conducted using a combination of the Mie theory for spherical raindrops and the bistatic radar equation, with realistic variations in rainfall along the propagation path taken into consideration. The results revealed that the BS cross section (BSCS) achieved its maximum for raindrops with a diameter of 1.5 mm within 1 mm/h rainfall events, with little contribution from raindrops larger than 1.5 mm or smaller than 1 mm. In very heavy rainfall events of up to 40 mm/h, the BSCS reached its maximum for the majority of raindrop types, and the values increased by 30% when the frequency was increased from 25.84 GHz to 77.54 GHz. Notably, raindrops around 0.5 mm in size did not significantly contribute to the overall BSCS for both frequencies. In the case of 77.54 GHz during medium rainfall events of 10 mm/h, raindrops in the range of 1-1.5 mm tended to be forward-oriented. For a bistatic scattering angle of 45°, rainfall events caused significant bistatic coupling, leading to changes in the order of 0.3-2.5 dB.

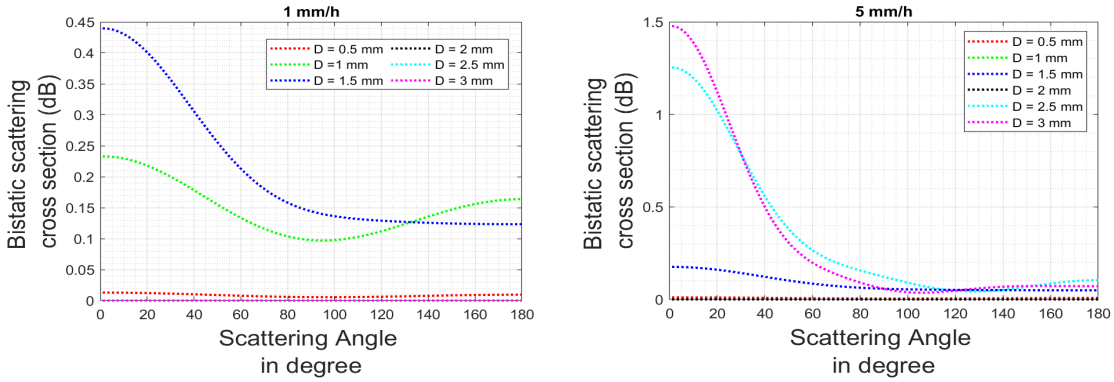

(a) *1 mm/h.*

(b) *5 mm/h.*

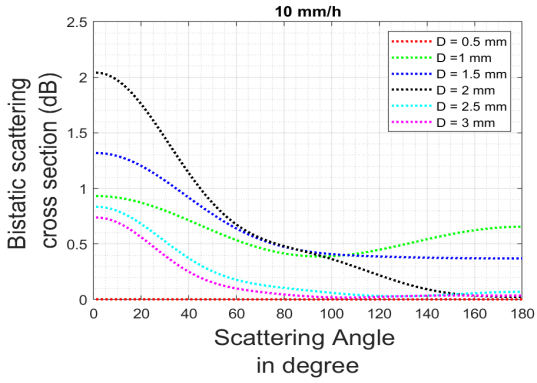

(c) *10 mm/h.*

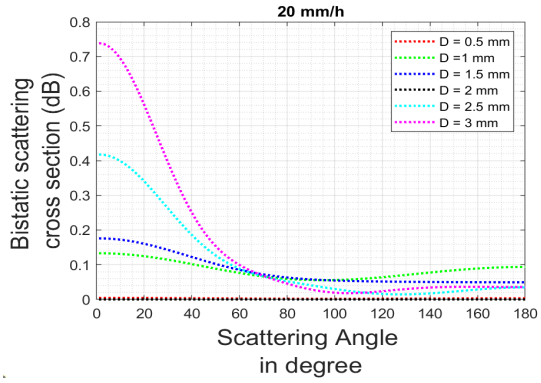

(d) *20 mm/h.*

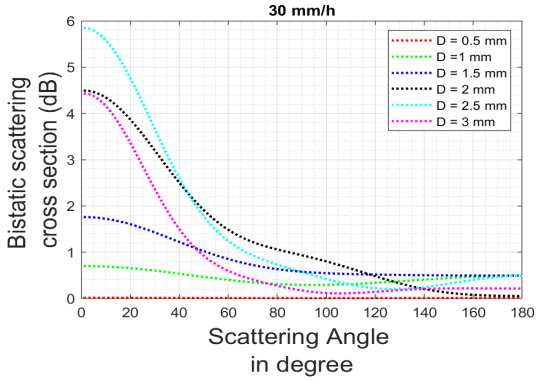

(e) *30 mm/h.*

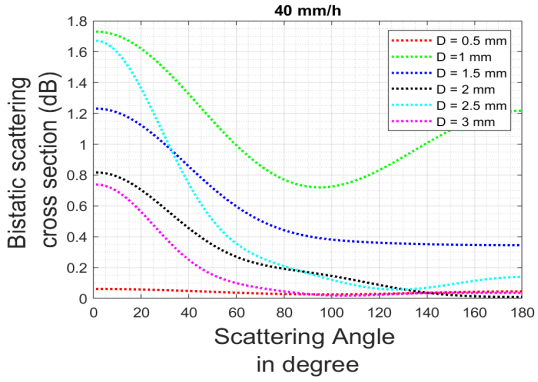

(f) *40 mm/h.*

Figure 5.25: 77.54 GHz Bistatic scattering cross section for different rainfall events.

The predictions from the analysis, which utilized the Mie theory and bistatic radar equation, showed that the BSCS values varied at different scaling angles ranging from 0° to 180° degrees, and this would symmetrically reflect a calculation ranging from 180° to 360°. The measurement results further confirmed that the values of the BSCS increased as the rainfall rate increased. Moreover, the frequency band was found to have a signifi-

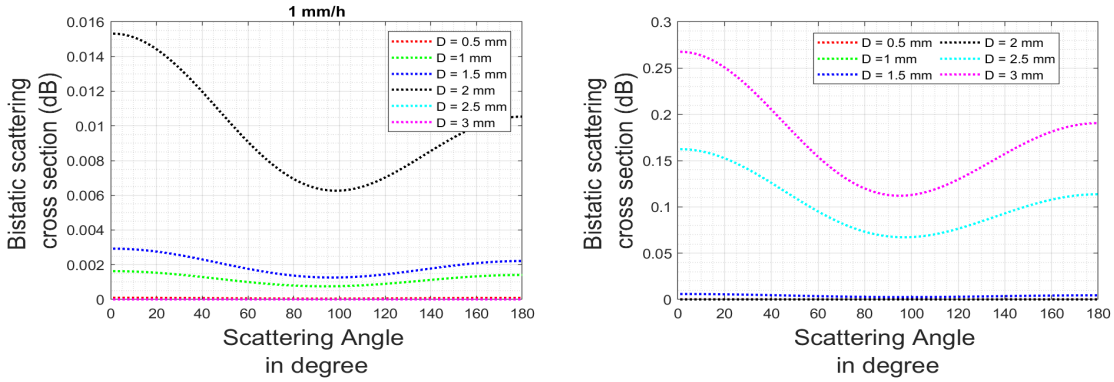

(a) *1 mm/h.* **(b)** *5 mm/h.*

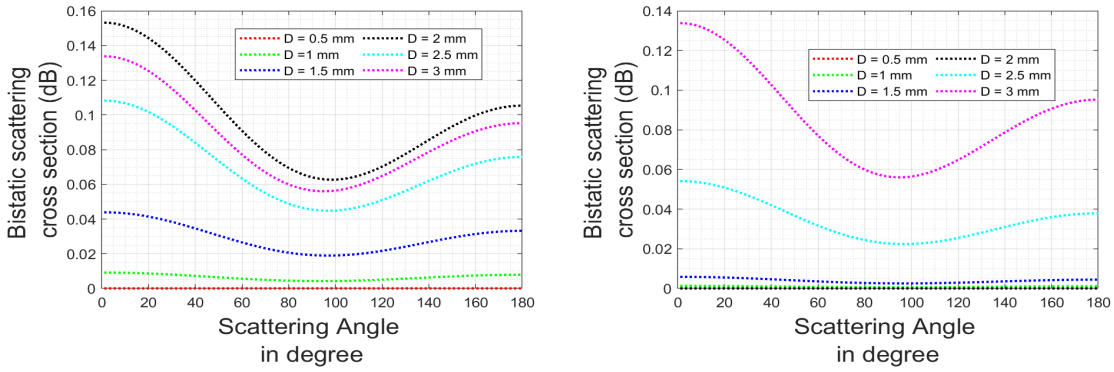

(c) *10 mm/h.* **(d)** *20 mm/h.*

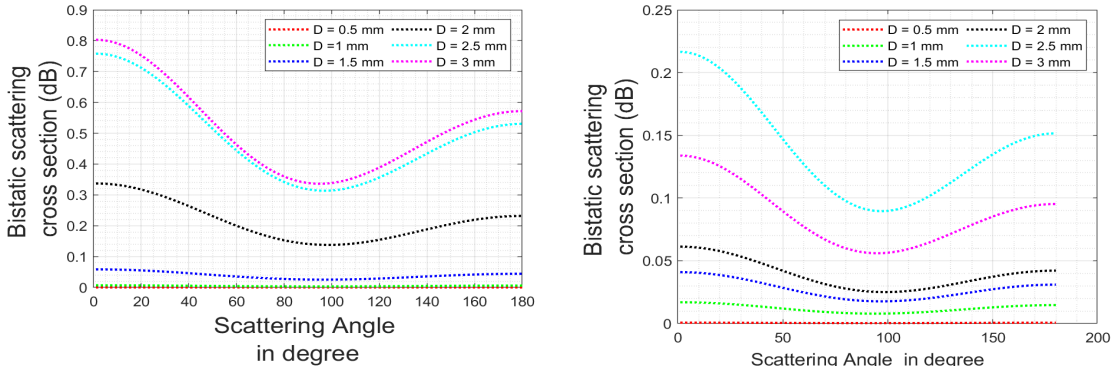

(e) *30 mm/h.* **(f)** *40 mm/h.*

Figure 5.26: 25.84 GHz Bistatic scattering cross section for different rainfall events.

cant impact on the estimation of the BSCS, with values rising as the frequency increased. The analysis was based on realistic disdrometer data measurements, which provided accurate and reliable input for the scattering calculations, allowing for a comprehensive understanding of rain-induced interference in communication links operating in various frequency bands.

In essence, the scattering behaviour at 25.84 GHz exhibits characteristics more akin to Rayleigh scattering, while at 77.54 GHz, it tends to favor forward scattering, particularly noticeable for droplets smaller than 1.5 mm. The findings suggest that droplets larger than or equal to 2 mm tend to scatter more energy forward, whereas at 25.84 GHz, droplets smaller than or equal to 1.5 mm scatter at angles less than 60°. Furthermore, the BSCS peaked for droplets of 1.5 mm size under light rainfall of 1 mm/h. These specific observations complement earlier studies such as Gloaguen and Lavergnat [152], which demonstrated minimal impact on bistatic scattering at 94 GHz for droplets smaller than 1 mm, while those larger than 2 mm significantly increased the bistatic cross-section. The finding that BSCS increases with higher rainfall rates and frequencies echoes similar observations in [152], although our analysis revealed a 30% increase in BSCS from 25.84 to 77.54 GHz, compared to the 20-25% increase observed from 44 to 94 GHz in [152]. While our current analysis delves into detailed scattering profiles under specific conditions, the overarching trends corroborate the established relationships between bistatic scattering properties, raindrop sizes, rainfall rates, and frequencies as outlined in prior research.

5.6 Frequency Scaling for Rain Attenuation Side Link

The measurement results of the side link provide valuable data for rain attenuation scaling methodology, which proves to be instrumental in examining rain attenuation in a flexible manner. The cumulative distribution functions (CCDFs) of rain attenuation for different frequency bands (28 GHz, 39 GHz, 46 GHz, 60 GHz, and 81 GHz) were plotted as shown in Figures 5.27 and 5.28, showing the relationship between the measured and predicted attenuation values from well-known models. In the case of co-polarization, there was consistent alignment between the measured and predicted loss values for values lower than 1.5 dB, while the ITU-R model differed for all frequency bands. Statistically, the rain intensity was less than 50 mm/h for 99% of the measured data, and the attenuation was lower than 25 dB for the highest frequency band (77 GHz) and lower than 8 dB for 26 GHz. Notably, there was a range of 17 dB in attenuation from 28 GHz to 81 GHz, indicating that attenuation increases with frequency. For cross-polarization, the measured

and DSD model rain attenuation levels agreed for values greater than 6 dB for 80% of the data at 28 GHz and exceeded 10 dB for other frequencies for 80% of the data. These findings provide valuable insights into the behaviour of rain attenuation at different frequency bands, allowing for a better understanding of the impact of rain on communication links and aiding in the design and optimization of mmWave communication systems, especially for future networks that may operate in various frequency bands with different polarization schemes.

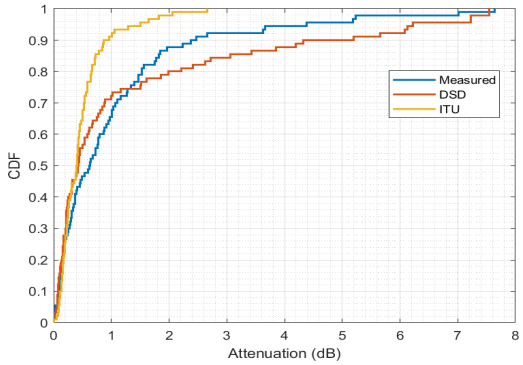

(a) *28 GHz co-pol d=36 m.*

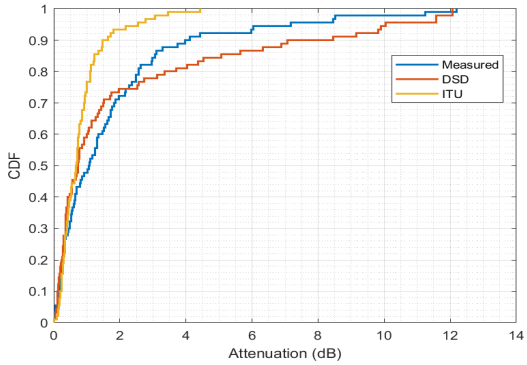

(b) *39 GHz co-pol d=36m.*

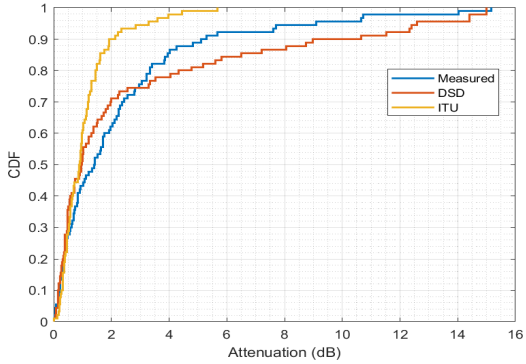

(c) *46 GHz co-pol d=36m .*

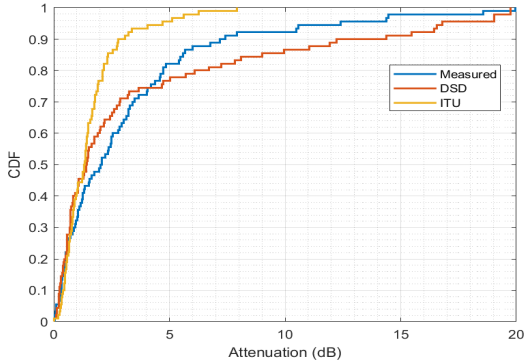

(d) *60 GHz co-pol d=36m.*

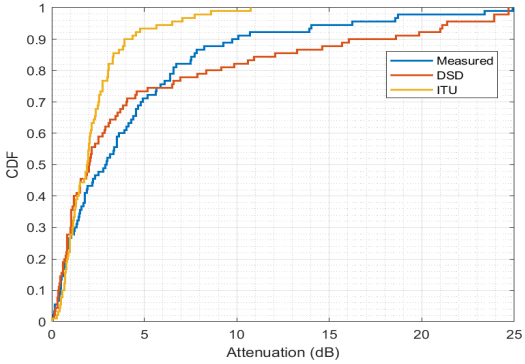

(e) *81 GHz co-pol d=36m.*

Figure 5.27: Cumulative distributions of measured rain attenuation mapped against the predicted using frequency scaling method for side 36 m link co-pol.

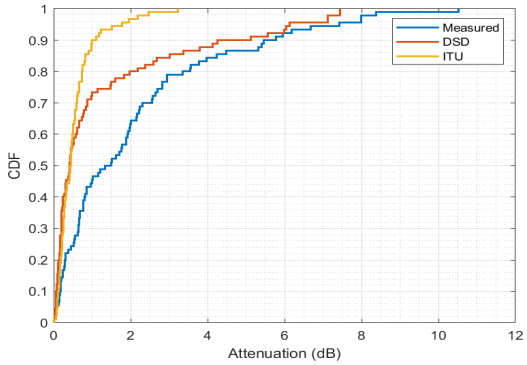

(a) *28 GHz cross-pol d=36 m.*

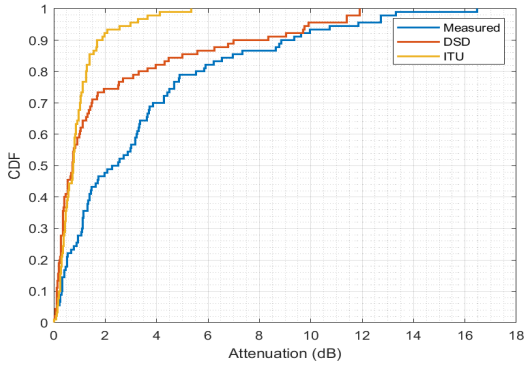

(b) *39 GHz cross-pol d=36m.*

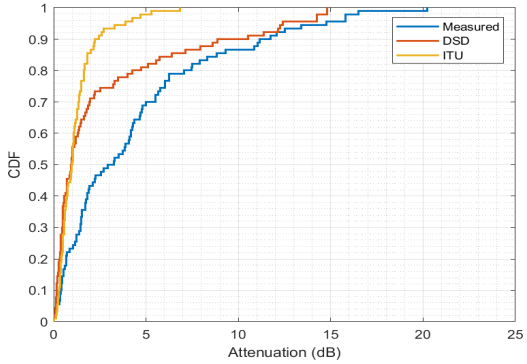

(c) *46 GHz cross-pol d=36m .*

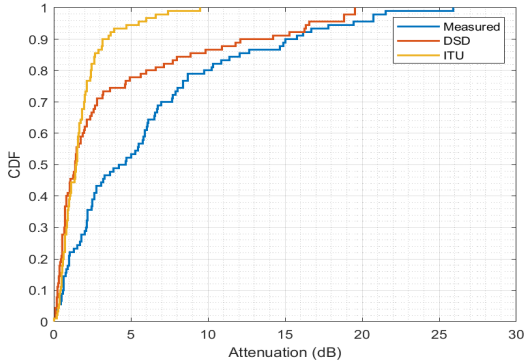

(d) *60 GHz cross-pol d=36m.*

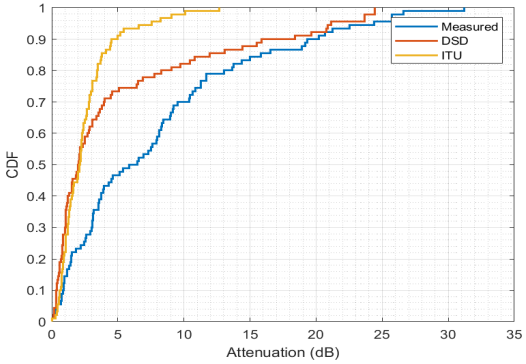

(e) *81 GHz cross-pol d=36m.*

Figure 5.28: Cumulative distributions of measured rain attenuation mapped against the predicted using frequency scaling method for side 36 m link cross-pol.

5.7 Summary

The chapter presented a comprehensive investigation of long-term rain attenuation measurements for both direct and side 36-meter fixed link systems. The findings highlighted notable variations in measured attenuation based on both rainfall intensity and the fre-

quency bands employed as highlighted in Table. 5.7. For instance, during heavy rainfall, the measured attenuation was 2.40 ± 0.12 dB for 25.84 GHz cross-polarization and 1.90 ± 0.10 dB for 25.84 GHz co-polarization. On the other hand, for light rainfall events with an intensity of 2 ± 0.1 mm/h, the attenuation was 0.26 ± 0.03 dB for cross-polarization and 1.44 ± 0.07 dB for co-polarization at 25.84 GHz.

In the E band (77.54 GHz) of the same link, the maximum attenuation reached 2.65 ± 0.13 dB when the rainfall rate was around 29 ± 1.5 mm/h for co-polarization and 4.72 ± 0.47 dB for cross-polarization at rainfall rates below 5 ± 0.25 mm/h. Regarding the prediction process, the data highlighted that the distance factor of 2.5 recommended by ITU-R was inappropriate for a link length of 36 m. Instead, the computed values from the measurement (8.8-9.5) were applied to the ITU-R model. Taking into account the realistic measurement data and rain attenuation modelling, the rain fade margin for a point-to-point short-range link of 36 m was calculated as 3-3.48 ± 0.2 dB and 1.02-1.73 ± 0.1 dB for 77.54 GHz and 25.84 GHz, respectively, with a link availability of 99.99% and a rain intensity of 29.57 ± 1.5 mm/h.

Table 5.7: Summary of the rain attenuation measurements for Direct 36 m link

Frequency (GHz)	Rainfall Intensity (mm/h)	Cross-pol Attenuation (dB)	Co-pol Attenuation (dB)
25.84	40 ± 2	2.40 ± 0.12	1.90 ± 0.10
25.84	2 ± 0.1	0.26 ± 0.03	1.44 ± 0.07
77.54	29 ± 1.5	5.8 ± 0.58	2.65 ± 0.13
77.54	$< 5 \pm 0.25$	4.72 ± 0.47	0.8 ± 0.06

A detailed examination of the contribution of different raindrop sizes to overall attenuation took place and Table. 5.8 summarise the findings. The analyses indicated that smaller raindrops in the range of 0.1-0.7 ± 0.04 mm significantly impacted the attenuation at the lower frequency band (25.84 GHz). In contrast, droplets up to 2 ± 0.1 mm in size contributed considerably to the attenuation at 77.54 GHz. Moreover, for an exceedance probability of 82%, the attenuation was 0.01 ± 0.001 dB and 0.10 ± 0.01 dB for 25.84 GHz and 77.54 GHz, respectively, at a rainfall intensity of 1 ± 0.05 mm/h. The maximum attenuation for a link availability of 99.99% did not exceed 3.5 ± 0.2 dB and 1.73 ± 0.09 dB at 77.54 GHz and 25.84 GHz, respectively, in February, which was the

month with the highest attenuation value throughout the year.

Table 5.8: Summary of the raindrop's contribution to the attenuation

Raindrop Size (mm)	Frequency (GHz)	Attenuation (dB)
0.1-0.7 ± 0.04	25.84	Significantly impacts the signal degradation
Up to 2 ± 0.1	77.54	Considerable contribution to the measured attenuation
1 ± 0.05	25.84	0.01 ± 0.001 dB (at 82% exceedance probability)
1 ± 0.05	77.54	0.10 ± 0.01 dB (at 82% exceedance probability)
	77.54	Maximum attenuation for 99.99% availability: 3.5 ± 0.2 dB
	25.84	Maximum attenuation for 99.99% availability: 1.73 ± 0.09 dB

The analysis of antenna wetness revealed significant impacts on both frequencies, particularly during light rainfall events. The wet antenna effect increased sharply during rainfall, reaching its maximum value, but correlated weakly with rainfall intensity.

For the side link measurement data, attenuation levels exhibited distinct features. During heavy rainfall events of 26 ± 1.3 mm/h, the observed values were higher than the expected values, with attenuation reaching 4.39 ± 0.44 dB for co-polarization at 25.84 GHz and 7.13 ± 0.71 dB for cross-polarization. Similarly, at 77.54 GHz, co-polarization and cross-polarization exhibited attenuation levels of 6.5 ± 0.46 dB and 9.87 ± 0.99 dB respectively, under very heavy rainfall events of 30 ± 3 mm/h (Table. 5.9). The link gain was reduced for visibility lower than 2 km, while it increased when visibility was higher than 1.5 km at 25.84 GHz. This indicated that raindrops-induced interference between the two 36 m fixed links was minimal when visibility was higher.

The Bistatic Scattering function of the side link was used to calculate the estimated magnitude of the signal that would be received by the second receiver. A summary measurement Smaller raindrops below 0.5 ± 0.03 mm had an almost negligible impact on the total Bistatic Scattering Cross Sections (BSCS) over both frequencies. The BSCS tended to increase beyond 1.5 ± 0.08 mm drop size during light rainfall events, while extremely heavy rainfall events of approximately 40 ± 4 mm/h showed that the BSCS reached its peak for

95% of raindrop varieties, with values increasing by 30 ± 3% when the frequency was increased from 25.84 GHz to 77.54 GHz. Notably, the bistatic scattering cross-section increased with increasing rain intensity and frequency.

Table 5.9: Summary of the rain attenuation measurements for Side 36 m link

Frequency (GHz)	Rainfall Intensity (mm/h)	Attenuation (dB)
25.84	26 ± 1.3	Co-pol: 4.39 ± 0.44 dB Cross-pol: 7.13 ± 0.71 dB
77.54	30 ± 3	Co-pol: 6.5 ± 0.46 dB Cross-pol: 9.87 ± 0.99 dB

Overall, the measurement and analysis showed that scattering effects due to raindrops were significant, especially for drops smaller than 1.5 mm, where the energy was greatly scattered at 25.84 GHz and below 60 degrees. Meanwhile, the energy was more forward-directed at 77.54 GHz for raindrops below 1.5 mm. 25.84 GHz revealed increased overall interference with a minimum at around 45 beam angle for the provided path of 36 m. Stronger interaction at small and large angles was due to the increased common volume, as scattering occurred in a Rayleigh-like pattern in the E band. With 77.54 GHz, interference was stronger at smaller beam angles due to the different wavelengths, resulting in more forward-directed scattering. While the overall level of received power for the E band was lower, it may have exceeded the K band at narrow angles. Because the first-order multiple scattering approximations may tend to enhance interference at small angles, further analysis is needed.

Chapter 6

Filtronic Fixed Link Measurement

6.1 Introduction

To ensure the accuracy and reliability of precipitation loss measurement, the extended 200 m link is utilized for investigating rain attenuation throughout this chapter. The experimental setup, referred to as the *Filtronic* setup, was described in chapter three and operates at 77.125 GHz. The reported measurement data spans from November 2020 to June 2021. A narrow beam lens antenna with an RF E-band commercial module is employed for the study. The analysis involves utilizing measurement data from the fixed link, as well as precipitation data, to examine rain attenuation. Additionally, the study will investigate the effect of raindrop diameter, the impact of the distance factor, and the influence of antenna wetness on rain attenuation.

6.2 Link Measurement and Analysis

6.2.1 Received Signal

Figure 6.1 depicts the received signal in dBm from the LoS link operating at 77.125 GHz over a distance of 200 m between the engineering building roof and the library roof. The signal exhibits variations in response to the precipitation rate, with signal losses differing across various rain events.

Notably, during winter seasons with rain and snowfall, the signal experiences significant

Figure 6.1: The received signal mapped against the precipitation occurrences for 200 m Filtronic link at 77.125 GHz (E band) between November 2020 and June 2021.

decreases. During data collection for the new link between November 2020 and June 2021, certain data points were eliminated due to abnormal behaviour of the received signal, such as unexpected increases in received power due to NLoS components or sudden drops during light rainy events. During a moderate rain event with a rate of 6 mm/h lasting 10 minutes, there was a noticeable attenuation of 3 dB. The signal strength decreased from -44 dBm before the rain to -47 dBm during the rain, and it stayed at this level for 60 minutes after the rain stopped. In contrast, after short but intense rain events, very heavy rainfall of approximately 30 mm/h for 2 minutes or heavy rainfall of 16 mm/h over a brief period, the signal swiftly returned to its original state within 4 minutes. A similar pattern was observed for light rainfall events of less than 2 mm/h lasting for 30 minutes, where the signal returned to its original level immediately after the rain event ended. Figure. 6.2 provides a more detailed view of four precipitation events and their impact on the received signal. For instance, during continuous light rainfall of less than 5 mm/h lasting 25 minutes, the signal dropped by 3 dB during the event but rapidly recovered to its original level once the event concluded, as demonstrated by the case on 09 November 2020. On the other hand, during short rainfall events lasting up to seven minutes with rainfall rates ranging from 8 to 21 mm/h, the signal did not experience significant degradation, with losses not exceeding 3.1 dB at the rainfall peak of 21.98 mm/h, as observed in the exam-

ple from December 2020. Moreover, the data revealed an inconsistent monthly trend on a shorter temporal scale of hours, particularly during the winter season. These fluctuations might be attributed to changes in the establishment of a uniform air boundary layer, leading to variations in the propagation path within the short-range fixed link of 200 meters.

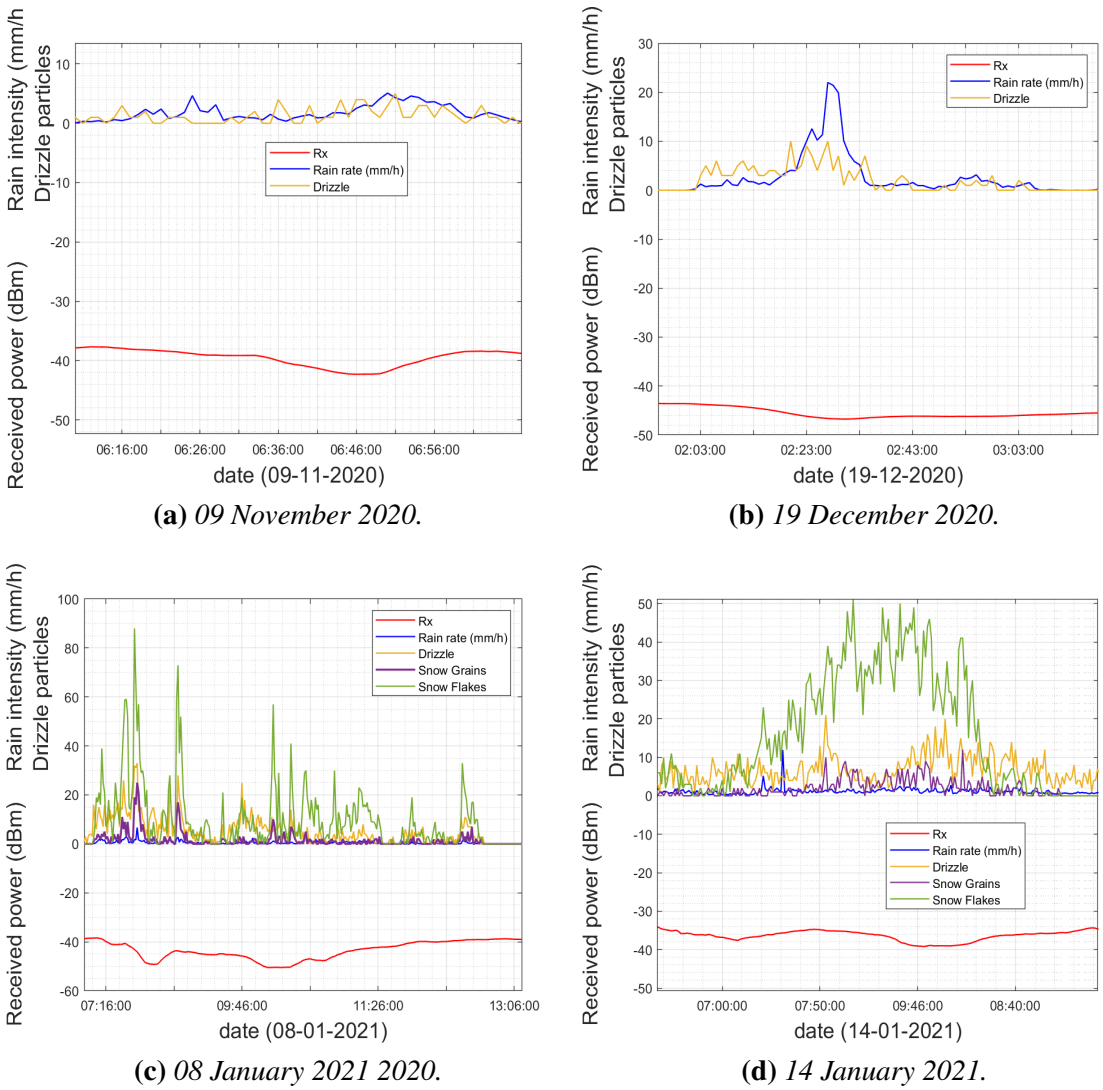

(a) *09 November 2020.*

(b) *19 December 2020.*

(c) *08 January 2021 2020.*

(d) *14 January 2021.*

Figure 6.2: Measured rain attenuation within different rainfall events duration for 200 m fixed link.

Furthermore, when a mixture of snow, rain, and drizzle occurs, the signal experiences a sharp drop and becomes snow-dominant. However, the signal typically recovers its strength quickly after the snow event has passed. In the case of a snow event lasting more than half an hour, the signal begins to fade, although not immediately when the event starts. This observation suggests that the wet antenna effect may be relatively low in this

scenario, but icing could still be a factor. Additionally, the antenna elevation is inclined down by 15 degrees. The antenna's downward slant might facilitate the accumulation of snow and ice on top of the lens antenna construction. When precipitation, such as rain, falls and freezes, the force of gravity causes it to attach to the antenna's surface, generating an ice layer. Moreover, the inclination of the antenna elevation may affect the shedding of accumulated snow and ice. Unlike horizontally positioned antennas where snow and ice can slide off more easily, the inclined orientation of the antenna may impede the natural shedding process. This can lead to prolonged periods of snow and ice accumulation, amplifying the potential impact on antenna performance. This aspect will be further explored in this chapter.

6.2.2 Distance Factor

The Filtronic link was employed to investigate rain attenuation in this study which is operating at 77.125 GHz, was utilized, and the measurement data covered the period between November 2020 and June 2021. The study focuses on utilizing the measurement data from the fixed link and precipitation data to examine rain attenuation, the effect of raindrop diameter, distance factor impact, and antenna wetness.

The comparison of rain attenuation predictions with measurements using the 200 m link at 77.125 GHz is presented in Figure 6.3 for both cases with and without the distance factor considered. The distance factor r was calculated based on different rain rates exceeded for 0.01% of the time ($R_{0.01}$) values. It was observed that, for most rainfall events, implementing the restricted distance factor of 2.5 underestimates the measured attenuation, with the degree of underestimation varying depending on the type of rainfall. Light and moderate rainfall events exhibited a larger underestimation compared to heavy rainfall. For instance, at a rain rate of 12 mm/h, the underestimation reached 4.17 dB, whereas, at a rain rate of 21 mm/h, the difference was only 0.45 dB. For light rain up to 5 mm/h, the underestimation was 1.09 dB. Practically, the calculations revealed that the distance factor r sharply increased to values greater than 1 for path lengths below 200 m, continuing to increase until reaching 3-3.5. Rainfall, being inherently convectional, occurs in a manner where the rain rate is highest at the central focus of the falling region and rapidly

decreases near the edges. Despite assuming a constant rain rate throughout the path due to its short length, it is evident that rainfall spatial variation cannot be constant along the link due to various factors such as the number of dominant drops, wind direction, and speed, site diversity of transmitters and receivers, and the local environment with seasonal and diurnal variations.

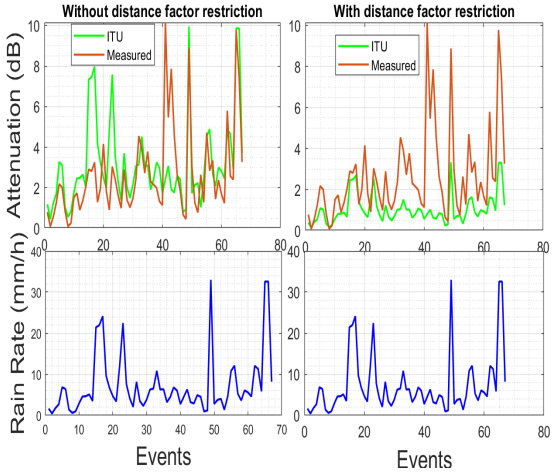

(a) $R_{0.01}$=*5 mm/h.*

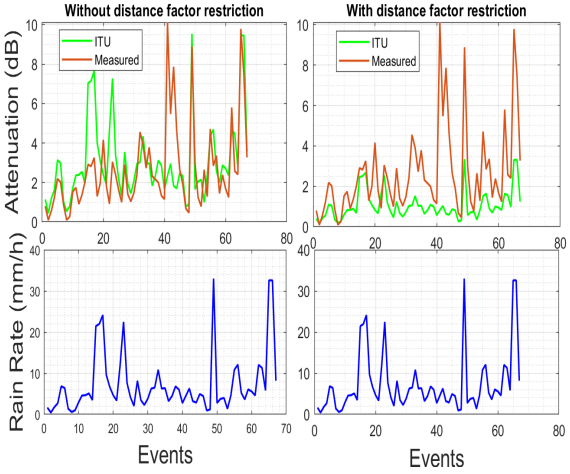

(b) $R_{0.01}$=*10 mm/h.*

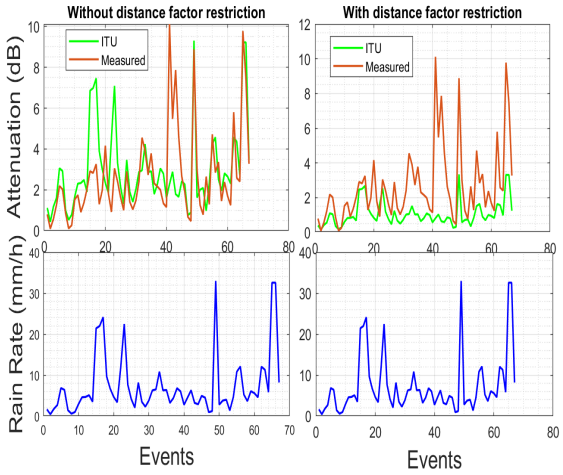

(c) $R_{0.01}$=*15 mm/h.*

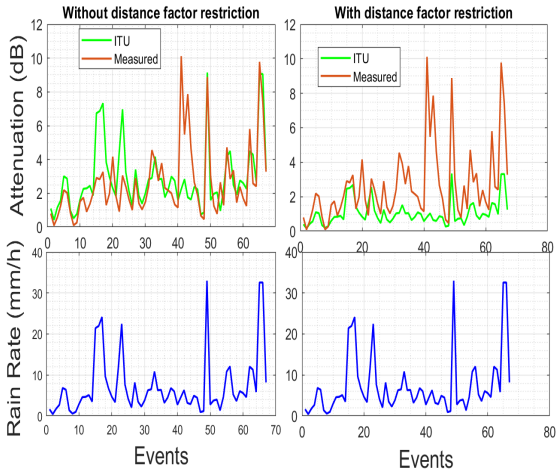

(d) $R_{0.01}$=*20 mm/h.*

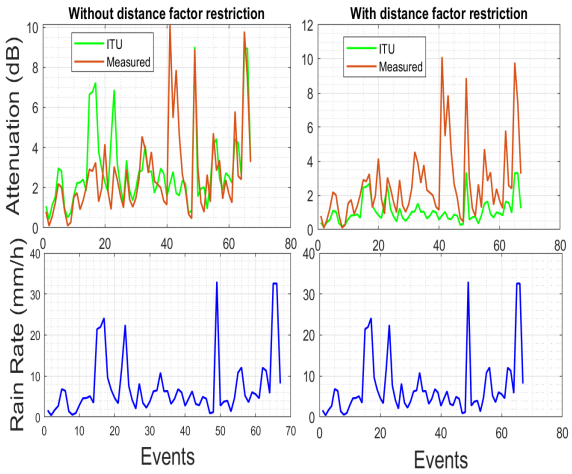

(e) $R_{0.01}$=*25 mm/h.*

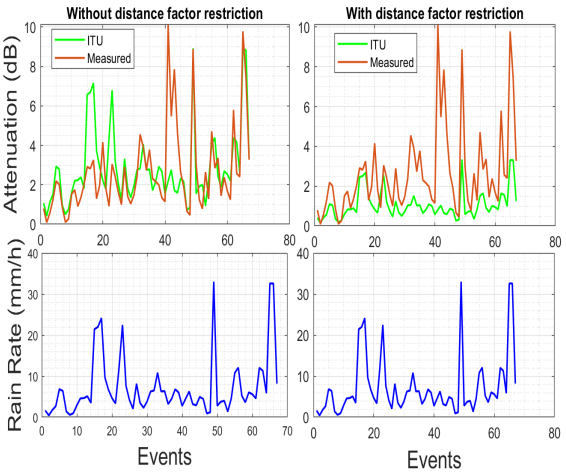

(f) $R_{0.01}$=*30 mm/h.*

Figure 6.3: The measured attenuation vs the predicted attenuation with and without using the maximum distance factor restriction of 2.5 for 77.125 GHz frequency band 200 m link within different $R_{0.01}$ values.

For short link conditions, the effective rain rate causing attenuation may be significantly larger than the average rain intensity of the rain cell. Additionally, there is a three-meter difference in height above sea level, which contributes to the variation in rainfall homogeneity, along with wind speed and direction. In previous works, like in [113], an increment factor (I_f) has been introduced for short links below 300 m instead of the standard distance factor to effectively account for the spatial inhomogeneity of rainfall along the link. Research in [65] also incorporated the spatial variability of the rain rate, along with the SC EXCELL model and the Lin model, as an alternative to the ITU-R model, with the conclusion that the path reduction factor is approximately equal to 1. From the measurement datasets, an optimal distance factor in the range of 3-3.3 was found, indicating that considering spatial variability is crucial for obtaining accurate predictions of rain attenuation in short links adopting the ITU-R model. Further analysis and consideration of path environment parameters would be necessary to investigate the impact of rainfall spatial variability and identify an appropriate value for the distance factor (r) for a given short link.

6.2.3 Measured Rain Attenuation

The empirical distribution function is illustrated in Figure 6.4, showing the CCDFs of the measured attenuation compared with the predicted values.

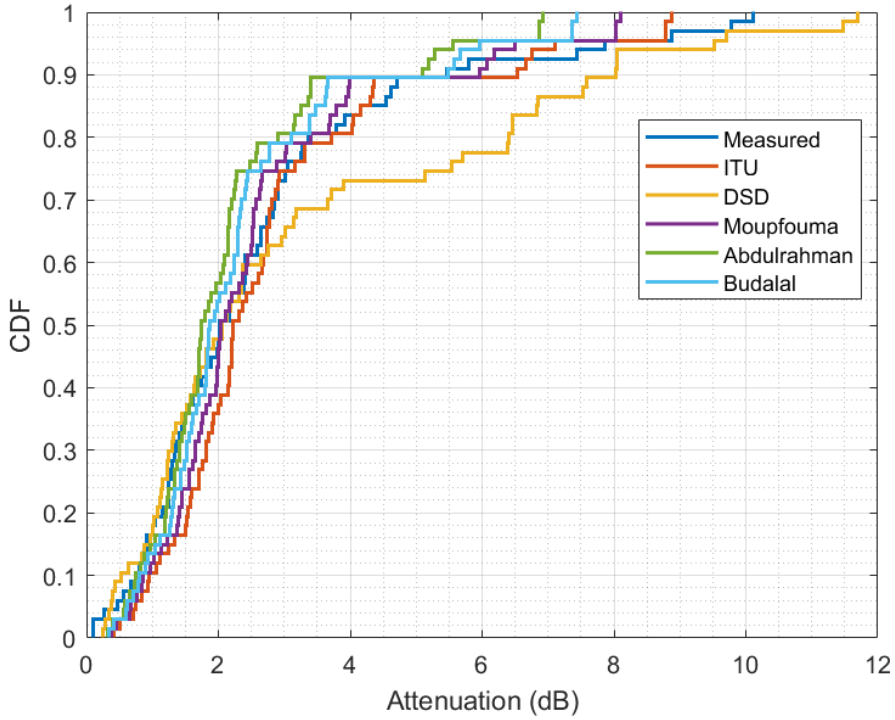

Figure 6.4: Measured rain attenuation versus rain intensity for 200 m link at 77.125 GHz.

For this section, the ITU-R prediction calculations were based on previous findings, and therefore, we used the computed values instead of the 2.5 restrictions of the path reduction factor. The measured attenuation generally correlates well with the estimated attenuation for most levels below 3 dB. However, at higher attenuation levels in the range of 3-8.04 ± 0.4 dB, the DSD model shows higher values than the measured ones for this extended link. This discrepancy is attributed to the Mie theory used by the DSD model, which relies on raindrop distribution, particularly in conditions with mixed precipitation such as rain and snow. In such cases, the accuracy of the DSD model is impacted. The measured attenuation reaches a maximum of 8.88 ± 0.44 dB for a maximum rain intensity of 33 ± 1.65 mm/h, while its lowest value is 0.79 ± 0.04 dB for light rainfall of 1.63 ± 0.08 mm/h. Approximately 60% of the measured data exhibit overall attenuation below 3 dB. Figure 6.5 presents the cumulative rain and attenuation statistics, providing information about the probability of exceedance - i.e., the total amount of time that a certain rain rate or attenuation will be exceeded after a sufficiently long observation period. Table. 6.1 summarises the measurement and analysis for the 200 m link.

For an exceedance probability of 40%, the rain rate is 6 ± 0.3 mm/h, and the attenuation is 2.4 ± 0.12 dB. For exceedance probabilities in the range of 14-36%, the DSD model adopting Mie theory tends to overestimate the measured attenuation. This is understandable, given that Mie's theory considers factors such as raindrop distribution, water refractive index, temperature, number of drops, and drop shape, all of which can be affected by mixed precipitation like rain and snow. For exceedance probabilities higher than 40% and rain intensities less than 6 ± 0.3 mm/h, the ITU prediction model returns slightly higher values than the DSD and measured data, with a difference not exceeding 0.46 ± 0.02 dB. The correlation between the models and measurements is observed for lower attenuation values and rain rates. The contribution of drops in the 0.8-1.8 ± 0.09 mm diameter range is reasonable but limited, ranging from 0.09 ± 0.005 to 2.72 ± 0.14 dB. The level of fit between theoretical and experimental values for the link was evaluated using the root mean square error (RMSE) of the regression curve values derived by fitting predicted and experimental values for 77.125 GHz along the 200 m path. The DSD model exhibits an RMSE of 0.0534 ± 0.003 for rain attenuation, while the ITU model has a lower RMSE value of 0.0046 ± 0.0002. In terms of prediction accuracy utilizing the measurement data, the DSD model achieves an accuracy of 86.9% ± 4%, while the ITU model performs better, with an accuracy of 96.60% ± 5% for the 200 m point-to-point link.

Table 6.1: Summary of the measured and predicted rain attenuation values for the 200 m link

Details	Observations
ITU-R prediction - Distance factor	Computed values used instead of 2.5 restrictions
Measurement vs. DSD Model	Correlation for attenuation $\leq$ 3 dB.
Measured attenuation	Max: 8.88 ± 0.44 dB at rain intensity of 33 ± 1.65 mm/h. Min: 0.79 ± 0.04 dB at light rainfall of 1.63 ± 0.08 mm/h.
Exceedance probability analysis	For 40% probability: Rain rate: 6 ± 0.3 mm/h, Attenuation: 2.4 ± 0.12 dB. DSD overestimates for 14-36% probabilities.
Evaluations	• RMSE at 77.125 GHz: – DSD model: 0.0534 ± 0.003 dB – ITU model: 0.0046 ± 0.0002 dB • Prediction accuracy: – DSD: 86.9% ± 4% – ITU: 96.60% ± 5%

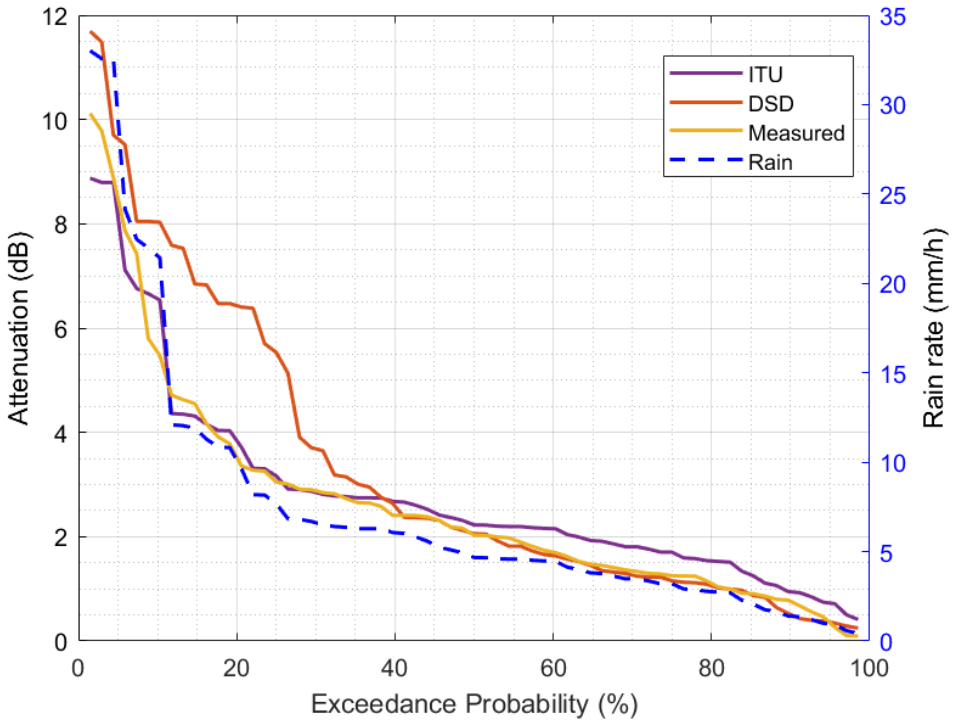

Figure 6.5: Rain attenuation and rainfall intensity exceedances measurements for 200 m link.

6.2.4 Raindrops Diameter Effect on Rain Attenuation

Figure. 6.6 depicts the correlation between raindrop diameter and detected attenuation, with a specific focus on the impact of the dominant number of drops on the overall attenuation, further investigating the effect of precipitation on the extended 200 m link. During light rainfall events, attenuation is particularly high for drops with diameters of 1.1-1.25 mm and 1.9-2.2 mm, especially when the drop count is no more than 10 drops. Even when there are reports of up to 45 drops with a diameter of 0.8 mm, the attenuation remains generally limited to 0.1 dB for this category of rainfall. For moderate rainfall, raindrop diameters of 2.7 mm, 3 mm, and 3.4 mm lead to the maximum attenuation values, with little influence from the number of drops. Furthermore, raindrops in the range of 0.1-2.6 mm and those above 3.5 mm contribute significantly to the overall attenuation. For heavy rainfall, raindrops with diameters of 2-2.2 mm and 3.4 mm contribute to a maximum attenuation of 10 dB. Smaller droplets of 0.1-0.2 mm and 0.4-0.5 mm provide much more attenuation at rainfall rates exceeding 20 mm/h. Interestingly, larger drops of 1.9 mm and 2.1-3.1 mm generate similar contributions. It is essential to emphasize that the investigation of the influence of raindrop diameter on measured attenuation excluded occurrences with a mixture of rain and snow, in order to focus exclusively on rain shape and its effect on attenuation. These analyses revealed that the number of droplets has no significant effect on the link losses due to rain in this particular link. Instead, the majority of raindrops with diameters ranging from 1.1 to 3.4 mm make a substantial contribution to attenuation. On average, raindrops with a diameter of 2 mm contribute considerably to the total attenuation, with a maximum value of 10.11 dB observed for rainfall intensity of 12 mm/h. Raindrops with diameters greater than 3.5 mm do not significantly contribute to attenuation in all rainfall events, with overall attenuation ranging from 0.09 to 2.9 dB.

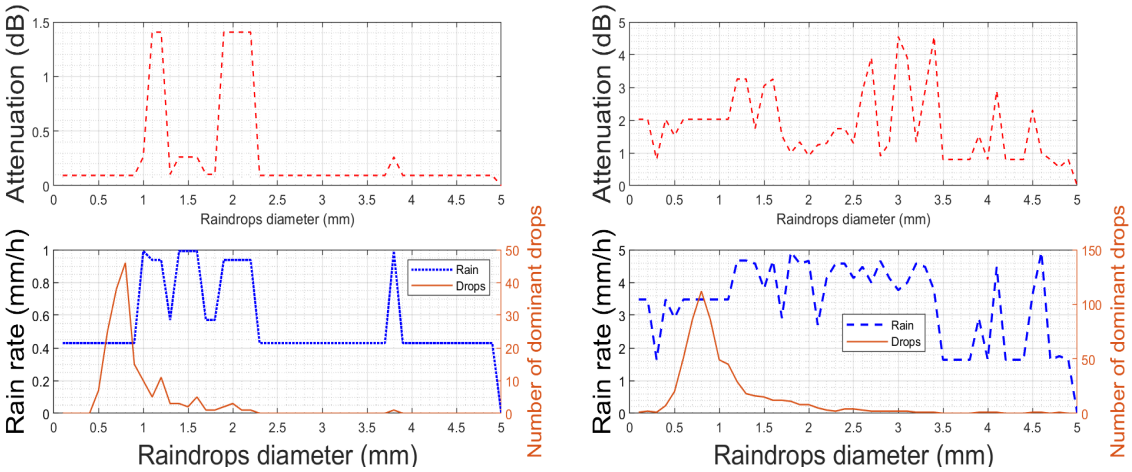

(a) *Light rainfall.*

(b) *Moderate rainfall.*

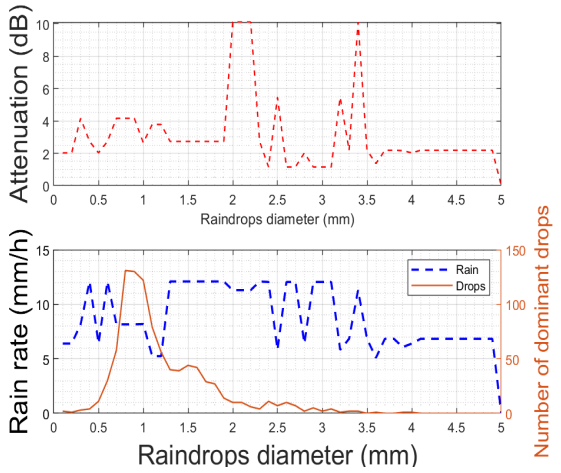

(c) *Heavy rainfall.*

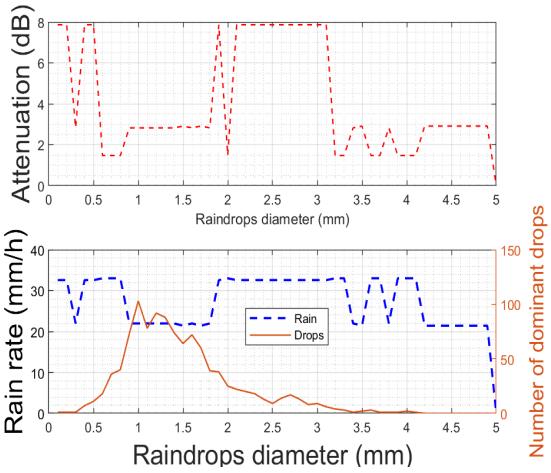

(d) *Very heavy rainfall.*

Figure 6.6: Measured rain attenuation versus raindrops diameter for light, moderate, heavy, and very heavy rainfalls mapped against the rain rate and the dominant drops for the 200 m link at 77.125 GHz.

6.3 Wet Antenna Effect

In the earlier sections, we initially assumed that the antenna wetness within this link might be relatively weak. To investigate the relationship between measured attenuation and wet antenna attenuation, we analyzed various peak rain rates and corresponding measured attenuation, as depicted in Figure 6.7. The majority of wet antenna losses fall within the range of 0.1-1.5 dB, with some exceptionally higher values reaching up to 8 dB when a mixture of snow and rain occurs.

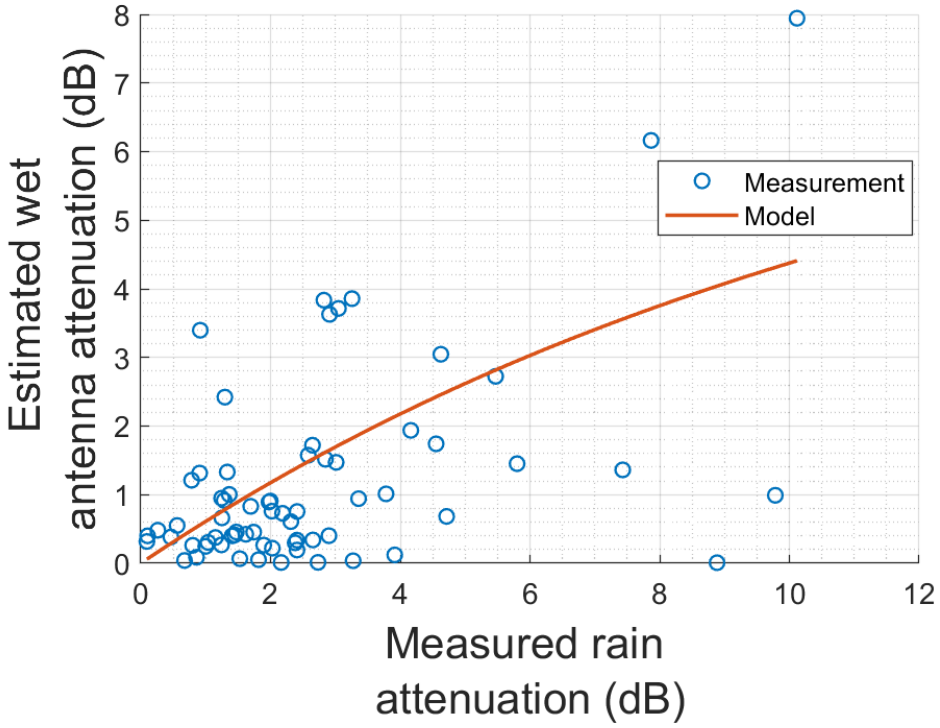

Figure 6.7: Relationship between measured rain attenuation and the estimated wet antenna attenuation of 200 m short range link.

Specifically, wet antennas account for 83% of the overall attenuation during light rainfall and 58% during moderate rainfall (Table. 6.2). However, with heavy rain, the contribution of antenna wetness to the overall attenuation is minimal. Similar to the 36 m link, snow significantly impacts the antennas and contributes to around 80% of the total attenuation. This finding clearly highlights that the contribution of wet antenna-induced attenuation to total channel fading during rain events is far from insignificant, and it should be taken into account in the design process. This is attributed to the fact that rain-induced attenuation is a linear function of the point-to-point path length.

Table 6.2: Percentage of the additional attenuation caused by the wet antennas of the total attenuation for 200 m link

	2 mm/	10 mm/h	20 mm/h	Snow
77.125 GHz 200 m link	83%	58%	14%	80%

During light rainfall events, the wet antenna effect is particularly pronounced, increasing exponentially by 1.5 dB during the first 10 minutes of rainfall and then gradually decreasing after 60 minutes when the rain event ends. However, during the transition from spring

to summer (June), the wet antenna effect shows a slight increase during the first 25 minutes of rainfall and then declines rapidly after the rainfall event concludes, taking only 9 minutes for the effect to subside.

6.4 Rainfall Velocity and Attenuation

Figure 6.8 illustrates the relationship between rainfall velocity and measured attenuation. The observed rain attenuation pattern follows the trend of rainfall speed. This observation takes into account rain intensity occurrences, as exemplified by a rain rate of 24.14 mm/h, which results in a rainfall velocity of 25 m/s, leading to an increased attenuation value of 3.68 dB. This value is relatively higher compared to the maximum reported attenuation value of 8.89 dB, which corresponds to a rainfall velocity of 33.01 m/s.

It should be noted that rainfall exhibits high variability in both space and time [153]. The received power and precipitation were recorded with a temporal resolution of one minute, and the temporal variability of rainfall is significantly higher throughout the measurement period, as previously observed in Chapter Three from weather data measurement. Additionally, the direction of rain area vibrations in relation to link space-temporal diversity orientation might be quite relevant. All these factors contribute to the variability of rainfall velocity and its impact on attenuation, as the long-term disdrometer measurement data indicate that short periods of heavier rain are intermixed with long duration of light rainfall. This variation in rainfall intensity and velocity further influences the measured attenuation values over time.

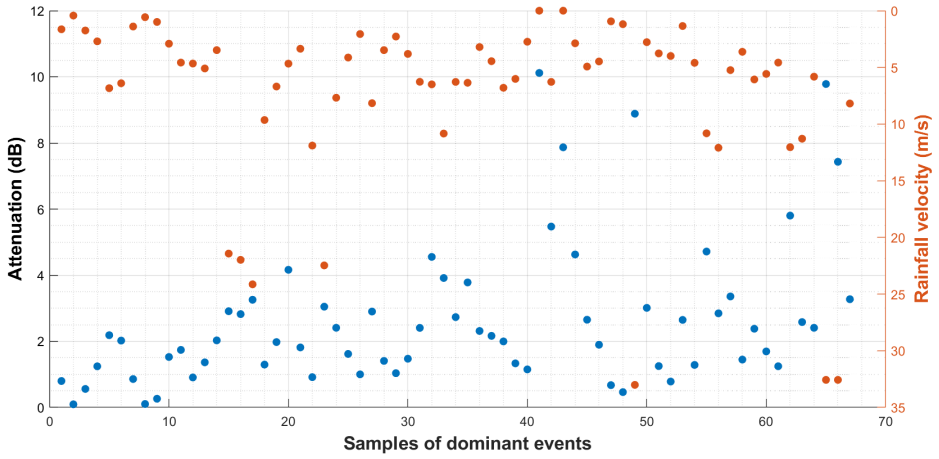

Figure 6.8: Measured rain attenuation versus measured rainfall velocity for 77.125 GHz at 200 m link.

6.5 Summary

The measurement data collected for the extended 200 m link provides valuable insights into rain attenuation levels, revealing that moderate rainfall events with rates below 10 mm/h generally have minimal impact on signal strength. Even in the case of relatively short and intense heavy rainfall occurrences lasting only a few minutes, the effect on the received power is found to be limited. However, in the presence of light and moderate rainfall events lasting more than half an hour, there is a significant lowering of the received power, although the signal quickly regains its strength after the rainfall subsides. Interestingly, rainfall events characterized by a combination of different particles such as raindrops, snow, and ice can lead to considerable attenuation levels of up to 9 dB.

The investigation of the path reduction factor, denoted by r, for this link, highlights the inadequacy of the commonly used restriction of 2.5. Instead, the optimal values of 3 to 3.5 have been employed to generate more accurate prediction attenuation values. The measured attenuation closely aligns with the expected values for lower attenuation levels below 3 dB, which account for approximately 60% of the total measured data. However, for higher attenuation levels in the range of 3-8.04 dB, the DSD model exhibits higher values compared to both the measured data and the ITU-R prediction. Employing the Root Mean Square Error (RMSE) technique, the ITU-R model is found to have a prediction accuracy of 9.66% greater than the DSD model.

The analysis of raindrop diameter reveals that drops with sizes ranging from 1.1 mm to 2.2 mm and those larger than 3.5 mm contribute the most to attenuation, with values reaching up to 10 dB. Interestingly, the number of droplets appears to have minimal impact on the losses induced by rain on the 200 m link. Additionally, it is worth noting that during light rainfall events, the wet antenna effect contributes to 83% of the overall attenuation observed, whereas in moderate rainfall events, it contributes to around 58% of the total attenuation. However, during heavy rainfall, the contribution of antenna wetness to overall attenuation becomes negligible. Similarly to the 36 m link, snowfall significantly affects the antennas, leading to them contributing to approximately 80% of the total attenuation during such events.

In summary, the findings from the extended 200 m link provide valuable information on rain attenuation and its various influencing factors. These results highlight the importance of considering the specific characteristics of each link and its environment when predicting attenuation values. The data also indicate that the wet antenna effect can significantly contribute to signal losses during rain events, underscoring the need to account for this factor in the design process. Overall, this chapter contributes to our understanding of rain attenuation in short fixed links and emphasizes the importance of accurate prediction models and measurement data in mitigating the impact of rain on wireless communication systems.

Chapter 7

Conclusions and Future Work

In conclusion, this research project has provided a comprehensive analysis of the impact of rain attenuation on short-range mmWave fixed links. Through the experimental setups operating at distinct frequency bands, we have explored the intricate relationship between rain intensity, frequency, link distance, and other factors affecting signal attenuation. Our findings underscore the complexity of this interplay and its implications for mmWave communication systems. In each case, we thoroughly examined the most dependable and well-measured data sets, ensuring the accuracy and reliability of the results. The empirical data from the fixed links were combined with realistic precipitation data acquired through the utilization of a highly precise weather station deployed during the measurements.

Before delving into the exploration of rain's impact on the measured received signal of the fixed links, we employed long-term weather data collected through the weather station only to calculate rain attenuation using prediction models. This approach enabled us to select suitable models for comparison with attenuation data from the setups. Over three years, disdrometer weather data formed the dataset, with a focus on 95% of data points, revealing rainfall rates consistently under 28 mm/h. Rainfall events were well-distributed across duration and cumulative rainfall. Most events had drop sizes of 0.125-2 mm, evident from DSD data. Utilizing weather data and prediction models only, the analyses highlighted variation between the ITU and DSD models for heavier events exceeding 20 mm/h. Raindrops of 1-4 mm brought the highest attenuation at 77.54 GHz, with intensity above 20 mm/h leading to substantial attenuation, reaching 15 dB/km and 28 dB/km

at 25.84 GHz and 77.54 GHz, respectively, for diameters under 2 mm. Attenuation increased steadily with rain intensity beyond 5 mm/h, observed in both 36 m and 200 m links. In general, prediction models varied in performance across frequency bands. The DSD model had lower RMSE in the *K* band than ITU-R. In the *E* band, ITU-R excelled in co-polarization, matching DSD closely. DSD's attenuation values differed from measured data uniformity. Rainfall minimally impacted 77.54 GHz co-polarization, except for attenuation $\leq 1dB$. However, 25.84 GHz saw higher attenuation with increased rainfall velocity, particularly cross-polarization.

Furthermore, in addition to the previously mentioned aspects, the following paragraphs encapsulate the key findings and emphasize the practical implications of this research project.

Rain intensity and frequency dependency: The initial inquiry that initiated this research project was focused on the performance of the fixed link at the designated frequency and the extent to which rain would impact them. The analyses showed that the signal strength decreases with increasing rain intensity. Even light and moderate rainfall can significantly reduce the signal power compared to very heavy rainfall. However, the measurement showed that the attenuation does not always strictly follow the trend of rain rate, indicating the presence of other factors influencing attenuation. The measurements indicated that higher frequencies experience higher attenuation due to rain. Rain-induced attenuation on 36-meter fixed links varies significantly with rain intensity and frequency bands. Distinct attenuation patterns emerge for different rainfall scenarios at both 25.84 GHz and 77.54 GHz, highlighting the need to account for these factors in mmWave system design. Rainfall with intensities ranging from 20 to 40 mm/h resulted in cross-polarization attenuation of over 2.40 dB at 25.84 GHz and co-polarization attenuation exceeding 1.90 dB at the same frequency. Conversely, light rainfall at 2 mm/h led to 0.26 dB attenuation for cross-polarization and 1.44 dB for co-polarization, both at 25.84 GHz. At 77.54 GHz, a maximum attenuation of 2.65 dB occurred at around 29 mm/h rainfall rate for co-polarization, and 4.72 dB for cross-polarization at rates under 5 mm/h. On the other hand, the side link (NLoS) measurements revealed distinctive attenuation patterns. Heavy rainfall (26 mm/h) led to higher observed values, reaching 4.39 dB at 25.84 GHz co-polarization and

7.13 dB for cross-polarization at 10 mm/h compared to LoS link. Similarly, at 77.54 GHz, very heavy rainfall (30 mm/h) yielded co-polarization and cross-polarization attenuation of 6.5 dB and 9.87 dB, respectively. Therefore, it is important to consider the impact of scattering due to raindrops for such types of links.

Rain-induced bistatic scattering: The bistatic scattering highlighted signal magnitudes at the second receiver. Raindrops below 0.5 mm minimally affected Bistatic Scattering Cross Sections (BSCS) over both frequencies. It increased beyond 1.5 mm during light rainfall. Heavy rainfall (20 - 40 mm/h) amplified BSCS significantly. For both frequencies, BSCS and intensity rose by 30% when transitioning from 25.84 GHz to 77.54 GHz. The study emphasized significant scattering effects from raindrops, particularly for sub-1.5 mm drops. At 25.84 GHz, interference peaked around 45 degrees for the 36 m path. In the E band, stronger interaction occurred at smaller angles due to wavelength differences. These need to be taken into account for NLoS link deployment in rainy regions.

Raindrop size effect and the insufficiency of rain intensity for prediction: The analyses using the DSD indicated that rain attenuation values can not be accurately estimated solely from rainfall rates. Various factors such as raindrop shape, distribution, dominant drop count, diameter, and velocity contribute to the overall attenuation. The analysis of raindrop sizes' impact on attenuation revealed distinct patterns: smaller droplets (0.1 - 0.7 mm) had a significant effect on attenuation at 25.84 GHz, whereas droplets up to 2 mm played a notable role in attenuation at 77.54 GHz, especially when particle speeds fall between 1 and 5 m/s. Larger raindrops contribute to the overall attenuation in a less regular manner when rainfall velocity and particle speed are between 5–10 m/s. Additionally, at an 82% exceedance probability, attenuation remained minimal, reaching 0.01 dB and 0.10 dB for 25.84 GHz and 77.54 GHz, respectively, during a 1 mm/h rainfall. Notably, even in February, the month with the highest attenuation, the maximum attenuation for 99.99% link availability did not surpass 3.5 dB at 77.54 GHz and 1.73 dB at 25.84 GHz.

Distance factor dependence: The distance factor, denoted as "r," is an important parameter in rain attenuation prediction models. As observed previously, for short links below 1 km, a maximum value of 2.5 is recommended. This research work measurements data over short-range fixed links suggested that employing recommendation ITU-R P.530-18

without the restricted distance factor proposed in P.530-17 yields attenuation values that align more closely with measured values taking into account the spatial homogeneity of precipitation and additional factors inducing supplementary attenuation. This includes effects from wet antennas and the system, which become more crucial as path length decreases and are essential in isolating the impact solely due to rain.

For the path lengths of 36 m and 200 m, it has been highlighted that the maximum value of the distance factor is found to be incompatible. Most rainfall events showed that using the restricted value of 2.5 led to underestimating measured attenuation, with variation based on rainfall type. Light and moderate rain exhibited more underestimation than heavy rain. For example, at 12 mm/h, the underestimation was 4.17 dB, compared to 0.45 dB at 21 mm/h. Underestimation for light rain (up to 5 mm/h) was 1.09 dB. Calculations indicated that the distance factor (r) rose sharply below 200 m, reaching 3-3.5. Rainfall's convective nature results in varying rain rates along the path due to drop count, wind, site diversity, and local environment. Accordingly, the analyses challenge the commonly used restriction of 2.5 and we suggested that the distance factor needs to be more than 2.5, suggesting accuracy-measured values of (3 - 3.3) for the 200 m link and (8.8 - 9.5) for the 36 m link, as emphasized in Chapters 5 and 6.

Wet antenna effect: The wet antenna phenomenon plays a significant role in signal degradation during rainy conditions. The analysis of antenna wetness demonstrated its significant impact on 77.54 GHz of all rainfall conditions. It is highly impacting the 25.84 GHz cross-polarization, particularly in light rainfall. It dominates light ($\approx 80\%$) and moderate ($\approx 58\%$) rainfall attenuation, diminishing during heavy rainfall. Snowfall substantially impacts antennas, contributing 80% of attenuation during such events. Consistent with the results, the main source of antenna wetness was identified as the combination of rain, snow, and ice buildup. Consequently, it is essential to treat snow-related attenuation separately and incorporate it into the link budget estimation.

Overall, the analysis highlights the complex interplay between rain intensity, frequency, link distance, and other factors in determining signal attenuation. It emphasizes the need for further investigation to optimize mmWave communication systems for varying weather conditions and refine prediction models for better accuracy. When predicting at-

tenuation levels, it is essential to consider the unique characteristics of each link and its surrounding environment.

Future research possibilities will involve:

- Studying the effect of other precipitation types like snow grains, snowflakes, hail, ice pellets, graupel, wind, and humidity on rain attenuation and scattering. A holistic approach to understanding how these factors interact could provide valuable insights for designing robust mmWave communication systems. One more area of development will be to explore how rain attenuation varies over very short time scales, such as seconds, within a rain event. Investigating rapid fluctuations in signal strength and their correlation with raindrop dynamics could lead to a better understanding of the temporal behaviour of rain attenuation.

- Investigating the rainfall spatial distribution and link heterogeneity, considering the effects of local geography and topography. This could lead to more accurate rain attenuation prediction models that account for the heterogeneity of rainfall within different link distances. The work could investigate the impact of increased temporal resolution rain rate measurements, using sub-minute data capture times to better analyze the peak intensities, correlation timescales, attenuation behaviour, and probability characteristics of heavy to torrential convective rain events.

- Develop real-time adaptive system control that can adjust transmission parameters based on current weather conditions and predicted rain attenuation. These systems could optimize link performance while ensuring efficient use of mmWave network resources.

Bibliography

[1] K. Aldubaikhy, W. Wu, N. Zhang, N. Cheng, and X. Shen, "mmWave IEEE 802.11ay for 5G Fixed Wireless Access," *IEEE Wireless Communications*, vol. 27, no. 2, pp. 88–95, 2020.

[2] "The Shape of a Raindrop." http://pmm.nasa.gov/education/articles/shape-of-a-raindrop.

[3] J. O. Laws and D. A. Parsons, "The relation of raindrop-size to intensity," *Eos, Transactions American Geophysical Union*, vol. 24, no. 2, pp. 452–460, 1943.

[4] S. Rangan, T. Rappaport, and E. Erkip, "Millimeter Wave Cellular Wireless Networks: Potentials and Challenges," *Proceedings of the IEEE*, vol. 102, 01 2014.

[5] *Multipath Fading*, ch. 9, pp. 320–347. John Wiley & Sons, Ltd, 2013. https://onlinelibrary.wiley.com/doi/abs/10.1002/9781118636336.ch9.

[6] *Rain Fading*, ch. 11, pp. 384–460. John Wiley & Sons, Ltd, 2013. https://onlinelibrary.wiley.com/doi/abs/10.1002/9781118636336.ch11.

[7] Utilities-One-Inc, "The Role of Copper in Communication Infrastructure," 2023. https://utilitiesone.com/the-role-of-copper-in-communication-infrastructure.

[8] Utilities-One-Inc, "The Future of Telecommunications Fiber Optic vs Copper Cables," 2023. https://utilitiesone.com/the-future-of-telecommunications-fiber-optic-vs-copper-cables.

[9] Electropages, "From Copper to Fibre: The UK's Telecom Network Evolution," 2023. https://www.electropages.com/blog/2023/09/copper-fibre-evolution-telecommunication-networks.

[10] M. Dano, "T-Mobile, Verizon disclose FWA usage stats," 2023. https://www.lightreading.com/fixed-wireless-access/

t-mobile-verizon-disclose-fwa-usage-stats.

[11] Fiercewireles, "Capacity, the key to successful FWA," 2023. https://www.fiercewireless.com/sponsored/capacity-key-successful-fwa.

[12] Ericsson, "5G FWA service provider adoption reaches 50 percent," 2023. https://www.ericsson.com/en/reports-and-papers/mobility-report/dataforecasts/fwa-outlook.

[13] E.-M. Oproiu, I. Gimiga, and I. Marghescu, "5G Fixed Wireless Access-Mobile Operator Perspective," in *2018 International Conference on Communications (COMM)*, pp. 357–360, 2018.

[14] C. Chen, O. Kedem, C. R. C. M. d. Silva, and C. Cordeiro, "Millimeter-Wave Fixed Wireless Access Using IEEE 802.11ay," *IEEE Communications Magazine*, vol. 57, no. 12, pp. 98–104, 2019.

[15] T. Schneider, A. Wiatrek, S. Preussler, M. Grigat, and R.-P. Braun, "Link Budget Analysis for Terahertz Fixed Wireless Links," *IEEE Transactions on Terahertz Science and Technology*, vol. 2, no. 2, pp. 250–256, 2012.

[16] T. Lok and T. Wong, "High capacity fixed wireless access systems with antenna arrays," in *2000 IEEE Wireless Communications and Networking Conference. Conference Record (Cat. No.00TH8540)*, vol. 1, pp. 415–419 vol.1, 2000.

[17] G. R. Maccartney, T. S. Rappaport, S. Sun, and S. Deng, "Indoor Office Wideband Millimeter-Wave Propagation Measurements and Channel Models at 28 and 73 GHz for Ultra-Dense 5G Wireless Networks," *IEEE Access*, vol. 3, pp. 2388–2424, 2015.

[18] S. Yong and C. Chia-Chin, "An Overview of Multi Giga bit Wireless through Millimeter Wave Technology: Potentials and Technical Challenges," *EURASIP Journal on Wireless Communications and Networking*, vol. 2007, 12 2006.

[19] A. Natarajan, A. Komijani, X. Guan, A. Babakhani, and A. Hajimiri, "A 77-GHz Phased-Array Transceiver With On-Chip Antennas in Silicon: Transmitter and Local LO-Path Phase Shifting," *IEEE Journal of Solid-State Circuits*, vol. 41, no. 12, pp. 2807–2819, 2006.

[20] ECMA, "High Rate 60 GHz PHY, MAC and HDMI PALs," 2010. https://www.ecma-international.org/publications/standards/Ecma-387.html.

[21] WirelessHD, "WiHD: 60 GHz WirelessHD Specification Version," 2010. `http://www.wirelesshd.org/about/specification-summary`.

[22] IEEE, "IEEE WPAN 802.15.3c millimeter-wave based alternative physical layer extension," 2009.

[23] A. Natarajan, A. Komijani, X. Guan, A. Babakhani, and A. Hajimiri, "A 77-GHz Phased-Array Transceiver With On-Chip Antennas in Silicon: Transmitter and Local LO-Path Phase Shifting," *IEEE Journal of Solid-State Circuits*, vol. 41, no. 12, pp. 2807–2819, 2006.

[24] Liebe, H.J. and Hufford, G.A. and Cotton, M.G., "Propagation modeling of moist air and suspended water/ice particles at frequencies below 1000 GHz," in *AGARD 52nd Specialists' Meeting of the Electromagnetic Wave Propagation Panel*, Advisory Group for Aerospace Research and Development, 1993.

[25] G. Raju, *Gaseous Absorption Bands in the Visible and IR Regions*, ch. 2. John Wiley Sons, 2017.

[26] F. T. Ulaby, R. K. Moore, and A. K. Fung, "Microwave Remote Sensing: Active and Passive Volume 1 - Microwave Remote Sensing Fundamentals and Radiometry," *Addison-Wesley Publishing Company*, pp. 456–466, 1981.

[27] L. Castanet, *Techniques adaptatives de lutte contre les affaiblissements de propagation pour les systèmes de télécommunications par satellite en EHF*. Doctoral dissertation, Ecole Nationale Supérieure de l'Aéronautique et de l'Espace, 2001.

[28] Van Kampen, N. and Tervonen, J. and Moraitis, G. and Filiol, E., "Analysis and modeling of tropospheric scintillation on low elevation links for modern dbs applications," *IEEE Transactions on Broadcasting*, vol. 50, no. 2, pp. 149–159, 2004.

[29] Y. Karasawa, Y. Matsudo, and F. Takahashi, "Effects of tropospheric fluctuations on millimeter-wave propagation," *IEICE Transactions on Communications*, vol. E90-B, no. 9, pp. 2473–2482, 2007.

[30] M. J. Willis, *Propagation of Radiowaves (3rd Edition)*, ch. Propagation in rain and clouds. London: The Institution of Engineering and Technology, 2012.

[31] M. Thurai, P. Gatlin, and V. Bringi, "Separating stratiform and convective rain types based on the drop size distribution characteristics using 2D video disdrometer data," *Atmospheric Research*, vol. 169, pp. 416–423, 2016.

[32] R. Gunn and G. D. Kinzer, "The terminal velocity of fall for water," *Journal of Meteorology*, p. 243–248, 1949.

[33] D. Atlas, R. C. Srivastava, and R. S. Sekhon, "Doppler radar characteristics of precipitation at vertical incidence," *Reviews of Geophysics*, vol. 11, no. 1, pp. 1–35, 1973.

[34] D. J. Segeistein, "The Complex Refractive Index of Water," master of science thesis, University of Missouri-Kansas City, Kansas City, Missouri, 1981.

[35] M. Marcus and B. Pattan, "Millimeter wave propagation: spectrum management implications," *IEEE Microwave Magazine*, vol. 6, no. 2, pp. 54–62, 2005.

[36] R. K. Crane, "Comparative evaluation of several rain attenuation prediction models," *Radio Science*, vol. 20, no. 4, pp. 843–863, 1985.

[37] D. de Wolf and L. Ligthart, "Multipath effects due to rain at 30-50 GHz frequency communication links," *IEEE Transactions on Antennas and Propagation*, vol. 41, no. 8, pp. 1132–1138, 1993.

[38] K. J. Jang, Y. Yoon, J. Kim, J. H. Kim, and G. Hwang, "Rain Attenuation Prediction Model for Terrestrial Links Using Gaussian Process Regression," *IEEE Communications Letters*, vol. 25, no. 11, pp. 3719–3723, 2021.

[39] C. Han and S. Duan, "Impact of Atmospheric Parameters on the Propagated Signal Power of Millimeter-Wave Bands Based on Real Measurement Data," *IEEE Access*, vol. 7, pp. 113626–113641, 2019.

[40] E. S. Hong, S. Lane, D. Murrell, N. Tarasenko, C. Christodoulou, and J. Keeley, "Estimating Rain Attenuation at 72 and 84 GHz From Raindrop Size Distribution Measurements in Albuquerque, NM, USA," *IEEE Geoscience and Remote Sensing Letters*, vol. 16, no. 8, pp. 1175–1179, 2019.

[41] I. Shayea, T. Abd. Rahman, M. Hadri Azmi, and M. R. Islam, "Real Measurement Study for Rain Rate and Rain Attenuation Conducted Over 26 GHz Microwave 5G Link System in Malaysia," *IEEE Access*, vol. 6, pp. 19044–19064, 2018.

[42] A. M. Al-Samman, M. Mohamed, Y. Ai, M. Cheffena, M. H. Azmi, and T. A. Rahman, "Rain Attenuation Measurements and Analysis at 73 GHz E-Band Link in Tropical Region," *IEEE Communications Letters*, vol. 24, no. 7, pp. 1368–1372, 2020.

[43] G. Hendrantoro, R. Bultitude, and D. Falconer, "Use of cell-site diversity in millimeter-wave fixed cellular systems to combat the effects of rain attenuation," *IEEE Journal on Selected Areas in Communications*, vol. 20, no. 3, pp. 602–614, 2002.

[44] F. D. Diba, M. A. Samad, and D.-Y. Choi, "The Effects of Rain on Terrestrial Links at K, Ka and E-Bands in South Korea: Based on Supervised Learning," *IEEE Access*, vol. 9, pp. 9345–9355, 2021.

[45] F. D. Diba, M. A. Samad, and D.-Y. Choi, "The Effects of Rain on Terrestrial Links at K, Ka and E-Bands in South Korea: Based on Supervised Learning," *IEEE Access*, vol. 9, pp. 9345–9355, 2021.

[46] F. D. Diba, M. A. Samad, and D.-Y. Choi, "The Effects of Rain on Terrestrial Links at K, Ka and E-Bands in South Korea: Based on Supervised Learning," *IEEE Access*, vol. 9, pp. 9345–9355, 2021.

[47] R. Olsen, D. Rogers, and D. Hodge, "The aRbrelation in the calculation of rain attenuation," *IEEE Transactions on Antennas and Propagation*, vol. 26, no. 2, pp. 318–329, 1978.

[48] T. S. Chu, "Rain-induced cross-polarization at centimeter and millimeter wavelengths," *The Bell System Technical Journal*, vol. 53, no. 8, pp. 1557–1579, 1974.

[49] International Telecommunication Union, "Characteristics of precipitation for propagation modelling," *ITU Radiocommunication Sector Recommendation*, no. ITU-R P.837-7, 2017.

[50] Q. Jing, D. Liu, and J. Tong, "Study on the Scattering Effect of Terahertz Waves in Near-Surface Atmosphere," *IEEE Access*, vol. 6, pp. 49007–49018, 2018.

[51] C. C. Chuang and K. V. Beard, "A Numerical Model for the Equilibrium Shape of Electrified Raindrops," *Journal of Atmospheric Sciences*, vol. 47, pp. 1374–1389, June 1990.

[52] T. Oguchi, "Scattering from hydrometeors: A survey," *Radio Science*, vol. 16, no. 5, pp. 691–730, 1981.

[53] T. Oguchi, "Electromagnetic wave propagation and scattering in rain and other hydrometeors," *Proceedings of the IEEE*, vol. 71, no. 9, pp. 1029–1078, 1983.

[54] R. Ekelund, P. Eriksson, and M. Kahnert, "Microwave single-scattering proper-

ties of non-spheroidal raindrops," *Atmospheric Measurement Techniques*, vol. 13, no. 12, pp. 6933–6944, 2020.

[55] A. Clément, "Coupling of Two Absorbing Boundary Conditions for 2D Time-Domain Simulations of Free Surface Gravity Waves," *Journal of Computational Physics*, vol. 126, no. 1, pp. 139–151, 1996.

[56] B. T. Draine and P. J. Flatau, "Discrete-Dipole Approximation For Scattering Calculations," *J. Opt. Soc. Am. A*, vol. 11, pp. 1491–1499, Apr 1994.

[57] K. V. Beard and C. Chuang, "A new model for the equilibrium shape of raindrops.," 1987.

[58] O. C. Acevedo, O. L. L. Moraes, R. da Silva, V. Anabor, D. P. Bittencourt, H. R. Zimmermann, R. O. Magnago, and G. A. Degrazia, "Surface-to-atmosphere exchange in a river valley environment," *Journal of Applied Meteorology and Climatology*, vol. 46, no. 8, pp. 1169 – 1181, 2007.

[59] H. T. van der Zanden, R. J. Watson, and M. H. A. J. Herben, "Rain-Induced Bistatic Scattering at 60 GHz," *Journal of Wireless Communications and Networking*, no. 053203, 2007.

[60] C. F. Bohren and D. R. Huffman, *Absorption and Scattering of Light by Small Particles*. John Wiley & Sons, 1983.

[61] H. Van de Hulst, *Light Scattering by Small Particles*. Dover Publications, 1957.

[62] C. Enjamio, E. Vilar, and F. Perez-Fontan, "Rain Scatter Interference in mm-Wave Broadband Fixed Wireless Access Networks Caused by a 2-D Dynamic Rain Environment," *IEEE Transactions on Wireless Communications*, vol. 6, no. 7, pp. 2497–2507, 2007.

[63] C. Capsoni, L. Luini, and M. D'Amico, "The MultiEXCELL model for the prediction of the radio interference due to hydrometeor scattering," in *Proceedings of the Fourth European Conference on Antennas and Propagation*, pp. 1–5, 2010.

[64] A. M. Al-Samman, M. Mohamed, Y. Ai, M. Cheffena, M. H. Azmi, and T. A. Rahman, "Rain Attenuation Measurements and Analysis at 73 GHz E-Band Link in Tropical Region," *IEEE Communications Letters*, vol. 24, no. 7, pp. 1368–1372, 2020.

[65] L. Luini, G. Roveda, M. Zaffaroni, M. Costa, and C. G. Riva, "The Impact of

Rain on Short *E* -Band Radio Links for 5G Mobile Systems: Experimental Results and Prediction Models," *IEEE Transactions on Antennas and Propagation*, vol. 68, no. 4, pp. 3124–3134, 2020.

[66] F. Norouzian, E. Marchetti, M. Gashinova, E. Hoare, C. Constantinou, P. Gardner, and M. Cherniakov, "Rain Attenuation at Millimeter Wave and Low-THz Frequencies," *IEEE Transactions on Antennas and Propagation*, vol. 68, no. 1, pp. 421–431, 2020.

[67] C. Han and S. Duan, "Impact of Atmospheric Parameters on the Propagated Signal Power of Millimeter-Wave Bands Based on Real Measurement Data," *IEEE Access*, vol. 7, pp. 113626–113641, 2019.

[68] S. Shrestha and D.-Y. Choi, "Rain attenuation statistics over millimeter wave bands in South Korea," *Journal of Atmospheric and Solar-Terrestrial Physics*, vol. 152-153, pp. 1–10, 2017.

[69] E. Hong, S. Lane, D. Murrell, N. Tarasenko, and C. Christodoulou, "Terrestrial link rain attenuation measurements at 84 GHz," in *2017 United States National Committee of URSI National Radio Science Meeting (USNC-URSI NRSM)*, pp. 1–2, 2017.

[70] K. Vaclav and G. Martin, "Rain Attenuation at 58 GHz: Prediction versus Long-Term Trial Results," *EURASIP Journal on Wireless Communications and Networking*, vol. 2007, 12 2007.

[71] E. S. Hong, S. Lane, D. Murrell, N. Tarasenko, C. Christodoulou, and J. Keeley, "Estimating Rain Attenuation at 72 and 84 GHz From Raindrop Size Distribution Measurements in Albuquerque, NM, USA," *IEEE Geoscience and Remote Sensing Letters*, vol. 16, no. 8, pp. 1175–1179, 2019.

[72] J. Hansryd, Y. Li, J. Chen, and P. Ligander, "Long term path attenuation measurement of the 71–76 GHz band in a 70/80 GHz microwave link," in *Proceedings of the Fourth European Conference on Antennas and Propagation*, pp. 1–4, 2010.

[73] J. Hansryd, Y. Li, J. Chen, and P. Ligander, "Long term path attenuation measurement of the 71–76 GHz band in a 70/80 GHz microwave link," in *Proceedings of the Fourth European Conference on Antennas and Propagation*, pp. 1–4, 2010.

[74] I. Shayea, T. Abd. Rahman, M. Hadri Azmi, and M. R. Islam, "Real measurement

study for rain rate and rain attenuation conducted over 26 ghz microwave 5g link system in malaysia," *IEEE Access*, vol. 6, pp. 19044–19064, 2018.

[75] M. Fencl, P. Valtr, M. Kvičera, and V. Bareš, "Quantifying Wet Antenna Attenuation in 38-GHz Commercial Microwave Links of Cellular Backhaul," *IEEE Geoscience and Remote Sensing Letters*, vol. 16, no. 4, pp. 514–518, 2019.

[76] P. Valtr, M. Fencl, and V. Bareš, "Excess Attenuation Caused by Antenna Wetting of Terrestrial Microwave Links at 32 GHz," *IEEE Antennas and Wireless Propagation Letters*, vol. 18, no. 8, pp. 1636–1640, 2019.

[77] C. Han and S. Duan, "Impact of Atmospheric Parameters on the Propagated Signal Power of Millimeter-Wave Bands Based on Real Measurement Data," *IEEE Access*, vol. 7, pp. 113626–113641, 2019.

[78] W. Åsen and C. J. Gibbins, "A comparison of rain attenuation and drop size distributions measured in Chilbolton and Singapore," *Radio Science*, vol. 37, no. 3, pp. 1–15, 2002.

[79] T. Halder, A. Adhikari, and A. Maitra, "Rain attenuation studies from radiometric and rain DSD measurements at two tropical locations," *Journal of Atmospheric and Solar-Terrestrial Physics*, vol. 170, 05 2018.

[80] S. Das, A. Maitra, and A. Shukla, "Rain attenuation modeling in the 10-100 GHz frequency using drop size distributions for different climatic zones in tropical India," *Progress In Electromagnetics Research B*, vol. 25, pp. 211–224, 01 2010.

[81] B. Bianchi, P. J. Van Leeuwen, R. Hogan, and A. Berne, "A Variational Approach to Retrieve Rain Rate by Combining Information from Rain Gauges, Radars, and Microwave Links," *Journal of Hydrometeorology*, vol. 14, pp. 1897–1909, 12 2013.

[82] P. Valtr, M. Fencl, V. Bareš, and P. Pechač, "Comparison of measured and theoretically predicted rain attenuation at 32 GHz and 38 GHz," in *12th European Conference on Antennas and Propagation (EuCAP 2018)*, pp. 1–3, 2018.

[83] S. Salous, "COST IC1004 white paper on channel measurements and modeling for 5G networks in the frequency bands above 6 GHz," *Euro-Cost: Durham, UK*, 2016.

[84] S. Salous, S. M. Feeney, X. Raimundo, and A. A. Cheema, "Wideband MIMO Channel Sounder for Radio Measurements in the 60 GHz Band," *IEEE Transac-*

tions on Wireless Communications, vol. 15, no. 4, pp. 2825–2832, 2016.

[85] X. Raimundo, S. Salous, and A. Cheema, "Indoor dual polarised radio channel characterization in the 54 GHz and 70 GHz bands," *IET microwaves, antennas & propagation.*, vol. 12, pp. 1287–1292, July 2018.

[86] O. Zahid and S. Salous, "Long-Term Rain Attenuation Measurement for Short-Range mmWave Fixed Link Using DSD and ITU-R Prediction Models," *Radio Science*, vol. 57, no. 4, p. e2021RS007307, 2022.

[87] B. Arbesser-Rastburg, A. Martellucci, O. Fiser, D. Vanhoenacker-Janvier, E. Salonen, C. Riva, T. Tjelta, P. Baptista, F. Perez Fontan, M. Döttling, S. Saunders, M. Vasquez-Castro, A. Formella, I. Frigyes, M. Pettinger, M. Schnell, L. Castanet, M. Filip, D. Mertens, and J. Habetha, *COST Action 255 Final Report: Radiowave Propagation for SatCom Services at Ku-Band and Above*. 03 2002.

[88] C. Ngongondo, C.-Y. Xu, L. Gottschalk, and B. Alemaw, "Evaluation of spatial and temporal characteristics of rainfall in Malawi: A case of data scarce region," *Theoretical and Applied Climatology*, vol. 106, pp. 79–93, 11 2011.

[89] O. Fiser, *The Role of DSD and Radio Wave Scattering in Rain Attenuation*. 02 2010.

[90] "The relation of raindrop-size to intensity," *Eos, Transactions American Geophysical Union*, vol. 24, no. 2, pp. 452–460, 1943.

[91] M. J. S. and P. W. McK., "The distribution of raindrop with size," *Eos, Transactions American Geophysical Union*, vol. 5, pp. 165–166, 1948.

[92] W. Åsen and C. J. Gibbins, "A comparison of rain attenuation and drop size distributions measured in Chilbolton and Singapore," *Radio Science*, vol. 37, no. 3, pp. 6–1–6–15, 2002.

[93] I. G. Doelling, J. Joss, and J. Riedl, "Systematic variations of Z–R-relationships from drop size distributions measured in northern Germany during seven years," *Atmospheric Research*, vol. 47, pp. 635–649, 1998.

[94] J. Joss and E. Gori, "Shapes of Raindrop Size Distributions," *Journal of Applied Meteorology*, vol. 17, pp. 1054–1061, 06 1978.

[95] D. Atlas, Ulbrich, and Carlton, "Path- and Area-Integrated Rainfall Measurement by Microwave Attenuation in the 1–3 cm Band," *Journal of Applied Meteorology*,

vol. 16, 01 1978.

[96] D. Atlas, R. Srivastava, and R. Sekhon, "Doppler Radar Characteristics of Precipitation at Vertical Incidence," *Rev. Geophys. Space Phys.*, vol. 11, pp. 1–35, 02 1973.

[97] M. A. Samad and D.-Y. Choi, "Learning-Assisted Rain Attenuation Prediction Models," *Applied Sciences*, 08 2020.

[98] J. Wu, L. Chen, Z. Zheng, M. Lyu, and Z. Wu, "Clustering Web services to facilitate service discovery," *Knowledge and Information Systems*, vol. 38, 01 2014.

[99] M. A. Samad, F. D. Diba, and D.-Y. Choi, "A Survey of Rain Attenuation Prediction Models for Terrestrial Links: Current Research Challenges and State-of-the-Art," *Sensors*, vol. 21, 02 2021.

[100] F. J. A. Andrade, A. M. de Medeiros, and L. A. R. da Silva Mello, "Short-Term Rain Attenuation Predictor for Terrestrial Links in Tropical Area," *IEEE Antennas and Wireless Propagation Letters*, vol. 16, pp. 1325–1328, 2017.

[101] Garcia-Lopez, J. Casares-Giner, and V., "Modified Lin's empirical formula for calculating rain attenuation on a terrestrial path," *Electron. Lett*, vol. 17, pp. 34–36, 1981.

[102] S. N. Livieratos and P. G. Cottis, "Rain Attenuation Along Terrestrial Millimeter Wave Links: A New Prediction Method Based on Supervised Machine Learning," *IEEE Access*, vol. 7, pp. 138745–138756, 2019.

[103] R. K. Crane, "A two-component rain model for the prediction of attenuation statistics," *Radio Science*, vol. 17, no. 6, pp. 1371–1387, 1982.

[104] J. Chebil, M. R. Islam, A.-H. Zyoud, M. H. Habaebi, and H. Dao, "Rain fade slope model for terrestrial microwave links," *International Journal of Microwave and Wireless Technologies*, vol. 12, no. 5, p. 372–379, 2020.

[105] R. Crane, "Prediction of Attenuation by Rain," *Communications, IEEE Transactions on*, vol. 28, pp. 1717–1733, 09 1980.

[106] A. D. Pinto-Mangones, J. M. Torres-Tovio, N. A. Pérez-García, L. A. R. da Silva Mello, A. F. Ruiz-Garcés, and J. León-Acurio, "Improved ITU Model for Rainfall Attenuation Prediction of in Terrestrial Links," in *Advances in Emerging Trends and Technologies* (M. Botto-Tobar, J. León-Acurio, A. Díaz Cadena, and

P. Montiel Díaz, eds.), (Cham), pp. 531–541, Springer International Publishing, 2020.

[107] R. Singh and R. Acharya, "Development of a New Global Model for Estimating One-Minute Rainfall Rate," *IEEE Transactions on Geoscience and Remote Sensing*, vol. 56, no. 11, pp. 6462–6468, 2018.

[108] R. Ghiani, L. Luini, and A. Fanti, "A physically based rain attenuation model for terrestrial links," *Radio Science*, vol. 52, no. 8, pp. 972–980, 2017.

[109] L. A. R. d. S. Mello and M. S. Pontes, "Improved unified method for the prediction of rain attenuation in terrestrial and earth space links," pp. 569–573, 2009.

[110] C. Capsoni, F. Fedi, and A. Paraboni, "A comprehensive meteorologically oriented methodology for the prediction of wave propagation parameters in telecommunication applications beyond 10 GHz," *Radio Science*, vol. 22, no. 3, pp. 387–393, 1987.

[111] F. Moupfouma, "Improvement of a rain attenuation prediction method for terrestrial microwave links," *IEEE Transactions on Antennas and Propagation*, vol. 32, no. 12, pp. 1368–1372, 1984.

[112] A. Y. Abdulrahman, T. A. Rahman, I. M. Rafiqul, B. J. Olufeagba, T. A. Abdulrahman, J. Akanni, and S. A. Y. Amuda, "Investigation of the Unified Rain Attenuation Prediction Method With Data From Tropical Climates," *IEEE Antennas and Wireless Propagation Letters*, vol. 13, pp. 1108–1111, 2014.

[113] A. A. H. Budalal, M. R. Islam, K. Abdullah, and T. Abdul Rahman, "Modification of Distance Factor in Rain Attenuation Prediction for Short-Range Millimeter-Wave Links," *IEEE Antennas and Wireless Propagation Letters*, vol. 19, no. 6, pp. 1027–1031, 2020.

[114] L. da Silva Mello and M. Pontes, "Improved Unified Method for the Prediction of Rain Attenuation in Terrestrial and Earth Space Links," pp. 569–573, 11 2009.

[115] P. Kántor, J. Bitó, and Drozdy, "Characteristics of 5G wireless millimeter wave propagation: Transformation of rain attenuation applying different prediction models," in *2016 10th European Conference on Antennas and Propagation (EuCAP)*, pp. 1–5, 2016.

[116] D. Cermak, O. Fiser, Z. Nemec, and V. Schejbal, "Study of electromagnetic scat-

tering by rain drops," 01 2004.

[117] G. Mcfarquhar and R. List, "The Effect of Curve Fits for the Disdrometer Calibration on Raindrop Spectra, Rainfall Rate, and Radar Reflectivity," *Journal of Applied Meteorology - J APPL METEOROL*, vol. 32, pp. 774–782, 04 1993.

[118] B. Sheppard and P. Joe, "Comparison of Raindrop Size Distribution Measurements by a Joss-Waldvogel Disdrometer, a PMS 2DG Spectrometer, and a POSS Doppler Radar," *Journal of Atmospheric and Oceanic Technology - J ATMOS OCEAN TECHNOL*, vol. 11, pp. 874–887, 08 1994.

[119] C. Williams, V. Bringi, L. Carey, V. Chandrasekar, P. Gatlin, Z. Haddad, R. Meneghini, s. Munchak, S. Nesbitt, W. Petersen, S. Tanelli, A. Tokay, A. Wilson, and D. Wolff, "Describing the Shape of Raindrop Size Distributions Using Uncorrelated Raindrop Mass Spectrum Parameters," *Journal of Applied Meteorology and Climatology*, vol. 53, pp. 1282–1296, 02 2014.

[120] M. Thurai, P. Gatlin, V. Bringi, W. Petersen, P. Kennedy, B. Notaros, and L. Carey, "Towards Completing the Rain Drop Size Spectrum: Case Studies Involving 2D-Video Disdrometer, Droplet Spectrometer, and Polarimetric Radar Measurements," *Journal of Applied Meteorology and Climatology*, vol. 56, 12 2016.

[121] Darley, Olufunke and Yussuff, Abayomi I.O. and Adenowo, Adetokunbo A., "Investigation into Rain Attenuation Prediction Models at Locations in Lagos Using Remote Sensing," *Journal Name*, vol. 6, no. 2, 2021.

[122] M. A. Samad, F. D. Diba, and D.-Y. Choi, "A Survey of Rain Attenuation Prediction Models for Terrestrial Links—Current Research Challenges and State-of-the-Art," *Sensors*, vol. 21, no. 4, 2021.

[123] P. Valtr and P. Pechač, "On Distance Factor in Rain Attenuation Predictions," in *2019 13th European Conference on Antennas and Propagation (EuCAP)*, pp. 1–3, 2019.

[124] A. A. H. Budalal, M. R. Islam, K. Abdullah, and T. Abdul Rahman, "Modification of Distance Factor in Rain Attenuation Prediction for Short-Range Millimeter-Wave Links," *IEEE Antennas and Wireless Propagation Letters*, vol. 19, no. 6, pp. 1027–1031, 2020.

[125] ITU-R, "Propagation data and prediction methods required for the design of ter-

restrial line-of-sight systems P Series radio wave propagation, Recommendation ITU-R P.530-17," recommendation, ITU, Geneva, Switzerland, 2017.

[126] M. Islam and A. Tharek, "Propagation study of microwave signals based on rain attenuation data at 26 GHz and 38 GHz measured in Malaysia," in *1999 Asia Pacific Microwave Conference. APMC'99. Microwaves Enter the 21st Century. Conference Proceedings (Cat. No.99TH8473)*, vol. 3, pp. 602–605 vol.3, 1999.

[127] A. A. H. Budalal, M. R. Islam, K. Abdullah, and T. Abdul Rahman, "Modification of Distance Factor in Rain Attenuation Prediction for Short-Range Millimeter-Wave Links," *IEEE Antennas and Wireless Propagation Letters*, vol. 19, no. 6, pp. 1027–1031, 2020.

[128] R. Crane and D. Rogers, "Comments on "Effect of wet antenna attenuation on propagation data statistics"," *IEEE Transactions on Antennas and Propagation*, vol. 50, no. 9, pp. 1331–1332, 2002.

[129] M. Schleiss, J. Rieckermann, and A. Berne, "Quantification and Modeling of Wet-Antenna Attenuation for Commercial Microwave Links," *IEEE Geoscience and Remote Sensing Letters*, vol. 10, no. 5, pp. 1195–1199, 2013.

[130] C. Moroder, U. Siart, C. Chwala, and H. Kunstmann, "Modeling of Wet Antenna Attenuation for Precipitation Estimation From Microwave Links," *IEEE Geoscience and Remote Sensing Letters*, vol. 17, no. 3, pp. 386–390, 2020.

[131] A. Pinto-Mangones, J. M. Torres Tovio, N. Perez García, L. da Silva Mello, A. Ruiz-Garcés, and J. León-Acurio, *Improved ITU Model for Rainfall Attenuation Prediction of in Terrestrial Links*, pp. 531–541. 01 2020.

[132] M. Kharadly and R. Ross, "Effect of wet antenna attenuation on propagation data statistics," *IEEE Transactions on Antennas and Propagation*, vol. 49, no. 8, pp. 1183–1191, 2001.

[133] S. abdul rahim, Y. Abdulrahman, T. Abd Rahman, and M. Islam, "Measurement of Wet Antenna Losses on 26 GHz Terrestrial Microwave Link in Malaysia," *Wireless Personal Communications*, vol. 64, pp. 225–231, 05 2010.

[134] M. Fencl, P. Valtr, M. Kvičera, and V. Bareš, "Quantifying Wet Antenna Attenuation in 38-GHz Commercial Microwave Links of Cellular Backhaul," *IEEE Geoscience and Remote Sensing Letters*, vol. 16, no. 4, pp. 514–518, 2019.

[135] Ericsson, "Microwave Towards 2020, Delivering High Capacity and Cost-Efficient Backhaul for Broadband Networks Today and in the Future," 2014.

[136] S. Okamura, "Electromagnetic wave propagation in rain and polarization," *IEEE Transactions on Antennas and Propagation*, vol. 58, no. 3, pp. 866–875, 2010.

[137] C. Han, "Characteristics of Rain-Induced Attenuation over Signal Paths," *Remote Sensing*, vol. 13, no. 11, p. 2156, 2021.

[138] J. Huang, Y. Cao, X. Raimundo, A. Cheema, and S. Salous, "Rain Statistics Investigation and Rain Attenuation Modeling for Millimeter Wave Short-Range Fixed Links," *IEEE Access*, vol. 7, pp. 156110–156120, 2019.

[139] M. Islam, J. Chebil, and A. Tharek, "Frequency scaling of rain attenuation from 23- to 38-GHz microwave signals measured in Malaysia," in *1999 Asia Pacific Microwave Conference. APMC'99. Microwaves Enter the 21st Century. Conference Proceedings (Cat. No.99TH8473)*, vol. 3, pp. 793–796 vol.3, 1999.

[140] M. A. Samad and D.-Y. Choi, "Scaling of Rain Attenuation Models: A Survey," *Applied Sciences*, vol. 11, no. 18, 2021.

[141] R. Acharya, "A simple real-time frequency scaling technique for rain attenuation and its performance," *International Journal of Satellite Communications and Networking*, vol. 38, no. 4, pp. 329–340, 2020.

[142] ITU-WRC, "Final Acts of the World Radiocommunication Conference (WRC-19)," recommendation, International Telecommunication Union (ITU), Sharm El-Sheikh, 2019.

[143] D. Kim and M. Zarri, "Fixed Wireless Access: economic potential and best practices," tech-report, GSMA, 2018.

[144] Y. Amarasinghe, W. Zhang, R. zhang, D. Mittleman, and J. Ma, "Scattering of Terahertz Waves By Snow," *Journal of infrared, millimeter and terahertz waves*, vol. 41, 02 2020.

[145] D. Zou and Z. Xu, "Information Security Risks Outside the Laser Beam in Terrestrial Free-Space Optical Communication," *IEEE Photonics Journal*, vol. 8, no. 5, pp. 1–9, 2016.

[146] H. Xiao, Y. Zuo, J. Wu, Y. Li, and J. Lin, "Non-line-of-sight ultraviolet single-scatter propagation model in random turbulent medium," *Optics letters*, vol. 38,

pp. 3366–9, 09 2013.

[147] D. Zou and Z. Xu, "Information Security Risks Outside the Laser Beam in Terrestrial Free-Space Optical Communication," *IEEE Photonics Journal*, vol. PP, pp. 1–1, 09 2016.

[148] H. Juttula, J. Kokkoniemi, J. Lehtomaki, A. Makynen, and M. Juntti, "Rain Induced Co-Channel Interference at 60 GHz and 300 GHz Frequencies," in *2019 IEEE International Conference on Communications Workshops (ICC Workshops)*, pp. 1–5, 2019.

[149] B. Joyce, "An investigation of the effects of different wavelengths of visible light on visual selective attention behavior in hyperactive and non-hyperactive children," 12 2021.

[150] O. Ajewole and T. Oguchi, "Effects of multiple scattering on communication at millimetre and centimetre wavelengths in tropical rainfall conditions," *Electronics Letters*, vol. 37, pp. 121 – 123, 02 2001.

[151] T. Oguchi, "Effects of incoherent scattering on microwave and millimetre wave communications through rain," *Electronics Letters*, vol. 27, pp. 759 – 761, 05 1991.

[152] C. Gloaguen and J. Lavergnat, "94 GHz bistatic scattering in rain," *IEEE Transactions on Antennas and Propagation*, vol. 44, no. 9, pp. 1247–1258, 1996.

[153] A. K. Fotiadi, D. A. Metaxas, and A. Bartzokas, "A statistical study of precipitation in northwest Greece," *International Journal of Climatology*, vol. 19, no. 11, pp. 1221–1232, 1999.

Appendix A

Matlab Codes

A.1 Direct link processing code

```
1
2  %% Direct Link
3  clear
4  clc
5  fs = 80e6; % sampling rate
6  f=50; % generator frequency
7  Tsweep =1/(2*f); %sweep time
8  SegSize=fs*Tsweep; % Segment size
9  N=1;
10 time=zeros(N,6);
11
12
13 for k=1:N
14     clc
15     k
16     Address = strcat('C:\Users\qfqt66\Fixed ...
           Link\ADC_Card1\S1_MO_',num2str(k),'.rd16');
17     fid=fopen(Address);
18     rawdata = fread(fid,'uint16');
19     fclose(fid);
```

```
20      ch1data= rawdata(1: 2:length(rawdata)); ch2data= ...
            rawdata(2:2:length(rawdata));
21      %clear rawdata
22      Nsweep=fix(length(ch1data)/(SegSize));
23      Data1 = importdata(strcat(Address,'.srdc'));
24      result = regexp(Data1{15,1}, regexstr, 'names');
25      Vpp = str2num(result.numbers);
26      ch1data = (-Vpp/2) + ((ch1data/65536)*Vpp);
27      ch2data = (-Vpp/2) + ((ch2data/65536)*Vpp);
28      chrx1=reshape(ch1data,SegSize,Nsweep); ...
            chrx2=reshape(ch2data,SegSize,Nsweep);
29      win = repmat(hamming(size(chrx1,1)),1,size(chrx1,2));
30      dataFreqrx1= fftshift(ifft(chrx1.*win)); dataFreqrx2= ...
            fftshift(ifft(chrx2.*win));
31      clear win chrx1 chrx2
32      lm=length(dataFreqrx1);
33      dataFreqrx1(1:lm/2,:)=[]; dataFreqrx2(1:lm/2,:)=[];
34      [kj,kk]=size(dataFreqrx1);
35      ch1ir=reshape(dataFreqrx1,kj,2,kk/2); ...
            ch2ir=reshape(dataFreqrx2,kj,2,kk/2);
36      tx1ch1=squeeze(ch1ir(:,1,:)); tx2ch1=squeeze(ch1ir(:,2,:));
37      tx1ch2=squeeze(ch2ir(:,1,:)); tx2ch2=squeeze(ch2ir(:,2,:));
38      rx11(:,k)=20*log10(mean(abs(tx1ch1),2)); ...
            rx21(:,k)=20*log10(mean(abs(tx2ch1),2));
39      rx12(:,k)=20*log10(mean(abs(tx1ch2),2)); ...
            rx22(:,k)=20*log10(mean(abs(tx2ch2),2));
40    sig11(:,k)=rx11([4001 1.2e4+1],k); sig21(:,k)=rx21([4e4+1 ...
        12e4+1],k);% Received signal
41      sig12(:,k)=rx12([4e4+1 12e4+1],k); sig22(:,k)=rx22([4e4+1 ...
            12e4+1],k);
42        FileInfo = dir(Address);
43      time(k,:) = datevec(FileInfo.datenum);
44      [fYear, fMonth, fDay, fHour, fMinute, ...
            fSecond]=datevec(FileInfo.datenum);
45  end
```

A.2 Side link processing code

```
1
2  %% Side Link S2
3  clear
4  %close all
5  clc
6  fs = 80e6;
7  f=50;
8  Tsweep =1/(2*f);
9  SegSize=fs*Tsweep;
10 N=1;
11 time=zeros(N,6);
12
13 for k=1:N
14     %clc
15     k
16     Address = strcat('I:\AutoRec\Fixed ...
           Link\202010-51310\ADC_Card2\S2_MO_',num2str(k),'.rd16');
17     fid=fopen(Address);
18     rawdata = fread(fid,'uint16');
19     fclose(fid);
20     ch1data= rawdata; %ch2data= rawdata(2:2:length(rawdata));
21     Nsweep=fix(length(ch1data)/(SegSize));
22     Data1 = importdata(strcat(Address,'.srdc'));
23     result = regexp(Data1{15,1}, regexstr, 'names');
24     Vpp = str2num(result.numbers);
25     ch1data = (-Vpp/2) + ((ch1data/65536)*Vpp);
26     chrx1=reshape(ch1data,SegSize,Nsweep); ...
           %chrx2=reshape(ch2data,SegSize,Nsweep);
27     win = repmat(hamming(size(chrx1,1)),1,size(chrx1,2));
28     dataFreqrx1= fftshift(ifft(chrx1.*win)); %dataFreqrx2= ...
           fftshift(ifft(chrx2.*win));
29     clear win chrx1 chrx2
30     lm=length(dataFreqrx1);
31     dataFreqrx1(1:lm/2,:)=[]; %dataFreqrx2(1:lm/2,:)=[];
```

```
    rx11(:,k)=20*log10(mean(abs(dataFreqrx1(:,1:2:end)),2)); ...
        rx21(:,k)=20*log10(mean(abs(dataFreqrx1(:,2:2:end)),2));
    sig11(:,k)=rx11([4e4+1 12e4+1],k); % HV
    sig21(:,k)=rx21([4e4+1 12e4+1],k); % VV
    FileInfo = dir(Address);
    time(k,:) = datevec(FileInfo.datenum);
    [fYear, fMonth, fDay, fHour, fMinute, ...
        fSecond]=datevec(FileInfo.datenum);
end
```

A.3 Filtronic link processing code

```
%% Filtronic: CH2  ===>> S2
fs = 80e6;
f=50;
Tsweep =1/(2*f);
SegSize=fs*Tsweep;
time=zeros(N,6);

for k=1:N
    clc
    k
    Address = strcat('I:\AutoRec\Raw ...
        Data\2021-5-16-0-40\ADC_Card2\S2_MO_',num2str(k),'.rd16');
    fid=fopen(Address);
    rawdata = fread(fid,'uint16');
    fclose(fid);
    ch1data= rawdata(1: 2:length(rawdata)); ch2data= ...
        rawdata(2:2:length(rawdata));
    %clear rawdata
    Nsweep=fix(length(ch1data)/(SegSize));
    Data1 = importdata(strcat(Address,'.srdc'));
    result = regexp(Data1{15,1}, regexstr, 'names');
    Vpp = str2num(result.numbers);
    ch1data = (-Vpp/2) + ((ch1data/4000)*Vpp);
```

```
22      ch2data = (-Vpp/2) + ((ch2data/770)*Vpp);
23      chrx1=reshape(ch1data,SegSize,Nsweep); ...
            chrx2=reshape(ch2data,SegSize,Nsweep);
24      win = repmat(hamming(size(chrx1,1)),1,size(chrx1,2));
25      dataFreqrx1= fftshift(ifft(chrx1.*win)); dataFreqrx2= ...
            fftshift(ifft(chrx2.*win));
26      clear win chrx1 chrx2
27      lm=length(dataFreqrx1);
28      dataFreqrx1(1:lm/2,:)=[]; dataFreqrx2(1:lm/2,:)=[];
29      [kj,kk]=size(dataFreqrx1);
30      ch1ir=reshape(dataFreqrx1,kj,2,kk/2); ...
            ch2ir=reshape(dataFreqrx2,kj,2,kk/2);
31      tx1ch1=squeeze(ch1ir(:,1,:)); tx2ch1=squeeze(ch1ir(:,2,:));
32      tx1ch2=squeeze(ch2ir(:,1,:)); tx2ch2=squeeze(ch2ir(:,2,:));
33      rx11(:,k)=20*log10(mean(abs(tx1ch1),2)); ...
            rx21(:,k)=20*log10(mean(abs(tx2ch1),2));% Side Link
34      rx12(:,k)=20*log10(mean(abs(tx1ch2),2)); % Filtronic
35      %rx22(:,k)=20*log10(mean(abs(tx2ch2),2));
36    sig11(:,k)=rx11([4e4+1 12e4+1],k); sig21(:,k)=rx21([4e4+1 ...
          12e4+1],k);
37    FB(:,k)=rx12(300000:350000,k); sig12(:,k)=max(FB(:,k));
38      %sig22(:,k)=rx22([4e4+1 12e4+1],k);
39        FileInfo = dir(Address);
40      time(k,:) = datevec(FileInfo.datenum);
41      [fYear, fMonth, fDay, fHour, fMinute, ...
            fSecond]=datevec(FileInfo.datenum);
42  end
```

A.4 Weather data processing code

```
1  clear
2  clc
3   TIMESTAMP_ =[];   % rawCellColumns(:, 1);
4  PWS100_PWCode_METAR_=[];   %rawCellColumns(:, 2); ...
       PWS100_PWCode_NWS_=[];   %rawCellColumns(:, 3);
```

```
PWS100_FaultStatus_EN_=[];  %rawCellColumns(:, 4);
PWS100_PowerStatus_=[];  %rawCellColumns(:, 5);\hfill \break.
 PWS100_AverageVisibility10min_=[];  ...
    %cell2mat(rawNumericColumns(:, 8));
PWS100_PWCode_WMO_=[];
 PWS100_AverageTemperature_=[];  %cell2mat(rawNumericColumns(:, ...
    10));
 PWS100_AverageRH_=[];  %cell2mat(rawNumericColumns(:, 11));
 PWS100_MinimumTemperature_=[];  %cell2mat(rawNumericColumns(:, ...
    12));
 PWS100_MaximumTemperature_=[];  %cell2mat(rawNumericColumns(:, ...
    13));
 PWS100_PrecipitationIntensity_=[];  ...
    %cell2mat(rawNumericColumns(:, 14));
PWS100_PrecipitationAccumulation_=[];  ...
   %cell2mat(rawNumericColumns(:, 15));
 PWS100_AverageVelocity_=[];  %cell2mat(rawNumericColumns(:, 16));
 PWS100_AverageSize_=[];  %cell2mat(rawNumericColumns(:, 17));
PWS100_PartType_Drizzle_=[];  %cell2mat(rawNumericColumns(:, 18));
PWS100_PartType_FreezingDrizzle_=[];  ...
   %cell2mat(rawNumericColumns(:, 19));
 PWS100_PartType_Rain_=[].............;
PWS100_FaultStatus_=[];  %cell2mat(rawNumericColumns(:, 35));
    or k=1:300
eval(['PWS100_Data_DropSizeDistribution',num2str(k),'_=[];']);
    end
fold_weather = 'G:\syst\System_File\WS\WS_ESR_Durham\Fixed ...
   link\weather data\PWS100_Data_';
dirs=dir(strcat(fold_weather,'\CR1000_PWS100_Data_2010.dat'));

dircell=struct2cell(dirs)';
filenames=dircell(:,1);
loop=size(filenames);
for kk = 1:loop(1,1)
    kk
delimiter = ',';
startRow = 5;
```

```
34 %% Read columns of data as strings:
35 % For more information, see the TEXTSCAN documentation.
36 %% Open the text file.
37 fileID = fopen(strcat(fold_weather,'\',filenames{kk}),'r');
38 %% Read columns of data according to format string.
39 % This call is based on the structure of the file used to ...
       generate this
40 % code. If an error occurs for a different file, try ...
       regenerating the code
41 % from the Import Tool.
42 dataArray = textscan(fileID, formatSpec, 'Delimiter', delimiter, ...
       'HeaderLines' ,startRow-1, 'ReturnOnError', false);
43 %% Close the text file.
44 fclose(fileID);
45 %% Convert the contents of columns containing numeric strings to ...
       numbers.
46 % Replace non-numeric strings with NaN.
47 raw = repmat({''},length(dataArray{1}),length(dataArray)-1);
48 for col=1:length(dataArray)-1
49     raw(1:length(dataArray{col}),col) = dataArray{col};
50 end
51 numericData = NaN(size(dataArray{1},1),size(dataArray,2));
52 for col=[2,3,4,5,....,340]
53     % Converts strings in the input cell array to numbers. ...
           Replaced non-numeric
54     % strings with NaN.
55     rawData = dataArray{col};
56     for row=1:size(rawData, 1);
57         % Create a regular expression to detect and remove ...
               non-numeric prefixes and
58         % suffixes.
59             result = regexp(rawData{row}, regexstr, 'names');
60             numbers = result.numbers;
61             % Detected commas in non-thousand locations.
62             invalidThousandsSeparator = false;
63             if any(numbers==',');
64                 thousandsRegExp = '^\d+?(\,\d{3})*\.{0,1}\d*$';
```

```
65                  if isempty(regexp(thousandsRegExp, ',', 'once'));
66                      numbers = NaN;
67                      invalidThousandsSeparator = true;
68                  end
69              end
70              % Convert numeric strings to numbers.
71              if ¬invalidThousandsSeparator;
72                  numbers = textscan(strrep(numbers, ',', ''), '%f');
73                  numericData(row, col) = numbers{1};
74                  raw{row, col} = numbers{1};
75              end
76          catch me
77          end
78      end
79  end
80  %% Split data into numeric and cell columns.
81  rawNumericColumns = raw(:, [2,3,4,5.....,340]);
82  rawCellColumns = raw(:, [1,11,12,39,40]);
83  %% Replace non-numeric cells with NaN
84  R = cellfun(@(x) ¬isnumeric(x) && ¬...
        islogical(x),rawNumericColumns); % Find non-numeric cells
85  rawNumericColumns(R) = {NaN}; % Replace non-numeric cells
86  numMeas = length(rawCellColumns(:, 1));
87   %% Concatinate the DATA
88  for ixx=1:1
89      TIMESTAMP_ =[TIMESTAMP_; rawCellColumns(:, 1)];
90      PWS100_PWCode_METAR_=[ PWS100_PWCode_METAR_ ...
            ;rawCellColumns(:, 2)];
91      PWS100_PWCode_NWS_=[ PWS100_PWCode_NWS_ ;rawCellColumns(:, 3)];
92      PWS100_FaultStatus_EN_=[ PWS100_FaultStatus_EN_ ...
            ;rawCellColumns(:, 4)];
93      PWS100_PowerStatus_=[ PWS100_PowerStatus_ ;rawCellColumns(:, ...
            5)];
94      PWS100_AverageVisibility10min_=[PWS100_AverageVisibility10min_ ...
             ;cell2mat(rawNumericColumns(:, 8))];
95      PWS100_PWCode_WMO_=[PWS100_PWCode_WMO_  ...
            ;cell2mat(rawNumericColumns(:, 9))];
```

```
96      PWS100_AverageTemperature_=[PWS100_AverageTemperature_  ...
            ;cell2mat(rawNumericColumns(:, 10))];
97      PWS100_AverageRH_=[PWS100_AverageRH_  ...
            ;cell2mat(rawNumericColumns(:, 11))];
98      PWS100_MinimumTemperature_=[PWS100_MinimumTemperature_  ...
            ;cell2mat(rawNumericColumns(:, 12))];
99      PWS100_MaximumTemperature_=[PWS100_MaximumTemperature_  ...
            ;cell2mat(rawNumericColumns(:, 13))];
100     PWS100_PrecipitationIntensity_=[PWS100_PrecipitationIntensity_ ...
             ;cell2mat(rawNumericColumns(:, 14))];
101     PWS100_PrecipitationAccumulation_=[ ...
            PWS100_PrecipitationAccumulation_ ...
            ;cell2mat(rawNumericColumns(:, 15))];
102     PWS100_AverageVelocity_=[ PWS100_AverageVelocity_ ...
            ;cell2mat(rawNumericColumns(:, 16))];
103     PWS100_AverageSize_=[ PWS100_AverageSize_ ...
            ;cell2mat(rawNumericColumns(:, 17))];
104     PWS100_PartType_Drizzle_=[PWS100_PartType_Drizzle_  ...
            ;cell2mat(rawNumericColumns(:, 18))];
105     PWS100_PartType_FreezingDrizzle_=[PWS100_PartType_FreezingDrizzle_ ...
             ;cell2mat(rawNumericColumns(:, 19))];
106     PWS100_PartType_Rain_=[ PWS100_PartType_Rain_ ...
            ;cell2mat(rawNumericColumns(:, 20))];
107     PWS100_PartType_FreezingRain_=[ ...
            PWS100_PartType_FreezingRain_ ...
            ;cell2mat(rawNumericColumns(:, 21))];
108     PWS100_PartType_SnowGrains_=[ PWS100_PartType_SnowGrains_ ...
            ;cell2mat(rawNumericColumns(:, 22))];
109     PWS100_PartType_SnowFlakes_=[PWS100_PartType_SnowFlakes_  ...
            ;cell2mat(rawNumericColumns(:, 23))];
110     PWS100_PartType_IcePellets_=[ PWS100_PartType_IcePellets_ ...
            ;cell2mat(rawNumericColumns(:, 24))];
111     PWS100_PartType_Hail_=[ PWS100_PartType_Hail_ ...
            ;cell2mat(rawNumericColumns(:, 25))];
112     PWS100_PartType_Graupel_=[PWS100_PartType_Graupel_  ...
            ;cell2mat(rawNumericColumns(:, 26))];
```

```
113     PWS100_PartType_Error_=[PWS100_PartType_Error_  ...
            ;cell2mat(rawNumericColumns(:, 27))];
114     PWS100_PartType_Unknown_=[PWS100_PartType_Unknown_  ...
            ;cell2mat(rawNumericColumns(:, 28))];
115     PWS100_VISAlarm1_=[PWS100_VISAlarm1_  ...
            ;cell2mat(rawNumericColumns(:, 29))];
116     PWS100_VISAlarm2_=[PWS100_VISAlarm2_  ...
            ;cell2mat(rawNumericColumns(:, 30))];
117     PWS100_VISAlarm3_=[ PWS100_VISAlarm3_ ...
            ;cell2mat(rawNumericColumns(:, 31))];
118     PWS100_CleanLaserWindow_=[PWS100_CleanLaserWindow_  ...
            ;cell2mat(rawNumericColumns(:, 32))];
119     PWS100_CleanUpperWindow_=[ PWS100_CleanUpperWindow_ ...
            ;cell2mat(rawNumericColumns(:, 33))];
120     PWS100_CleanLowerWindow_=[PWS100_CleanLowerWindow_  ...
            ;cell2mat(rawNumericColumns(:, 34))];
121     PWS100_FaultStatus_=[ PWS100_FaultStatus_ ...
            ;cell2mat(rawNumericColumns(:, 35))];
122 for ii=1:300
123 eval(['PWS100_Data_DropSizeDistribution',num2str(ii),
124 '_=[PWS100_Data_DropSizeDistribution',num2str(ii),
125 '_;cell2mat(rawNumericColumns(:,',num2str(ii+35),'))];']);
126     end
127 end
128 end %% This is the for loop into all the files in the ...
        WeatherStation Data
129 %% Create output variable
130 CR_PWS_Data = table;  % Use this command to turn it inot
131     CR_PWS_Data.TIMESTAMP_ =TIMESTAMP_;   %  ...
            CR_PWS_Data.PWS100rawCellColumns(:, 1)];
132     CR_PWS_Data.PWS100_PWCode_METAR_= PWS100_PWCode_METAR_ ;   % ...
             rawCellColumns(:, 2)];   %
133     CR_PWS_Data.PWS100_PWCode_NWS_= PWS100_PWCode_NWS_ ;   %  ...
            rawCellColumns(:, 3)];   %
134     CR_PWS_Data.PWS100_FaultStatus_EN_= PWS100_FaultStatus_EN_ ; ...
             %  rawCellColumns(:, 4)];   %
```

```
135     CR_PWS_Data.PWS100_PowerStatus_= PWS100_PowerStatus_ ;   % ...
            rawCellColumns(:, 5)];   %
136
137     CR_PWS_Data.PWS100_PWCode_WMO_=PWS100_PWCode_WMO_  ;   % ...
            cell2mat(rawNumericColumns(:, 9))];   %
138     CR_PWS_Data.PWS100_AverageTemperature_=PWS100_
139     AverageTemperature_  ;   % cell2mat(rawNumericColumns(:, ...
            10))];   %
140     CR_PWS_Data.PWS100_AverageRH_=PWS100_AverageRH_  ;   % ...
            cell2mat(rawNumericColumns(:, 11))];   %
141     CR_PWS_Data.PWS100_MinimumTemperature_=PWS100_
142     MinimumTemperature_  ;   % cell2mat(rawNumericColumns(:, ...
            12))];   %
143 CR_PWS_Data.PWS100_MaximumTemperature_=PWS100_MaximumTemperature_ ...
        ;   % cell2mat(rawNumericColumns(:, 13))];
144
145 CR_PWS_Data.PWS100_PrecipitationIntensity_=PWS100_
146 PrecipitationIntensity_ ; %
147
148 cell2mat(rawNumericColumns(:, 14))];   %
149 CR_PWS_Data.PWS100_PrecipitationAccumulation_= ...
        PWS100_PrecipitationAccumulation_ ;   %
150
151 cell2mat(rawNumericColumns(:, 15))];   %
152 CR_PWS_Data.PWS100_AverageVelocity_= PWS100_AverageVelocity_ ;   %
153
154 cell2mat(rawNumericColumns(:, 16))];   %
155 CR_PWS_Data.PWS100_AverageSize_= PWS100_AverageSize_ ;   % ...
        cell2mat(rawNumericColumns(:, 17))];   %
156 CR_PWS_Data.PWS100_PartType_Drizzle_=PWS100_PartType_Drizzle_  ; ...
          % cell2mat(rawNumericColumns(:, 18))];  %
157
158 CR_PWS_Data.PWS100_PartType_FreezingDrizzle_=PWS100_
159 PartType_FreezingDrizzle_ ; %
160 cell2mat(rawNumericColumns(:, 19))];   %
161 CR_PWS_Data.PWS100_PartType_Rain_= PWS100_PartType_Rain_ ;   % ...
        cell2mat(rawNumericColumns(:, 20))];   %
```

```
162 CR_PWS_Data.PWS100_PartType_FreezingRain_= ...
      PWS100_PartType_FreezingRain_ ;   %  ...
      cell2mat(rawNumericColumns(:, 21))];   %
163 CR_PWS_Data.PWS100_PartType_SnowGrains_= ...
      PWS100_PartType_SnowGrains_ ;   %  ...
      cell2mat(rawNumericColumns(:, 22))];   %
164 CR_PWS_Data.PWS100_PartType_SnowFlakes_=PWS100_PartType_SnowFlakes_ ...
       ;   %  cell2mat(rawNumericColumns(:, 23))];   %
165 CR_PWS_Data.PWS100_PartType_IcePellets_= ...
      PWS100_PartType_IcePellets_ ;   %  ...
      cell2mat(rawNumericColumns(:, 24))];   %
166 CR_PWS_Data.PWS100_PartType_Hail_= PWS100_PartType_Hail_ ;   %  ...
      cell2mat(rawNumericColumns(:, 25))];   %
167 CR_PWS_Data.PWS100_PartType_Graupel_=PWS100_PartType_Graupel_  ; ...
       %  cell2mat(rawNumericColumns(:, 26))];   %
168 CR_PWS_Data.PWS100_PartType_Error_=PWS100_PartType_Error_  ;   % ...
      cell2mat(rawNumericColumns(:, 27))];   %
169 CR_PWS_Data.PWS100_PartType_Unknown_=PWS100_PartType_Unknown_  ; ...
       %  cell2mat(rawNumericColumns(:, 28))];   %   ...
      CR_PWS_Data.PWS100_VISAlarm1_=PWS100_VISAlarm1_  ;   %  ...
      cell2mat(rawNumericColumns(:, 29))];   %
170     CR_PWS_Data.PWS100_VISAlarm2_=PWS100_VISAlarm2_  ;   %  ...
         cell2mat(rawNumericColumns(:, 30))];   %
171     CR_PWS_Data.PWS100_VISAlarm3_= PWS100_VISAlarm3_ ;   %  ...
         cell2mat(rawNumericColumns(:, 31))];   %
172     CR_PWS_Data.PWS100_CleanLaserWindow_=PWS100_CleanLaserWindow_ ...
          ;   %  cell2mat(rawNumericColumns(:, 32))];   %
173     CR_PWS_Data.PWS100_CleanUpperWindow_= ...
         PWS100_CleanUpperWindow_ ;   %  ...
         cell2mat(rawNumericColumns(:, 33))];   %
174     CR_PWS_Data.PWS100_CleanLowerWindow_=PWS100_CleanLowerWindow_ ...
          ;   %  cell2mat(rawNumericColumns(:, 34))];   %
175 CR_PWS_Data.PWS100_FaultStatus_= PWS100_FaultStatus_ ; %  ...
      cell2mat(rawNumericColumns(:, 35))];   %
176 for jj=1:300
177 eval(['CR_PWS_Data.PWS100_Data_DropSizeDistribution',num2str(jj),
178
```

```
179 '_=PWS100_Data_DropSizeDistribution',num2str(jj),'_;']);
180     end
181 save(strcat('G:\syst\System_File\weather data_2020\10_20.mat'));
```

Appendix B

Data acquisition and RF heads programming

B.1 PLL programming

```
1  CheckBox: AutosetRegister9Box.Checked = True
2  CheckBox: RefDoublerBox.Checked = False
3  CheckBox: RefD2Box.Checked = False
4  CheckBox: ADCClockAutosetBox.Checked = True
5  CheckBox: BleedAutosetBox.Checked = True
6  CheckBox: RepeatSweepBox.Checked = False
7  CheckBox: SweepCustomWriteSequenceBox.Checked = False
8  CheckBox: SweepDontAddSpacingBox.Checked = False
9  CheckBox: SweepPowerOffsetCCheckBox.Checked = False
10 CheckBox: SweepPowerOffsetBCheckBox.Checked = False
11 CheckBox: SweepPowerOffsetACheckBox.Checked = True
12 CheckBox: SimulateGPIBBox.Checked = False
13 CheckBox: TCMOGPIBCopyToRFSettingsBox.Checked = True
14 CheckBox: TCMOGPIBWriteToEEPROMBox.Checked = True
15 RadioButton: ADF4355_2Ux.Checked = False
16 RadioButton: ADF5355U2.Checked = False
17 RadioButton: ADF5355U1.Checked = False
18 RadioButton: ADF4355_1Ux.Checked = False
19 RadioButton: ADF4355_2U4.Checked = False
```

```
20 RadioButton: ADF4155.Checked = False
21 RadioButton: ADF4355_1U4.Checked = False
22 RadioButton: ADF4355_3.Checked = False
23 RadioButton: ADF4401.Checked = False
24 RadioButton: ADF5356.Checked = False
25 RadioButton: ADF4356.Checked = False
26 RadioButton: ADF5355U4.Checked = True
27 RadioButton: ADF4355.Checked = False
28 RadioButton: USBselector.Checked = False
29 RadioButton: SDPSelector.Checked = True
30 RadioButton: ADF4401HisideInjectionBox.Checked = False
31 RadioButton: ADF4401LosideInjectionBox.Checked = True
32 ComboBox: GPIO7ADF4401Box.SelectedIndex = 0
33 NumericUpDown: ADF4401ExternalLOFrequencyBox.Value = 6000
34 NumericUpDown: ADF4401ExternalPFDFrequencyBox.Value = 500
35 ComboBox: VCOHoldBox.SelectedIndex = 0
36 NumericUpDown: VCOBandDivBox.Value = 34
37 NumericUpDown: SynthLockTimeoutBox.Value = 12
38 NumericUpDown: TimeoutBox.Value = 134
39 NumericUpDown: ALCTimeoutBox.Value = 30
40 RadioButton: AutomaticRadio.Checked = True
41 RadioButton: ManualRadio.Checked = False
42 ComboBox: UseOtherxHzBox.SelectedIndex = 4
43 NumericUpDown: StepSizeOtherBox.Value = 80.000000
44 NumericUpDown: MOD2Box.Value = 16383
45 NumericUpDown: FRAC2Box.Value = 3277
46 NumericUpDown: RFoutBox.Value = 6461.000000
47 TextBox: ActualVCOoutputBox.Text = 6461.000000000116422427688
48 NumericUpDown: VCOFreqBox.Value = 6461.000000
49 TextBox: VCOOutputFrequencyErrorBox.Text = 0.000116422428
50 NumericUpDown: FRAC1Box.Value = 12792627
51 TextBox: PFDBox.Text = 80
52 NumericUpDown: INTBox.Value = 80
53 ComboBox: OutputDividerBox.SelectedIndex = 0
54 NumericUpDown: VCOFreqx2Box.Value = 12922.000000
55 NumericUpDown: RefFreqBox.Value = 80.000000
56 NumericUpDown: RcounterBox.Value = 1
```

```
57 ComboBox: ADCEnableBox.SelectedIndex = 1
58 ComboBox: ADCConversionBox.SelectedIndex = 1
59 NumericUpDown: ADCClockBox.Value = 200
60 ComboBox: CounterResetBox.SelectedIndex = 0
61 ComboBox: MuxLevelBox.SelectedIndex = 1
62 ComboBox: CP3StateBox.SelectedIndex = 0
63 ComboBox: REFinModeBox.SelectedIndex = 0
64 ComboBox: PowerdownBox.SelectedIndex = 0
65 ComboBox: ChargePumpCurrentBox.SelectedIndex = 9
66 ComboBox: PDPolarityBox.SelectedIndex = 1
67 ComboBox: DoubleBuffBox.SelectedIndex = 0
68 ComboBox: MuxoutBox.SelectedIndex = 6
69 NumericUpDown: BleedCurrentBox.Value = 40
70 ComboBox: GatedBleedBox.SelectedIndex = 0
71 ComboBox: NegativeBleedOnOffBox.SelectedIndex = 1
72 ComboBox: FeedbackSelectBox.SelectedIndex = 1
73 ComboBox: RFoutAPowerBox.SelectedIndex = 3
74 ComboBox: RFoutBPowerBox.SelectedIndex = 0
75 ComboBox: RFoutBEnableBox.SelectedIndex = 0
76 ComboBox: RFoutAEnableBox.SelectedIndex = 1
77 ComboBox: RFoutBSelectBox.SelectedIndex = 0
78 ComboBox: MTLDBox.SelectedIndex = 0
79 ComboBox: AutocalBox.SelectedIndex = 0
80 ComboBox: PrescalerBox.SelectedIndex = 0
81 ComboBox: FracNLDPrecisionBox.SelectedIndex = 0
82 ComboBox: LESELPolarityBox.SelectedIndex = 0
83 ComboBox: LESyncBox.SelectedIndex = 1
84 ComboBox: LDModeBox.SelectedIndex = 0
85 ComboBox: LOLModeBox.SelectedIndex = 0
86 ComboBox: LDCyclesBox.SelectedIndex = 0
87 NumericUpDown: PhaseResyncTimerBox.Value = 1
88 ComboBox: SDLoadResetBox.SelectedIndex = 0
89 ComboBox: PhaseAdjustBox.SelectedIndex = 0
90 ComboBox: PhaseResyncBox.SelectedIndex = 0
91 NumericUpDown: PhaseValueBox.Value = 0
92 TextBox: ValuesToWriteBox.Text =
93 TextBox: HopCurrent.Text =
```

```
94 TextBox: HopDelayBox.Text = 100
95 TextBox: HopFBBox.Text = 4100
96 TextBox: HopFABox.Text = 4000
97 RadioButton: KeysightButton.Checked = False
98 RadioButton: RSButtonBox.Checked = True
99 NumericUpDown: CarrierOffsetBox.Value = 0
100 NumericUpDown: SweepPowerOffsetCBox.Value = 75
101 NumericUpDown: SweepPowerOffsetBBox.Value = 50
102 NumericUpDown: SweepPowerOffsetABox.Value = 25
103 NumericUpDown: BleedSweepValueBox.Value = 0
104 TextBox: BleedSweepOffsetDBox.Text = 100
105 TextBox: BleedSweepOffsetCBox.Text = 50
106 TextBox: BleedSweepOffsetBBox.Text = 10
107 TextBox: BleedSweepOffsetABox.Text = 1
108 TextBox: GPIBIDNBox.Text =
109 TextBox: SweepCurrent.Text =
110 ComboBox: GPIBaddressBox.SelectedIndex = 19
111 TextBox: SweepDelayBox.Text = 100
112 TextBox: SweepSpacingBox.Text = 1
113 TextBox: SweepStopBox.Text = 6010
114 TextBox: SweepStartBox.Text = 6000
115 ComboBox: VCOAutocalBox.SelectedIndex = 1
116 ComboBox: VCOLDOPowerdownBox.SelectedIndex = 1
117 ComboBox: VtuneCalSetBox.SelectedIndex = 1
118 ComboBox: ExtVCOSelBox.SelectedIndex = 0
119 ComboBox: BandSelectClockModeBox.SelectedIndex = 0
120 ComboBox: ChargeCancellationBox.SelectedIndex = 0
121 ComboBox: VCOPowerdownBox.SelectedIndex = 0
122 ComboBox: DivisionModeBox.SelectedIndex = 1
123 ComboBox: PowerdownSDBox.SelectedIndex = 0
124 ComboBox: Dither2ndStageBox.SelectedIndex = 1
125 ComboBox: VCOVTuneCalBox.SelectedIndex = 4
126 ComboBox: VCOBiasCodeBox.SelectedIndex = 3
127 ComboBox: VCOSelectBox.SelectedIndex = 1
128 NumericUpDown: VCOBandSelectBox.Value = 0
129 ComboBox: PDSynthBox.SelectedIndex = 0
130 NumericUpDown: ActualREFinReadBox.Value = 0
```

```
131 TextBox: TCMORefFreqBox.Text = 80.000000
132 RadioButton: TCMOGPIBRadio.Checked = False
133 ComboBox: TCMOGPIBaddressBox.SelectedIndex = 19
134 RadioButton: TCMOManualRadio.Checked = True
135 NumericUpDown: ActualRFoutBox.Value = 6000.000000
136 NumericUpDown: ActualREFinWriteBox.Value = 124.911461
137 ComboBox: VCOReadbackBox.SelectedIndex = 0
138 ComboBox: VCOReadbackBiasBox.SelectedIndex = -1
139 ComboBox: ReadbackVCOBox.SelectedIndex = -1
140 ComboBox: ReadSelBox.SelectedIndex = 0
141 TextBox: ReadbackRegReadyBox.Text = 0
142 TextBox: ReadbackVCOBandBox.Text = 0
143 TextBox: ReadbackStringBox.Text = 0
144 TextBox: ReadbackVersionBox.Text = 0
145 ComboBox: PLLTestmodesBox.SelectedIndex = 0
146 ComboBox: SDTestmodesBox.SelectedIndex = 0
147 ComboBox: R10DB3129Box.SelectedIndex = 0
148 TextBox: DirectWriteBox.Text =
149 ComboBox: ADF5355U4Dither2Box.SelectedIndex = 0
150 ComboBox: ADF5355U4Dither1Box.SelectedIndex = 0
151 ComboBox: DitherScaleBox.SelectedIndex = 0
152 ComboBox: PulsedBleedDelayBox.SelectedIndex = 0
153 ComboBox: PulsedBleedBox.SelectedIndex = 0
154 NumericUpDown: ClockDividerValueBox.Value = 2
155 ComboBox: CLKDivModeBox.SelectedIndex = 0
156 ComboBox: ABPBox.SelectedIndex = 1
157 ComboBox: CSRBox.SelectedIndex = 0
158 ComboBox: ALCBox.SelectedIndex = 0
159 NumericUpDown: CalibrationSweepStartBox.Value = 4000
160 TextBox: CalibrationSweepEndBox.Text = 4050
161 NumericUpDown: CalibrationSweepStepSizeBox.Value = 1000
162 NumericUpDown: CalibrationSweepStepsBox.Value = 50
163 NumericUpDown: BypassDelayBeforeR0Box.Value = 0
```

B.2 C code for automatic data recording

The C code below was developed to automate data collection by a PhD fellow and member of our communication centre group Mohammed Abdulali. I employed the DeepCode AI tool to refine and optimize the code to better fit our requirements.

```
#include "stdafx.h"
#include <windows.h> // for time
#include <stdio.h>  // for time
#include <string>
#include <sstream>
#include <conio.h>
#include <cstdlib>
#include <direct.h>
#include<sys/stat.h>
#include<sys/types.h>
#include <iostream>
#include <fstream>
#include <sstream>
#include <time.h>
#include <cstdio>
#include <ctime>
#include <direct.h>
using namespace std;

// Serial number (or ordinal number if < 32) of PX14400 device to use
//#define MY_ACQ_BRD_NUM 2 // first board in system
// Selects the sampling rate to use. If not defined, app will prompt user
#define MY_SAMPLING_RATE_MHZ 80 // 40 MHz

double ClkRate;
int Mast_ch = 2;
```

```
int Slav_ch = 2;
#define MY_REMOTE_SERVER_ADDR "127.0.0.1"
#define MY_REMOTE_SERVER_PORT PX14_SERVER_PREFERRED_PORT
#endif



#define DUMP_SAMPLES 16  // added
void clearScreen(void);
int rain(string a);
string printTime();
bool checktime(int a, int b);

int real_main(int argc, char* argv[], string a,int counert1)
{
unsigned int serial_num;
HPX14 hBrd2, hBrd;

int res;
char choose = '2';
int MY_ACQ_BRD_NUM = 2;
unsigned int FileNum = 1; //1440 for 24 hours
char pDestFolder[35];  // Link into the destination folder
char foldername[25];
char ptemp[20] = { 'M','0','\0' };  // keep track of the file name
char temp[10];  // keep track of the file number
char ptemp2[30]; // keep track of the file number
clearScreen();
/*printf ("Press ESC to quit or Any other key to continue\n");
if (27 == _getch())
return 0;*/
//Number of Card to be used
```

```
//printf ("Choose The number of PX14400 devices Acquisition Cards to be used:
//printf("\n Enter your selection:");
//choose=_getch();
choose = '2';
switch (choose)
{
case '1':
{ MY_ACQ_BRD_NUM = 1; printf("\n You have choosen 1 ADC Card as stand alone.");
break; }
case '2':
{   MY_ACQ_BRD_NUM = 2; printf("\n You have choosen 2 ADC Cards as Slave/Slave c
break; }
default:
{ MY_ACQ_BRD_NUM = 2; printf("\n You have choosen 2 ADC Card as stand alone.");
break; }
}


//printf ("\nConnecting to PX14400 device(s)...\n");

res = ConnectToDevicePX14(&hBrd2, 1); // Connected to the second card Master
if (SIG_SUCCESS != res)
{
DumpLibErrorPX14(res, "Failed to connect to PX14400 device: ");
return -1;
}

if (MY_ACQ_BRD_NUM == 2)
{
res = ConnectToDevicePX14(&hBrd, 2); // Connected to the first card Slave
if (SIG_SUCCESS != res)
```

```
{
DumpLibErrorPX14(res, "Failed to connect to PX14400 device: ");
return -1;
}
}
#endif

fflush(stdin);
/*printf("\n Data Saving Folder Location:");
printf("\n please input the Main folder Name where data is to be saved: ");*/
// gets(foldername);  // the name of Main folder
strcpy(foldername, a.c_str());
/*printf("\n please input the file name:   ");
gets(ptemp); */ // Name of the files

if (!_mkdir(foldername))
printf("Folder %s has been created\n", foldername);
else
printf("Folder has not been created\n");

if (MY_ACQ_BRD_NUM == 2) // For Dual Card Recording
{
sprintf(pDestFolder, "%s\\%s", foldername, "ADC_Card2");

if (!_mkdir(pDestFolder))
printf("The folder %s has been created\n", pDestFolder);
else
printf("The folder has not been created \n");

sprintf(pDestFolder, "%s\\%s", foldername, "ADC_Card1");
if (!_mkdir(pDestFolder))
```

```
printf("ADC Card-2\n", pDestFolder);

}

/*printf ("\nDo you like to Stop now\n");
printf ("Press ESC to quit the program or Any other key to continue\n");
if (27 == _getch())
return 0;*/

if (MY_ACQ_BRD_NUM == 2)
{
GetSerialNumberPX14(hBrd, &serial_num);
printf(" - Connected to PX14400 #%u - Card 1\n", serial_num);
GetSerialNumberPX14(hBrd2, &serial_num);
printf(" - Connected to PX14400 #%u - Card 2\n", serial_num);

}
else
{
GetSerialNumberPX14(hBrd2, &serial_num);
printf(" - Connected to PX14400 #%u - Card 1\n", serial_num);
}


// Initialize data acquisition hardware settings
printf("Initializing hardware settings...\n");

res = AcqDeviceSetup(hBrd, hBrd2, MY_ACQ_BRD_NUM);  // Hardware settings

if (SIG_SUCCESS != res)
{
```

```
if (MY_ACQ_BRD_NUM == 2)
{

DisconnectFromDevicePX14(hBrd);
DisconnectFromDevicePX14(hBrd2);   // Disconnect from the device
}
else
{
DisconnectFromDevicePX14(hBrd2);   // Disconnect from the device
}
return -1;
}
Sleep(0000);
clearScreen();
if(counert1==1)
FileNum = 1;
else
FileNum = 60;
SYSTEMTIME  lt, ltp;
printf("\n Data acquisition in process ...\n");
GetLocalTime(&ltp);
printf(" Time %d : %d (hh:mm) \n", ltp.wHour, ltp.wMinute);

for (unsigned int counter = 1; counter <= FileNum; counter++)
{
if (_kbhit() && 27 == _getch())
{
break;   // Coming out of the loop by pressing the escape button
}
if ((counter % 50) == 0)
{
```

```
printf("\n  DisConnecting to PX14400 device(s)...\n");
res = DisconnectFromDevicePX14(hBrd2);
if (SIG_SUCCESS != res)
{
DumpLibErrorPX14(res, "Failed to disconnect to PX14400 device: ");
return -1;
}
Sleep(1000);
printf("\nConnecting to PX14400 device(s)...\n");
Sleep(1000);
res = ConnectToDevicePX14(&hBrd2, 1); // Connected to the second card Master
if (SIG_SUCCESS != res)
{
DumpLibErrorPX14(res, "Failed to connect to PX14400 device: ");
return -1;
}
Sleep(1000);

}

itoa(counter, temp, 10); // int to string

sprintf(ptemp2, "%s_%s", ptemp, temp);

clearScreen();
// Loops for record the files
printf("\n Data acquisition in process ...\n");

if (_kbhit() && 27 == _getch())
{
break;   // Coming out of the loop by pressing the escape button
```

```
}
res = RecordingMain(hBrd, hBrd2, 2, foldername, ptemp2, MY_ACQ_BRD_NUM);

if (SIG_SUCCESS != res)
{
if (MY_ACQ_BRD_NUM == 2)
{
DisconnectFromDevicePX14(hBrd);
DisconnectFromDevicePX14(hBrd2);   // Disconnect from the device
printf("One of the devices Failed to Record");
}
else
{
DisconnectFromDevicePX14(hBrd2);   // Disconnect from the device
printf("One of the devices Failed to Record");
}
return -1;
}



GetLocalTime(&lt);

lt.wHour, lt.wMinute);
while (1)
{
GetLocalTime(&lt);
// printf ("Time  %d : %d (hh:mm)", lt.wHour, lt.wMinute) ;
if (lt.wMinute == 0)
{
lt.wMinute = 60;
}
```

```
if (ltp.wMinute + 1 == lt.wMinute)
{
ltp.wMinute = lt.wMinute;
if (ltp.wMinute == 60)
{
ltp.wMinute = 0;
}
break;
}

if (_kbhit() && 27 == _getch())
{
break;
}
}
//printf ("Time  %d : %d (hh:mm) \n", lt.wHour, lt.wMinute) ;

}
printf("\n Data Acquisition Finished ...\n");

SetOperatingModePX14(hBrd2, PX14MODE_STANDBY);

// Disconnect from hardware.
if (MY_ACQ_BRD_NUM == 2)
DisconnectFromDevicePX14(hBrd);
DisconnectFromDevicePX14(hBrd2);

#if defined(CONNECT_TO_REMOTE_DEVICE)
SocketsCleanupPX14();
#endif
```

```
return 0;
}



int main(int argc, char* argv[])
{



int  month, read_month, res;
bool flag_a = true;
printf("Please select the month when to end the recording\n");
printf("1.January\n2.February\n.....\n12.December\n");
cin >> read_month;
if (read_month < 1 || read_month>12) {
printf("Error fail to select the monthe\n");
return(-1);
}
else {
switch (read_month)
{
case(1):
printf("You have selected January\n");
break;
case(2):
printf("You have selected February\n");
break;
case(3):
printf("You have selected March\n");
break;
case(4):
```

```
printf("You have selected April\n");
break;
case(5):
printf("You have selected May\n");
break;
case(6):
printf("You have selected June\n");
break;
case(7):
printf("You have selected July\n");
break;
case(8):
printf("You have selected August\n");
break;
case(9):
printf("You have selected September\n");
break;
case(10):
printf("You have selected October\n");
break;
case(11):
printf("You have selected November\n");
break;
default:
printf("You have selected December\n");
break;

}
}
int counter1 = 0;
while (flag_a)
```

```
{
clock_t timew;
timew = clock();

struct tm newtime;
time_t now = time(0);
localtime_s(&newtime, &now);
int Month = 1 + newtime.tm_mon;
int yy = newtime.tm_year;

if (read_month > Month)
yy = 0;
else
yy = yy + 1901;
if (checktime(read_month, yy))
yy = yy + 0;
else
{
cout << "The set time for recoding is finished\n";
Sleep(1000);
flag_a = false;
return 0;
break;
}

ostringstream oss;
oss << printTime();
//_mkdir(oss.str().c_str());

string lastLine;
```

```
string filename = "CR1000_PWS100_Data.dat";
ifstream fin;
fin.open(filename);
if (fin.is_open()) {

fin.seekg(-5, ios_base::end);                // go to one spot before the EOF

bool keepLooping = true;
while (keepLooping) {
char ch;
fin.get(ch);                              // Get current byte's data

if ((int)fin.tellg() <= 1) {
keepLooping = false;                 // So stop there
cout << "one\n";
}
else if (ch == '\n') {                    // If the data was a newline
keepLooping = false;                 // Stop at the current position.
cout << "two\n";
}
else {
fin.seekg(-2, ios_base::cur);

}
}



getline(fin, lastLine);                       // Read the current line
//cout << "Result: " << lastLine << '\n';     // Display it
```

```
fin.close();


}
else {
printf("the file couldn't be opned\n");
return(-1);
}
int n = rain(lastLine);

//cout << "time process = " << timew << endl;
//cout << "the lenght is =" << lastLine.length() << endl;
//cout<<"I am still\n";
Sleep(1000);
if (n) {
counter1 = 0;
res = real_main(argc, argv, oss.str().c_str(),60);
}
else {

clearScreen();
if (counter1 == 59) {
res = real_main(argc, argv, oss.str().c_str(),1);
counter1 = 0;
}
else {
counter1++;
}
timew = clock() - timew;
Sleep(60000 - timew);
}
//printf ("Press any key to exit...\n");
```

```
//_getch();
}
return res;
}

int AcqDeviceSetup (HPX14 hBrd,HPX14 hBrd2,int MY_ACQ_BRD)
{
int res, res2;
char choose= '1';

#if defined(MY_SAMPLING_RATE_MHZ)
ClkRate = MY_SAMPLING_RATE_MHZ;
#else
if (MY_ACQ_BRD==2)
   { printf("\n  Master and Slave configuration: \n\n");
res2 = SetMasterSlaveConfigurationPX14  (hBrd2, 0 );
if (SIG_SUCCESS == res2)
  printf(" - Card-2 set has the Master\n");
else {
DumpLibErrorPX14(res2, "Failed to set has master: ", hBrd2);
return -1;
}
res = SetMasterSlaveConfigurationPX14  (hBrd, 0 );
if (SIG_SUCCESS == res)
  printf(" - Card-1 set has the slave\n");
else {
DumpLibErrorPX14(res, "Failed to set has the slave: ", hBrd);
return -1; }
   }
Sleep (0000);
clearScreen();
```

```
printf("\n     Clock Source Settings ...\n");
  /* if (MY_ACQ_BRD==2)
   {
res =SetAdcClockSourcePX14 (hBrd, 1 );
if (SIG_SUCCESS == res)
  printf(" - Card-1 External clock\n");
else {
DumpLibErrorPX14(res, "Failed to set clock source: ", hBrd);
return -1;
}
}
   res2 = SetAdcClockSourcePX14 (hBrd2, 0 );
if (SIG_SUCCESS == res2)
  printf(" - Card-2 internal clock\n");
else {
DumpLibErrorPX14(res2, "Failed to set clock source: ", hBrd2);
return -1;
}*/
     Sleep (0000);
clearScreen();
// locking to external 10 MHz
printf("\n     Locking to external clock Settings ...\n");
    res2 = SetInternalAdcClockReferencePX14 (hBrd2, 1 );
if (SIG_SUCCESS == res2)
  printf(" - Card-2 lock the external clock\n");
else {
DumpLibErrorPX14(res2, "Failed to lock into external clock: ", hBrd2);
return -1;
}
Sleep (0000);
clearScreen();
```

B.3 PWS100 User Guide

The user guide can be accessed at: `https://s.campbellsci.com/documents/eu/manuals/pws100%20-%20658.pdf`

B.4 Sample of weather data table

CR_PWS_Data

44639x329 table

	1 TIMESTAMP_	2 PWS100_FaultStatus_	3 PWS100_AverageVisit	4 PWS100_AverageTem	5 PWS100_AverageRH_	6 PWS100_MinimumTemper	7 PWS100_MaximumTemperature_	8 PWS100_PrecipitationIntensity_	PWS
15398	2020-01-11 16:38:...	'Ok'	1.9998e+04	11.6400	84.3100	11.6500	11.6300	0.0744	
15399	2020-01-11 16:39:...	'Ok'	1.9998e+04	11.6300	84.4900	11.6300	11.6100	0.0864	
15400	2020-01-11 16:40:...	'Ok'	1.9998e+04	11.6000	84.4100	11.6100	11.5800	0.0406	
15401	2020-01-11 16:41:...	'Ok'	1.9998e+04	11.5700	84.5600	11.5800	11.5600	0.0140	
15402	2020-01-11 16:42:...	'Ok'	1.9998e+04	11.5500	84.6900	11.5600	11.5400	0.0243	
15403	2020-01-11 16:43:...	'Ok'	1.9998e+04	11.5400	84.7900	11.5500	11.5200	0.0065	
15404	2020-01-11 16:44:...	'Ok'	1.9998e+04	11.5100	84.7000	11.5200	11.4900	0.0480	
15405	2020-01-11 16:45:...	'Ok'	1.9998e+04	11.4900	84.8000	11.5000	11.4800	0.0448	
15406	2020-01-11 16:46:...	'Ok'	1.9998e+04	11.4900	84.9700	11.4900	11.4700	0.0035	
15407	2020-01-11 16:47:...	'Ok'	1.9998e+04	11.4700	84.8500	11.4700	11.4600	0.0081	
15408	2020-01-11 16:48:...	'Ok'	1.9998e+04	11.4600	84.7900	11.4700	11.4500	0.0219	
15409	2020-01-11 16:49:...	'Ok'	1.9998e+04	11.4500	84.7900	11.4500	11.4500	0.0038	
15410	2020-01-11 16:50:...	'Ok'	1.9998e+04	11.4500	84.8500	11.4600	11.4300	0	
15411	2020-01-11 16:51:...	'Ok'	1.9998e+04	11.4400	84.9800	11.4700	11.4200	0	
15412	2020-01-11 16:52:...	'Ok'	1.9998e+04	11.4200	84.6800	11.4300	11.4000	0	
15413	2020-01-11 16:53:...	'Ok'	1.9998e+04	11.3700	84.5100	11.3900	11.3400	0	
15414	2020-01-11 16:54:...	'Ok'	1.9998e+04	11.3500	82.2400	11.3700	11.3300	0	
15415	2020-01-11 16:55:...	'Ok'	1.9998e+04	11.3900	81.9300	11.4000	11.3800	0	
15416	2020-01-11 16:56:...	'Ok'	1.9998e+04	11.4100	81.9600	11.4100	11.3800	0	
15417	2020-01-11 16:57:...	'Ok'	1.9998e+04	11.3900	79.7000	11.3900	11.3700	0	
15418	2020-01-11 16:58:...	'Ok'	1.9998e+04	11.4000	79.0500	11.4100	11.3900	0	
15419	2020-01-11 16:59:...	'Ok'	1.9998e+04	11.4100	78.5900	11.4300	11.4000	0	

Figure B.1: Sample of raw weather data extracted from the .dat file.

Appendix C

Measurement Environment

C.1 Engineering building roof

Figure C.1: Direct 36 m link system environment: View of Tx from Rx1 position.

Figure C.2: Direct 36 m link system environment: View of Rx1 from Tx position.

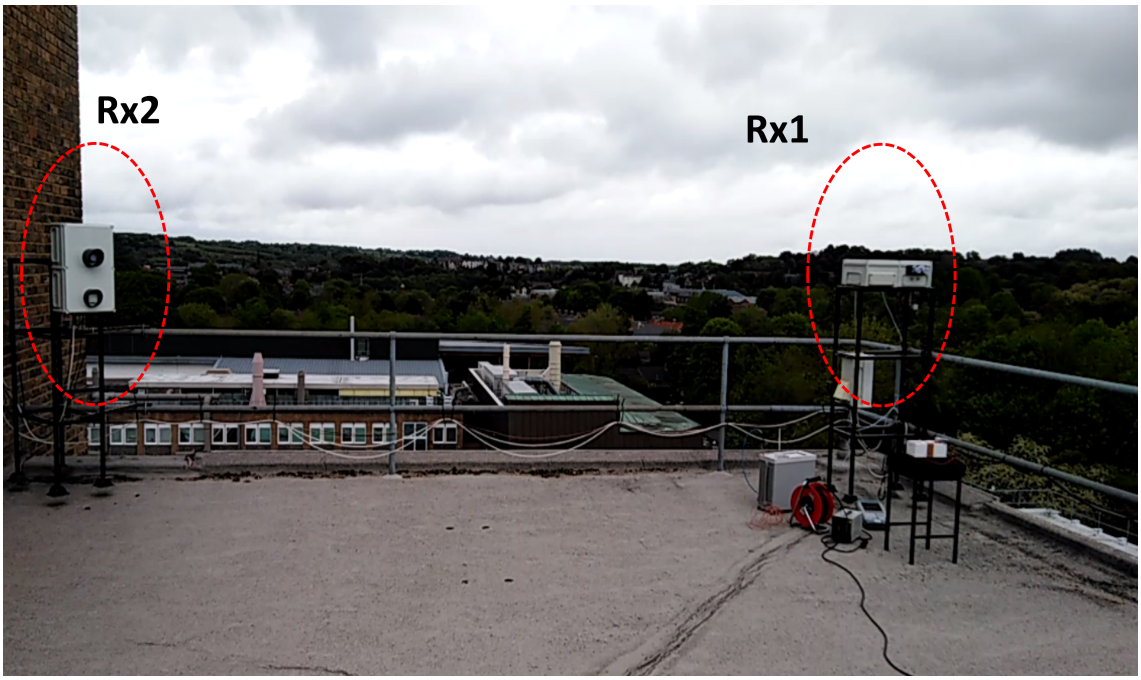

Figure C.3: Direct and Side 36 m receiver boxes system environment.

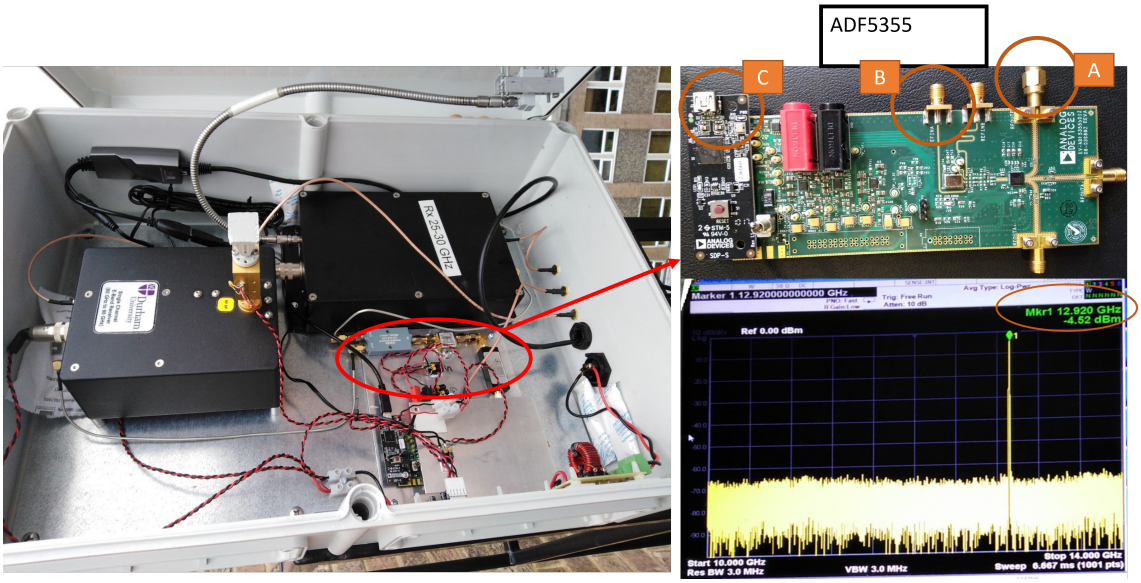

Figure C.4: Direct and Side 36 m receiver boxes signal stability test and PLL programming.

C.2 Library roof

Figure C.5: Filtronic measurement system between library roof and engineering roof building.